



New optical techniques and hardware for  
studying live cell dynamics.

Peter William Tinning

Submitted in fulfilment of the requirements for the degree of  
Doctor of Philosophy

Department of Physics

Faculty of Science

University of Strathclyde

August 29, 2018

# Declaration of Authenticity and Author's Rights

This thesis is the result of the author's original research. It has been composed by the author and has not been previously submitted for examination which has led to the award of a degree.

The copyright of this thesis belongs to the author under the terms of the United Kingdom Copyright Acts as qualified by University of Strathclyde Regulation 3.50. Due acknowledgement must always be made of the use of any material contained in, or derived from, this thesis.

X

---

Peter William Tinning

August 29, 2018

# Abstract

**F**luorescence optical microscopy has become an integral technique in the life sciences and has opened the door to investigating live biological specimens non-invasively at sub-cellular spatial resolutions with high specificity and temporal resolutions. One of the limiting factors of optical microscopy is that the spatial resolution is dictated by the diffraction limit of light.

This work shows the first use of LEDs to carry out widefield axial super-resolution standing wave microscopy with high temporal resolution. The technique was used to image red blood cell membrane dynamics in real time with no increase in photobleaching or toxicity rates compared to standard widefield imaging. This work also presents 3D computational reconstructions of the data allowing for easier visualisation and the possibility of carrying out further quantitative analysis.

Following on from Chapter 2, is an investigation into the development and application of multi-wavelength standing wave microscopy on live specimens in both emission and excitation modalities. These techniques are henceforth referred to in this thesis as TartanSW. This investigation found that using multiple excitation wavelengths allowed for a reduction in the nodal contribution of the images resulting in obtaining 32.3 % more spatial information about the structure of the specimen. It is also shown that by taking the difference images between each excitation channel the standing wave antinodal planes could be reduced in thickness enabling axial resolutions on the order of 55 nm when imaging live cell experiments. The multi-emission technique was shown that it could be

applied to be applied to imaging biological specimens using both widefield and confocal microscopy. However, the widefield data was not in line with the expected theoretical structure. There is the possibility of using plane ordering though to infer the directionality of a specimen structure and extract height maps though further work to develop computational tools to enable this will have to be implemented.

Finally, this thesis describes the work carried out making use of a new high-brightness 340 nm LED to develop a fast switching 340/380 nm illuminator and demonstrate its application for ratiometric Fura-2  $\text{Ca}^{2+}$  imaging of live cell specimens with sub-5 nM precision that supports full frame video-rate temporal resolutions.

# Contents

Chapter One: Introduction	pg. 35
1.1) Optical microscopy	pg. 35
1.1.1) Brightfield microscopy	pg. 36
1.1.2) Dark-field microscopy	pg. 38
1.1.3) Differential interference contrast microscopy	pg. 39
1.1.4) Phase contrast microscopy	pg. 40
1.2) Fluorescence microscopy	pg. 41
1.3) Spatial resolution in optical microscopy	pg. 48
1.4) Optical interference microscopy techniques	pg. 52
1.4.1) Interference reflection microscopy	pg. 53
1.4.2) Total internal reflection fluorescence microscopy	pg. 56
1.4.3) 4Pi microscopy and I <sup>5</sup> M	pg. 59
1.4.4) Structured illumination microscopy	pg. 64
1.4.5) Interference photoactivated localisation microscopy	pg. 65
1.4.6) Standing wave microscopy	pg. 68
1.5) Overview of thesis	pg. 68
Chapter Two: Single-colour widefield multi -planar standing wave imaging of red blood cells with high temporal resolution	pg. 71
2.1) Introduction	pg. 71

2.1.1)	Standing wave microscopy	pg. 73
2.1.2)	Red blood cells	pg. 77
2.1.3)	Motivation for work	pg. 78
2.2)	Materials and methods	pg. 79
2.2.1)	Preparation of fluorescently coated lens specimen	pg. 79
2.2.2)	Red blood cell isolation and staining	pg. 81
2.2.3)	Imaging apparatus and LED characterisation	pg. 82
2.2.4)	Image analysis and computational reconstruction	pg. 88
2.3)	Results	pg. 90
2.3.1)	Standing wave PSF simulation	pg. 90
2.3.2)	Standing wave imaging of fluorescently coated lens specimens	pg. 93
2.3.3)	Video-rate standing wave imaging of red blood cells	pg. 95
2.3.4)	Comparison between standing wave imaging and standard widefield epifluorescence imaging	pg. 98
2.4)	Discussion	pg. 102
2.5)	Conclusions	pg. 107

## Chapter Three: TartanSW emission and excitation imaging of live cell specimens

pg. 108

3.1)	Introduction	pg. 109
3.1.1)	TartanSW excitation microscopy	pg. 109
3.1.2)	TartanSW emission microscopy	pg. 112

3.2)	Materials and methods	pg. 116
3.2.1)	Specimen preparation and LED characterisation	pg. 116
3.2.2)	TartanSW emission imaging setup	pg. 120
3.2.3)	TartanSW excitation imaging setup	pg. 123
3.3)	Results	pg. 124
3.3.1)	Theoretical TartanSW PSF simulation and comparison to experimental lens standing wave data	pg. 124
3.3.2)	TartanSW emission imaging of live cell specimens	pg. 134
3.3.3)	TartanSW excitation imaging of live cell specimens	pg. 140
3.4)	Discussion	pg. 148
3.5)	Conclusions	pg. 158

## Chapter Four: Ratiometric Ca<sup>2+</sup> imaging of live cell specimens loaded with Fura-2 AM using a rapid switching 340/380 nm LED illuminator

pg. 160

4.1)	Introduction	pg. 160
4.1.1)	Methods for detecting intracellular Ca <sup>2+</sup>	pg. 161
4.1.2)	Light sources used for Fura-2 Ca <sup>2+</sup> imaging	pg. 164
4.2)	Materials and methods	pg. 166
4.2.1)	Characterisation of 340/380 nm and 350/380 nm LED system	pg. 166

4.2.2)	tsA-201 cell culture	pg. 170
4.2.3)	Primary hippocampal neuron culture	pg. 171
4.2.4)	Fluo-4 Ca <sup>2+</sup> imaging of pharmacologically induced Ca <sup>2+</sup> transients in live cell specimens	pg. 171
4.2.5)	Fura-2 ratiometric Ca <sup>2+</sup> imaging of pharmacologically-induced Ca <sup>2+</sup> transients in live cell specimens	pg. 174
4.2.6)	Imaging trypsin mediated Ca <sup>2+</sup> transients in tsA-201 cells using low concentrations of Fura-2 AM	pg. 178
4.2.7)	Fura-2 video-rate ratiometric Ca <sup>2+</sup> imaging of synaptically-driven Ca <sup>2+</sup> transients in hippocampal neurons using the 340/380 nm illuminator	pg. 178
4.2.8)	Data analysis and statistics	pg. 179
4.3)	Results	pg. 180
4.3.1)	Fluo-4 Ca <sup>2+</sup> imaging of pharmacologically induced Ca <sup>2+</sup> transients in live cell specimens	pg. 180
4.3.2)	Fura-2 ratiometric Ca <sup>2+</sup> imaging of pharmacologically-induced Ca <sup>2+</sup> transients in live cell specimens	pg. 181
4.3.3)	Full duration at the half maximum of the Ca <sup>2+</sup> responses obtained in hippocampal neurons when illuminating with either LED system	pg. 188
4.3.4)	Fura-2 Ca <sup>2+</sup> baseline fluctuation	

	measurements	pg. 189
4.3.5)	Imaging trypsin mediated $\text{Ca}^{2+}$ transients in tsA-201 cells using low concentrations of Fura-2 AM	pg. 195
4.3.6)	Fura-2 video-rate ratiometric $\text{Ca}^{2+}$ imaging of synaptically-driven $\text{Ca}^{2+}$ transients in hippocampal neurons using the 340/380 nm illuminator	pg. 197
4.4)	Discussion	pg. 199
4.5)	Conclusions	pg. 202
<b>Chapter Five: Conclusions</b>		pg. 203
5.1)	Summary	pg. 203
5.2)	Future work	pg. 206
<b>References</b>		pg. 208
<b>Appendix 1 – Calcium analysis MATLAB</b>		
	script	pg. 241

# List of Figures

Figure 1.1; A schematic diagram demonstrating the basic set up of a brightfield microscope. The illumination originates from below and propagates through a condenser lens to the specimen. The light that passes through the specimen plane is then collected by an objective lens after which it is projected onto a detector. Contrast between the specimen and background in this set up is only obtained through attenuation of the light which passes through the specimen. This figure is reproduced from [8].

pg. 37

Figure 1.2; A) Demonstration of how the illumination passes through the dark-field annulus and only light scattered by the specimen is collected by the objective lens. Adapted from [12]. B) Dark-field microscopy images of mammalian red blood cells infected with Plasmodium Vivax. Reproduced from [13].

pg. 38

Figure 1.3; A) Schematic diagram of the propagation of the illumination in a DIC microscope. B) DIC image of primary oocytes of the surf clam. Areas of shading occur in locations in which changes in the optical path length occur. A) and B) are reproduced from [14].

pg. 39

Figure 1.4; A) Optical path of the illumination in phase contrast microscopy. Diagram reproduced from [9]. Phase contrast image of a mammalian cell showing B) positive phase contrast and C) negative phase contrast on the right. B) and C) are reproduced from [16].

pg. 41

Figure 1.5; Jablonski diagram demonstrating the excitation and emission of light in a fluorophore. Reproduced from [67].

pg. 43

Figure 1.6; Diagram of light path from an arc lamp through upright widefield epifluorescence microscope to the specimen. The resultant emission light then propagates up through the filter cube to the eyepiece or photodetector Reproduced from [39]. pg. 45

Figure 1.7; Optical pathway through a laser scanning confocal microscope showing the rejection of out of focus light to the detector. The galvanometers are not included in this figure but would be placed between the dichroic mirror and the objective lens in order to raster scan the specimen. Reproduced from [42]. pg. 47

Figure 1.8; Demonstration of chromatic aberration as different wavelength of light are focussed to different locations. Reproduced from [88]. pg. 49

Figure 1.9; Demonstration of spherical aberration showing the light impinging upon the edges of the lens being focussed to a different point than those propagating near the centre. Reproduced from [91]. pg. 50

Figure 1.10; Demonstration of Rayleigh criterion showing a) a single diffraction pattern, b), two Airy discs at the minimum resolution, c), and two Airy discs being clearly resolved. Reproduced from [96]. pg. 51

Figure 1.11; Light path and microscope configuration for interference reflection microscopy. Reproduced from [103]. pg. 55

Figure 1.12; Human glioma cells, A) imaged using phase contrast microscopy B) using interference reflection microscopy showing the adherence points which are not visible in A). Reproduced from [65] . pg. 56

Figure 1.13; Diagram demonstrating the two objective lens illumination and collection of light with the theoretical maximum of  $4\pi$  and the experimentally realised detection angle. Reproduced from [121].

pg. 61

Figure 1.14; Schematic diagram showing components and beam paths in the original 4Pi microscope. Reproduced from [118].

pg. 61

Figure 1.15; Schematic diagram demonstrating the optical setup required to conduct I5M. Excitation light propagates from the bulb source through a short pass dichroic mirror and through a 50:50 beam splitter to illuminate the specimen from both sides. Emission is collected through both objective lenses and undergoes interference at the CCD camera. Reproduced from [87].

pg. 63

Figure 1.16; Demonstration of utilising the moiré effect to obtain a resolution enhancement. If an unknown structure A) is multiplied by a known pattern B) then the resulting image C) contains an increase in information on structure A). Reproduced from [146].

pg. 65

Figure 1.17; A) Schematic diagram of the microscope setup used for iPALM. The excitation and activation light sources are introduced to the specimen via the bottom objective lens only, with emission being collected through both objective lenses. The emission undergoes self-interference within the 3-way beamsplitter which is shown in greater detail in B). The spatially dependent phase difference induced intensity modulation which is seen in C) can then be used to determine the axial location of the emitting molecule by comparing the relative intensities

observed on each of the cameras. Figure reproduced from [103].

pg. 67

Figure 2.1; Cartoon diagram of the generation of an optical standing wave using a plane mirror, shown at the 0 location. The blue line is the incoming wave and the red line is the reflected wave. The black line is the standing wave which results from the interference between the red and blue waves.

pg. 72

Figure 2.2; Experimental setup from the initial standing wave experiments in 1985 showing the total internal reflection of the excitation light at the coverglass causing self-interference to occur within the specimen. [116].

pg. 74

Figure 2.3; A) Chemical structure of the fluorescent lipophilic dye, DiI. B) Excitation and emission spectra of DiI suspended in PBS [31].

pg. 81

Figure 2.4; Output spectra of A) 525 nm LED and B) 550 nm LED obtained at the specimen plane using the 525/50 clean-up filter.

pg. 84

Figure 2.5; Power of A) 525 nm LED and B) 550 nm LED measured at the specimen plane under an Olympus 100x/1.4 oil immersion lens.

pg. 85

Figure 2.6; A) Schematic diagram of experimental setup demonstrating the coupling of the 525 and 550 nm LEDs to the BX50 microscope system via liquid light guide and collimator. The excitation light then reflects off a >561 nm dichroic mirror to generate a standing wave due to self-interference at the mirror located at the specimen plane. This standing

wave of light causes fluorescence emission at the standing wave antinodes which then propagates upwards through the lens, dichroic mirror and long pass filter to be detected by the sCMOS camera. The fluorescence signals are recorded by the computer which synchronises and triggers the LED and camera. B) Magnified view of the specimen plane demonstrating on how the standing wave antinodal planes interact with the red blood cell.

pg. 87

Figure 2.7; Flow chart demonstrating the key computational steps carried out in order to obtain either the 2D reconstruction or the 3D reconstruction of the red blood cell standing wave movies.

pg. 90

Figure 2.8; Theoretical standing wave point spread function using a 525 nm LED as the excitation source and with a NA = 0.4 objective lens in air.

pg. 91

Figure 2.9; Theoretical standing wave point spread using a 525 nm LED as the excitation source and with a NA = 1.4 objective lens in 4% BSA and PBS.

pg. 92

Figure 2.10; Theoretical standing wave point spread function using a 550 nm LED as the excitation source and with a NA = 0.4 objective lens in air.

pg. 92

Figure 2.11; Theoretical standing wave point spread function using a 550 nm LED as the excitation source and with a NA = 1.4 objective lens with 4% BSA and PBS.

pg. 93

Figure 2.12; Standing wave images of the lens specimens obtained using the 525nm LED in A) air and C) 4% BSA and PBS. The radial averaged

plots obtained of the antinodal axial locations in B) air and D) 4% BSA and PBS using a camera binning  $n = 2$ . pg. 95

Figure 2.13; Single frames taken from the 525 nm LED video-rate standing wave movie of the bottom half of a red blood cell labelled with the membrane dye DiI using a camera binning  $n = 2$ . The frames presented as A-F are frames 1, 200, 400, 600, 800 and 999. pg. 96

Figure 2.14; Single frames taken from the 2D computational reconstruction of the 525 nm LED video-rate standing wave movie. The frames presented as a-f are frames 1, 200, 400, 600, 800 and 999. pg. 97

Figure 2.15; A 3D reconstruction of frame one of the standing wave red blood cell in which A) the axial aspect ratio has been increased to 13.33 to aid visualisation and B) the aspect ratios have not been altered. pg. 98

Figure 2.16; Average normalised intensity obtained from A) standing wave movies and B) widefield epifluorescence imaging of red blood cells ( $n = 10$ ) excited using a 550 nm LED with a power at the specimen plane of  $1.71 \pm 0.01$  mW. Errors in the values listed above are the SEM. pg. 100

Figure 2.17; Cropped and contrast adjusted standing wave images of a red blood cell. The frames presented as A-F are at time points 15, 360, 720, 1080, 1440 and 1800 s. pg. 101

Figure 2.18; Cropped and contrast adjusted standing wave images of a red blood cell. The frames presented as A-F are at time points 15, 360, 720, 1080, 1440 and 1800 s. pg. 101

Figure 3.1; Cartoon representation of the excitation intensity resulting from standing wave illumination along the optical axis of a microscope. A) A single standing wave excitation plot (red boxes) showing the separation between the bands and the widths of the antinodal and nodal planes. Location coinciding with the nodal planes result in zero fluorescence emission as the intensity of the standing wave is zero. B) A demonstration of the total reduction in the nodal plane contributions due to the addition of two extra optical standing waves of light (shown in green and blue) which have different wavelengths from the one in red. C) Demonstrates the colour mixing that occurs when the different excitation wavelength images are assigned RGB lookup tables and composited on top of each other. This diagram assumes that all standing wave excitation channels are normalised to each other. pg. 111

Figure 3.2; Confocal standing wave image of a lens specimen coated with a fluorescent monolayer of Atto 532, excited using a 514 nm laser line with emission and detected with a 5 nm emission bandwidth centred around 580 nm demonstrating the resulting moiré pattern generated by the interference of the excitation standing wave and the emission standing wave. Reproduced from [133]. pg. 114

Figure 3.3; Measured output spectra, taken at the specimen plane of a BX50 widefield microscope, of the A) 490 nm LED, and the B) filtered 525 nm LED. pg. 119

Figure 3.4; Schematic diagram of experimental setup for widefield TartanSW emission imaging of both lens and biological specimens. Specimen illumination was provided by a filtered 550 nm LED from the TartanSW-LED system that was coupled to the microscope using a universal collimator. The resulting fluorescence emission propagates

upwards through the 561 nm dichroic mirror and longpass filter through the extra camera magnification to the emission camera chip splitter. The emission is split using a  $>594$  nm dichroic mirror and is filtered through two bandpass filters before being detected by the sCMOS camera.

pg. 122

Figure 3.5; A) Theoretical standing wave structure simulated for 550 nm LED excitation. B) Theoretical standing wave structure simulated for 550, 525 and 490 nm LED excitation. C) Standing wave image of lens specimen using 550 nm LED excitation. D) Radially averaged intensity of the 550 nm LED excitation standing wave image. E) Standing wave image of lens specimen excited using 550, 525 and 490 nm LEDs showing a reduction in the information gap in the image. F) Radially averaged intensity of the 550, 525 and 490 nm LED excitation standing wave image showing the antinodal planes of the different excitation wavelengths coinciding with the nodal planes of the other standing wave structures.

pg. 126

Figure 3.6; A) Theoretical plot of the  $|550-525|$  difference standing wave structure (red) and the  $|525 - 490|$  difference standing wave structure (green) both obtained using equation (3.2). B) TartanSW difference image acquired from the difference of the 525 nm standing wave image of the lens specimen in figure 3.5 from the 550 nm standing wave image in air. C) TartanSW difference image acquired from the difference of the 490 nm standing wave image of the lens specimen in figure 3.5 from the 525 nm standing wave image in air. D) Composite of the two TartanSW difference images with B) in red and C) in green. E) Radially averaged line intensity plot taken of the composite image.

pg. 128

Figure 3.7; A) Widefield TartanSW emission PSF simulated for an 0.4 NA objective lens in air using an excitation wavelength of 549 nm and emission wavelengths of 570 nm (blue line) and 620 nm (red line) using equation (3.1). B) TartanSW emission image of a lens specimen excited using the 550 nm LED with the detection bandwidths centred around 576 nm and 620 nm. C) Line intensity plot for the 570 nm detection channel (blue line) and the 620 nm emission channel (red line) taken through the TartanSW emission image of the lens in B). pg. 131

Figure 3.8; Theoretical standing wave structure calculated using equation (3.1) for an excitation wavelength of 514 nm excitation and emission bandwidths A) 617 – 622 nm C) 592 – 597 nm and E) 567 – 572 nm. Experimental line intensity plot through a confocal TartanSW emission image of a lens specimen excited at 514 nm and emission detected at bandwidths B) 617 – 622 nm D) 592 – 597 nm and F) 567 – 572 nm. pg. 133

Figure 3.9; A) Frame one from a widefield TartanSW movie of a red blood cell imaged acquired at a rate of 30.30 Hz and excited using the 550 nm LED. B) Line intensity plot taken through the red blood cell (Gaussian blur = 2 applied) where the green line is the 570/10 nm emission band and the red line is the 620/14 nm emission band pg. 134

Figure 3.10; A) Confocal TartanSW emission image of a red blood cell excited at 543 nm and using emission detection bands of 550 - 555 nm (blue), 565 - 570 nm (green) and 580 - 585 nm (red) B) Line intensity profile taken through the red blood cell (Gaussian blur = 5 applied). pg. 136

Figure 3.11; A) Widefield TartanSW emission image of MCF-7 breast cancer cells excited using a 550 nm LED with emission detected at bandwidths of 570/10 nm (blue) and 620/14 nm (red). B) Line intensity plot taken through the periphery of the multi-emission image (with a Gaussian blur = 2 applied) with the shorter emission band being plotted in blue and the longer band plotted in red. pg. 137

Figure 3.12; Figure 3.12; Confocal TartanSW emission imaging of MCF-7 cells using emission detection bands 567 – 572 nm (blue), 592 – 597 nm (green) and 617 – 622 nm (red) and excited at A) 514 nm or B) 543 nm. Yellow arrow on A) demonstrates the direction and location that the line intensity plots were taken. C) Line intensity plot through the 514 nm excitation image (Gaussian blur = 5 applied) D) Line intensity plot through the 543 nm excitation image (Gaussian blur = 5 applied). It can be seen from a comparison of A) and B) as well as C) and D) that the TartanSW emission structures obtained using different excitation wavelengths are different from each other. This is to be expected as the TartanSW emission phenomena occurs due to the self-interference of the emission standing wave and the excitation standing wave. pg. 139

Figure 3.13; Widefield standing wave images of a red blood cell excited using A) the 490 nm LED B) the 525 nm LED and C) the 550 nm. D) A TartanSW excitation image made up of the images shown in A) through C). E) A line intensity profile taken through the composite TartanSW excitation image showing slight spectral separation between the excitation channels D) where fluorescence emission obtained from the 490 nm LED excitation is plotted in blue, the 525 nm LED is plotted in green and the 550 nm LED is plotted in red. pg. 141

Figure 3.14; A) Confocal TartanSW excitation imaging of red blood cells excited at 489 nm (blue), 513 nm (green) and 543 nm (red) with Gaussian blur = 2 applied. B) Line intensity profile taken through the right red blood cell in A). pg. 142

Figure 3.15; A) Widefield TartanSW excitation image of a DiI stained MCF-7 breast cancer cells excited using the 490 nm LED (blue), the 525 nm LED (green) and the 550 nm LED (red). B) Line intensity plot taken through the periphery of one of the MCF-7 cells in the TartanSW excitation image (with a Gaussian blur = 2 applied). pg. 143

Figure 3.16; A) TartanSW difference image of the MCF-7 cells shown in figure 3.15A where the difference of the 550 nm from the 525 nm is shown in red and the difference of the 525 nm from the 490 nm shown in green. B) Line intensity plot taken through the periphery of A) (with a Gaussian blur = 2 applied) demonstrating a reduction in the antinodal FWHMs compared to figure 3.15B and an increased image contrast. pg. 146

Figure 3.17; A) Widefield TartanSW excitation image of a MCF-7 breast cancer cell and B) TartanSW difference image between the excitation wavelengths showing the presence of structures within the cell that can be observed even through the nucleus. C) Confocal TartanSW excitation image of a MCF-7 breast cancer cell and D) TartanSW difference image between the excitation wavelengths also demonstrating an internal structure that can be seen in the bottom most cell pg. 147

Figure 3.18; Time lapse TartanSW difference multi-excitation images of MCF-7 cells with the  $|550 \text{ nm} - 525 \text{ nm}|$  channel in red and the  $|525 \text{ nm} - 490 \text{ nm}|$  in green showing an internal membrane structure that appears to

swell and burst throughout the imaging duration. The frames presented as A-F are frames 9, 17, 25, 33, 41 and 48. pg. 148

Figure 4.1; Chemical structures of the fluorescent molecule Fura-2 when either unbound or bound to intracellular  $\text{Ca}^{2+}$  adapted from [242].

pg. 163

Figure 4.2; Excitation spectrum of Fura-2 in buffer obtained at an emission wavelength of 510 nm in the presence of different concentrations of free  $\text{Ca}^{2+}$  [241]. pg. 163

Figure 4.3; Output spectra of 340 nm and 380 nm LEDs obtained at a driving current of  $1.52 \pm 0.16$  A. pg. 167

Figure 4.4; Output spectra of 350 nm and 380 nm LED. pg. 167

Figure 4.5; A )Optical powers measured at the specimen plane of an Olympus BX50 microscope under a 20x water dipping lens at increasing driving currents. B) Enlarged plot of ROI in A) showing the power ranges used in this Chapter. pg. 169

Figure 4.6; Generalised schematic diagram of experimental imaging setup showing the location of the specimen in relation to the objective lens and where the perfused solution flows over the specimen and gets removed from the bath. The light paths of the 470 nm LED are also shown to be collimated and then illuminate the specimen after being reflected by a  $> 505$  dichroic mirror. The emitted Fluo-4 fluorescence propagates upwards through the objective lens,  $>505$  nm dichroic mirror (Olympus) and 515 nm longpass filter (Olympus) to the camera. The camera and pE-4000 are connected to a computer system for triggering and recording fluorescent signals. pg. 174

Figure 4.7; Generalised schematic diagram of experimental imaging setup showing the location of the specimen in relation to the objective lens and where the perfused solution flows over the specimen and gets removed from the bath. The light paths of the 340/380 nm LEDs are also shown to converge through the use of 365 nm dichroic mirror and then illuminate the specimen in the perfusion bath sequentially. The emitted Fura-2 AM fluorescence propagates upwards through the objective lens, >400 nm dichroic mirror (Olympus) and 420 nm longpass filter (Olympus) to the camera. The camera and power supplies for both LEDs are connected to a computer system for triggering and recording fluorescent signals.

pg. 176

Figure 4.8; Representative trace of Fluo-4 emission fold increases above the baseline in tsA-201 cells with emission increases being induced by application of ATP (5  $\mu$ M) and trypsin (100 nM) and imaged a 470 nm LED.

pg. 181

Figure 4.9; A) Representative trace of normalised emission ratio changes in tsA-201 cells with  $\text{Ca}^{2+}$  changes being caused by application of ATP (5  $\mu$ M) and trypsin (100 nM) and imaged using the 350/380 nm LED illuminator. B) Representative trace of normalised emission ratio changes in hippocampal neurons with changes being caused by washes of glutamate (20  $\mu$ M) and KCl (20 mM) and imaged using the 350/380 nm LED illuminator.

pg. 182

Figure 4.10; A) Representative images of tsA-201 cells excited at both 340 nm and 380 nm. B) Representative images of hippocampal neurons excited at both 340 nm and 380 nm.

pg. 183

Figure 4.11; A) Representative trace of normalised emission ratio changes in tsA-201 cells with  $\text{Ca}^{2+}$  changes being caused by application of ATP (5  $\mu\text{M}$ ) and trypsin (100 nM) and imaged using the 340/380 nm LED illuminator. B) Representative trace of normalised emission ratio changes in hippocampal neurons with changes being caused by washes of glutamate (20  $\mu\text{M}$ ) and KCl (20 mM) and imaged using the 340/380 nm LED illuminator. pg. 184

Figure 4.12; Comparison of the pharmacologically-induced fluorescent fold increases above the baseline in tsA-201 cells obtained when illuminating with either the 340/380 nm illuminator or the 350/380 nm illuminator. pg. 185

Figure 4.13; Comparison of the pharmacologically-induced fluorescent fold increases above the baseline in hippocampal neurons obtained when illuminating with either the 340/380 nm illuminator or the 350/380 nm illuminator. pg. 186

Figure 4.14; A) Representative trace of cytosolic  $\text{Ca}^{2+}$  concentrations in tsA-201 cells with  $\text{Ca}^{2+}$  increases being caused by application of ATP (5  $\mu\text{M}$ ) and trypsin (100 nM) and imaged using the 340/380 nm LED illuminator. B) Representative trace of cytosolic  $\text{Ca}^{2+}$  concentrations in hippocampal neurons with calcium increases being caused by washes of glutamate (20  $\mu\text{M}$ ) and KCl (20 mM) and imaged using the 340/380 nm LED illuminator. pg. 187

Figure 4.15; FDHM of the  $\text{Ca}^{2+}$  responses evoked in hippocampal neurons imaged using either the 350/380 nm and the 340/380 nm LED illuminators. pg. 189

Figure 4.16; Representative plot of the noise observed in the normalised baselines of the hippocampal neuron whilst carrying out 0.5 Hz ratiometric Fura-2 Ca<sup>2+</sup> imaging of the specimens using the 340/380 nm illuminator. pg. 190

Figure 4.17; Representative plot of the noise observed in the normalised baselines of the hippocampal neuron whilst carrying out 0.5 Hz ratiometric Fura-2 Ca<sup>2+</sup> imaging of the specimens using the 350/380 nm illuminator. pg. 191

Figure 4.18; A comparison of the average baseline noise obtained in each specimen when illuminated with either the 340/380 nm system or the 350/380 nm system. pg. 192

Figure 4.19; Representative plot of normalised emission ratio obtained when imaging HEK-293 cells not loaded with Fura-2 AM. pg. 193

Figure 4.20; Representative plot of normalised emission ratio obtained when imaging hippocampal neurons not loaded with Fura-2 AM. pg. 194

Figure 4.21; Background corrected 340/380 nm emission ratios obtained from imaging solution with different concentrations of free Ca<sup>2+</sup>. The errors observed in the background corrected emission ratios is the SEM over the 60 second imaging period and the errors in the free calcium is the systematic error in the pipettes used. pg. 195

Figure 4.22; Comparison of 340/380 nm emission ratios obtained from cytosolic Ca<sup>2+</sup> increase when tsA-201 cells loaded with different concentrations of Fura-2 AM were perfused with trypsin (100 nM). pg.196

Figure 4.23; Comparison of 350/380 nm emission ratios obtained from cytosolic  $\text{Ca}^{2+}$  increase when tsA-201 cells loaded with different concentrations of Fura-2 AM were perfused with trypsin (100 nM).

pg.197

Figure 4.24; Spontaneous  $\text{Ca}^{2+}$  events are induced in  $\text{Mg}^{2+}$ -free HBS. A) representative trace from a single hippocampal neuron of  $\text{Mg}^{2+}$ -free induced  $\text{Ca}^{2+}$  events imaged at 0.5 Hz and B) representative trace from two hippocampal neurons of  $\text{Mg}^{2+}$ -free induced  $\text{Ca}^{2+}$  events imaged at 24.39 Hz.

pg.198

# List of Tables

Table 2.1; Antinodal spacings and FWHM in different media obtained from the theoretical PSFs of a 0.4 NA and 1.4 NA lens that were simulated using the excitation wavelength of 532 nm or 548 and an emission wavelength of 570 nm. pg. 91

Table 3.1; Comparison of experimentally determined anti-nodal spacings and FWHM obtained from 30 mm focal length lens specimen imaging in air and the theoretically determined values obtained using equation (2.5) where the peak excitation wavelengths were 490 nm, 524 nm and 549 nm, the peak emission wavelength was 570 nm. pg. 124

Table 3.2; A comparison of the experimentally and theoretically determined average FWHM and separation of the antinodal planes observed in the TartanSW difference images obtained in air. pg. 129

Table 3.3; A comparison of the experimentally and theoretically determined average FWHM and separation of the antinodal planes observed in the TartanSW images obtained in 4 % BSA and PBS. pg. 130

Table 3.4; Comparison of the imaging capabilities of interference based widefield super-resolution microscopy techniques. pg. 155

Table 4.1; Experimentally determined variables required for equation (4.1) at the experimental optical powers at the specimen plane used for each LED. pg. 180

Table 4.2; Baseline emission counts for each excitation wavelength obtained in specimens that were either unlabelled or loaded with Fura-2 AM.

pg. 192

# List of abbreviations

1,1'-Dioctadecyl-3,3,3',3'-Tetramethylindocarbocyanine	
Perchlorate	DiI
$\alpha$ -amino-3-hydroxy-5-methyl-4-isoxazolepropionic acid	AMPA
Acetoxymethyl esters	AM
Acid citrate dextrose	ACD
Aluminium gallium indium nitride	AlGaInN
Bovine serum albumin	BSA
Days in vitro	DIV
Differential interference contrast	DIC
Dimethyl sulfoxide	DMSO
Dulbecco's modified eagle medium	DMEM
Electron microscopy	EM
Fluorescence interference contrast	FLIC
Full duration at the half maximum	FDHM
Full width at the half maximum	FWHM
Gallium indium nitride	GaInN
Graphics processing unit	GPU
HEPES buffered saline	HBS

Infrared	IR
Interference reflection microscopy	IRM
Intracellular calcium	Ca <sup>2+</sup>
Light emitting diode	LED
Magnesium	Mg <sup>2+</sup>
N-methyl-D-aspartate	NMDA
Oxygen	O <sub>2</sub>
Phosphate buffered saline	PBS
Photoactivated green fluorescent protein	PA-GFP
Photoactivated localisation microscopy	PALM
Point spread function	PSF
Potassium chloride	KCl
Protease activated receptor 2	PAR2
Region of interest	ROI
Scanning probe microscopy	SPM
Standard error in the mean	SEM
Stimulated emission depletion	STED
Stochastic optical reconstruction microscopy	STORM
Structured illumination microscopy	SIM
Total internal reflection fluorescence	TIRF
Ultraviolet	UV

**All work included in this thesis, unless explicitly stated in the text, is the result of original research carried out by the author.**

# Acknowledgements

The road to this stage has been long, bumpy but entirely fulfilling with many enjoyable twists and turns. I'd like to thank first of all my supervisor Gail McConnell for always fighting my corner and giving me constant support. If it weren't for you, I would not be in this privileged position which some days I still can't believe has happened. Thank you to all my colleagues at CoolLED who made this work possible, specifically Gerry and Andy. The technical advice and custom equipment they provided was above and beyond what I could've expected, and I hope we can continue working together, or at the very least, keep in touch going into the future. I'd like to thank all of my fellow colleagues in the Mesolabs and everyone who I've had the pleasure of working with in SIPBS. I would not have been able to complete this body of work without you all. Of course, I would be remiss if I did not mention my loving family and friends, I think without them I would've broke down long ago. To anyone that I have overlooked or failed to mention it is not because you mean any less to me or your efforts are any less appreciated, I have just been writing for too long and I am glad to be done.

# Publications

[1] **P. W. Tinning, A. J. P. M. Franssen, S. U. Hridi, T. J. Bushell, and G. McConnell**, “A 340/380 nm light-emitting diode illuminator for Fura-2 AM ratiometric Ca<sup>2+</sup> imaging of live cells with better than 5 nM precision,” *Journal of Microscopy*, vol. 269, no. 3, pp. 1–9, 2017.

[2] **P. W. Tinning, R. Scrimgeour, and G. McConnell**, “Widefield standing wave microscopy of red blood cell membrane morphology with high temporal resolution,” *Biomedical Optics Express*, vol. 9, no. 4, pp. 1745–1761, 2018.

Few if any seemed to have grasped the Principle of Reality; new knowledge leads always to yet more awesome mysteries. Greater physiological knowledge of the brain makes the existence of the soul less possible yet more probable by the nature of the search.

STEPHEN KING

# Chapter One:

## Introduction

It is the aim of this Chapter to give the reader an overview of optical microscopy for life science imaging and a brief description of some interference based super-resolution microscopy techniques. It will first give details of label-free techniques which follows on to widefield fluorescence and confocal fluorescence microscopy. The Chapter will explore the resolution limits dictated by the diffractive nature of light and will conclude with a description of optical microscopy techniques that make use of the interference of light to surpass the diffraction limit of resolution.

### 1.1) Optical Microscopy

There are arguably three different families of microscopy which are available to the researcher. These are scanning probe microscopy (SPM), electron microscopy (EM) and optical microscopy [1]. While each of these different types of microscopy have their advantages and applications, for the imaging of live biological specimens optical microscopy has been predominantly employed [1] due to its ability to image live specimens on a cellular level, non-invasively and in atmospheric conditions. The ability to image in these conditions is an advantage that is not readily available in the other two categories of microscopy [1], though it should be noted that whilst environmental EMs are becoming more wide spread the technique is still more suited for fixed specimens [2] and are often used in conjunction with optical microscopy as is the case in correlative light and electron microscopy [3], [4]. Though optical microscopy is one of the most commonly used techniques for the imaging of live biological specimens, it has the limitation of not being able to achieve the atomic level spatial resolutions that are possible when using SPM or EM [5], [6].

### **1.1.1) Brightfield microscopy**

When carrying out the bright field imaging of biological specimens, cellular features and structures, which are typically colourless and translucent, can be difficult to distinguish from the background [7]. This is due to the fact that in bright field optical microscopy the only contrast that can be obtained from the specimen is due to attenuation and absorption of the light propagating through the specimen (a schematic diagram of how illumination light is passed through the specimen and detected is shown in figure 1.1). Though the contrast can be enhanced by utilising the application of an absorption stain to the cell [8], it cannot always be carried out on live specimens. This is due to the Beer-Lambert law, where the absorbance observed as light passes through a substance is related to the optical path length the light travels through and the concentration of the absorbing media. It follows from this that as cells are very thin, in order to obtain sufficient absorption of light the cells would tend to be prepared with toxic concentrations of stain, leading to death of the specimens. As such, the application of these stains usually necessitated for the specimens to be chemically fixed.

In many studies it can be advantageous, or even necessary, to image biological specimens live. The imaging of live biological specimens allows researchers to observe the behaviour of cells in a gas, humidity and temperature controlled environment that promotes healthy growth. Once a cell has been chemically fixed it can be thought of as being frozen in time, and whilst this allows for the observation of how the cell was behaving at the exact moment of fixation, without knowledge of how the cell dynamics were prior or how they would've progressed means that a greater depth of understanding about dynamic cellular processes cannot be obtained [9], [10]. This interest in imaging cells live has led to the necessary development of microscope techniques capable of optically increasing the image contrast between specimens and the background but facilitate imaging of the cells live.

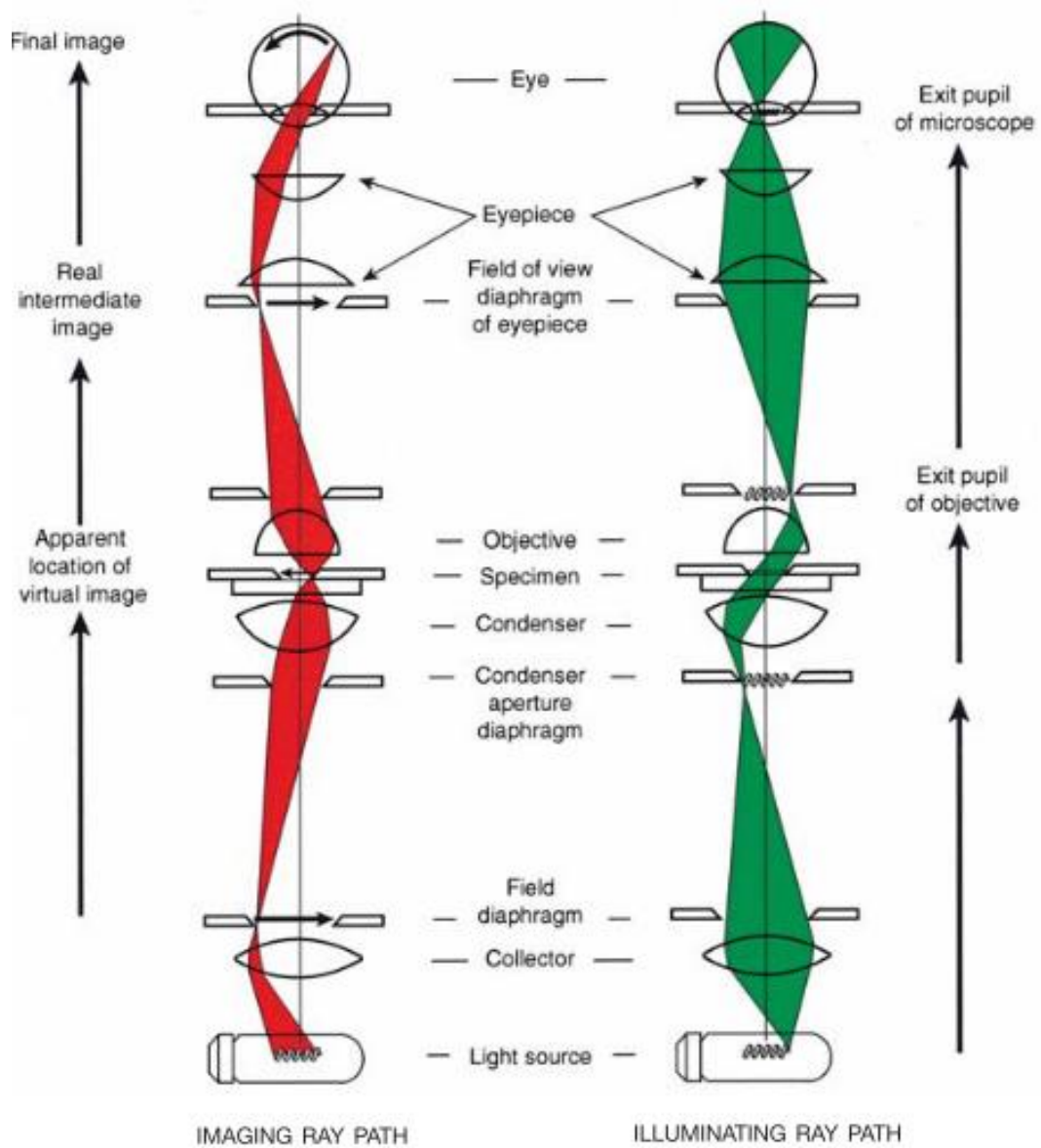


Figure 1.1; A schematic diagram demonstrating the basic set up of a brightfield microscope. The illumination originates from below and propagates through a condenser lens to the specimen. The light that passes through the specimen plane is then collected by an objective lens after which it is projected onto a detector. Contrast between the specimen and background in this set up is only obtained through attenuation of the light which passes through the specimen. This figure is reproduced from [8].

### 1.1.2) Dark-field microscopy

Dark-field microscopy has been used to enhance the contrast by making use of a hollow cone of light that originates from the very edges of the condenser lens, through the use of a special dark field condenser annulus, to illuminate the specimen. When the light passes through locations that are not occupied by the specimen it will appear dark in the image as only light scattered by the specimen is collected by the objective lens [11]. Limitations in this technique can be associated with the fact that only the periphery of the cells can be imaged meaning no internal structure is obtained, and also it is possible that contaminants, such as dust, at the specimen plane could also scatter the light and be detected in the image [12]. The process of how illumination interacts and is scattered by the specimen and an example image obtained using dark-field microscopy can be seen in figure 1.2.

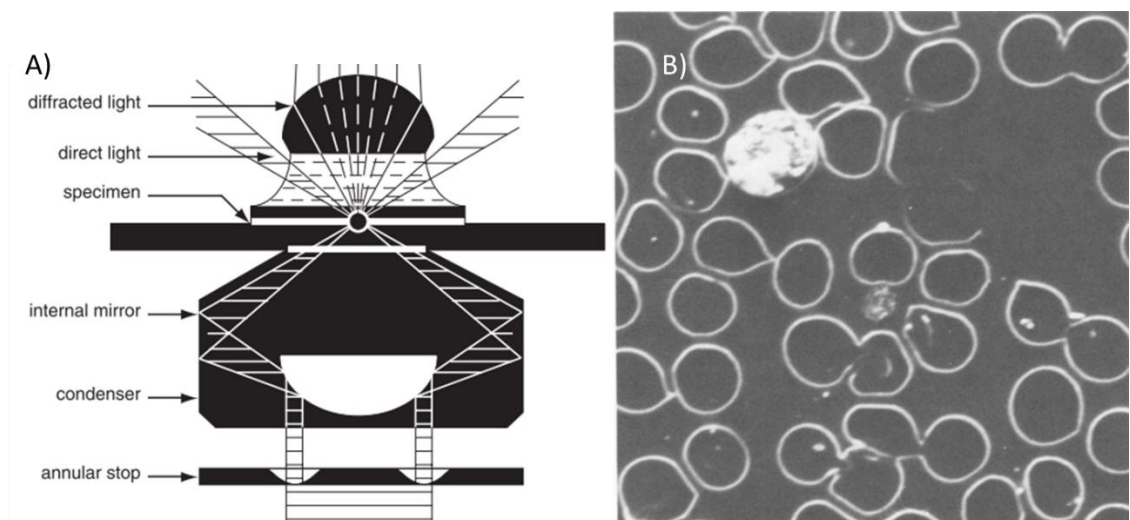


Figure 1.2; A) Demonstration of how the illumination passes through the dark-field annulus and only light scattered by the specimen is collected by the objective lens. Adapted from [12]. B) Dark-field microscopy images of mammalian red blood cells infected with *Plasmodium Vivax*. Reproduced from [13].

### 1.1.3) Differential interference contrast microscopy

Other methods for increasing image contrast make use of the different thicknesses or refractive indices that exist within cell specimens. One such technique is differential interference contrast imaging (DIC), in which polarized light is split into two separate light beams by a Wollaston quartz prism. These two beams then propagate through the specimen at spatially separate points and are recombined by another Wollaston prism before passing through an analyser [14]. In DIC, the contrast of the image is enhanced by observing the difference in the optical path lengths of the split polarized light. If one light path travels through an area with a different refractive index or thickness than the other, then it will begin propagating slightly out of phase with the other. When the two beams are recombined interference will occur causing darker locations on the resulting image where the cellular refractive index changes occur [15]. A schematic diagram of DIC microscope and a DIC image can be seen in figure 1.3.

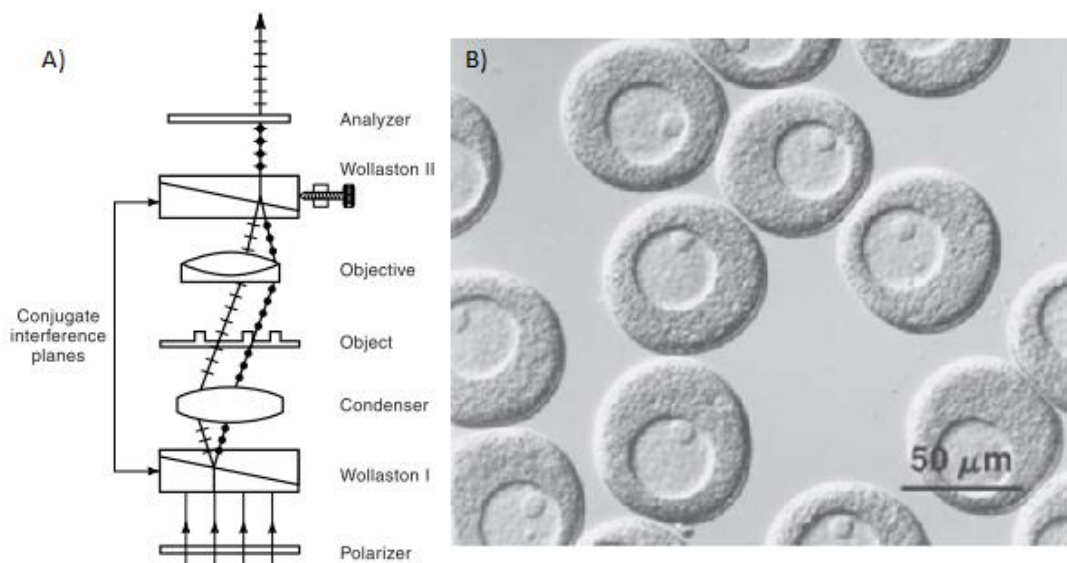


Figure 1.3; A) Schematic diagram of the propagation of the illumination in a DIC microscope. B) DIC image of primary oocytes of the surf clam. Areas of shading occur in locations in which changes in the optical path length occur. A) and B) are reproduced from [15].

#### 1.1.4) Phase contrast microscopy

Another well-established label-free technique to improve the contrast of cell imaging is phase contrast microscopy. In this method, a condenser annulus is placed before the condenser lens in a microscope which causes the light passing through to take on a 'ring' shaped beam profile, shown in figure 1.4. Any light which propagates through the specimen will be diffracted and undergo a phase shift, typically  $\lambda/4$  but even less can occur, where  $\lambda$  is the wavelength of light used for illumination [16]. The light that does not interact with the specimen remains unchanged until it encounters a phase plate placed, or etched, in the back focal plane of the microscope objective lens which must be precisely aligned to the condenser annulus. This phase plate affects only the non-diffracted light and causes either a phase shift advance of  $\lambda/4$  or a phase retardation of  $3\lambda/4$ , depending on whether positive or negative phase contrast is being employed [17]. In negative phase contrast imaging the diffracted and non-diffracted beam undergo destructive interference causing objects with a higher refractive index than the surroundings to appear brighter whilst the opposite occurs in the more commonly used positive phase contrast imaging [17].

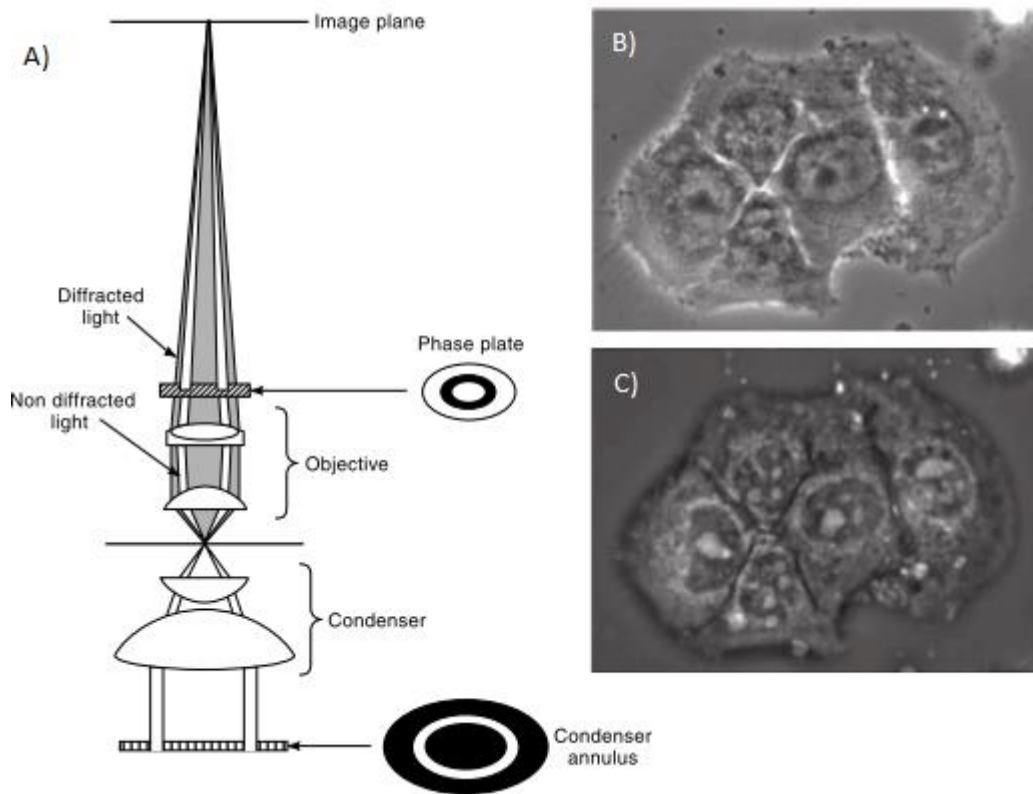


Figure 1.4; A) Optical path of the illumination in phase contrast microscopy. Diagram reproduced from [11]. Phase contrast image of a mammalian cell showing B) positive phase contrast and C) negative phase contrast on the right. B) and C) are reproduced from [17].

## 1.2) Fluorescence Microscopy

Though the techniques described in Section 1.1 can enhance the contrast of biological specimens from the background, they do not help to identify internal structures or proteins with any specificity or contrast from the surrounding cell which led to the development of fluorescent microscopy.

The properties of fluorescence were first described and named by G. G. Stokes in 1852 [18] but had been observed as far back as 1565 by Nicholas Monardes [19]. Fluorescence microscopy is now one of the most commonly used techniques for imaging biological specimens and has a wide range of organic and synthetic

fluorophores which are capable of binding to, or labelling, specific cellular structures. The use of fluorophores in conjunction with live cell specimens, or even whole organisms, has allowed for the study of dynamic cellular processes of specific sub-cellular structures in response to different stimuli or over time. The ability to label the membrane or cytoskeleton of cells means that the morphological changes can be observed during processes such as mitosis or blebbing [20], [21], voltage-sensitive dyes are available which means that the firing of neurons can be quantified or tracked [22], and the detection of intra-cellular ion concentration changes has allowed for pharmacological studies to be carried out revealing the effects drugs have on different types of cells [23]–[25], none of these would be possible to do with fixed cell specimens. Using fluorescence labelling, even multiple parts of the cell can be labelled with different fluorophores which allows greater distinction between these labelled structures using multi-colour imaging and also the added advantage that the behaviour of multiple structures can be measured in response to the same stimuli providing a greater understanding of how the entire cell reacts.

When a photon is absorbed by a fluorophore the energy transfer can excite an orbital electron from the ground state into a higher singlet excited state. From this excited state it may undergo radiative decay back to ground state and emit a photon [26]. There is an increase in wavelength observed in the emitted photon which is due to non-radiative energy decay, typically phonon vibrations, before the electron returns to the ground state. This emission occurring at a longer wavelength is known as a Stokes shift [26] and the entire process is known as fluorescence. A diagram demonstrating this process can be seen in figure 1.5 and is known as a Jablonski diagram.

The excitation and emission of fluorescence is a rapid process but not every photon which is absorbed by a fluorophore will cause fluorescence emission. A fluorophore has an associated quantum yield which is defined as the ratio of the number of photons emitted to the number of photons absorbed by the fluorophore [27]. This quantum yield will always be less than one due to the presence of some non-radiative decay processes occurring.

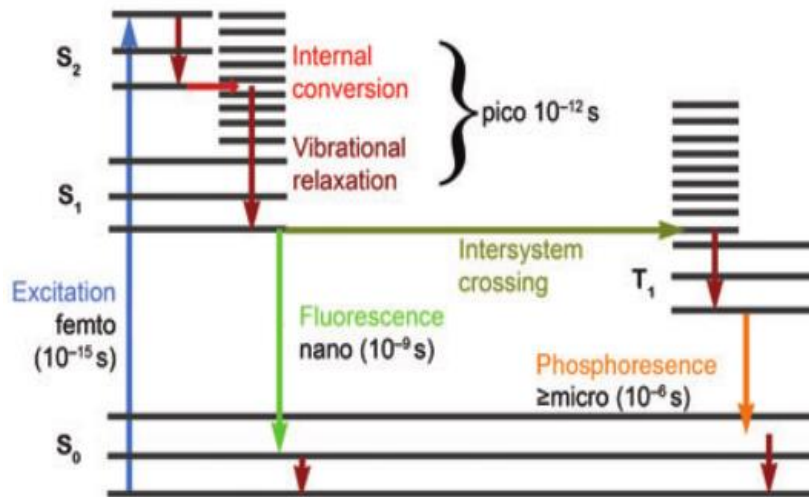


Figure 1.5; Jablonski diagram demonstrating the excitation and emission of light in a fluorophore. Reproduced from [28].

If a fluorophore is repeatedly excited over a prolonged period or with an intense light source the fluorescence emission will begin to fade and eventually stop altogether. This is due to a phenomena known as photobleaching [29]. Photobleaching is a process in which the fluorophore undergoes permanent photochemical destruction whilst the molecule is in the excited state and once it has occurred the fluorescence cannot be recovered [30]. This process has been attributed to molecular oxygen interacting with the fluorophore when in the excited triplet state or generating highly toxic oxygen species [31], [32]. Photobleaching can be a major issue when using fluorophores for microscopy though it has been shown that the addition of oxygen scavenging molecules to remove the molecular oxygen in the system can reduce the rate at which photobleaching occurs [33]–[36]. Another method used to reduce the rate of photobleaching to the dye is to make use of stroboscopic illumination which reduces the light dosage exposed to the specimen [37], [38].

Another issue which can occur when using fluorescence in conjunction with live biological specimens is known as phototoxicity. Phototoxicity is the process in which during imaging the specimen undergoes unwanted and harmful changes which can lead to cell death. This process can occur when the specimen is exposed to high intensity light which may cause a heat stress response in the specimen resulting in cell death [39]. Another mechanism leading to phototoxicity is caused by the production

of free radicals which can detrimentally interact with different cellular structures within the specimen [40]. Similar to the techniques used to reduce photobleaching rates during imaging, in order to lessen the phototoxic effects a reduced light dosage can be used or imaging can be carried out using techniques such as light sheet or two-photon microscopy [37], [38], [41], [42]. It should be noted though that reducing the excitation light by too much can significantly reduce the signal to noise ratio and impact the quality of the images recorded [42] so efficient detection of the resultant emission must be carried out.

To utilise fluorescent probes in life science imaging, a microscope had to be developed which was capable of separating the shorter wavelength excitation light from the emitted longer wavelengths of light from which the image is formed. This led to the first widefield epifluorescence microscope in 1959 that was further developed into what is now regarded as the modern widefield epifluorescence microscope by Johan Sebastiaan Ploem in 1967 [43]. This type of microscope uses dichroic filters to separate the excitation and emission light and uses a single objective lens for illumination and light collection.

The widefield epifluorescence microscope can either be of the inverted configuration, where illumination of the specimen comes from below, or upright type, where the specimen is illuminated from above. Widefield epifluorescence microscopes can use a variety of sources for illumination such as high power light emitting diodes (LEDs), mercury/xenon arc lamps or lasers (though the latter may not be entirely suitable for widefield microscopy as the highly coherent laser may generate reflections from dust particles or imperfections in the optical path and undergo interference which can cause artefacts on the image [44], [45]). The illumination is passed through a filter cube which typically comprises of an excitation filter, which limits the propagating bandwidth of light, a dichroic mirror and an emission filter. The light is then reflected off the dichroic mirror which is set at an angle of 45 degrees in reference to normal incidence and then propagates through an objective lens which then illuminates the specimen.

If the illumination light is of an appropriate wavelength to excite the orbital electrons of the fluorophore to an excited state then any emitted fluorescence is collected

through the same objective lens and propagates through the dichroic mirror which is designed to reflect light which is shorter than a chosen wavelength. For instance, if light of 470 nm is used to excite a fluorophore which will emit at 520 nm, a 505 nm dichroic mirror will reflect all excitation light as it is shorter than 505 nm and will transmit all of the fluorescence emission. The light then passes through an emission filter, typically a longpass filter which is chosen to reject all the shorter excitation wavelengths which may have bled through to this optical element but accept all of the emission light [36]. This light then propagates either to an eyepiece for visual inspection or to a photodetector device for digital imaging and recording. A general diagram of the light path through an upright widefield epifluorescence microscope is shown in to figure 1.6.

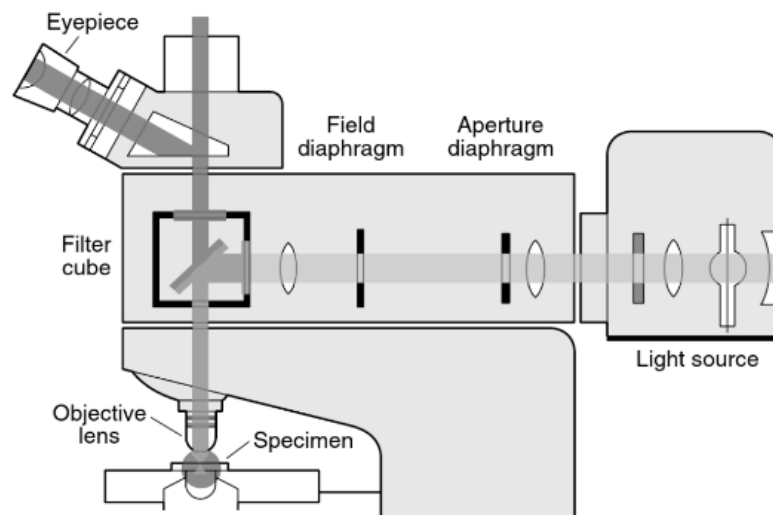


*Figure 1.6; Diagram of light path from an arc lamp through upright widefield epifluorescence microscope to the specimen. The resultant emission light then propagates up through the filter cube to the eyepiece or photodetector Reproduced from [46].*

While the widefield epifluorescence microscope has many uses and is very versatile, there are some disadvantages to its operation. One of these is due to the illumination of the specimen not just occurring at the focal plane but the microscope also provides excitation above and below this plane. This causes a large amount of out of focus fluorescence to be generated causing the background intensity to be increased and a loss of contrast in the images [47]. This excitation of the volume surrounding the focal

plane also causes a high amount of photobleaching to fluorophores that are not of interest [47].

The need to increase the contrast in images taken of three-dimensional specimens by reducing the out of focus fluorescence present in the image led to the development of the confocal microscope. The first concepts and microscope development for the elimination of the out of focus light came from Marvin Minsky in 1957 [22] but it was not until 1987 when the two separate groups, Carlsson and Aslund, and White, Amos and Fordham produced the first laser scanning confocal microscopes [48].

The basic principle behind confocal detection is the use of a point source of illumination and a pin hole which is placed in the focal plane before the detector. The pin hole will reject all of the out of focus light so only the light from the focal point reaches the detector [47]. Figure 1.7 shows this in operation and as a result of the reduction in the out of focus light the background fluorescence is greatly reduced increasing the contrast of the images [47].

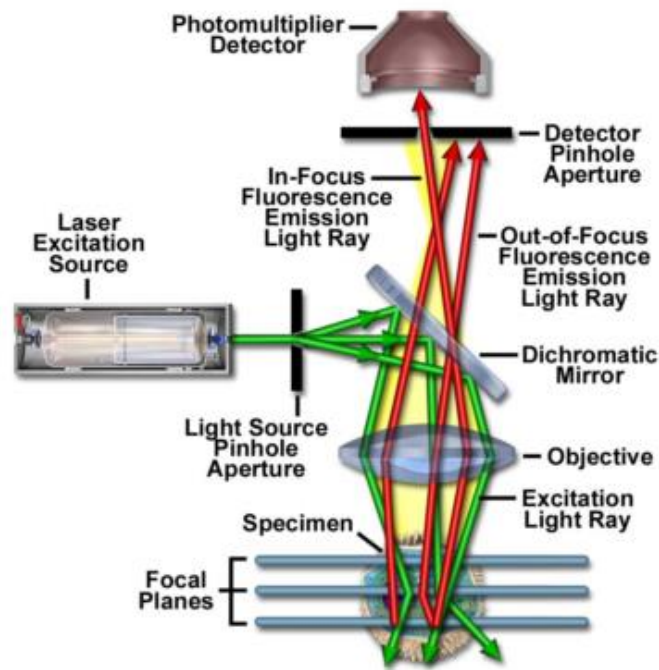


*Figure 1.7; Optical pathway through a laser scanning confocal microscope showing the rejection of out of focus light to the detector. The galvanometers are not included in this figure but would be placed between the dichroic mirror and the objective lens in order to raster scan the specimen. Reproduced from [49].*

A laser scanning confocal microscope has many of the same optics as the widefield epifluorescence to select excitation wavelengths and isolate the emitted light from the specimen. The main difference, aside from the pin hole, is the inclusion of the two mirror galvanometers that are used to raster the laser point across the specimen in the x and y direction to create an image point by point rather than illuminating the entire field like in a widefield epifluorescence microscope which results the confocal microscope having a lower temporal resolution [48]. Due to the rejection of the unwanted light, the laser scanning confocal microscope is capable of performing optical sectioning which is the imaging of clear focal planes within the specimen, though the out of focus fluorophores are still being excited so photobleaching of these molecules can still be an issue [50] .

While the confocal microscope can reject the out of focus light, both this and the widefield epifluorescence microscope have their spatial resolutions dictated by what is known as the diffraction limit.

### 1.3) Spatial resolution in optical microscopy

A commonly held definition for the spatial resolution of an optical microscope is the smallest separation between two objects at which they can still be distinguished as two separate points [51]. The limits of resolution of a microscope were first described by Ernst Abbe in 1873 [52]. Abbe demonstrated the need for optical lenses to be designed in such a way that the resolution of systems were limited by only the diffraction of light between the specimen (which can be treated as a diffraction grating) and the lens rather than any optical aberrations in the lens [52].

Lens aberrations that are commonly corrected for include chromatic aberrations, a process in which light of different wavelengths are focused to different points after passing through the same lens (shown in figure 1.8). This type of aberration is caused by the refractive index of a material,  $n$ , being related to the wavelength of light propagating through the material due to a property known as dispersion [53]. The refractive index of a material can be obtained from:

$$n^2(\lambda) = 1 + \frac{B_1\lambda^2}{\lambda^2 - c_1} + \frac{B_2\lambda^2}{\lambda^2 - c_2} + \frac{B_3\lambda^2}{\lambda^2 - c_3} \dots \quad (1.1)$$

In equation (1.1),  $B$  and  $C$  are known as the Sellmeier coefficients of a material and  $\lambda$  is the speed of light in a vacuum. The refractive index of a material can also be described as the ratio of the speed of light in a vacuum,  $c$ , over the phase velocity of the light when propagating through the medium,  $v_p$  [54]:

$$n = c/v_p \quad (1.2)$$

The phase velocity of the light is wavelength dependent which effects the angle of refraction experienced by different wavelengths of light [54]. To correct for this type of aberration, objective lenses have been designed to incorporate multiple lens elements with different levels of dispersion to bring different wavelengths of light to the same focus [53].

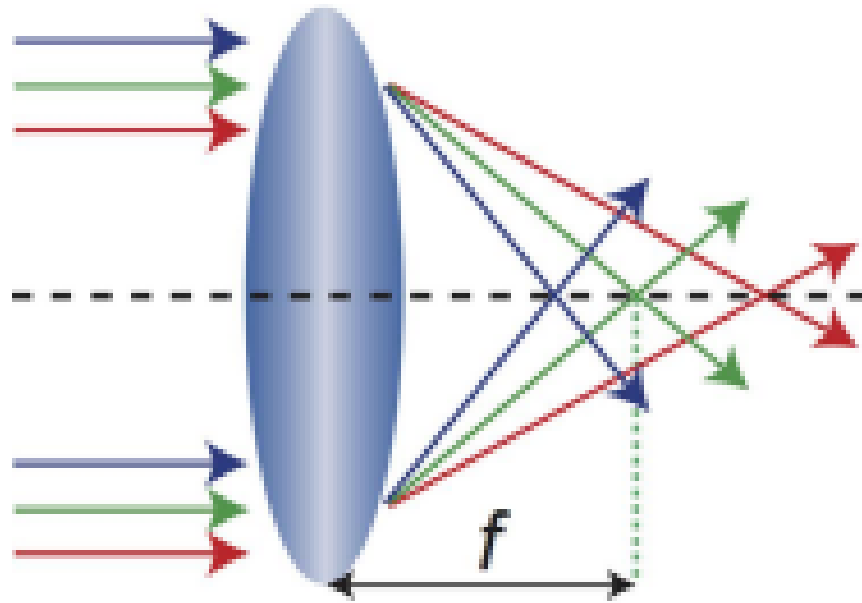


*Figure 1.8; Demonstration of chromatic aberration as different wavelength of light are focussed to different locations. Reproduced from [53].*

Another common type of aberration is known as spherical aberration. Spherical aberration is a phenomenon where light propagating through the periphery of a lens is focussed to a point closer to the lens than the light which propagates near the centre of the lens (shown in figure 1.9) [55]. This aberration is worsened as the diameter of the lens increases [56]. This process can also occur when using a microscope with an incorrect tube length [57] or the specimen being imaged has a different refractive index from the surrounding mounting medium [58]. Methods to reduce the presence of this aberration are to use the correct tube length for the microscope system, reduce the difference between the refractive indices of the specimen and surrounding medium or by reducing the diameter of the lens through which the light is focussing [55].

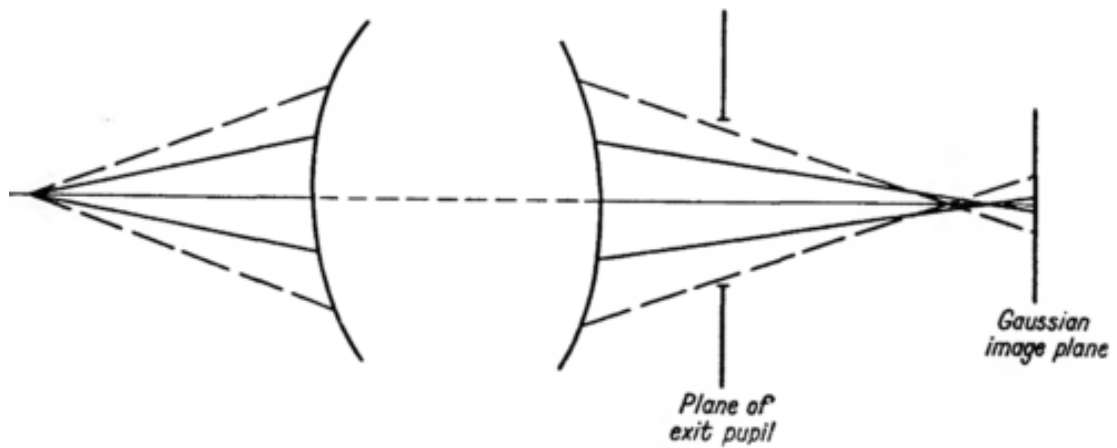


*Figure 1.9; Demonstration of spherical aberration showing the light impinging upon the edges of the lens being focussed to a different point than those propagating near the centre. Reproduced from [56].*

There are several different criteria which can be applied to an optical microscope system to describe the resolution such as; Nyquist theorem, full width at half maximum (FWHM) of the point spread function (PSF), Fourier based definitions or the Sparrow criteria [59]. Each criterion is capable of giving a resolution limit to a microscope system, but this section will describe the Rayleigh criterion which is commonly used to describe the resolution of microscope systems [60].

When light is focused through a theoretical aberration free objective lens it forms a diffraction limited spot of finite size. When magnified this focal spot has a central maxima spot (containing 84% of the light) surrounded by a series of concentric rings of decreasing intensity [61]. The central maxima of this diffraction spot is known as an Airy disk, named after Sir George Airy, and its diameter is related to the wavelength of light [61]. This diffraction limited spot occurs in all three dimensions and is known as the PSF.

In the lateral directions,  $x$  and  $y$ , the Rayleigh minimum resolution limit states that the diffraction patterns of two spatially close objects are resolved at the point which the Airy disk centre of one object overlaps with the first minimum of the others diffraction spot [51] and this is illustrated in figure 1.10.

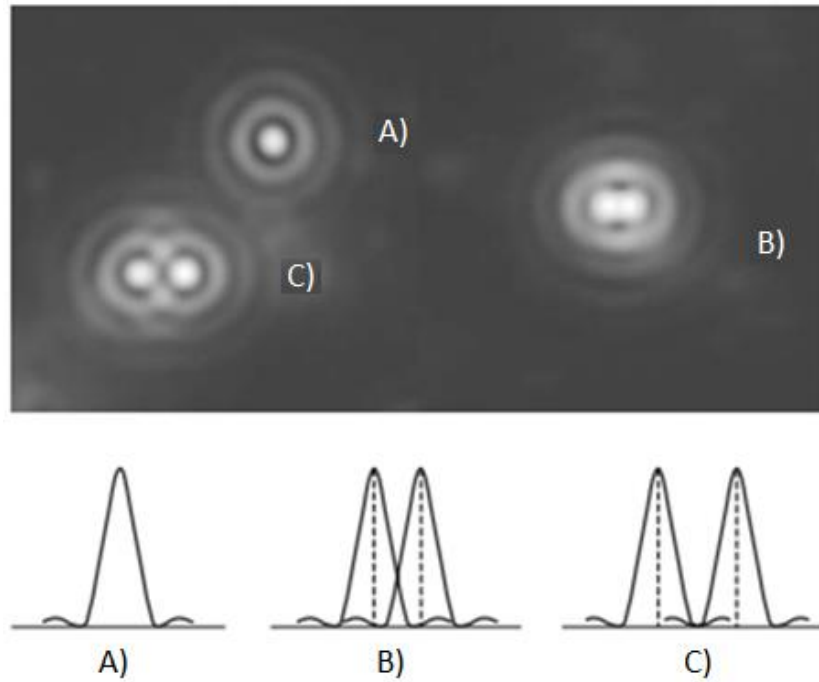


Figure 1.10; Demonstration of Rayleigh criterion showing a) a single diffraction pattern, b), two Airy discs at the minimum resolution, c), and two Airy discs being clearly resolved. Reproduced from [62].

The equation describing the minimum lateral resolution is given by [60]:

$$d = \frac{1.22\lambda}{NA_{objective} + NA_{condenser}} \quad (1.3)$$

In equation (1.3),  $d$  is the minimum resolvable distance,  $\lambda$  is the wavelength of light, and NA is the numerical aperture of the condenser or objective lens used. The numerical aperture is given by the equation:

$$NA = n \sin(\theta) \quad (1.4)$$

In equation (1.4),  $n$  is the refractive index of the medium between the specimen and the lens, and  $\theta$  is the half angle of the cone of light which is either emitted by the condenser or accepted by the objective lens. In both widefield and confocal epifluorescence microscopy the excitation illumination and fluorescence emission propagate through same objective lens and as a result the condenser and the objective lens have the same NA. Equation (1.3) can therefore be rewritten to give the minimum lateral resolution of a widefield epifluorescence microscope:

$$d = \frac{0.61\lambda}{NA_{objective}} \quad (1.5)$$

From these equations, it is evident that the theoretical minimum lateral resolution of a microscope system is dictated by the wavelength of light used and the NA of the objective lens.

The PSF is a 3D spot but does not have a uniform intensity distribution in all three directions [59]. The PSF is elongated in the axial direction (z) compared to the lateral (x, y). This elongation is due to the self-interference of a spherical wave front cap [1]. The axial PSF, like the lateral, has a central maxima intensity, but in an oval shape, with surrounding periodic “side lobe” maxima of decreasing intensity [63]. The minimum resolvable axial distance is given by the following equation [60]:

$$z = \frac{2n\lambda}{NA^2} \quad (1.6)$$

It was long thought that these limits on the resolution in microscopy were unable to be surpassed, though using a confocal laser scanning microscope [48] offers a resolution improvement on the order of  $\sqrt{2}$  over widefield epifluorescence microscopy [64]. In recent years, there have been a wide variety of techniques developed which can surpass the resolution limits stated above and have raised many new and exciting possibilities in life science imaging.

## **1.4) Optical interference microscopy techniques**

Many cellular processes cannot always be imaged using widefield or confocal microscopy as they are smaller than the resolution limit, and these structures would remain inaccessible to optical microscopy until the development of super-resolution techniques. Whilst there are now many different super-resolution techniques that are compatible with live cell imaging such as stimulated emission depletion (STED) microscopy [65]–[67] or stochastic optical reconstruction microscopy (STORM) [68]–[70]. Since the majority of the work in this thesis is exploring the application of standing wave microscopy to carry out live cell super-resolution imaging, this section

will only discuss and give the background on microscopy techniques that make use of optical interference to achieve super-resolution.

### 1.4.1) Interference reflection microscopy

The first comprehensive study of optical interference was carried out by Newton in 1717 where he observed the successive reflections of light between a convex lens and a piece of glass which were caused by constructive and destructive interference due to the differences in optical path length and relative phase changes [71].

Interference reflection microscopy (IRM) was originally developed to investigate thin films of oil [72] and was first used in cell biology by Adam Curtis in 1964 to study embryonic chick heart fibroblasts and their adhesion to glass substrates [73]. This technique operates using the principle of light reflection at refractive index boundaries. When using this method to measure cellular adhesion to a glass coverslip these boundaries will either be between the coverslip and the cell or the coverslip and the specimen media [73]. The ratio of the incident light intensity and the reflected light intensity, known as reflectivity,  $R$ , and is given by the following equation [73]:

$$R = \left(\frac{n_1 - n_2}{n_1 + n_2}\right)^2 \quad (1.7)$$

Where  $n_1$  is the refractive index of the medium the light is propagating from and  $n_2$  is the refractive index of the medium on the other side of the boundary. Whilst it may appear that cells are fully adhered to a coverslip or an adjacent cell using EM it has been shown that there is actually a gap of between 10 and 20 nm [73]. Due to this gap the first reflection will typically occur at the coverslip and cell media boundary, with the next occurring between the cell media and the cell specimen [74]. When the intermediate cell media between the coverslip and the cell has a thickness comparable to the wavelength of light used,  $\lambda$ , the reflections at the two boundaries can interfere with each other [74]. As there are differences in the optical path length between the two reflections it is possible that their phase relative to each other may change. This difference in optical path lengths,  $\Delta$ , is given by the following equation [75]:

$$\Delta = 2n_m d (\cos\phi) + \frac{\lambda}{2} \quad (1.8)$$

where  $n_m$  is the refractive index of the cell media,  $d$  is the distance between the coverslip and the cell and  $\phi$  is the angle of refraction within the media. If the optical path length is a whole integer of the wavelength of light, then the two reflections will undergo constructive interference and generate a maximum intensity in the image. If the path length is offset by half of the wavelength of light, then the reflections will become completely out of phase with each other resulting in destructive interference and a minimum intensity in the image. From equation (1.8) it is apparent that as the distance between the cell and the coverslip becomes zero (when the cell is in contact with the coverslip) that the resulting image will be a zero-order minimum.

When imaging is carried out with monochromatic light the minima and maxima will appear as dark and bright sections with a corresponding grey intensity for optical path differences between the minima and maxima.

In order to carry out widefield IRM, an epifluorescence light source is first passed through a bandpass filter so as to confine the excitation light to a specific bandwidth, typically 546 nm due to high intensity light output at this wavelength from mercury arc lamps [74] though in modern experiments it is possible to make use of LED illumination instead. The light passes through a linear polarizer and is incident upon a beam splitting mirror which is set at 45 degrees. The light is then passed through a  $\lambda/4$  plate and then introduced to the specimen through an objective lens [74]. The reflections generated from the refractive index boundaries are collected through the objective lens, pass through the  $\lambda/4$  plate and the beam splitting mirror. An analyser is placed to accept light which is polarised linearly but rotated through 90 degrees from the original illumination. Due to this all of the reflection light will be passed through the analyser but any light origination from reflections within the objective lens or outside the focal plane will be rejected [74]. The reflections then propagate towards either the eyepiece or towards a photodetector device for imaging. A schematic diagram of an IRM set up is shown in figure 1.11.

Interference reflection microscopy has been used to study the underside of many different types of unlabelled specimens and their adhesion to glass coverslips [74].

[76], [77]. Though this technique offers no increase in lateral resolution in the axial direction it is able to determine cell-coverslip separations on the order of 100 nm. Quantitative analysis of the images can become a challenging task as the technique cannot distinguish points of cell and glass contact from separations of less than 15 nm [75] as both will appear as dark regions on the image. Another source of difficulty occurs if the cell has a thickness of less than  $1\mu\text{m}$  which can lead to the generation of a reflection from the upper cell to media boundary [74]. This upper boundary reflection undergoes interference with the other two reflections and can contribute heavily to the image and its interpretation.

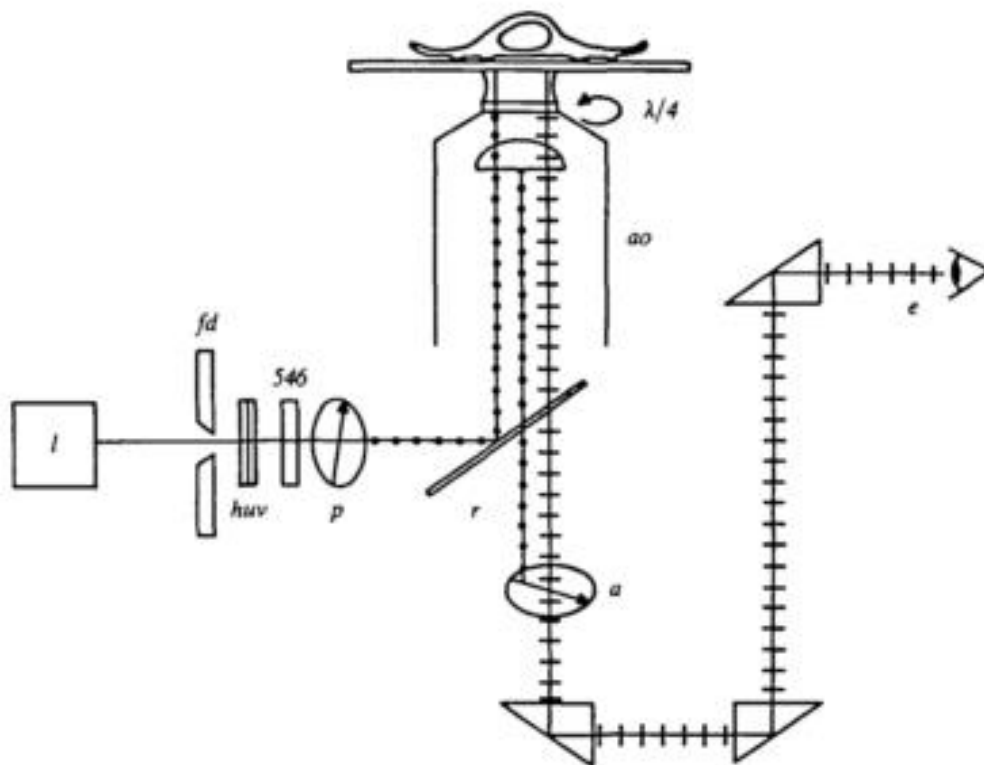


*Figure 1.11; Light path and microscope configuration for interference reflection microscopy. Reproduced from [74].*

However, using an oil immersion lens with a NA greater than 1 the image generated comprises only of reflections occurring in areas where the cell media is less than 250 nm in thickness and reflections from the upper boundary of the cell can be completely discounted so long as the cytoplasm has a thickness greater than  $1\mu\text{m}$ . The configuration described above can be combined with other microscopy techniques

such as phase contrast, DIC, or fluorescence imaging [74]. IRM is also compatible for use in a laser scanning confocal microscope provided that the optical path allows for the propagation of the reflected excitation illumination to reach the detector [75]. An example of an IRM image is shown in figure 1.12.

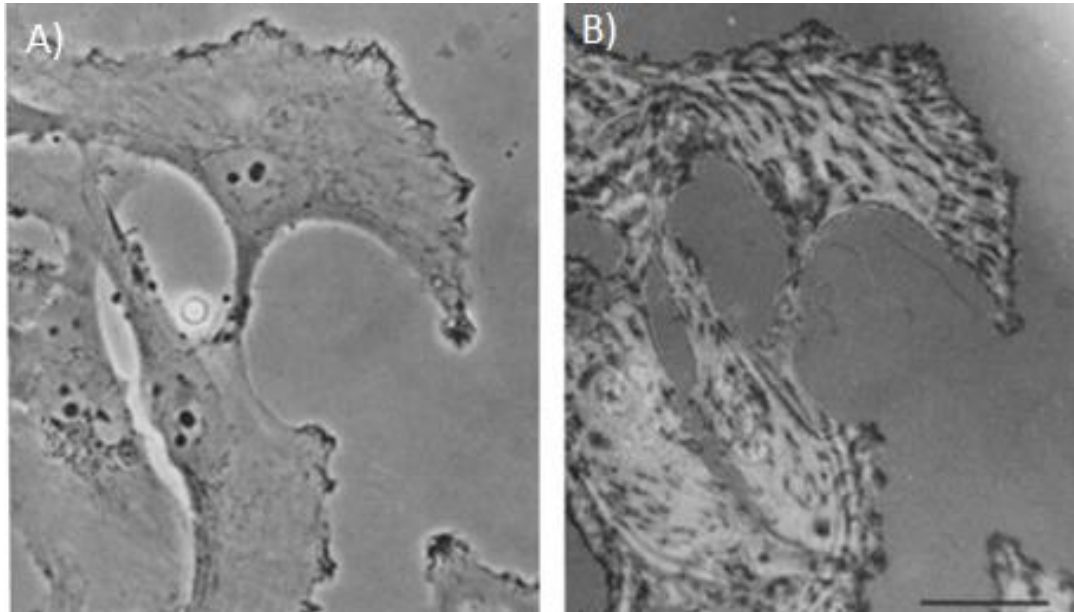


*Figure 1.12; Human glioma cells, A) imaged using phase contrast microscopy B) using interference reflection microscopy showing the adherence points which are not visible in A). Reproduced from [78].*

#### **1.4.2) Total internal reflection fluorescence microscopy**

Total internal reflection fluorescence (TIRF) microscopy was first demonstrated by Daniel Axelrod in 1981 [79] and is used as a method for generating sub-diffraction limited resolution improvements in the axial direction by utilising the principle of total internal reflection. TIRF microscopy has seen application for investigating cellular membrane contact regions which are typically obscured by out of focus fluorescence [80] [81], visualisation of single fluorescent molecules [82] [83] and localised  $\text{Ca}^{2+}$  transients near the cell membrane [84].

When a light wave propagates from a medium into that of a different refractive index at an incidence which is not normal to the boundary between the two medium it is refracted, causing a deviation of the light path. At a specific angle of incidence, known as the critical angle, the light will instead propagate at 90 degrees along the boundary between the two media [85]. The equation to determine this critical angle,  $\theta_c$ , is derived from Snell's law and is as follows:

$$\theta_c = \arcsin\left(\frac{n_2}{n_1}\right) \quad (1.9)$$

in this equation  $n_1$  is the refractive index of the medium that the light begins propagating from and has the larger refractive index and  $n_2$  is the lower refractive index of the medium after the refractive index boundary. The critical angle is measured perpendicular or normal to the boundary.

If light impinges upon the refractive index boundary at an angle larger than the critical angle, then instead of propagating along the boundary it is completely reflected into the original medium and as such this process is known as total internal reflection [85].

During the process of total internal reflection an electromagnetic wave is generated over the medium boundary which is known as an evanescent wave. The evanescent wave will have the same frequency as the reflected light and the intensity of this electromagnetic field decreases exponentially the further into the medium it propagates [79]. The equation describing this exponential decay is given by:

$$I(z) = I_0 \exp\left(-\frac{z}{d}\right) \quad (1.10)$$

where  $z$  is the distance travelled perpendicular to the medium boundary, and  $d$  is the decay depth of the wave which is related to the reflected wavelength of light,  $\lambda$ . The decay depth can be expressed by:

$$d = \frac{\lambda}{4\pi n_2} \left(\frac{\sin\theta}{\sin\theta_c} - 1\right)^{-\frac{1}{2}} \quad (1.11)$$

This equation relies on the incident angle of the light  $\theta$  to be greater than the critical angle, as dictated by the requirement for total internal reflection, and due to the rapid exponential decay of the evanescent waves results in a penetration distance on the order of 100 nm [79]. As the wave will only propagate a short distance into the

specimen only fluorophores close to the specimen-coverslip boundary will be excited and fluoresce. This short propagation distance leads to a much-improved axial resolution which is equivalent to the penetration depth of the evanescent wave. In this technique there is no change from the lateral resolution observed in widefield epifluorescence microscopy [86].

There are two main methods to conduct TIRF microscopy. In the first method, a focussed laser beam is introduced beyond the critical angle to the coverslip through a prism positioned below the coverslip. The emitted fluorescence is then collected by an objective lens directly above the specimen. This method has several drawbacks including, limiting the accessibility of the specimen, water dipping objective lenses must be used and the weak fluorescence signal propagates through the entire specimen before being collected [87]. This technique however, is easier to implement in existing microscope systems at a relatively low cost [87].

The other method for TIRF is to use a high NA objective lens to generate total internal reflection illumination which also collects the emitted fluorescence. By using an objective lens with an NA  $\Rightarrow$  1.45 an incident angle greater than the critical angle can be achieved [88]. To achieve this, a laser beam must propagate through the very periphery of the objective rear aperture to ensure light incidence greater than the critical angle. Incoherent light sources may be used for this method by constructing an opaque mask which is fitted into the objective back aperture [87]. This mask will restrict all but the very edge of the objective back aperture blocking off much of the light. Using this high NA TIRF approach allows a greater amount of specimen accessibility, and the use of high magnification lenses. In contrast to these benefits the signal to noise ratio is decreased when compared to the prism method due to some of the excitation within the specimen being generated by scattered illumination from within the objective lens [88] and the alignment of the laser can be difficult if not using a commercial system.

TIRF microscopy is a useful technique for investigating cellular substrates and plasma membranes, structures which are typically obscured by out of focus fluorescence [81], with a high degree of axial resolution in the region of 100 nm and has also been shown to be capable of single molecule imaging [83]. Unfortunately, due to the very nature

of TIRF only structures that are near the coverslip-specimen interface can be imaged and as such it is not suitable for high resolution imaging of deep internal cellular structures.

### **1.4.3) 4Pi microscopy and I<sup>5</sup>M**

As discussed previously, the smaller the PSF volume, the higher the resolution of the images that can be recorded using the microscope. The PSF volume is dictated by the wavelength of the light and the NA of the objective lens, (see equations (1.5) and (1.6)) but since the wavelength of light used for illumination is chosen depending on the excitation of specific fluorophores then one is typically limited to decreasing the PSF volume by increasing the NA.

In lens design the maximum light collection angle for an objective lens, and therefore its NA, has an upper limit in the range of 140° [59]. It was not until the development of the 4Pi microscope by Stefan Hell in 1992 [89] that the effective NA of a microscope system could be increased.

If the PSF volume is decreased by increasing the objective lens NA it would eventually lead to a PSF which is perfectly spherical and as such light would be collected over 12.5667 steradians (equal to  $4\pi$ ) [90] [91]. Using illumination and collection from only one side means that the theoretical maximum illumination and collection is limited to  $2\pi$  and so to collect the remaining  $2\pi$  of the PSF another objective lens would have to be placed directly opposite from the first. The use of this second lens is the foundations upon which 4Pi microscopy is based and reduces the PSF by the interference of two propagating spherical wave front caps reducing the elongation in the axial direction [1]. As mentioned above, an objective lens can typically only collect light or illuminate a specimen over a maximum angle of 140° so even using two high NA objective lenses leads to a collection over a total of 280°, which is obviously less than the  $4\pi$  theoretically desired. Due to this, the resulting PSF is not perfectly spherical in shape but the axial elongation is significantly reduced. As the collection angles are less than

360° Hell named his microscopy technique 4Pi to illustrate the basic idea of the process [89].

The 4Pi microscope makes use of a confocal laser scanning fluorescence microscope setup with a notable exception; there are two objective lenses used for illumination or emission collection which are focussed onto the same plane within the specimen. The two objective 4Pi principle and set up is shown in figures 1.13 and 1.14.

There are three different imaging methods when using 4Pi microscopy [89] each of which provide higher resolution than obtained using a standard confocal and are as follows –

Type A – The excitation light from each lens interferes at the specimen and the resulting emission is collected through one of the lenses.

Type B – The specimen is excited through one lens and the emission is collected through both lenses and interferes at the photo detector.

Type C- The specimen is excited through both lenses and the emission is also collected through both lenses causing interference at the specimen and at the detector.

Due to the need for interference between the two objective lenses the path lengths of the light have to be very precise to avoid any phase differences between the two beams [92]. When using these techniques, it was found that “side lobes” of light were created due to the wave front interference which are located approximately half of the wavelength of light above and below the PSF [89]. These “side lobes” create image artefacts known as “ghost images” which can be suppressed through mathematical deconvolution, though only if the intensity of these “side lobes” are typically less than 50 % of the PSF [93] [94]. As a method to reduce the side lobe intensities, 4Pi microscopy was combined with two photon excitation as in this technique there is a quadratic dependence between the excitation efficiency and the intensity of the illumination source [91] the removal of the “side lobes” is also aided as their locations are shifted away from the focal plane due to the longer wavelength of excitation when using two-photon excitation [95].

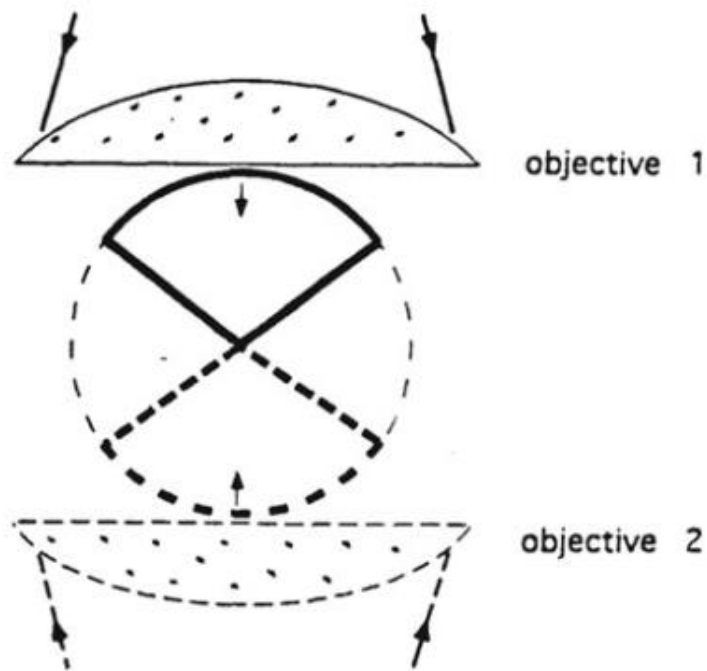


Figure 1.13; Diagram demonstrating the two objective lens illumination and collection of light with the theoretical maximum of  $4\pi$  and the experimentally realised detection angle. Reproduced from [96].

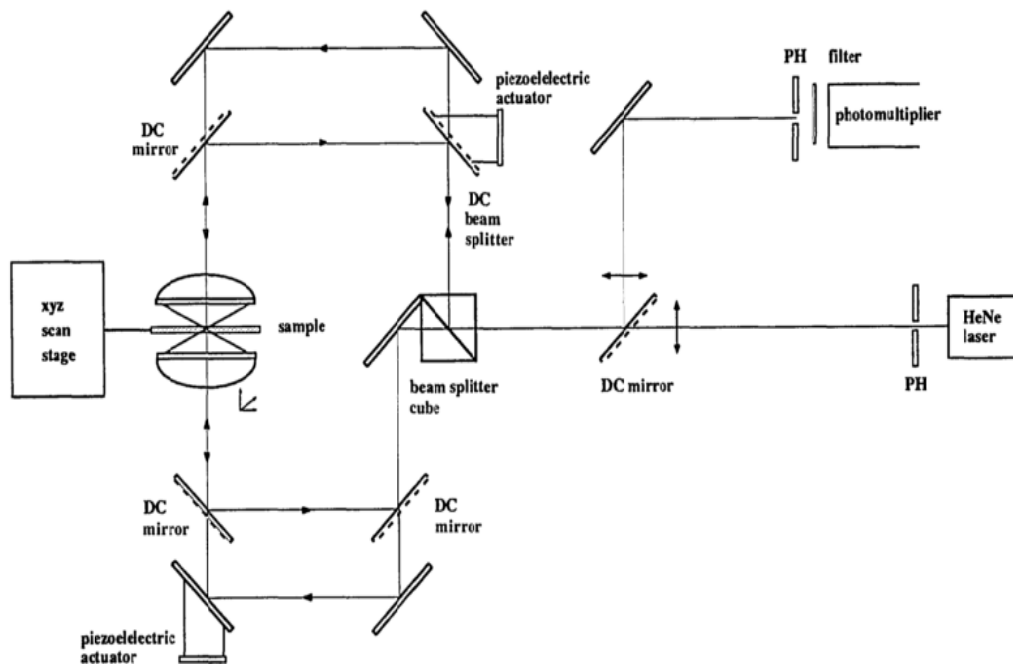


Figure 1.14; Schematic diagram showing components and beam paths in the original  $4\pi$  microscope. Reproduced from [89].

It has been suggested that 4Pi microscopy does not break the diffraction limit of resolution but is rather a PSF engineering technique as it manipulates the NA of the microscope system to increase resolution [97]. Regardless of this three-dimensional resolution of 100 nm has been shown [98]. 4Pi has been used in biological systems to image fine structures such as actin filaments or microtubules in live cells [99] [100]. When performing 4Pi microscopy one must be mindful of the refractive index of the specimen or the immersion oil as slight variations can cause phase differences between the two light paths negating the benefits of using this technique [99].

Another technique that uses an approach that is very similar to that of 4Pi microscopy, in that it utilises two opposing objective lenses to increase the effective NA of the imaging system, is known as I<sup>5</sup>M [101]. I<sup>5</sup>M was developed by Gustafsson *et al.* in 1999 [102] and was a combination of the previously developed techniques of I<sup>2</sup>M and I<sup>3</sup>M [103], [104]. I<sup>2</sup>M resembles type A 4Pi microscopy utilising only interference with the excitation light and I<sup>3</sup>M is similar to type B 4Pi with the interference occurring with the emission collection from each objective lens. I<sup>5</sup>M is a combination of the interference with the excitation and the emission light just like type C 4Pi microscopy with the major difference that the I<sup>n</sup>M techniques are widefield super resolution techniques and remove the need for raster scanning [95] and thus improving the temporal resolutions achievable [102], [103].

In I<sup>5</sup>M the laser required for confocal laser scanning 4Pi microscopy can be replaced with an incoherent light source, and the specimen is exposed to uniform Köhler illumination from both high NA objective lenses which undergo interference with each other at the specimen plane creating an axially varying field of illumination [102]. The resulting fluorescence emission is collected through both objective lenses and interfere with each other at a photodetector. A schematic diagram of a I<sup>5</sup>M microscope is shown in figure 1.15.

Like in 4Pi microscopy once the image is acquired computational deconvolution is then carried out in order to remove the “side lobes” in the image and achieve an axial resolution on the order of 100 nm but with no change from the conventional lateral resolution [102], [103], [105]. Though I<sup>5</sup>M offers brighter images than those obtained using two-photon 4Pi microscopy due to the use of single photon fluorescence, and

higher temporal resolution due to the widefield nature of the technique, the ability to carry out type C 4Pi microscopy using two-photon excitation allows for the easier removal of the “side lobes” in computational deconvolution which is not the case in  $\hat{F}M$  where the lack of confocal confinement in the PSF means that the “side lobes” have much higher intensity [93], [95]. It also has the other limitations encountered with 4Pi techniques of requiring little to no refractive index variations within a thin specimen and precise optical alignment [101], [102].

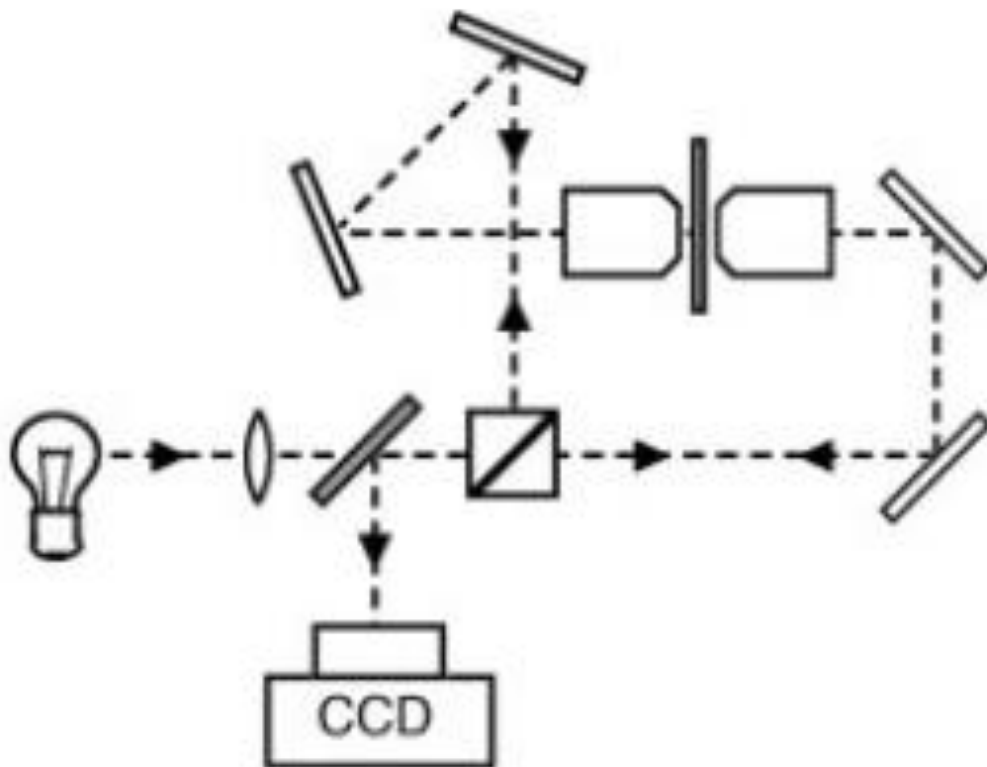


*Figure 1.15; Schematic diagram demonstrating the optical setup required to conduct  $\hat{F}M$ . Excitation light propagates from the bulb source through a short pass dichroic mirror and through a 50:50 beam splitter to illuminate the specimen from both sides. Emission is collected through both objective lenses and undergoes interference at the CCD camera. Reproduced from [102].*

#### **1.4.4) Structured illumination microscopy**

Another technique reported by Gustafsson in 2000 is known as structured illumination microscopy (SIM) which was developed in later stages of the 1990s [106], and since then the technique has seen many uses in biological research [107]–[110]. The principle of this technique is to project a fine grating onto the specimen and then create a reconstruction using images with the grating in different positions [106]. When a known pattern is superimposed onto an unknown pattern it creates a moiré, or beats, pattern which contains increased information about the unknown structure (this principle is demonstrated in figure 1.16). This is done by allowing the detection of high spatial frequencies that are not typically possible using a normal microscope [106], [111].

In the case of SIM, the known pattern is the grating, and the unknown is the fluorescently labelled specimen and it is possible to obtain a resolution enhancement in all spatial directions by approximately a factor of two [107], [110], [112], [113]. Though a greatly improved resolution is made possible, the requirement of taking multiple images with the different grating orientations greatly reduces the temporal resolutions available using this technique compared to standard widefield microscopy and also increase rates of photobleaching [111], [114]. The technique is also highly susceptible to spherical aberrations which distort the grating [107]. This technique has seen further application through as a complimentary add on to other microscopy methods such as F<sup>5</sup>M [105], multi-photon excitation [115] or light sheet microscopy [116].

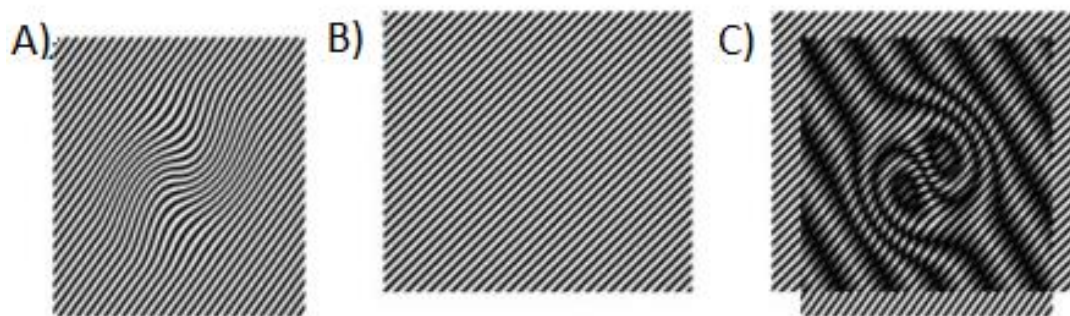


*Figure 1.16; Demonstration of utilising the moiré effect to obtain a resolution enhancement. If an unknown structure A) is multiplied by a known pattern B) then the resulting image C) contains an increase in information on structure A. Reproduced from) [117].*

#### **1.4.5) Interference photoactivated localisation microscopy**

In the mid-2000s widefield techniques were developed which were able to localise single fluorophores with a high degree of precision to achieve super-resolution microscopy on the order of 20 nm [118], [119]. These techniques were STORM [120] and photoactivated localisation microscopy (PALM) [121]. Since then there has been further developments of the PALM technique which utilise optical interference effects and is called iPALM [118].

The principle of operation behind PALM is essentially the use of fluorescent proteins (such as the photoactivatable green fluorescent protein (PA-GFP) which are able to have their emission switched on and off using an excitation source [122], [123]. As the closely spaced molecules are switched to the emitting state and subsequently photobleached whilst imaging, the single fluorescent molecules are separated from each other allowing localisation to be carried out [124]. The localisation of each sub-resolution molecule can be carried out by determining the centre of each molecule and then applying a Gaussian fit to each object. The central location of each molecule can be more precisely determined as a function of the inverse square root of the number of photons recorded from each molecule [121], [125]. This technique is typically carried

out using a TIRF setup to reduce the amount of background signal recorded [121]. In the early years of this technique an issue observed was that it was only applicable in the lateral plane with no axial information be obtained from the molecule [125].

Phase-shifting interferometric methods have been used for many different applications where high degrees of spatial precision are required and utilise two coherent light waves where one is a reference wave and the other is the measurement wave [118]. The measurement wave is reflected off a specimen of interest and is recombined with the reference wave just before the detector allowing highly precise position measurements to be carried out. With iPALM, the microscope is altered to have opposing objective lenses in a 4Pi configuration (shown in figure 1.17). The emission of a fluorophore is collected through both objective lenses and recombined to create self-interference [126]. The recombination takes place at a three-way beam splitter with each of the three output beams being detected by separate detectors [118], [127]. As the phase-difference recorded by each camera is spatially dependent the axial position of the fluorescent molecule can be determined with a theoretical precision on the order of 10 nm with no change in the lateral resolution from standard PALM [127].

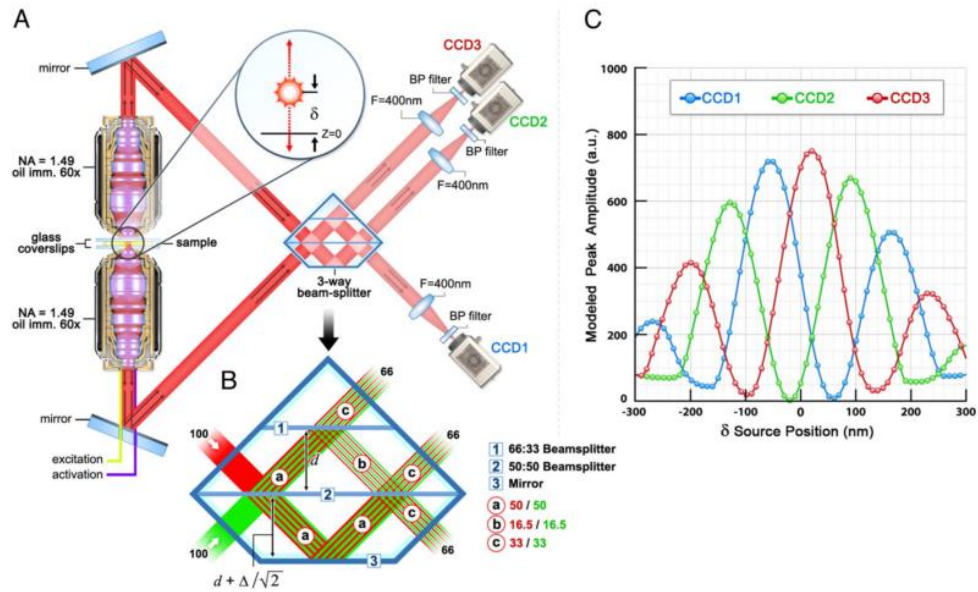


Figure 1.17; A) Schematic diagram of the microscope setup used for iPALM. The excitation and activation light sources are introduced to the specimen via the bottom objective lens only, with emission being collected through both objective lenses. The emission undergoes self-interference within the 3-way beamsplitter which is shown in greater detail in B). The spatially dependent phase difference induced intensity modulation which is seen in C) can then be used to determine the axial location of the emitting molecule by comparing the relative intensities observed on each of the cameras. Figure reproduced from [118].

Though iPALM can offer 3D resolutions which far surpass the diffraction limit of far-field microscopy there are several drawbacks to this technique. One of these is the maximum depth of focus is on order of 225 nm due to the use of high NA TIRF objective lenses which can limit imaging to either the periphery of the specimen or very thin specimens [118], [127]. The temporal resolution of this technique is directly limited by the spatial resolution as reducing the exposure time of imaging reduces the number of photons collected and the number of localisation molecules that are obtained to reconstruct the specimen [122]. This limits the application of this technique when desiring to image dynamic processes in live cells, and as such it is typical that cell specimens are fixed to increase the spatial resolution [127], [128].

#### **1.4.6) Standing wave microscopy**

A much expanded literature review of standing wave microscopy will be presented in Chapter 2. However, in brief, the first efforts to utilise optical standing waves for optical microscopy was carried out by F. Lanni in 1985 and were combined with total internal reflection with modest success in imaging the actin of 3T3 cells though was limited due to engineering constraints [129]. It was not until 1993 that Bailey *et al.* [130] demonstrated that by mounting the specimen upon a mirror or by making use of opposing objective lenses that a standing wave could be generated through either two-counter propagating or a single reflected laser beam in a widefield microscope. By using this experimental setup it was possible to make use of a single antinode of the standing wave to obtain optical sectioning of specimens with a greater temporal resolution than was possible using confocal microscopy with an axial resolution of  $\lambda/4n$  [130], [131].

The concept of using standing wave excitation was taken further and combined with a confocal laser scanning microscope [132], [133]. Amor *et al.* showed that by utilising multiple antinodal planes generated within a red blood cell that a topographical map of the membrane morphology could be obtained in healthy and unhealthy red blood cells with a resolution on the order of 90 nm [133]. Prior to the work presented in this thesis the most recent study making use of this technique has been combined with stimulated emission depletion microscopy to obtain a resolution of 19 nm [134].

### **1.5) Overview of thesis**

The following Chapters in this thesis will discuss the work that was carried out investigating and developing the use of standing wave microscopy for imaging live cell specimens and the development and testing of 340/380 nm LED illuminator for ratiometric  $\text{Ca}^{2+}$  imaging. A full background of  $\text{Ca}^{2+}$  imaging in live cells will be given

in the introduction section of Chapter 4. The structure of these Chapters will be as follows.

Chapter 2 reports single colour video-rate standing wave microscopy of red blood cells. This work presents a characterisation of the LEDs used along with a comparison between the experimental resolutions and theoretical values using fluorescent lens specimens. There is also a demonstration of the 2D and 3D reconstruction of the standing wave movies that allowed the possibility of carrying visualisation of the specimen. Finally, a comparison of the effects the standing wave technique has upon the red blood cell specimens against standard widefield microscopy is presented by analysing the average photobleaching rates and imaging the specimens over a longer time scale.

Chapter 3 is an investigation of utilising TartanSW emission and excitation microscopy of red blood and MCF-7 breast cancer cells to assist in overcoming some of the limitations encountered when using single colour standing wave imaging. By carrying out these experiments it was possible to reduce the information gap seen in standing wave microscopy, resulting in a much more complete topographical representation of the fluorescent lens and biological specimens. This Chapter also makes use of the multiple excitation channels to take the difference between them in order to reduce the antinodal plane thicknesses and hence increase the resolution of the standing wave technique. This work also looked into reducing the ambiguity in the relative axial localisation of the antinodal planes with reference to each other using multiple emission bandwidths. However, it was found that it was not possible to reconcile the lens results obtained experimentally with the theoretical values, but this was possible using confocal microscopy. The technique was applied to live cell specimens where spectral differences were able to be observed which in future could be utilised to give a precise location above the mirror for each plane.

Chapter 4 is about the work that was carried out into utilising a new 340/380 nm LED illuminator to perform Fura-2 AM ratiometric  $\text{Ca}^{2+}$  imaging of live cell specimens. This work compares the performance of this new system to a commercially available 350/380 nm LED illuminator and present the advantages discovered when using the 340/380 nm system.

Chapter 5 presents a summary of the work presented in this thesis along with some possible directions that this work could be taken forward in the future.

## **Chapter Two:**

# **Single colour widefield multi-planar standing wave imaging of live cells with high temporal resolution**

**T**his Chapter will discuss the experiments utilising an LED illuminator to carry out single colour widefield standing wave imaging of fluorescently labelled red blood cells at a video-rate. Through this work, it was first confirmed that standing wave images were being generating that had antinodal FWHMs and spacings between subsequent antinodes that were within 7 nm to the theoretical. The technique was then used to recorded standing wave movies of red blood cells which allowed the imaging of rapid membrane deformations to be carried out in real time. The resulting membrane contour maps were then used to create a 3D reconstruction of the specimen using a MATLAB script (written by my colleague Ross Scrimgeour). This work also compared the standing wave imaging technique to standard widefield epifluorescence imaging of red blood cells by analysing the photobleaching rates and carrying out more long-term imaging of the red blood cell specimens. It was found through these experiments that photobleaching rates were not significantly different between standing wave and standard widefield imaging and that both techniques caused red blood cell decay that occurred at the same rate.

### **2.1) Introduction**

An optical standing wave is a phenomenon that results from the constructive and destructive interference that occurs between two light waves with equal wavelength

travelling in opposite directions due to either counter-propagating sources or the incoming and reflected components from a plane mirror [135]. A standing wave has stationary points in constant fixed positions, nodes are points of zero intensity and are separated from the subsequent node by a distance of  $\lambda/2n$ , where  $\lambda$  is the wavelength of light and  $n$  is the refractive index of the media in which it propagates [136]. Between these nodes there are fixed points of maximum intensity, known as antinodes, which are located at a distance of  $\lambda/4n$  from the previous node and separated from the next antinode by  $\lambda/2n$  [137]. A cartoon demonstration of the standing wave generation and structure can be seen in figure 2.1.

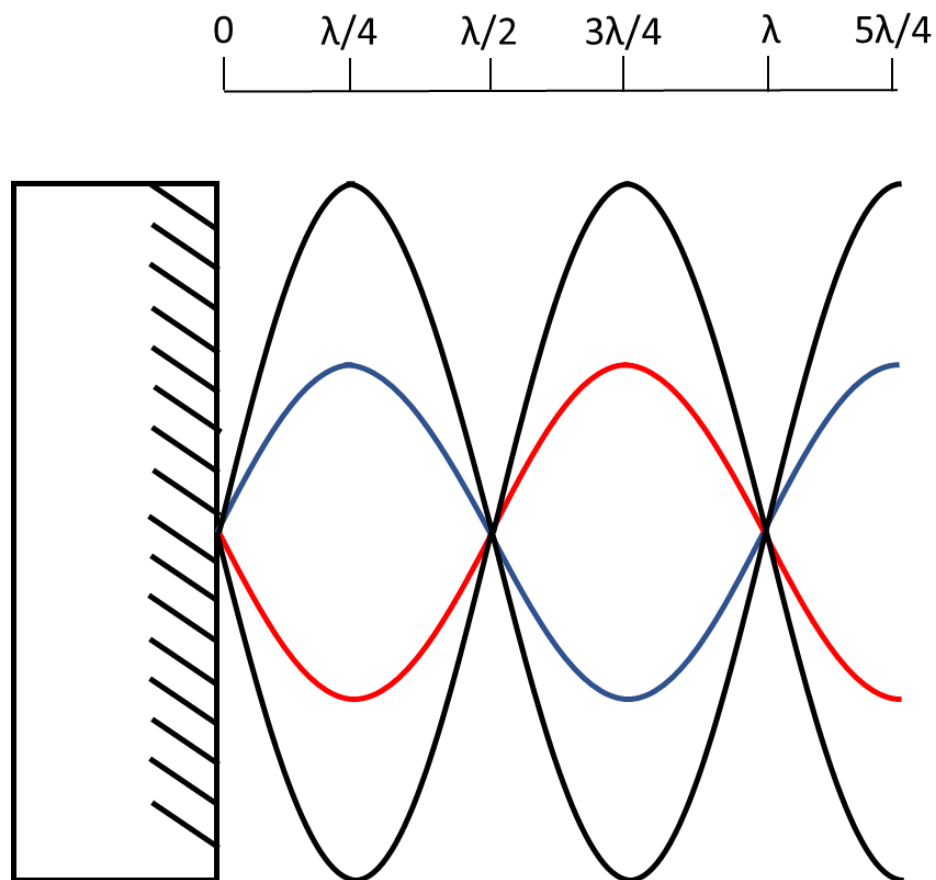


*Figure 2.1; Cartoon diagram of the generation of an optical standing wave using a plane mirror, shown at the 0 location. The blue line is the incoming wave and the red line is the reflected wave. The black line is the standing wave which results from the interference between the red and blue waves.*

The first experiments into the detection of optical standing wave were carried out by Otto Wiener in 1890 [138]. To do these experiments, first, a thin photographic film

was deposited onto a glass plate which was then placed in front of silver plane mirror at a small angle. The mirror was then illuminated at normal incidence to generate an optical standing wave. When the photographic film was developed it was found that the film was blackened at points which corresponded to the antinodes of the standing wave and remained unaffected at the nodal points. Further to this, through the experiment it was found that the optical standing wave component being detected by the photographic film was the electric field rather than the magnetic field. This was determined as the point at which the glass plate made contact with the mirror was not blackened after exposure and as such corresponded to a node of the standing wave and the electric field at the metal surface is zero (as it is cancelled out by the free electrons in the metal). These experiments were then repeated by Drude and Nernst in 1892 with the alteration that the photographic film was replaced with a fluorescent coating which reconfirmed the results, this time recording fluorescence excitation at the location of the antinodes and the fluorophores in the nodal regions not fluorescing [139].

### **2.1.1) Standing wave microscopy**

The first experiments into utilising optical standing wave for sub-diffraction limited optical microscopy were carried out by F. Lanni in 1986 [129]. In these experiments, he created an optical standing wave within the specimen by propagating a collimated laser source in such a way to undergo total internal reflection at the coverslip boundary above the specimen. The incident and reflected light then interfered with each other and resulted in nodal spacings of  $\lambda/2n(\cos\theta_c)$ , where  $\theta_c$  is the angle of incidence which must be larger than the critical angle. Fluorescence emission was collected by a dry objective lens above the specimen which meant that high lateral resolution was not achievable as the use of high NA immersion objective lenses would result in total internal reflection not occurring at the correct boundary. Also, as the light was introduced to the specimen at an angle different from the normal meant the minimum nodal spacings was not obtained which limited the axial resolution achieved [129]. Even with these constraints it was possible to image the actin filaments of fixed 3T3

cells stained with rhodamine-phalloidin. The experimental set up for these experiments is shown in figure 2.2.

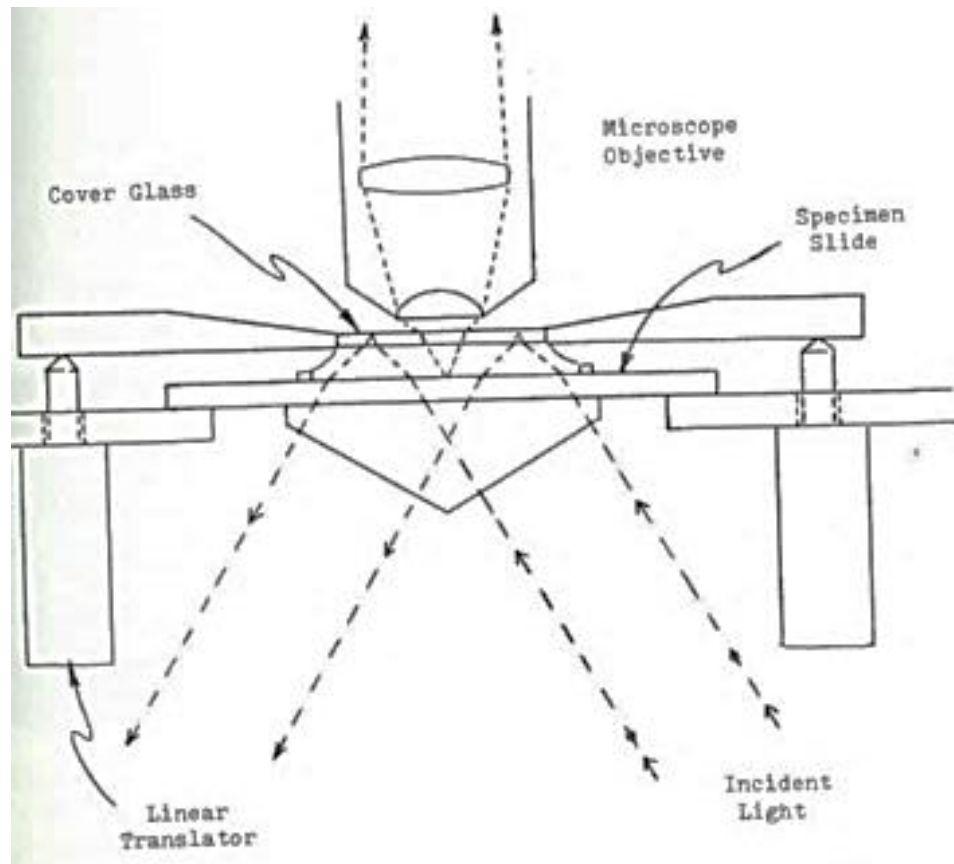


Figure 2.2; Experimental setup from the initial standing wave experiments in 1985 showing the total internal reflection of the excitation light at the coverglass causing self-interference to occur within the specimen. [129].

The next investigation into using a standing wave field to increase axial resolution was carried out in 1993 by Bailey, *et al.* [130], [131]. In this study a much simpler approach than proposed previously was implemented utilising widefield 4Pi opposing objective lens geometry in order for two counter propagating collimated lasers beams to undergo interference within the specimen creating the standing wave. The other technique for generating a standing wave made use of a single objective lens and a mirror placed beyond the specimen where the standing wave was created through interference of the incident and reflected components of the laser beam [130]. Utilising these methods, the minimum node spacing of  $\lambda/2n$  was achieved which gave an axial resolution equal to the FWHM of the antinodes,  $\lambda/4n$ , [140]. Using the standing wave technique, the

axial resolution is defined as the FWHM of the antinodes as this represents the axial uncertainty in the position of any excited fluorophore due to everything within the FWHM being excited simultaneously [129], [130], [133]. By changing the phase of the propagating illumination, the location of the nodes and antinodes could be shifted and it was proposed that this technique could be used as a method to carry out optical sectioning with greater axial and temporal resolution than possible using a confocal microscope [130]. Using this technique it was possible to image actin stress fibres in fixed 3T3 cells labelled with rhodamine phalloidin and Lanni went on to use this approach to measure F actin densities in the leading edge of 3T3 cells in order to study their migration [141].

More recent work using standing waves was carried out by Elsayad *et al.* who combined the specimen and mirror standing wave approach making use of laser scanning confocal microscope for the first time [132]. In these experiments, fluorescent specimens were directly cultured onto a reflector and utilised the first antinode of the standing wave field to precisely map fluorophore locations based on the spectral shape of the recorded emission self-interference with an axial depth of up to 150 nm and with a precision of 5- 10 nm [132]. Amor *et al.* built upon this experimental work by carrying out experiments that not only utilised a single antinodal plane, as in previous work, but imaged specimens that were much thicker than the antinodal separation using a laser scanning confocal microscope which resulted in acquiring multiple antinodes simultaneously [133]. To do this, a fluorescently coated lens specimen upon a mirror was first used which provided an image comprising of concentric rings of fluorescent emission, which were at the locations of the antinodes. These images have encoded in them 3D axial information within the concentric rings and as such by using this result and the known geometry of the lens specimen it was possible to directly compare the experimentally recorded antinodal spacings and FWHM with the theoretical values. After confirming the experimental values, the study then went on to use the technique to image fluorescently labelled red blood cells on a mirror. It was found that a contour map of the membrane topography was obtained in both healthy and unhealthy intact red blood cells and red blood cell ghosts. This technique allowed for the observation of the bi-concave section of the red blood cell which was not possible when imaging without a mirror and allowed for an axial

resolution on the order of 90 nm to be achieved. Whilst axially super-resolved maps of the specimens were acquired, the use of a confocal laser scanning microscope limited their acquisition time to 40 seconds per frame [133] which results in rapid membrane movements being temporally averaged and therefore lost.

The work presented here utilises the mirror based standing wave imaging approach to achieve widefield axial super-resolution images. As a mirror is being used to generate the standing wave there will be a node located at the surface of the mirror with the first antinode occurring at a height of  $\lambda/4n$  above the mirror. The equation used to describe the intensity of the standing wave excitation field is [129], [135],

$$I_e = I_0[1 - \cos(Kz - \varphi)] \quad (2.1)$$

where  $z$  denotes a coordinate along the  $z$  axis (optical axis),  $\varphi$  is the relative phase of the two counter-propagating light waves and  $K = \frac{4\pi n \cos(\theta)}{\lambda}$  [140], [142]. The spacing between the nodes and antinodes,  $\Delta s$ , is given by

$$\Delta s = \frac{2\pi}{K} = \frac{\lambda}{2n \cos(\theta)}. \quad (2.2)$$

where  $n$  is the refractive index of the media in which the light is propagating,  $\lambda$  is the wavelength of excitation light and  $\theta$  is the angle of propagation relative to the optical axis. As the light is propagating along the optical axis it results in the minimum antinodal separation and equation (2.2) can be written as

$$\Delta s = \frac{\lambda}{2n} \quad (2.3)$$

As these experiments are utilising multiple antinodal planes to image the specimens an expression for the full standing wave PSF must be used for simulating the data. The full axial PSF for standing wave microscopy can be described as a convolution of the excitation standing wave field and the widefield epifluorescence axial emission point spread function [143], [144]. The axial intensity distribution of the widefield epifluorescence emission point spread function can be described by the following equation [131], [143], [145].,

$$PSF_{epi} = \left[ \text{sinc} \left( \frac{NA^2}{2n\lambda_{em}} z \right) \right]^2 \quad (2.4)$$

were  $\lambda_{em}$  is the peak emission wavelength. This full axial PSF for standing wave microscopy can be hence written as [143],

$$PSF_{SW} = [1 - \cos(Kz)][\text{sinc}\left(\frac{NA^2}{2n\lambda_{em}}z\right)]^2 \quad (2.5)$$

The result of this PSF is a series of antinodal planes which decrease in intensity throughout the axial widefield microscopy PSF. It is clear the resolution of the standing wave technique being  $\lambda/4n$  that in the case of visible wavelengths the resolution achievable using standing wave microscopy can be significantly below the axial diffraction limit, for instance, using an excitation wavelength of 490 nm with a specimen submerged in fluid with a refractive index of 1.33 would give an antinodal plane resolution of 92.1 nm though the number of these planes which are detected is dictated by the NA of the microscope objective as this will limit the depth of focus. The effect of the NA is explored in section 2.3.1.

### **2.1.2) Red blood cells**

Adult mammalian red blood cells are a unique cell type which lacks a nucleus, mitochondria and other organelles. In most mammalian species red blood cells have a characteristic biconcave shape that permits increased manoeuvrability and faster diffusion of oxygen and carbon dioxide across the plasma membrane [146]. The red blood cell membrane exhibits an inherent age-dependent flickering which has been widely reported and was documented as early as 1890 [147] and it has been suggested may be due to either thermal processes or a combination of dynamic remodelling of the cytoskeleton and active membrane mechanisms [148]–[150]. The investigation of red blood cell diseases has been of considerable interest in biology and many of these disorders can be identified through membrane morphology changes such as sickle cell disease [151], [152], hereditary spherocytosis [153], [154], and elliptocytosis [154]. These clearly defined morphological shapes between healthy or unhealthy red blood cells allows them to be a perfect candidate for optical microscopy techniques to aid in diagnosis or investigation.

### 2.1.3) Motivation for work

Through this work, the aim was to build on the experiments carried out by Amor, *et al.* [133] to carry out widefield multi-planar standing wave imaging of red blood cells at a video-rate, so as to visualise rapid membrane deformations and create a 3D topographical map of the specimen. As all previous investigations using standing wave microscopy have utilised a laser for illumination, it was one of the aims of this work to make use an LED illuminator instead. The use of lasers for dual objective lenses standing wave microscopy was necessary as the ability to shift the antinode location by changing the phase of the two beams could only be achieved with laser illumination [130]. Conversely, by using the mirror based standing wave method the standing wave is always forced to a node at the mirror surface meaning that requirement for altering the phase of the illumination is removed opening up the possibility of utilising LEDs. The optical standing wave can be achieved using an incoherent light source for widefield microscopy by ensuring that the illumination is collimated as it exits the objective lens as the flat wavefronts will reflect perpendicularly off the planar reflector in order to undergo self-interference between the two components.

With the rapid rate of progress and development in technology, high-brightness LEDs are now a common feature in microscopy labs as researchers make use of many of the advantages held over conventional light sources. Other sources of illumination such as lasers or arc lamps have limitations that include their high initial and maintenance costs, comparatively short operational lifetime, and the ability to generate only certain wavelength outputs in lasers or the broad spectrum output of arc lamps (this can be seen as an advantages depending on the applications) [155].

Current commercial LED systems are capable of outputting spectrally narrow illumination across a wide range of the electromagnetic spectrum from ultraviolet (UV) to infrared (IR) allowing users to excite a wide range of dyes [156] with a high optical power, provide rapid rise-fall switching between on and off (not limited by neutral density filters and mechanical shutters) and have typical operational lifetimes in excess of 10,000 hours [157]. The precise electronic control of the output power of

an LED is another benefit which can reduce photo-toxicity in biological specimens and fluorophore photobleaching. This also allows a regular widefield microscope to be very simply made capable of carrying out high speed super-resolution microscopy, using only a mirror to create the standing wave illumination.

## **2.2) Materials and methods**

In order to carry out video-rate widefield standing wave microscopy utilising an incoherent LED source for illumination, it first had to be confirmed that the standing wave structures obtained were comparable to that which was expected theoretically. To do this, the LEDs had to be first characterised so to know the peak output wavelengths which dictate the standing wave structure. A microscope set up also had to be developed which supported video-rate imaging that also synchronised the illumination source to the camera along with the optimum collection of fluorescence emission. The specimens used for these experiments were a fluorescent lens specimen, which allows the experimental antinodal FWHM and spacings to be obtained for each LED, and red blood cells, due to the dynamic nature of the cell membrane which could possibly be observed at a video-rate.

### **2.2.1) Preparation of fluorescently coated lens specimens**

Uncoated silica plano-convex lenses, with either a focal length of 60 mm or 30 mm, both with a diameter of 6 mm (Edmund Optics), were cleaned using deionised water and then blow dried with compressed air to remove any contaminants. The lens preparation protocol which was described by Amor *et al.* [133], was amended by replacing the APTMS coating with a solution of 0.01% mass concentration poly-L-lysine in H<sub>2</sub>O (Sigma Aldrich) to allow the binding of 1,1'-Diocadecyl-3,3,3',3'-Tetramethylindocarbocyanine Perchlorate (DiI) to the lens surface. The specimens and

poly-L-lysine solution were placed on a platform rocker for 45 - 60 minutes to evenly coat the curved surface of the lenses in the solution, after which the lenses were thoroughly washed in deionised H<sub>2</sub>O and blow dried.

A fluorescent layer was deposited on the lens specimen in order to compare the theoretical and experimental standing wave antinodal spacings and FWHM in the same manner as carried out in the work of Amor *et al.* [133]. To deposit a monolayer of DiI on the curved surface of the lens specimen, a 30  $\mu$ M solution was prepared by diluting 560  $\mu$ L of a 1 mg/mL stock solution of DiI (Invitrogen) in 20 mL of dimethyl sulfoxide (DMSO, Sigma).

The lens specimen was coated with DiI which was also used to label the red blood cells and has been used extensively in red blood cell membrane studies [133], [158], [159]. Specimens are labelled through direct application of the dye allowing the two lipophilic hydrocarbon tails to diffuse laterally into the membrane after which it fluoresces brightly and is reported to not cause toxicity to the specimen [160]–[162]. The chemical structure of DiI and the excitation/emission spectra are shown in figure 2.3.

The lens specimens were placed in a glass petri dish with the curved surface submerged in the dye solution and gently rocked overnight. The petri dish was wrapped in aluminium foil to prevent photo-damage to the dye during this period. The following day the specimens were washed three times in deionised water, then dried using compressed air and kept out of direct light until imaging.

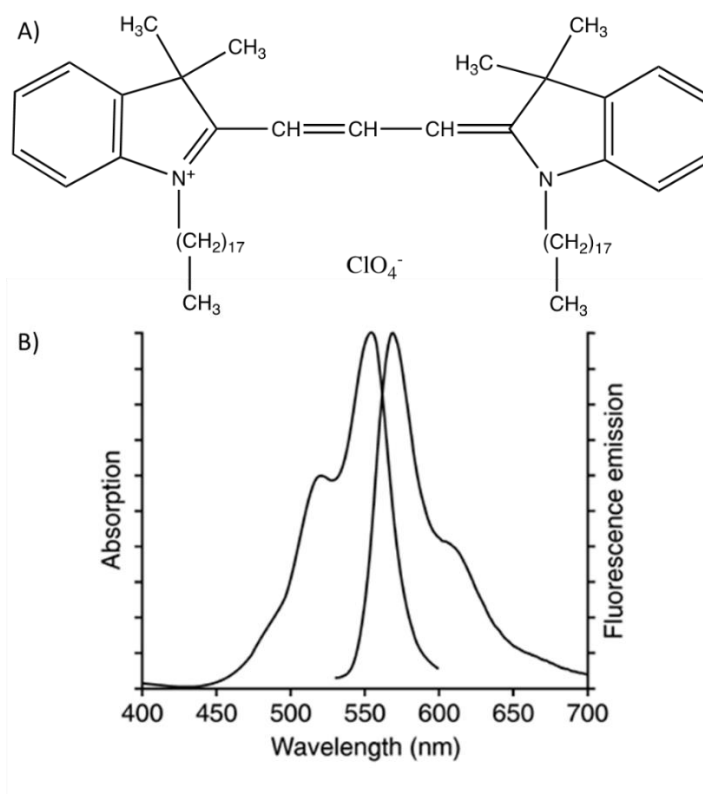


Figure 2.3; A) Chemical structure of the fluorescent lipophilic dye, DiI. B) Excitation and emission spectra of DiI suspended in PBS[163].

### 2.2.2) Red blood cell isolation and staining

Blood specimens were obtained on the day of the experiments via the cardiac puncture of a single mouse, which was euthanised through carbon dioxide exposure, and the collected blood immediately mixed in a centrifuge tube (Star Labs) with acid citrate dextrose (ACD), an anti-coagulant. The ACD comprised of 1.32 g trisodium citrate (Fisher Scientific), 0.48 g citric acid (Arcos Organics) and 1.40 g dextrose (Fisher Scientific) and was made up in 100 mL of distilled water. ACD for these experiments was provided by Dr Margaret Cunningham (University of Strathclyde) and cardiac punctures were performed by either the author, or the technical staff from the University of Strathclyde's Biological Procedures Unit in accordance with UK Home Office guidelines and approved by the University of Strathclyde Ethics Committee.

The process for isolating and staining the red blood cells has been adapted from the protocol described by Amor *et al.* [133].

The mouse blood and ACD suspension was spun down at 2000 rpm for 10 minutes with the supernatant removed and the pellet resuspended with 500  $\mu\text{L}$  of 4% bovine serum albumin (BSA) (Sigma) in phosphate-buffered saline (PBS) (Gibco). The 4% BSA and PBS had a refractive index of 1.341 that was measured using an Abbe 60 refractometer (Bellington and Stanley Ltd.) which had been calibrated using methanol and glycerol. This process was repeated another three times so only a suspension of red blood cells remained.

Red blood cells were fluorescently labelled by adding 200  $\mu\text{L}$  of the red blood cell suspension to 790  $\mu\text{L}$  4% BSA in PBS along with 10  $\mu\text{L}$  of a 1 mg/mL stock solution of DiI. The solution was then incubated at 37 °C for 60 minutes whilst being gently shaken to ensure even distribution of the dye. After this, the fluorescently labelled red blood cell suspension was spun down and resuspended a further four times to remove all excess dye.

Silver broadband mirrors (Thorlabs) were prepared for imaging by first being thoroughly cleaned in ethanol (purity > 99.8 %, Sigma). Then, to promote specimen adhesion to the mirrors the reflective surface was coated with a solution 0.1% mass concentration poly-L-lysine (Sigma) and incubated at 37 °C for 45 – 60 minutes whilst being gently rocked. This was done so as to leave a layer of positively charged ions on the mirror which will cause an electro-static interaction with negatively charged ions in the membrane of the red blood cells [164]. The preparation was then washed with PBS and sterilised using UV light. 5  $\mu\text{L}$  of the red blood cell suspension was pipetted onto the mirrors under a coverslip (VWR, thickness = 1.5) 10 minutes prior to imaging.

### **2.2.3) Imaging apparatus and LED characterisation**

Video-rate standing wave imaging of the fluorescently labelled specimens was carried out using an upright epifluorescence microscope (BX50, Olympus) using a 10x/0.4

dry objective lens (UPlanSApo, Olympus) for imaging the lens specimens and with a 100x/1.4 oil immersion objective lens (UPlanSApo, Olympus) when imaging the red blood cells. The lens specimens were imaged in air or with a layer of 4% BSA in PBS between the specimen and the mirror to confirm the antinodal spacings and FWHM were comparable to theoretical values calculated using equation (2.5).

Illumination of the specimens was provided by either a 525 nm LED (pE-4000, CoolLED) with a bandpass filter (525/50, Olympus) which had a peak wavelength of  $532 \pm 1.50$  nm (FWHM -  $32.5 \pm 1.50$  nm), or a 550 nm LED (pE-4000, CoolLED) with a bandpass filter (535/30, Olympus) with a peak wavelength of  $549 \pm 1.50$  nm (FWHM -  $11.9 \pm 1.50$  nm). Output spectra of the LEDs (shown in figure 2.4) were measured using a spectrometer (USB2000 spectrometer, OceanOptics) and the peak wavelength and FWHM were determined by reading the spectra into OriginPro 2016 and using the inbuilt Quick peaks and Integrate functions. The bandpass filters mentioned above were used to prevent bleed-through to the detector, and the LEDs were coupled to the microscope using a liquid light guide and collimator (Universal collimator, CoolLED).

An average optical power at the specimen plane of  $1.32 \pm 0.01$  mW for the 525 nm LED (control pod intensity of 20 % and drive current of  $0.78 \pm 0.02$  A) and  $1.71 \pm 0.01$  mW for the 550 nm LED (control pod intensity of 20 % and drive current of  $0.85 \pm 0.02$  A) was used for these experiments. These measurements were the average result of three recordings at the specimen plane under the 100x objective lens using a power meter (Fieldmax II, Coherent) with a thermal head (PM10, Coherent) and a three second integration time (shown in figure 2.5).

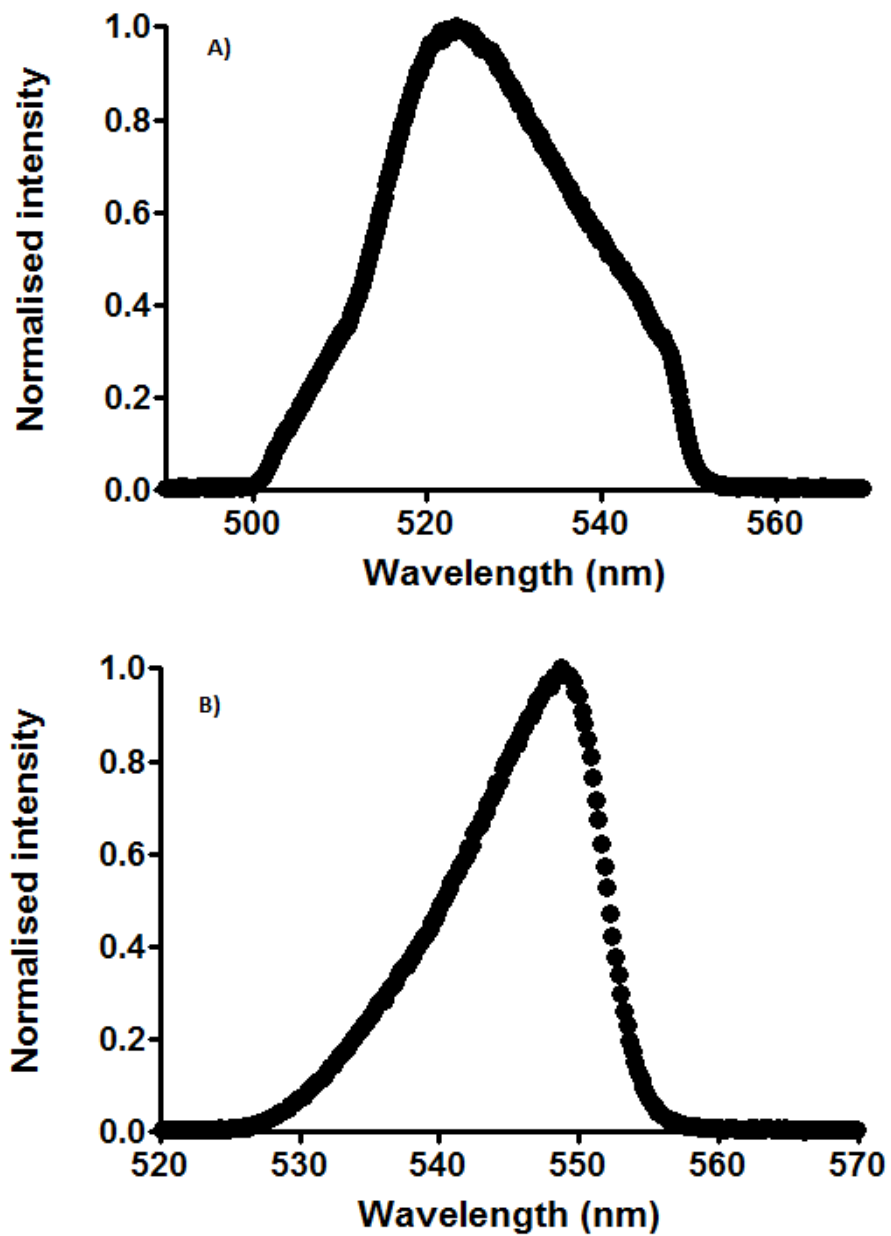


Figure 2.4; Output spectra of A) 525 nm LED and B) 550 nm LED obtained at the specimen plane using the 525/50 clean-up filter.

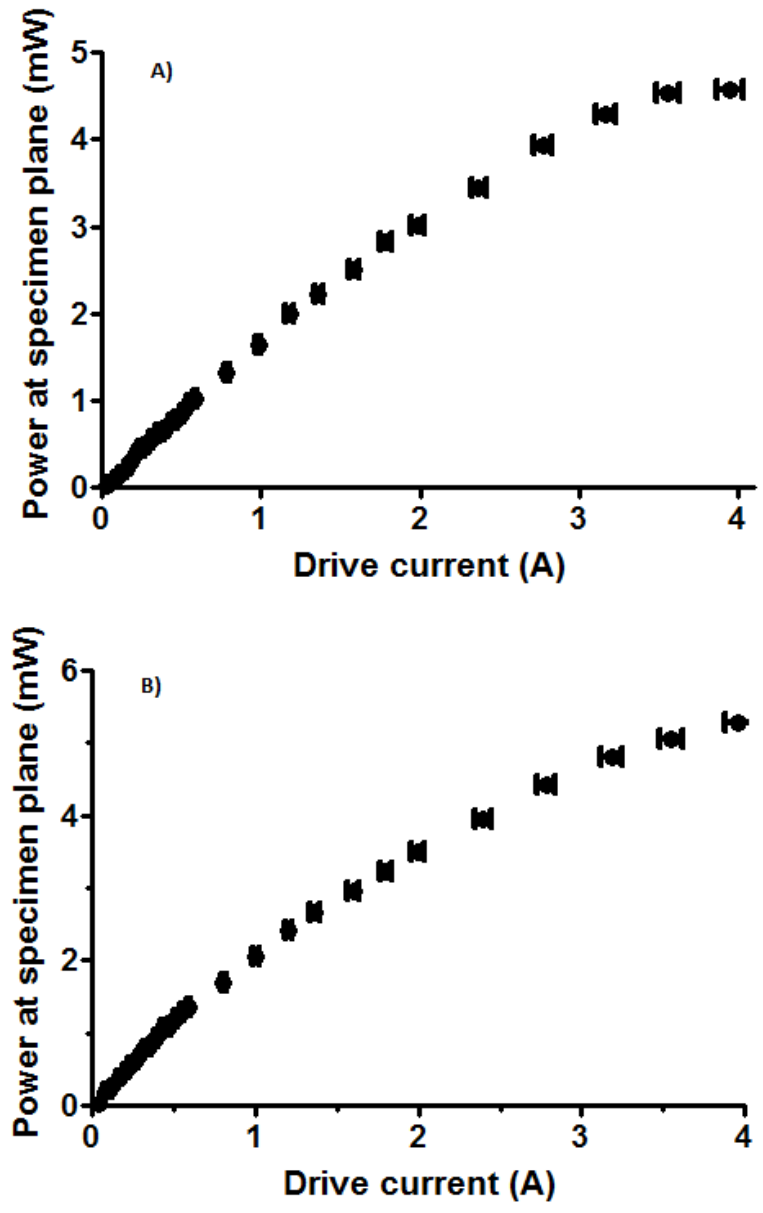


Figure 2.5; Power of A) 525 nm LED and B) 550 nm LED measured at the specimen plane under an Olympus 100x/1.4 oil immersion lens.

Fluorescence emission was collected at wavelengths longer than 561 nm using a CMOS camera (ORCA-Flash 4.0LT, Hamamatsu) with a binning  $n = 2$  and an exposure time of 33 ms. Extra magnification was added before the camera to increase the number of pixels used for imaging the specimen and reduce the number of red blood cells present in the field of view which allows for easier computational reconstruction. The extra magnification comprised of an elongated camera mount tube which contained an eyepiece that magnified the images by 2.99x. The LED and camera

were synchronised and triggered using the WinFluor imaging and electrophysiology analysis software [165], which also recorded continuous imaging at a rate of 30.3 Hz. High temporal resolution imaging experiments had a duration so as to provide a final standing wave movie size of 1000 frames. A schematic diagram of the experimental setup can be seen in figure 2.6.

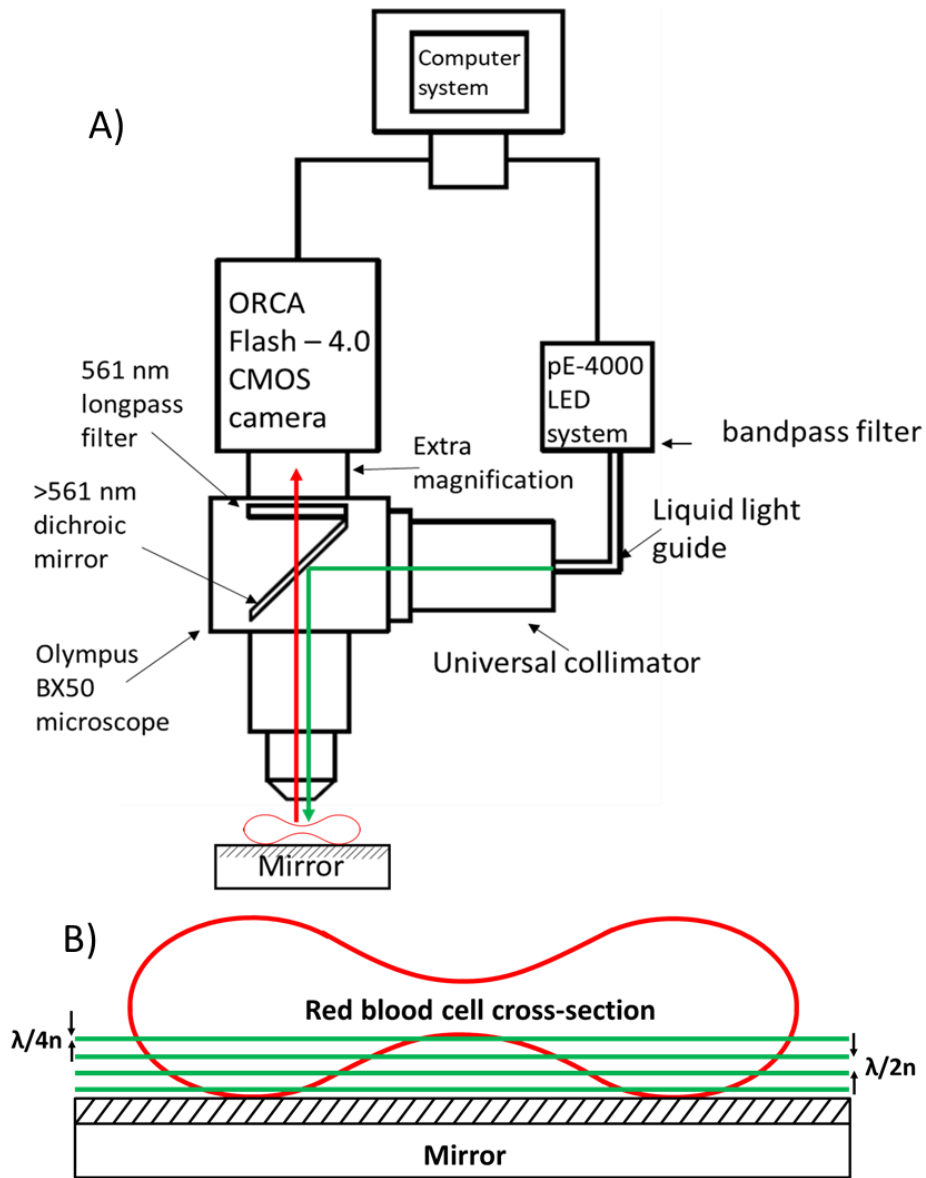


Figure 2.6; A) Schematic diagram of experimental setup demonstrating the coupling of the 525 and 550 nm LEDs to the BX50 microscope system via liquid light guide and collimator. The excitation light then reflects off a  $>561$  nm dichroic mirror to generate a standing wave due to self-interference at the mirror located at the specimen plane. This standing wave of light causes fluorescence emission at the standing wave antinodes which then propagates upwards through the lens, dichroic mirror and long pass filter to be detected by the sCMOS camera. The fluorescence signals are recorded by the computer which synchronises and triggers the LED and camera. B) Magnified view of the specimen plane demonstrating on how the standing wave antinodal planes interact with the red blood cell.

When experiments were carried out using the extra magnification and a camera binning  $n = 2$  the camera had a pixel size of 44.0 nm. The theoretical resolutions according to equations (1.5) and (1.6) with the 525 nm LED and 550 nm LEDs were calculated to be 248 nm laterally and 881 nm axially. The emission wavelength of 570 nm was used as  $\lambda$  for these calculations as the experiments are making use of widefield collimated excitation light and as such the different excitation wavelengths should make little difference to the widefield resolution measurements. This was checked experimentally by imaging 200 nm diameter fluorescent bead mounted in gelvatol, taking a line intensity profile through the centre of the beads and determining the FWHM of the profile. Through this process, it was found that the lateral resolution when using the 525 nm LED was  $304 \pm 44.0$  nm and  $290 \pm 44.0$  nm for the 550 nm LED. These difference between experimental and theoretical resolutions can be attributed to a refractive index mismatch between the immersion oil ( $n = 1.515$  at a wavelength of 546 nm at room temperature [166]) gelvatol ( $n = 1.482$  at a wavelength of 546 nm at room temperature [167]) and the coverslip or perhaps slight aberrations in the optical system.

#### **2.2.4) Image analysis and computational reconstruction**

Standing wave movies were exported from WinFluor as a .TIFF stack and opened in ImageJ. The images were then cropped to give a square region of interest (ROI) around the specimens of interest and were brightness and contrast adjusted to allow the antinodal planes to be distinguished more easily from the background. All computational reconstructions were performed using MATLAB R2017a and a desktop computer running 64-bit Windows 7 operating system with an 7<sup>th</sup> generation Intel core i7-770 3.6 GHz quad-core processor and 64 Gb of 2400 MHz DDR4 RAM.

The .TIFF stacks were then opened in the MATLAB script created by Ross Scrimgeour. The first process that was carried out on the images was to apply a Gaussian blur. The purpose of this was to reduce the amount of high frequency noise present in the images to allow for easier processing. The images were then intensity

thresholded to isolate only the antinodal planes and transform the image into a binary matrix. This was done using a standard MATLAB local adaptive threshold function with a sensitivity of 0.60.

It was found in some of the movie frames that antinodal planes at different height appeared to come into contact. This would not be possible unless the plane moved axially through a node or coinhabited the same axial location as the touching plane and as such it was determined that the effect was caused by the limited lateral resolution of the widefield microscope. In order to create a 3D reconstruction, it was necessary to computationally separate these planes, so the antinodal planes were recognised as separate objects by MATLAB and axial height values could be assigned. To do this, it was first necessary to detect all the nodal planes in the images. Once these were extracted the planes were then thinned to single pixel thick lines and by rotating the image in one-degree intervals the radial coordinates for each plane was recorded. As this step was detecting the nodal plane locations, any discontinuity in a nodal plane would be at the locations where the antinodal planes appeared to be in contact. Using a cubic interpolation, it was possible to fill in the missing data points and remove the discontinuities in the nodal planes. These were then subtracted from the threshold antinodal plane images to remove any touching antinodes and allow 3D reconstruction to be carried out.

Once the antinodal planes were separated, the images were run through a Canny edge detection function. This was done to detect only the boundaries for each antinodal plane and allowed an axial height, based on the antinodal spacing and FWHM, to be assigned to each edge. The resulting 3D structure then had a cubic interpolation applied so as to determine the locations of points that fell between the two plane edges. Using the obtained equation, the remaining points had an axial location assigned. The final step was to assign to each 3D point the original intensity value taken from the starting 2D frame and store the resulting movie as a .TIFF stack. The key steps in the image reconstruction are presented in a flow chart in figure 2.7.

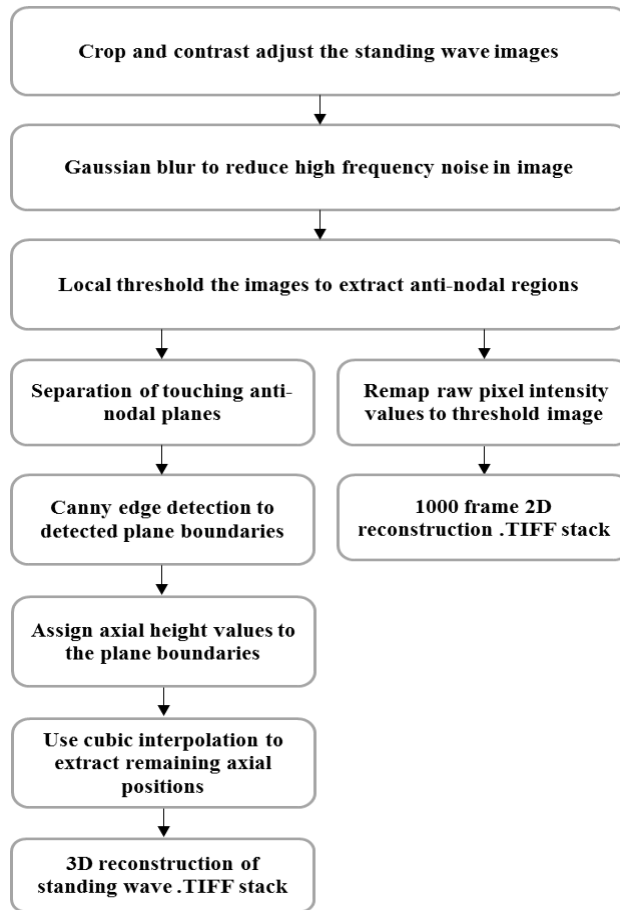


Figure 2.7; Flow chart demonstrating the key computational steps carried out in order to obtain either the 2D reconstruction or the 3D reconstruction of the red blood cell standing wave movies.

## 2.3) Results

### 2.3.1) Standing wave PSF simulation

In order to compare the experimentally obtained antinodal spacing and FWHM to the theoretical values the PSFs were computationally simulated using different imaging media and objective lenses with different NA. To do this equation (2.5) was used with the excitation wavelengths equal to the peak wavelengths of the 525 nm or the 550 nm

LEDs and the peak emission wavelength equal to 570 nm. A table of these results and plots of the resulting PSFs can be seen in table 2.1 and figures 2.8 – 2.11.

*Table 2.1; Antinodal spacings and FWHM in different media obtained from the theoretical PSFs of a 0.4 NA and 1.4 NA lens that were simulated using the excitation wavelength of 532 nm or 548 and an emission wavelength of 570 nm.*

LED	NA 0.4 and refractive index of media = 1		NA 1.4 and refractive index of media = 1.314	
	Antinodal spacing (nm)	Antinodal FWHM (nm)	Antinodal spacing (nm)	Antinodal FWHM (nm)
525 nm	266	133	194	97.0
550 nm	274	137	199	99.7

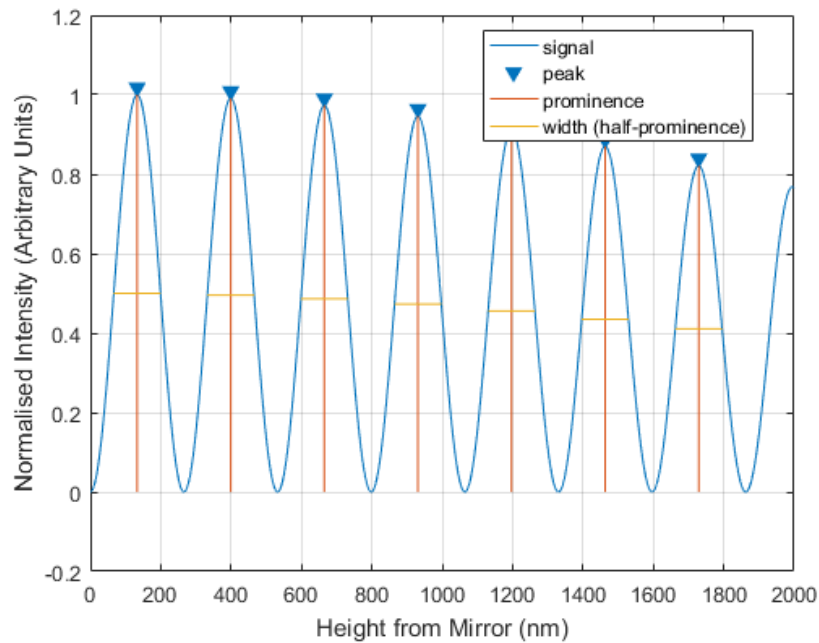


*Figure 2.8; Theoretical standing wave point spread function using a 525 nm LED as the excitation source and with a NA = 0.4 objective lens in air.*

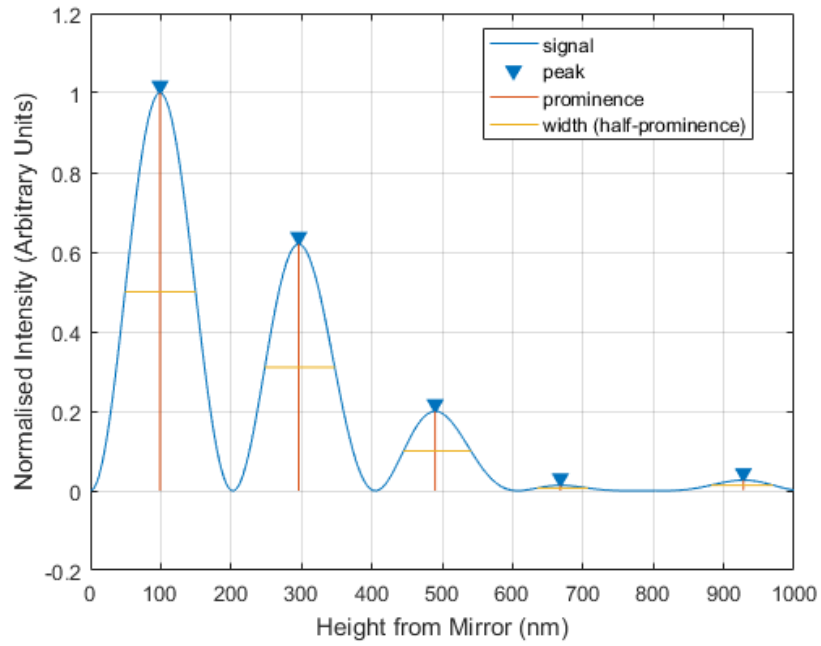


Figure 2.9; Theoretical standing wave point spread using a 525 nm LED as the excitation source and with a  $NA = 1.4$  objective lens in 4% BSA and PBS.

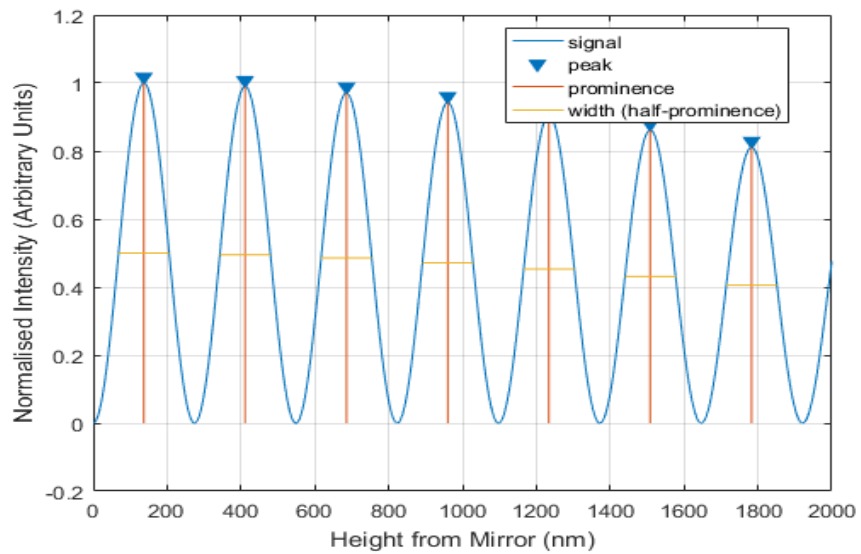
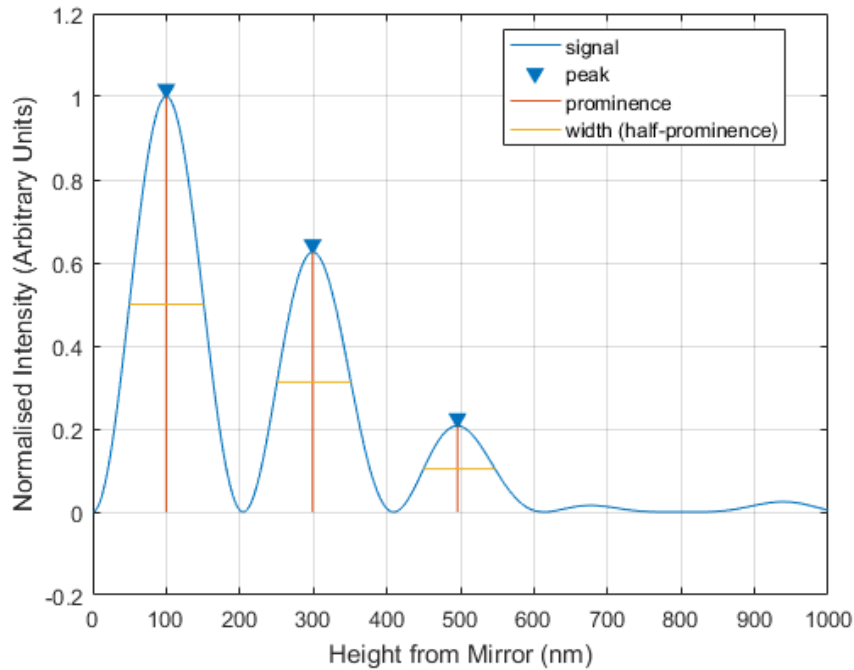


Figure 2.10; Theoretical standing wave point spread function using a 550 nm LED as the excitation source and with a  $NA = 0.4$  objective lens in air.



*Figure 2.11; Theoretical standing wave point spread function using a 550 nm LED as the excitation source and with a NA = 1.4 objective lens with 4% BSA and PBS.*

It is apparent from the above plots that whilst the excitation wavelength dictates the location of the antinodes and their FWHM the NA of the objective lens is what determines the number of planes which will be detected. This is due to the emission intensity drop off of the standing wave PSF within the focal depth of the objective lens used. The objective lens in this work is used only as the collection of the emission as our excitation illumination is collimated exiting the objective lens.

### **2.3.2) Standing wave imaging of fluorescently coated lens specimens**

In order to confirm that using a LED for imaging that it was possible to obtain antinodal spacings and FWHMs that were comparable to the theoretical values fluorescently labelled lens specimens were imaged with different media between the specimen and the mirror (figure. 2.12A and C). Radial averaging of the lens specimen

images was done by using a custom MATLAB script called *radialavg* [168]. In order to apply the script, the images were crossed in ImageJ, so they contain only eight antinodal planes. The MATLAB script was then to take a line from the centre of the image to the edge and sweep it radially through 360° at 1° intervals whilst recording the intensity value at each point along the line. An average at each point was then obtained from each rotation. Then using the known geometry of the lens and the following equation it was possible to transform these radial values into axial ones above the mirror,

$$d = -\sqrt{R^2 - r^2} + R \quad (2.6)$$

where  $R$  is the radius of curvature of the lens specimen and  $r$  is the radial distance from the centre. The next step was to compare the average axial antinodal spacings and FWHMs (figure 2.12B and D) to the theoretical values that were calculated from the analysis of the theoretical PSF calculated using equation (2.5). To determine if the theoretical and experimental values were statistically different a single sample t test was applied to the theoretical values where  $P < 0.05$  was considered significant. All uncertainties expressed with the average spacings and FWHM are the standard error in the mean.

The standing wave images recorded with the 525 nm LED and the 60 mm focal length lens imaged in air had an average antinodal space of  $265 \pm 10.2$  nm ( $P > 0.05$  compared to theoretical value 266 nm) and FWHM was  $137 \pm 3.6$  nm ( $P > 0.05$  compared to theoretical value 133 nm). The image in the 4% BSA and PBS had an antinodal spacing and FWHM of  $197 \pm 4.4$  nm ( $P > 0.05$  compared to the theoretical value 194 nm) and  $91.4 \pm 5.7$  nm ( $P > 0.05$  compared to the theoretical value 97.0 nm), respectively.

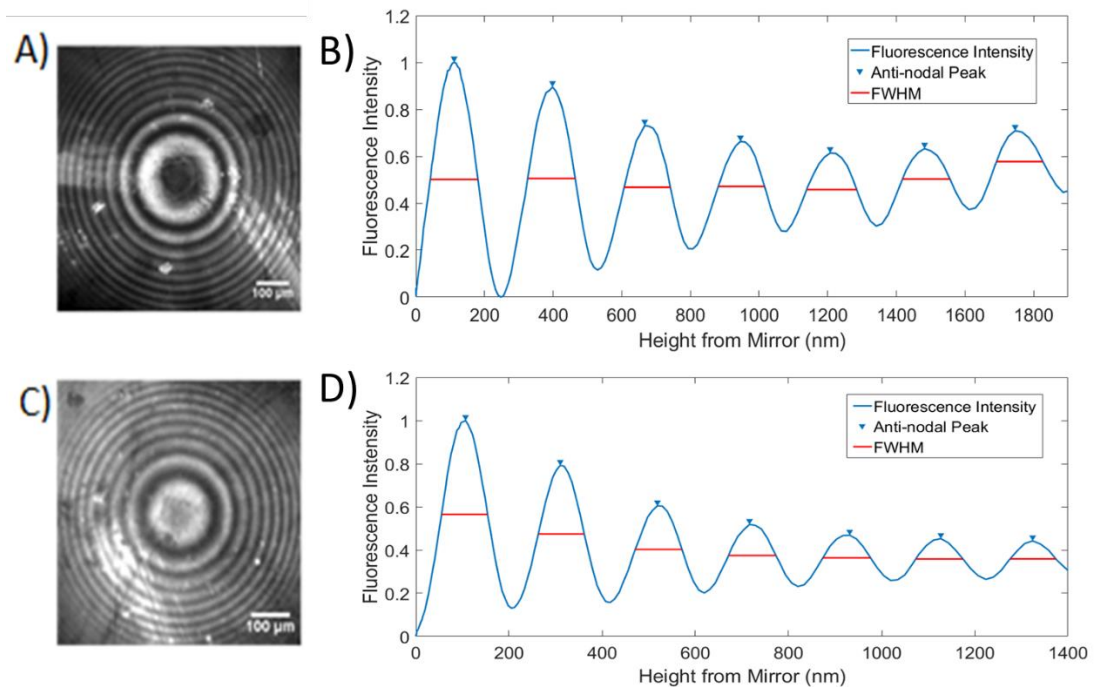


Figure 2.12; Standing wave images of the lens specimens obtained using the 525nm LED in A) air and C) 4% BSA and PBS. The radial averaged plots obtained of the antinodal axial locations in B) air and D) 4% BSA and PBS using a camera binning  $n = 2$ .

The lens imaging experiments were repeated for the 550 nm LED using the 30 mm focal length lens in 4% BSA and PBS had an average experimental antinodal spacing of  $192 \pm 3.5$  nm ( $P > 0.05$  compared to theoretical value of 199 nm) and an antinodal FWHM of  $93.0 \pm 6.8$  nm ( $P > 0.05$  compared to the theoretical value of 99.7 nm).

### 2.3.3) Video-rate standing wave imaging of red blood cells

Using the optical setup shown in figure 2.6 it was possible to carry out widefield standing wave imaging of the bottom half of a fluorescently labelled red blood cells upon a mirror at speeds in excess of video-rate (see figure 2.13). The optical attenuation by a single red cell has been measured previously to be around 20 % in the green spectral region which was used to excite DiI [169], which supports the propagation of the excitation light and, following reflection from the mirror surface

below the cell, allowing the formation of the standing wave. By carrying out this technique small and rapid membrane fluctuations were able to be imaged in real time that resemble the characteristic membrane flickering that is reported to occur in red blood cells [150] which would not be detected using point scanning methods due to the limited temporal resolution available [133]. Using the data from the resolution measurements and the imaging of the fluorescently coated lens specimens in 4% BSA and PBS it can be concluded that a lateral resolution of  $304 \pm 44.0$  nm and an axial resolution of  $91.4 \pm 5.7$  nm using 525 nm LED illumination and  $290 \pm 44.0$  nm laterally for the 550 nm LED images with an axial resolution of  $93.0 \pm 3.5$  nm is being achieved using this technique.

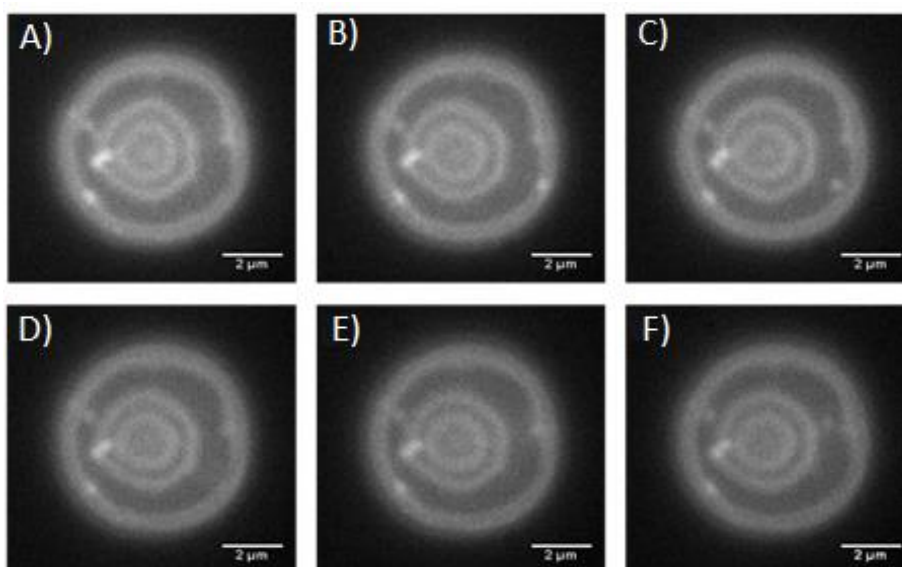


*Figure 2.13; Single frames taken from the 525 nm LED video-rate standing wave movie of the bottom half of a red blood cell labelled with the membrane dye DiI using a camera binning  $n = 2$ . The frames presented as A-F are frames 1, 200, 400, 600, 800 and 999.*

To aid visualisation of the standing wave movies of the red blood cell specimen computational reconstructions of the data were performed. To do this the antinodal planes were extracted and separated using the method described in section 2.2.4. This allowed the original intensity data to be normalised and have the axial heights mapped to each pixel. The 2D result of this can be seen in figure 2.14 and the 3D reconstruction in figure 2.15 with both an exaggerated and actual axial aspect ratio. Through the

bottom bi-concave section of the red blood cell as well as the very outer section of the cell membrane can be clearly seen. As the data has been computationally extracted it makes it not only easier to visualise but for further quantitative analysis to be carried out.

It was possible to create 3D movies consisting of 835 frames from the full 525 nm excitation standing wave movie and 981 frames from a 550 nm excitation standing wave movie. The frames that are missing are due to limitations in the script and data resulting in some frames being unable to undergo 3D reconstruction. As axial heights or antinodal separation was not required to be carried out for 2D reconstructions it was possible to generate full 1000 frame movies of these.

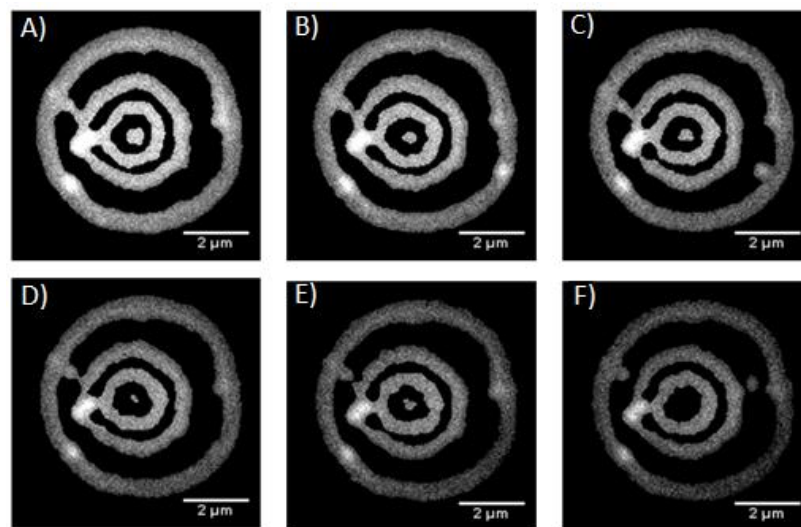


*Figure 2.14; Single frames taken from the 2D computational reconstruction of the 525 nm LED video-rate standing wave movie. The frames presented as A-F are frames 1, 200, 400, 600, 800 and 999.*

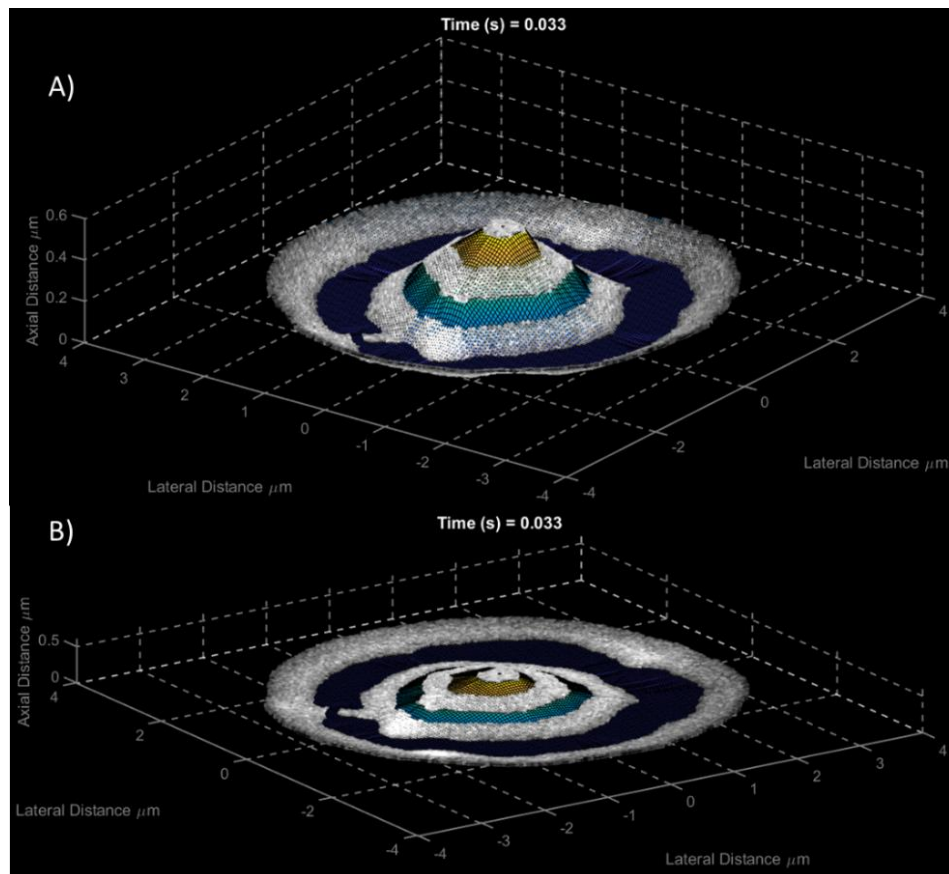


Figure 2.15; A 3D reconstruction of frame one of the standing wave red blood cell in which A) the axial aspect ratio has been increased to 13.33 to aid visualisation and B) the aspect ratios have not been altered.

#### 2.3.4) Comparison between standing wave imaging and standard widefield epifluorescence imaging

After successfully carrying out video-rate standing wave microscopy and generating 2D and 3D reconstructions of the red blood cell movies it was then of interest to investigate the effect of the standing wave imaging technique on the rate of specimen photobleaching and compare this to that recorded using video-rate widefield epifluorescence microscopy. To do this standing wave imaging of 10 red blood cells excited using the 550 nm LED was carried out using the method described above. To investigate the photobleaching rates the cropped and contrast adjusted movies were

inputted into the MATLAB script to obtain a normalised 2D reconstruction for each one. As before, the MATLAB script applied a local threshold to isolate the anti-nodal planes and the average intensity of all the non-zero intensity pixels were determined and outputted for each time point. This process was repeated but with the red blood cells on standard microscope slides rather than a mirror to image the cells using standard widefield epifluorescence illumination rather than with a standing wave. The average normalised intensity along with the standard error of the mean for each time point ( $n = 10$ ) for standing wave microscopy can be seen below in figure 2.16A and for widefield epifluorescence imaging in figure 2.16B.

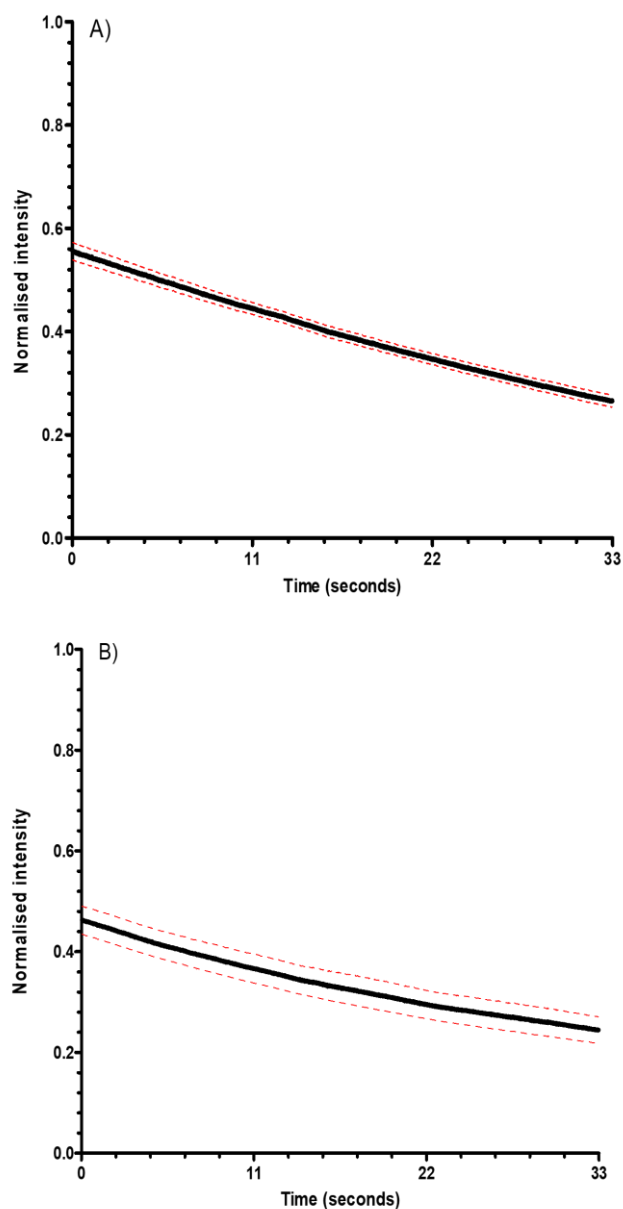


Figure 2.16; Average normalised intensity obtained from A) standing wave movies and B) widefield epifluorescence imaging of red blood cells ( $n = 10$ ) excited using a 550 nm LED with a power at the specimen plane of  $1.71 \pm 0.01$  mW. Errors in the values listed above are the SEM.

When comparing the data using both techniques it was found that the average intensity decrease observed across the 1000 frames when using standing wave imaging was  $51.9 \pm 2.28$  % and for standard widefield epifluorescence imaging it was  $47.8 \pm 4.78$  %. These rates were compared using a student t-test after which it was found that there

was no significant difference between the average photobleaching rates recorded with each technique ( $P > 0.05$ ).

The average initial normalised intensity values when using each technique were compared and it was found that the standing wave imaging provided an initial normalised intensity of  $0.55 \pm 0.02$  which was significantly larger than that when using widefield epifluorescence microscopy using the same power at the specimen plane ( $n = 10$ ,  $P < 0.05$  compared to an initial intensity using widefield epifluorescence imaging of  $0.46 \pm 0.03$ ). The increased brightness of the standing wave images compared to the widefield epifluorescence images could be attributed to the multiple bright fluorescent antinodal planes being present in the standing wave images. In widefield epifluorescence microscopy there is only a single bright plane with the rest of the image being composed of out of focus fluorescence.

The effect of the imaging technique on red blood cells was also explored over a longer timescale. Red blood cells were placed on either a mirror or a microscope slide and imaged the specimens using the 550 nm LED. An LED and camera exposure time of 100 ms and capture an image every 15 seconds for a duration of 30 minutes. Six timepoint images from these experiments can be seen in figure 2.17 for imaging with a standing wave and figure 2.18 for widefield epifluorescence imaging.

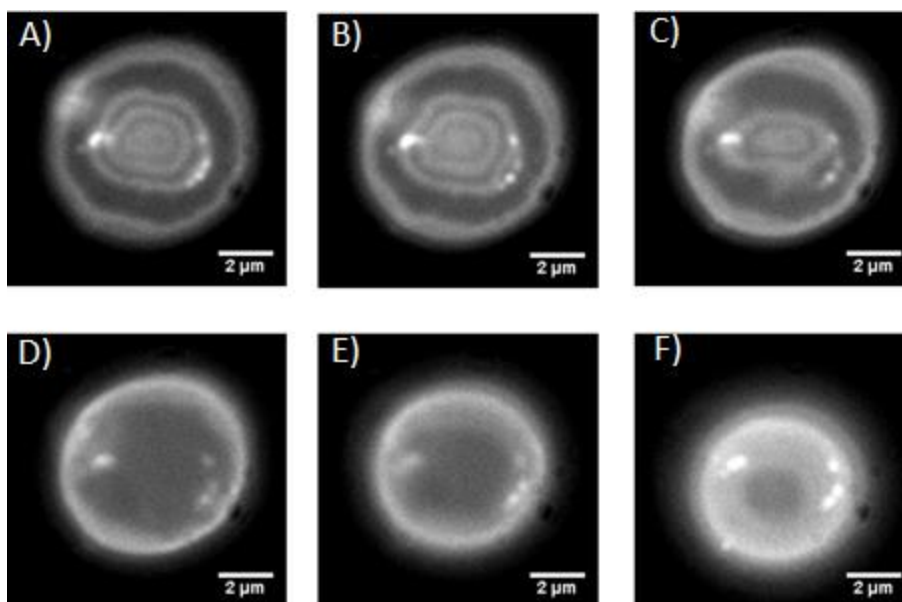


*Figure 2.17; Cropped and contrast adjusted standing wave images of a red blood cell. The frames presented as A-F are at time points 15, 360, 720, 1080, 1440 and 1800 s.*

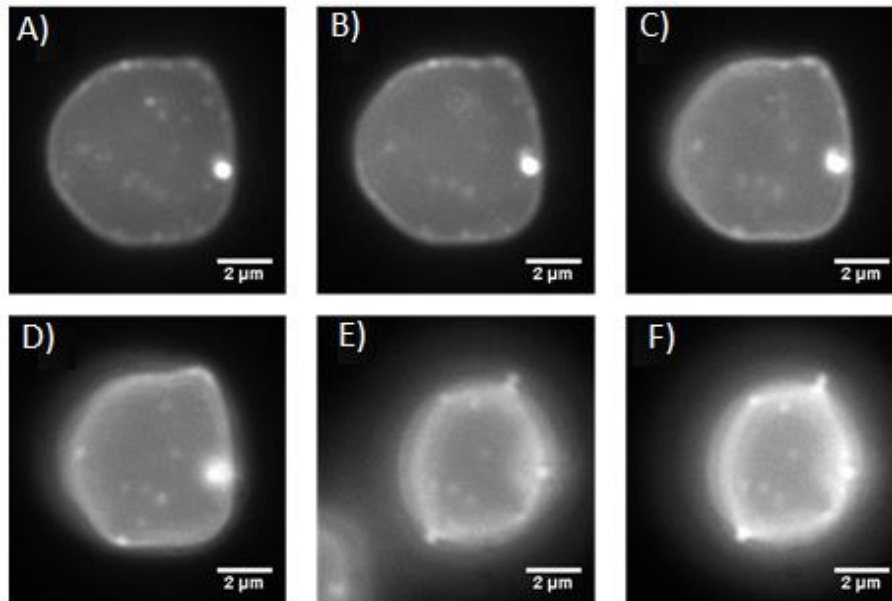


Figure 2.18; Cropped and contrast adjusted standing wave images of a red blood cell. The frames presented as A-F are at time points 15, 360, 720, 1080, 1440 and 1800 s.

As can be seen from the above figures, standing wave microscopy reveals a greater amount of topographical information about the decay of the red blood cell. It is also apparent that both red blood cells appear to turn unhealthy, flatten and undergo membrane deformations at approximately the same rate regardless of which technique was used.

## 2.4) Discussion

All previous applications of standing wave microscopy have utilised lasers [130], [132]–[134], [140] for illumination, but in this research, an LED source has been utilised instead. As this was the first use of a LED illuminator, it was first necessary to confirm that it was able to generate experimental standing wave antinodal spacing and FWHMs that were comparable to the theoretical values. To do this the model fluorescent lens specimen imaging experiments of Amor *et al.* were replicated with media of different refractive indices between specimen and the mirror. It was found through these experiments that in all media, antinodal spacings and FWHMs were

obtained that were not significantly different from the theoretical values ( $P > 0.05$ ). It was also found that the 550 nm LED provided better results than 525 nm LED, this is to be expected as the 550 nm LED more closely matches the excitation peak of DiI. The reason for why the 550 nm LED was not used exclusively is because it was not obtained until a much later date.

It has been reported previously that DiI is resistant to photobleaching [160]–[162]. However, in these experiments an intensity decrease of approximately a 50 % was observed over the 33 second imaging period. This photobleaching can be attributed to either the majority of the decay occurring during the specimen preparation and finding of the specimens prior to imaging or to perhaps a contribution of a dye interaction with reactive oxygen which has been observed to increase the photobleaching rates of DiI [170]–[172]. Photobleaching rates have always been a limiting factor when carrying out microscopy and can be especially problematic when carrying out super-resolution microscopy [173], [174] so the ability to cause no increased rate in bleaching compared to widefield epifluorescence imaging can be a significant advantage. Other membrane dyes were investigated for use in these experiments, such as DiO, DiA and Di-8-ANEPPS, but it was found that they were unsuitable as either the dyes were internalised by the red blood cells or photobleached too rapidly for practical use.

IRM has also been used previously to image red blood cells allowing the specimens to be imaged without using a fluorescent probe, and results in images that resemble those obtained using the standing wave technique [175], [176]. It has been shown previously though that IRM has provided membrane topography results that are not in agreement with those obtained using other methods. One such study that demonstrated this was by Gingell, *et al.* [177]. The aim of the study was to measure the thickness of the gap between coverslip and the membrane of chick fibroblasts which was done by filling this region with a fluorescent dye that was not able to be taken up by the cell and it was observed through TIRF excitation that there were close contact regions devoid of dye over almost the entire area of the cell. This was contrary to what was observed using IRM which in addition demonstrated a dark band around the boundary of the cell which was not seen in TIRF. It was speculated that the IRM image was influenced not by the membrane topography but by the thickness of the cytoplasm in that region. The observations of this study were also replicated by Iwanaga *et al.* [178] who carried

this out using a standing wave based method known as Fluorescence interference contrast microscopy (FLIC). DiI was used to label the membrane of the cells which were grown on silica micro-steps and demonstrated that the standing wave-based technique provided an unequivocal axial ruler and as such was a reliable method for studying membrane topography, whereas IRM was not.

As discussed in Chapter 1, it is also common to find that super-resolution techniques or point scanning techniques typically sacrifice temporal resolution in order to increase spatial resolution [179], [180], whereas in this study it was possible to improve the widefield axial resolution by a factor of approximately 8 and maintain high temporal resolution imaging of live cell specimens in 3D. This was not possible in the work carried out by Amor *et al.* as the study utilised a scanning confocal microscope for imaging [133]. The ability to carry this out on a widefield microscope also allows for the possibility of multiple red blood cells to be investigated simultaneously which could be an advantage for diagnostic purposes or studies requiring a high data throughput.

It has also been discussed in Chapter 1 that many super-resolution microscopy techniques are able to provide a spatial resolution improvement both axially and laterally, something which is not possible in standing wave microscopy, so it is likely that there will be circumstances where standing wave microscopy is not a suitable technique, such as when very high lateral resolution is required. Even with this limitation though, it was possible to carry out video-rate standing wave microscopy which allowed rapid membrane fluctuations and membrane morphology of red blood cells to be imaged which can be an advantage for researchers looking to investigate membrane flickering and the biomechanical characteristics of red blood cells [148], [149], [181] or the behaviour of diseased or healthy red blood cells undergoing morphological changes [151], [182]–[185].

One of the antinodal planes generated within the specimen by standing wave microscopy could be thought of as analogous to the illumination pattern generated by light sheet microscopy. In light sheet microscopy the light is focussed into a single uniform illumination plane which is scanned through the specimen which reduces photobleaching and photo-toxicity with the fluorescence emission being collected in a

widefield fashion by an objective lens perpendicular to the illumination [41], [186], [187]. As the light is focussed into a single plane, only fluorophores coinciding with the illumination are excited leaving the rest of the specimen non-fluorescing. Whereas light sheet microscopy typically comprises of a single light sheet which must be scanned through the specimen, in standing wave microscopy multiple axial planes are excited and obtained simultaneously, though it is not possible to illuminate the entire specimen using a single excitation wavelength due to the nodal planes of the standing wave. The resolution possible in light sheet microscopy suffers from the principles of gaussian beams. If a thin light sheet is required, then it can only be done over a short distance as the beam will rapidly diverge [188], [189]. Though this limitation can be overcome through the use of specialised beams such as Bessel or Airy beams [188], [190], by the very nature of standing wave microscopy we are able to obtain optical planes with a thickness of  $\lambda/4n$  over the entire field of view of the objective lens.

The high temporal resolution available with the widefield standing wave technique has allowed the observation of rapid membrane morphological changes in real time which in the data sets presented here appears to indicate that the entire membrane is in motion with whole-cell vibrations being observed and small movements taking place in the bi-concave section. The entire cell motion may be due to whole cell Brownian motion, or weak electro-static interaction between the poly-L-lysine coating and the membrane, though the ability to observe whole cell movements with super-resolved axial sections demonstrates that this technique may also have applications in cell tracking or motility studies. The motion observed in the concave surface resembles the movements which occur at the boundary between the concave section and the outer membrane [150], though the majority of this boundary inhabits a nodal plane. It was not possible to detect the very small membrane dimpling observed in other studies using quantitative phase imaging which appear to be on the order of approximately 40 nm [184], and is to be expected as the dimpling events are not large enough to cross the boundaries between an anti-nodal or nodal plane and this technique is not able to axially resolve small movements ( $\sim 100$  nm) within planes. It is also possible that the rapid flickering motion is suppressed at the surface being imaged due to the electro-static attraction of the poly-L-lysine coating.

From the datasets obtained using this technique it was possible to extract axial information from the movies in order to generate 2D and 3D reconstructions of the red blood cell membranes that clearly showed the bi-concave surface, providing the user with easier visualisation of their specimen and can allow them the opportunity to carry out further quantitative analysis. The 2D reconstruction process took on the order a few minutes and the 3D on the order of 10 minutes to complete after image pre-processing and utilised only a standard desktop computer without a graphics processing unit (GPU) along with only inbuilt MATLAB functions allowing the technique to be easily accessible to most general users.

There were specific circumstances that arose from the data that resulted in the code being unable to reconstruct some frames in 3D, it is worth noting that the code was capable of generating 2D reconstructions of the full 1000 frame standing wave movies. The first circumstance was one where free clumps of dye were present between antinodal places, the MATLAB script detected these as separate objects but was unable to assign an axial height to them which caused issues. The other situation was when there were large amounts of missing data, either due to poor thresholding or poor interpolation of the nodal planes. The script was able to automatically detect images that met these criteria and remove them from the reconstruction. Even with these limitations the code was able to generate 3D reconstruction movies which comprised of 835 and 981 frames from the 1000 frame 525 nm and the 550 nm excitation video-rate standing wave movies, respectively and further improvements to the robustness of the script could result in even more frames being reconstructed, though it is entirely dependent upon the quality of the data analysed.

This work also investigated whether the standing wave technique caused any further photo-toxicity to the specimen compared to widefield epifluorescence imaging. It was observed that when using either imaging method, the red blood cell appeared to decay at a similar rate and in a manner that resembled the decay observed previously over 12 minutes under periodic focused laser illumination [191]. In the study of Wong *et. al*, it was found that membrane damage occurred even at low laser powers as the result of reactive oxygen species being generated via photo-hemolysis. This process has been hypothesised to be due to interactions between the reactive oxygen species and the membrane proteins, band 3 and spectrin [191] which has also been reported in studies

using widefield illumination [192], [193]. It has also been found that when using multiphoton microscopy, red blood cell photodamage could be observed on timescales in the region of tens of seconds [194], however, when video-rate experiments were carried out in this study, there were no observable photo-toxicity effects over the 33 second duration.

## **2.5) Conclusion**

The work in this Chapter presents the first demonstration of video-rate widefield standing wave imaging of fluorescently labelled red blood cells illuminated using a LED source. Through the simple method of placing specimens upon a mirror it was possible to achieve axial super-resolution imaging below 100 nm of the morphology and deformations of the red blood cell membrane in real time with no increase in photobleaching rates or cellular toxicity compared to video-rate widefield epifluorescence imaging.

## Chapter Three:

# TartanSW emission and excitation imaging of live cell specimens

The contents of this Chapter explore the application of widefield and confocal TartanSW emission and excitation microscopy and also demonstrates the first application of the standing wave technique to image the membrane structure of whole adherent mammalian cells. The multi-emission and excitation standing wave techniques have been dubbed TartanSW as both a homage to the geographical location of our lab and due to the striking different colour antinodal banding observed in the images.

This work demonstrates the use of widefield and confocal TartanSW emission microscopy to image model lens specimens in order to compare the experimental emission modulated structures to those calculated theoretically. Though it was found that the widefield data was inconsistent with the calculated data, the technique was also used to image red blood cells and MCF-7 breast cancer cells where the relative locations of the different emission bandwidth antinodal planes could suggest at the directionality of a surface.

Widefield TartanSW excitation imaging of fluorescent lens specimens has shown that the nodal plane contribution of missing information to an image can be reduced from 44.3 % in a single colour standing wave image to 12.0 % with the two additional wavelengths which is accurate to the theory within 1.6 %. It was also shown through this work that by taking the difference between each of the standing wave excitation channels that in the resulting image it was possible to increase the post-acquisition axial resolution of the images by approximately a factor of 2 and obtain standing wave images of MCF-7 breast cancer cells with an experimental axial resolution less than 50 nm.

These TartanSW imaging modalities allow for a more complete topographical map of the specimen to be obtained and the ability to simply gain an improved resolution that surpasses what was previously possible with single colour standing wave microscopy and also may in the future allow for the ability to generate precise maps about the specimen structure without any prior knowledge.

### **3.1) Introduction**

It has been demonstrated in the previous Chapter that widefield multi-planar standing wave microscopy is an easy to implement technique that can allow axial sub-diffraction limited topographical maps of the membrane dynamics to be acquired at high temporal resolutions. Although the advantages of single colour standing wave microscopy are many, it is not without some limitations which are the contribution of the nodal planes to the image and the unknown relative axial location of the antinodal planes. Through the course of this Chapter, it is the aim to provide an overview of these two of the inherent drawbacks of the single colour standing wave microscopy technique and through the application of TartanSW emission and excitation microscopy investigate the ability of these modalities to surpass these limits.

#### **3.1.1) Tartan SW excitation microscopy**

Though the standing wave illumination pattern allows for sub-diffraction limited axial resolution it is quite apparent that there exist periodic dark regions in the acquired images. This is because for each antinodal plane of emitted fluorescence there is a corresponding nodal plane of zero intensity due to destructive interference. These nodal planes contribute unavoidable periodic planes of missing information to the image where nothing about the specimen can be known, these regions are known as the standing wave information gap [143]. This effect can be seen clearly in the standing

wave images of the fluorescent lens specimens, shown in section 2.3.2, where between each fluorescent concentric ring there is a dark band and these information gaps can be an issue where a much more complete map of the specimen is required.

As seen by equations (2.1) to (2.5), the axial locations of the antinodal planes, and hence the nodal planes, are directly related to the wavelength of the excitation standing wave illumination. Even though this information gap will be present regardless of whatever excitation wavelength is used, the axial positions of the nodal and antinodal planes will be shifted at different excitation wavelengths meaning that different excitation antinodes will illuminate portions of the specimen that may coincide with the nodal plane locations at different wavelengths. This is the concept that the TartanSW excitation experiments are based around, and if it were possible to sequentially excite a fluorescent specimen rapidly at different wavelengths then by creating a composite of the different excitation images a more complete topographical map could be generated as the total nodal plane contribution would be reduced. A cartoon representation of this process can be seen in figure 3.1.

In order to facilitate this work, a LED illuminator had to be developed that was capable of rapidly switching between three excitation wavelengths which would allow the TartanSW excitation technique to support high temporal resolution imaging where each TartanSW excitation frame was a composite of the three different excitation images. This work first used a fluorescent lens specimen to compare the experimental and theoretical antinodal FWHM and separation as well as calculate an experimental and theoretical value for the information gap reduction, and then applied the method to study biological specimens with widefield and confocal microscopy.

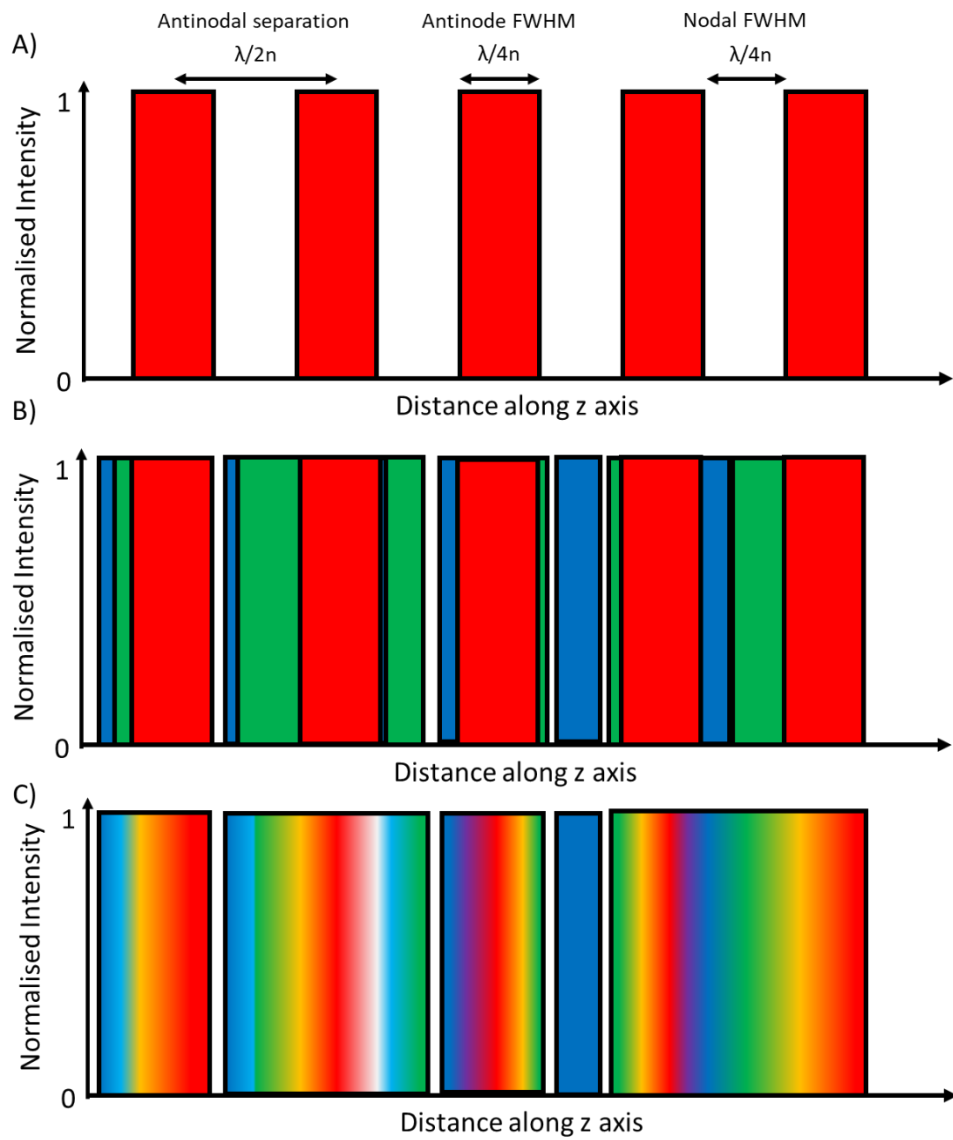


Figure 3.1; Cartoon representation of the excitation intensity resulting from standing wave illumination along the optical axis of a microscope. A) A single standing wave excitation plot (red boxes) showing the separation between the bands and the widths of the antinodal and nodal planes. Location coinciding with the nodal planes result in zero fluorescence emission as the intensity of the standing wave is zero. B) A demonstration of the total reduction in the nodal plane contributions due to the addition of two extra optical standing waves of light (shown in green and blue) which have different wavelengths from the one in red. C) Demonstrates the colour mixing that occurs when the different excitation wavelength images are assigned RGB lookup tables and composited on top of each other. This diagram assumes that all standing wave excitation channels are normalised to each other.

### 3.1.2) TartanSW emission microscopy

Though standing wave microscopy allows for the simultaneous acquisition of multiple antinodal planes within the focal volume of the specimen allowing a topographical map of the specimen to be obtained, if the basic geometry of the specimen is unknown then the axial location of antinodal planes relative to one another can be difficult to determine. In order to reduce the ambiguity in the axial plane locations TartanSW emission looks to use the modulated intensity pattern caused by the resulting interference between the excitation standing wave and the emission standing wave.

It is a well-documented phenomenon that the resultant emission from excited fluorophores that are placed close to a reflective surface generates wide-angle interference patterns between the reflected and un-reflected light waves as the fluorophore behaves like an oscillating electric dipole [195], [196]. The detected emission intensity is then modulated due to interference effects occurring between the excitation and emission standing waves of light in the same manner as an acoustic beats pattern [197]–[199]. This excitation-emission standing wave interference results in a detected structure in which not only is the intensity modulated but whilst the nodes are at axial locations that are in agreement with theory, the antinodes are not [200].

A microscopy technique which makes use of this phenomena in order to generate precise axial maps of specimens was touched upon in the discussion section of Chapter 2 and is known as FLIC [197], [198]. The FLIC method utilises the interference between emission and excitation standing waves with cell specimens grown on a specially constructed substrate [197], [198], [201]. The substrate is comprised of two parts, the first being a reflective silicon layer, used to generate the reflection required for standing wave formation, and the second are small raised sections of silicon oxide which are of different height upon which the biological specimen is grown [178], [201]–[203]. By carrying out fluorescence microscopy of the specimens and observing the axial dependent intensity variation due to the specimen being grown on substrates,

FLIC can then be used to obtain a highly precise axial map of the specimen [197], [198].

Amor. *et. al.* observed that when the fluorescence emission was detected only over a limited bandwidth of 5 nm the recorded standing wave images of the a fluorescently coated lens specimens had a modulated beating intensity pattern (figure 3.2) [133]. The intensity modulation observed had an inverse spatial period that corresponded to the subtraction of the inverse of the peak excitation wavelength and the detected peak emission wavelength [204]. This demonstrated that it was caused by a moiré pattern generated from the interference of the excitation standing wave and an emission standing wave. The emission standing wave is created in the same manner as the excitation one, by undergoing self-interference between the un-reflected emission and a component reflected from the mirror.

Amor *et al.* investigated this intensity modulation further by generating standing wave images of a fluorescent lens specimen utilising emission self-interference alone and observed that intensity modulation was not present. When the emission only standing wave image was subtracted from an excitation standing wave image the result was an image that was intensity modulated in the same manner as the moiré image obtained previously with an experimental modulation that was within 4 % of theoretical values [133]. As with the work carried out in Chapter 2, the experiments presented in this Chapter aim to build upon the modulated intensity standing wave patterns observed by Amor *et.al.*

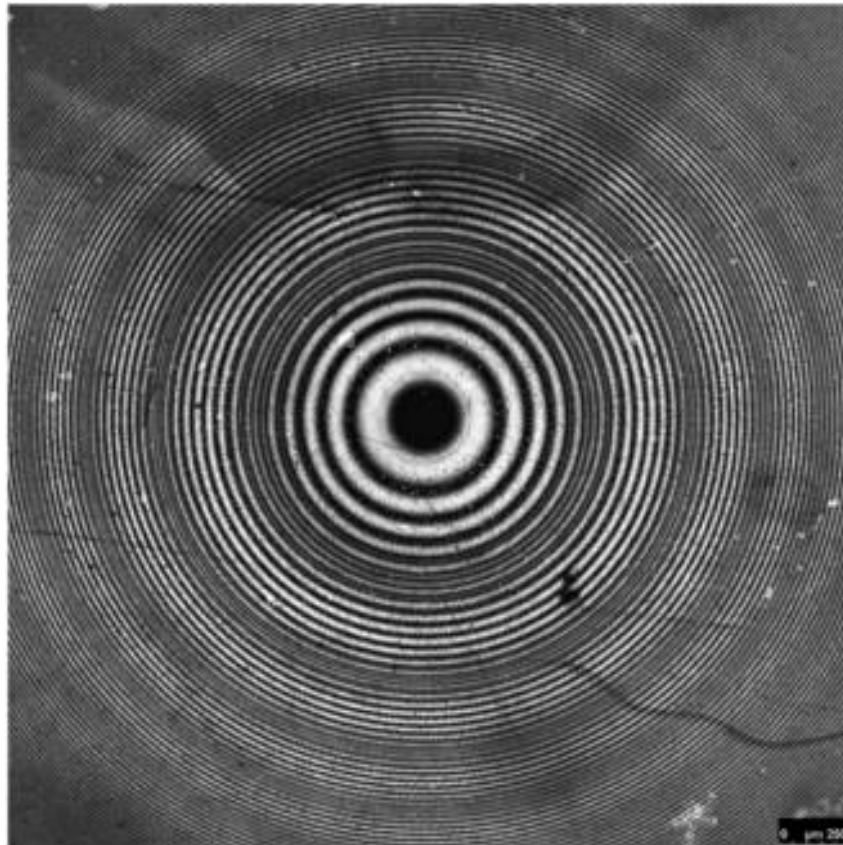


*Figure 3.2; Confocal standing wave image of a lens specimen coated with a fluorescent monolayer of Atto 532, excited using a 514 nm laser line with emission and detected with a 5 nm emission bandwidth centred around 580 nm demonstrating the resulting moiré pattern generated by the interference of the excitation standing wave and the emission standing wave. Reproduced from [133].*

The precise manner in which the intensity modulation takes place could be used to assist in reducing the ambiguity in axial antinodal plane ordering and unequivocally assign axial locations to each antinodal plane. In order to do this the experimentally recorded intensity modulation data would have to be normalised and compared to the amplitudes of standing wave structure obtained from the theoretically simulated PSF.

As the beating pattern has an inverse spatial period which is equal to the difference between the inverse of the peak excitation wavelength and the detected peak emission wavelength, the detected intensity modulation would be non-repeating within the focal volume of the experiments presented in this Chapter. For example, if an excitation standing wave of 550 nm was used for illumination with the emission being detected

at 570 nm the emission modulation has a spatial period equal to approximately 16  $\mu\text{m}$ . As for the imaging of mammalian cells an objective lens with an NA of 0.8 is used, according to equation (1.6), antinodal planes will only be detected up 2.5  $\mu\text{m}$  above the mirrored surface. This means that intensity modulation of any detected antinodal plane will be unique within this axial range and as such could be assigned an axial height value obtained from the theory.

The theoretical TartanSW emission structure can be obtained from the following equation which describes the interference that occurs between the excitation and emission standing wave illumination,

$$PSF_{SWME} = [1 - \cos\left(\frac{4\pi n}{\lambda_{em}} z\right)][1 - \cos(Kz)][\text{sinc}\left(\frac{NA^2}{2n\lambda_{em}} z\right)]^2 \quad (3.1)$$

This equation is an extended version of equation (2.5) which includes a term at the beginning in order to account for the standing wave of the emission which is present and interferes with the excitation standing wave causing the observed intensity modulation.

In the TartanSW emission experiments presented in this Chapter, multiple emission bandwidths have been used for imaging. This has been done as the standing wave intensity modulation is dependent upon the wavelength of the detected emission standing wave meaning that for each imaging bandwidth a structure with a different intensity modulation pattern will be obtained. By observing the ordering of the separate emission bandwidth standing wave planes relative to each other could give a qualitative indication of whether a surface is ascending or descending meaning that prior knowledge of the specimen structure may no longer be necessary. Though in combination with the theoretical values from equation (3.1) this could also be done quantitatively.

It was the aim of this work to utilise widefield video-rate and confocal single colour excitation standing wave technique along with the detection of multiple discrete emission bandwidths to investigate whether a more accurate topographical map of biological specimens could be obtained and if the directionality of the surface could be determined by observing the plane ordering.

## **3.2) Materials and methods**

### **3.2.1) Specimen preparation and LED characterisation**

Fluorescently coated lens specimens and red blood cells were prepared and stained using the same procedure described in Chapter 2. Widefield imaging of the red blood cell specimens utilised a 100x/1.4 oil immersion objective lens (UPlanSApo, Olympus) and the fluorescent lens specimen was under taken with a 10x/0.4 dry objective lens (UPlanSApo, Olympus).

For the TartanSW excitation lens imaging experiments, instead of mirrors microscope slides with 300 nm thickness of aluminium evaporated on were used instead (deposited on the slide using an Edwards coating system, E306A). For the TartanSW emission lens imaging experiments bare aluminium microscope slides (bare aluminium test slides, Dynasil) were used instead of mirrors. The reason for this was to ensure that the lenses were directly in contact with the reflective surface and not offset by the magnesium fluoride protective coating that was applied to the commercial mirrors used in the live cell imaging experiments. For all live cell experiments commercial aluminium mirrors were used as the imaging substrate.

MCF-7 cells, an immortalised endothelial breast cancer cell line, were cultured at 37 °C in a 5% CO<sub>2</sub> humidified incubator. MCF-7 cells have become one of the most widely used cell types for breast cancer research since their isolation almost 50 years ago [205]. They have led to the furthering of the fundamental understanding of how breast cancer develops leading to important discoveries in cancer migration, invasion and platelet aggregation [206]–[208]. Researchers, with whom we routinely collaborate, were exploring the effect that JNK knockdown has upon MCF-7 cell proliferation, cell cycle and death [209]. Due to the morphological changes that can occur during these processes we looked to use these cells for our experiments to investigate whether the TartanSW technique could be used in order to gain additional

morphological information about the specimens so that it may be applied in future studies investigating these processes.

The MCF-7 cells were grown in 75 cm<sup>2</sup> tissue culture flasks containing 10 mL of Dulbecco's Modified Eagle's Medium (DMEM) low glucose, pyruvate medium (Gibco, Paisley, UK) including 10% foetal calf serum (Biosera, Sussex, UK), and 1% penicillin-streptomycin (Sigma, Dorset, UK). Once cells were sufficiently confluent they were dissociated from the flask using 2 mL of TrypLE (Gibco, Paisley, UK) and incubated at 37 °C until all cells were detached. Cells were then resuspended in 8 mL of the modified DMEM media. 0.5 mL of the cell suspension was then seeded into wells of a 6 well plate that contained 20 mm diameter, 3 mm thick aluminium mirrors (laser2000) and 4 mL of DMEM per well. Cells were then left to adhere and grow for one day prior to imaging.

Prior to imaging the MCF-7 cells grown upon mirrors were washed three times in 4% BSA and PBS. After washing, a solution containing 4 mL of 4% BSA and PBS and 20 µL of a 1 mg/mL stock solution of DiI was added to a petri dish containing the specimens. These petri dishes were then incubated at 37 °C for 60 minutes whilst being protected from light. The specimens were washed a further three times before imaging. Imaging the MCF-7 cells was done in a custom 3D printed perfusion chamber with the specimens submerged in 4% BSA and PBS. The objective lens used for the widefield imaging experiments was a 40x/0.8 water dipping objective lens (LUMPLFLN, Olympus).

To carry out the widefield TartanSW excitation experiments but also retain the ability to achieve high temporal widefield imaging, an illuminator was required that was capable of rapidly switching between three wavelengths that were able to provide the optimum excitation of DiI. This work looked to follow on from that done in Chapter 2 by utilising LEDs for illumination, this would allow for the temporal resolution of the technique to be limited not by the electronic microsecond switching between different LEDs but the frame rates of the camera. The CMOS camera (ORCA-Flash 4.0LT, Hamamatsu) used in these experiments can support full frame imaging speeds of approximately 50 frames per second with a camera binning  $n = 2$  (which can be increased further by taking sub-regions on the camera chip) where as if an arc lamp

with monochromator/moving filter wheel were used for illumination the temporal resolution would be limited by the mechanical shifting between excitation wavelength. The LEDs chosen for these experiments were a 550 nm, 525nm and 490 nm.

The LED system that was used for the experiments in Chapter 2 (pE-4000, CoolLED Ltd) is made up of 16 LEDs laid out onto four different channels and can achieve switching speeds between LEDs on the order of 20  $\mu$ s, but only between LEDs on different channels. LED switching that occurs between LEDs on the same single channel is limited by a mechanical shift and can be on the order of seconds which could result in the specimen changing morphology whilst switching excitation wavelengths.

Two of the three LEDs that were required for the TartanSW excitation experiments were laid out onto the same channel and as such, in order to maintain a high temporal resolution, a custom pE-4000 system had to be developed. At the same time as this development began CoolLED had recently started implementing new brighter LED chips into their pE-300 systems which were made available to us and as such the custom standing wave pE-4000 was the first unit to be developed using these new high brightness LEDs. As this was a new custom system, output spectra and power characterisation had to be carried out for the 525 nm and 490 nm LEDs (the new 550 nm LED had been previously characterised in Chapter 2).

Wavelength measurements were recorded using a spectrometer (USB2000 spectrometer, OceanOptics) and the peak wavelength and FWHM were determined using the same methods as in section 2.2.3. Average power readings were recorded by taking three readings at each of the different LED drive currents at the specimen plane of the microscope (BX50, Olympus) under each objective lens used for the different specimen using the same equipment and settings as described in section 2.2.3.

As the LEDs were required to be spectrally separate from each other and prevent any excitation bleed through to the detector, the 550 nm LED and 525 nm LEDs were used in conjunction with clean up filters (535/30 nm bandpass filter, Olympus and a 531/40 nm bandpass filter, Semrock for the 550 nm and 525 nm LEDs, respectively). The 490 nm LED had an output spectrum which was short enough to be used unfiltered.

It was found that the 525 nm LED a peak wavelength of  $524 \pm 1.50$  nm (FWHM -  $26.8 \pm 1.50$  nm) and the 490 nm LED had a peak wavelength of  $490 \pm 1.50$  nm (FWHM -  $12.3 \pm 1.50$  nm). The spectra measured at the specimen plane under the 100x/1.4 oil immersion objective lens for the LEDs can be seen in figure 3.3 and below.

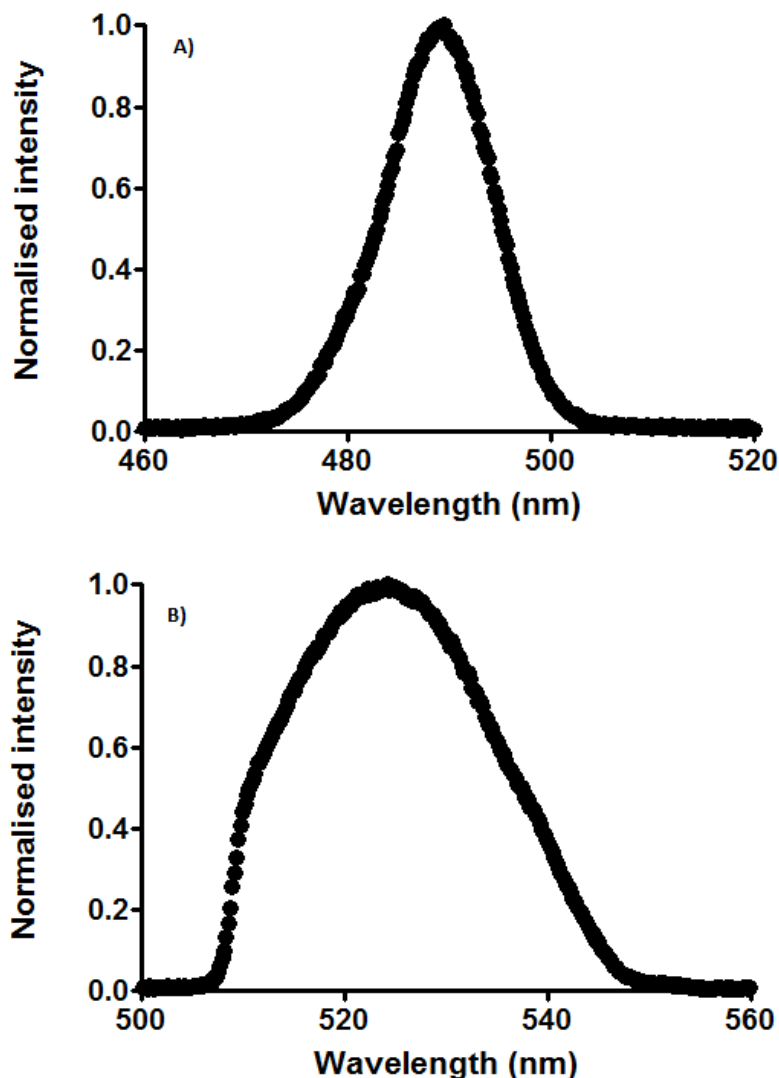


*Figure 3.3; Measured output spectra, taken at the specimen plane of a BX50 widefield microscope, of the A) 490 nm LED, and the B) filtered 525 nm LED.*

The final characterisation that was carried out on the LEDs was to determine the experimental lateral resolutions in order to make a comparison to the theoretical values. To do this, 200 nm fluorescent beads mounted in gelvatol were imaged using the 100x/1.4 oil immersion objective lens and a sCMOS camera using no camera

binning. Using equation (1.5) it was found that theoretical lateral resolution using the 525 nm and 490 nm LEDs with an emission wavelength of 570 nm was 248 nm. As in the work carried out in Chapter 2, the peak emission wavelength is the one used for the calculations as the experiments are making use of widefield collimated excitation illumination.

After analysing the FWHM of the intensity profile taken through one of the fluorescent beads it was found that both of the LEDs used for illumination resulted in obtaining a lateral resolution that was  $290 \pm 22.0$  nm. The differences observed between the theoretical and experimental results could again be attributed to slight aberrations present in the microscope system or the slight refractive index mismatch between the immersion oil used for the objective lens and the gelvatol the beads were mounted in. It is also worth to note that the measured lateral resolutions are consistent with those obtained in Chapter 2 section 2.2.3.

### **3.2.2) TartanSW emission imaging setup**

In order to carry out widefield TartanSW emission imaging the microscope setup described in Chapter 2 was used with some modification. As the experiments looked to make use of multiple emission bandwidths, an emission image splitter (W-VIEW GEMINI, Hamamatsu) was added between the additional camera magnification and the camera which then allowed two bandwidths of the DiI emission spectrum to be imaged onto separate sides of the sCMOS camera chip.

Inside the image splitter the following optics were installed to facilitate the imaging. The fluorescence emission was first split using a dichroic mirror (594 nm longpass dichroic beamsplitter, Semrock) and the resulting two emission bands had their bandwidths reduced by propagating through bandpass filters (576/10 nm and a 620/14 nm bandpass filters, Semrock) before being imaged on to different halves of the imaging chip.

Excitation was provided by the 550 nm LED from the custom LED system which was coupled to the microscope through a liquid light guide and a collimator (Universal collimator, CoolLED). The sCMOS camera and LED were TTL controlled using the WinFluor software [165] which also recorded the images.

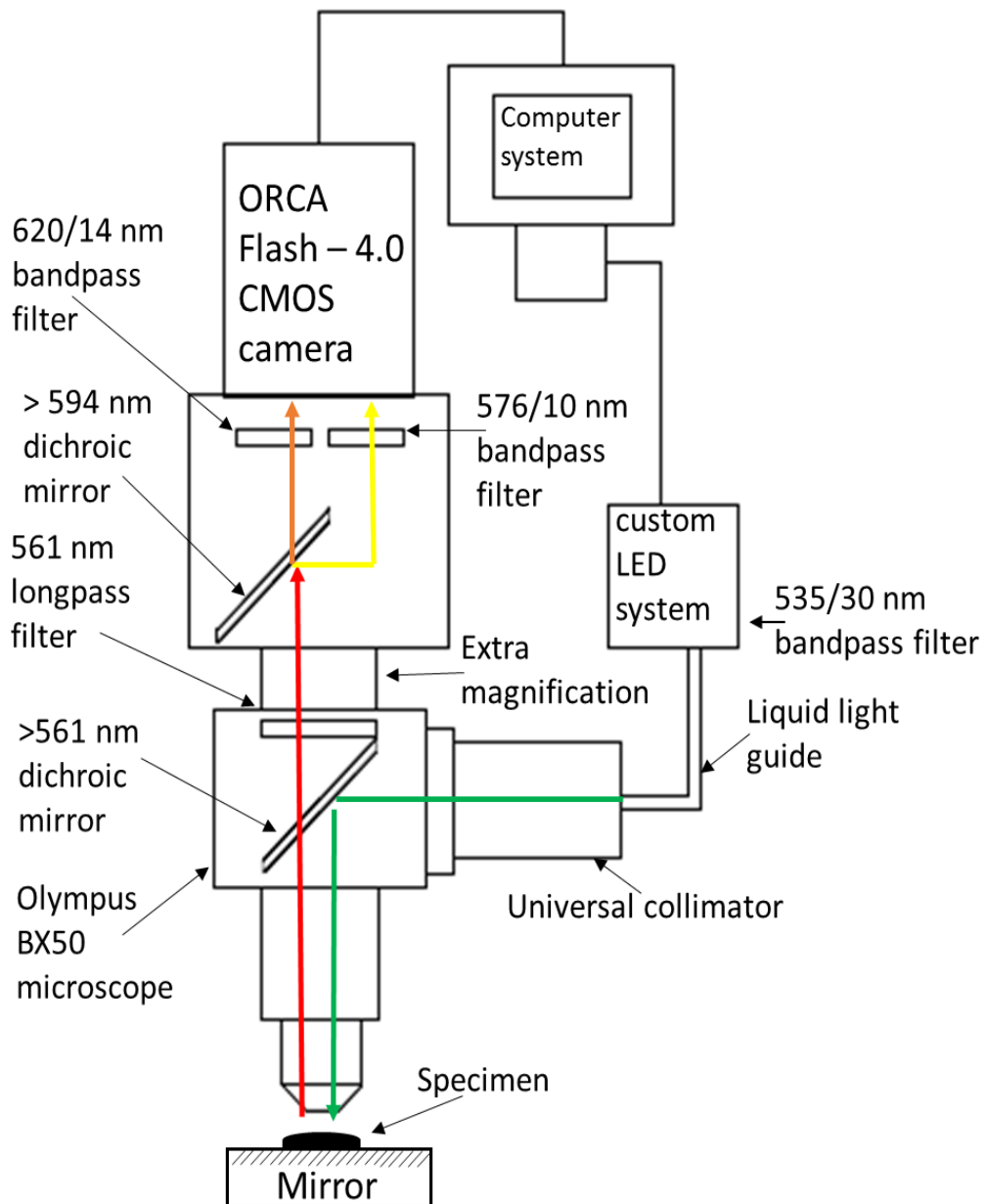


Figure 3.4; Schematic diagram of experimental setup for widefield TartanSW emission imaging of both lens and biological specimens. Specimen illumination was provided by a filtered 550 nm LED from the TartanSW-LED system that was coupled to the microscope using a universal collimator. The resulting fluorescence emission propagates upwards through the 561 nm dichroic mirror and longpass filter through the extra camera magnification to the emission camera chip splitter. The emission is split using a >594 nm dichroic mirror and is filtered through two bandpass filters before being detected by the sCMOS camera.

The TartanSW emission experiments on model and live specimens were also carried out using laser scanning confocal microscopy. For these experiments a Leica SP5 DM600 confocal microscope was used. For the model specimen imaging a 10x/0.4 dry objective lens was used (HC PL APO, Leica), for the MCF-7 imaging a 40x/0.8 water dipping objective (HCX APO, Leica) was used and a 100x/1.3 oil immersion lens (PL FLUOTAR, Leica) was used for the red blood cell imaging experiments. Using the Leica SP spectral detector three separate 5 nm emission bandwidths were able to be imaged onto separate photo multiplier tubes simultaneously which were then recorded using the Leica application suite software.

### **3.2.3) TartanSW excitation imaging setup**

To enable carrying out of widefield TartanSW excitation imaging, the same microscope and optics setup described in Chapter 2 was used with the exception that illumination was provided by the custom TartanSW-LED system which was TTL controlled to provide sequential excitation using the three different wavelengths and synchronised to the CMOS camera using WinFluor which also recorded the emission signal.

For the confocal TartanSW excitation experiments the same experimental set up described in section 3.3.3 was used but with the exception that single broadband detection channel was used rather than multiple narrow one.

### 3.3) Results

#### 3.3.1) Theoretical TartanSW PSF simulation and comparison to experimental lens standing wave data

In order to quantify the information gap reduction using TartanSW excitation imaging, first the experimental and theoretical antinode FWHM and spacings had to be compared. This was done by imaging a fluorescently coated lens specimen in air using each LED and the same methodology described in section 2.2.3 but with the mirror replaced with the aluminium coated microscope slides and using no camera binning. The average experimental standing wave antinodal spacings and FWHM for each excitation LED were compared to the theoretical values (calculated using equation (2.5)) by using a single sample t test where  $P < 0.05$  was considered significant and expressed uncertainties in the results are the standard error in the mean. The results from this are shown in table 3.1.

*Table 3.1; Comparison of experimentally determined anti-nodal spacings and FWHM obtained from 30 mm focal length lens specimen imaging in air and the theoretically determined values obtained using equation (2.5) where the peak excitation wavelengths were 490 nm, 524 nm and 549 nm, the peak emission wavelength was 570 nm.*

LED	Experimental antinodal spacing (nm)	Theoretical antinodal spacing (nm)	Statistical significance	Experimental antinodal FWHM (nm)	Theoretical antinodal FWHM (nm)	Statistical significance
490	$245.3 \pm 8.6$	244	$P > 0.05$	$123.3 \pm 3.2$	122	$P > 0.05$
525	$267.4 \pm 10.7$	262	$P > 0.05$	$126.9 \pm 1.8$	131	$P > 0.05$
550	$275.0 \pm 3.8$	274	$P > 0.05$	$134.0 \pm 4.4$	137	$P > 0.05$

After comparing the theoretical and experimental antinodal spacings and FWHM it was then possible to characterise the theoretical and experimental information gap reduction using all three excitation LEDs compared to a single 550 nm LED excitation. To do this, the lens analysis MATLAB script described in Chapter 2 was utilised in order to obtain the experimental radially averaged intensity profiles of the lens images. Using this it was then possible to determine how much of the total image was comprised of the information gap and determine how much of a reduction was observed when using three excitation wavelengths and compare these to the theoretical information gap reduction modelled using equation (2.5). The lens images were cropped to include 6 nodal and antinodal planes for the 550 nm excitation and the theoretical and experimental multi-excitation standing wave images and line intensity plots of a lens specimen can be seen in figure 3.5.

Through these experiments it was found that according to equation (2.5) a standing wave structure containing 6 nodes and antinodes when excited using the 550 nm LED has an information gap of 48.0 %. When the two additional excitation sources are included, this information gap is reduced to 17.3 % of the image. The experimental information gap observed for the 550 nm excitation was 44.3 % and when using all three wavelengths was found to be reduced to 12.0 %. This reduction can be seen in the line intensity plots in figure 3.5. The antinodal planes from the different excitation wavelengths occur at locations that coincide with the nodal planes of the other excitation wavelengths resulting in a more complete image of the lens specimen.

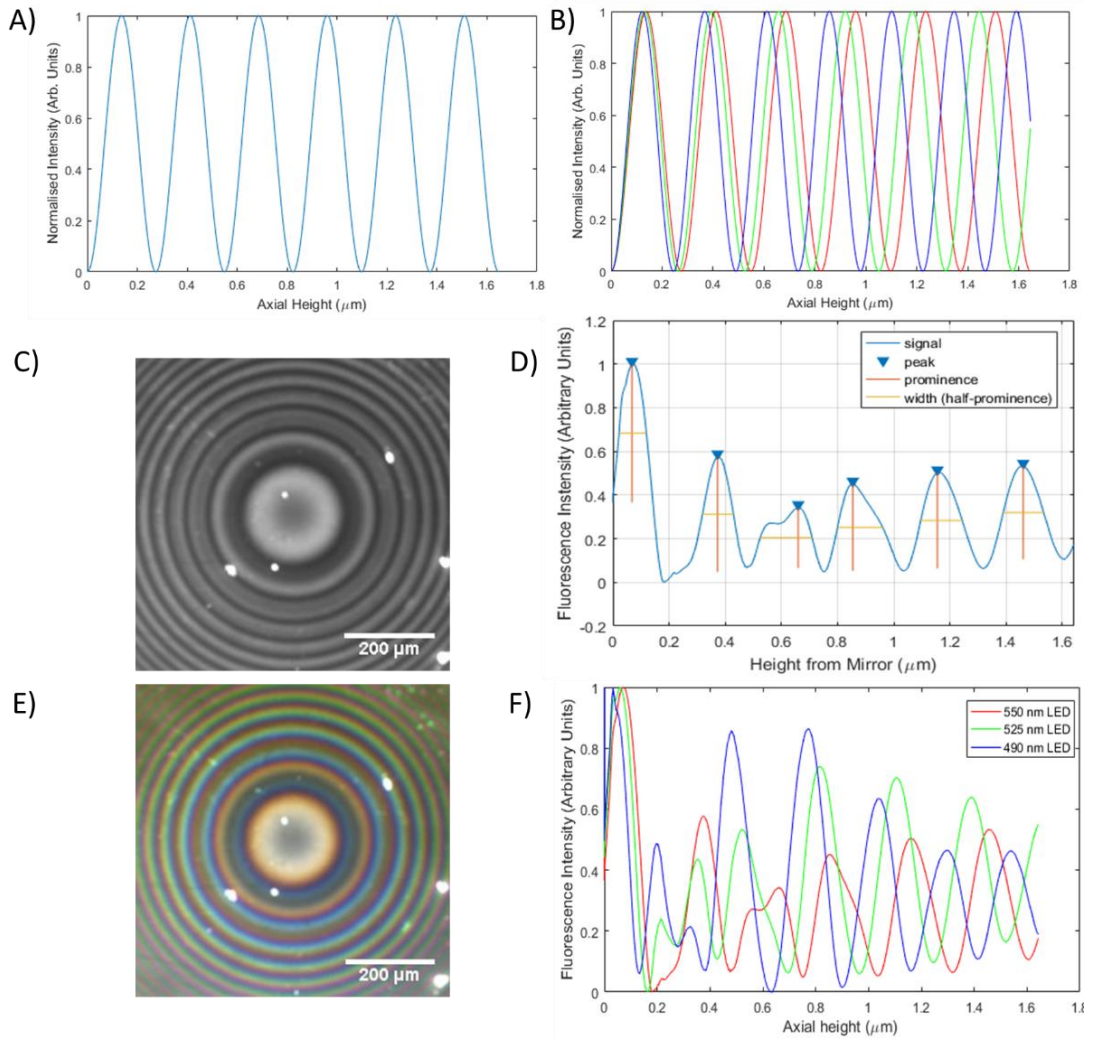


Figure 3.5; A) Theoretical standing wave structure simulated for 550 nm LED excitation. B) Theoretical standing wave structure simulated for 550, 525 and 490 nm LED excitation. C) Standing wave image of lens specimen using 550 nm LED excitation. D) Radially averaged intensity of the 550 nm LED excitation standing wave image. E) Standing wave image of lens specimen excited using 550, 525 and 490 nm LEDs showing a reduction in the information gap in the image. F) Radially averaged intensity of the 550, 525 and 490 nm LED excitation standing wave image showing the antinodal planes of the different excitation wavelengths coinciding with the nodal planes of the other standing wave structures.

Using the TartanSW excitation data it was also investigated if it were possible to reduce the antinodal plane FWHMs and hence increase the axial resolution in the images by taking the difference between two excitation channels. It was first

hypothesised that this would be possible due to the overlapping antinodal planes that were observed in the lens images obtained using the TartanSW excitation technique. As there exist locations of these overlaps, by taking the difference between the separate excitation images means that the antinodal planes of the longer excitation wavelength images would be reduced in width and hence provide a greater axial resolution in the images.

To do this, the different excitation images were differenced using the image calculator in ImageJ so as to obtain two images which were the result of  $|550 \text{ nm} - 525 \text{ nm}|$  and  $|525 \text{ nm} - 490 \text{ nm}|$ . The resulting structure obtained from the difference between the two excitation standing waves, *TartanSW difference*, can be described by the following equation,

$$TartanSW \text{ difference} = |SWPSF_{long} - SWPSF_{short}| \quad (3.2)$$

In the above equation  $SWPSF_{long}$  is the standing wave structure calculated using equation (2.5) for the longer excitation wavelength and  $SWPSF_{short}$  is the one calculated for the shorter wavelength. The theoretical TartanSW difference structure was obtained using equation (3.2) in order to compare the theoretical and experimental reduced antinodal FWHM and spacings. The theoretical data and experimentally obtained lens data are shown in figure 3.6.

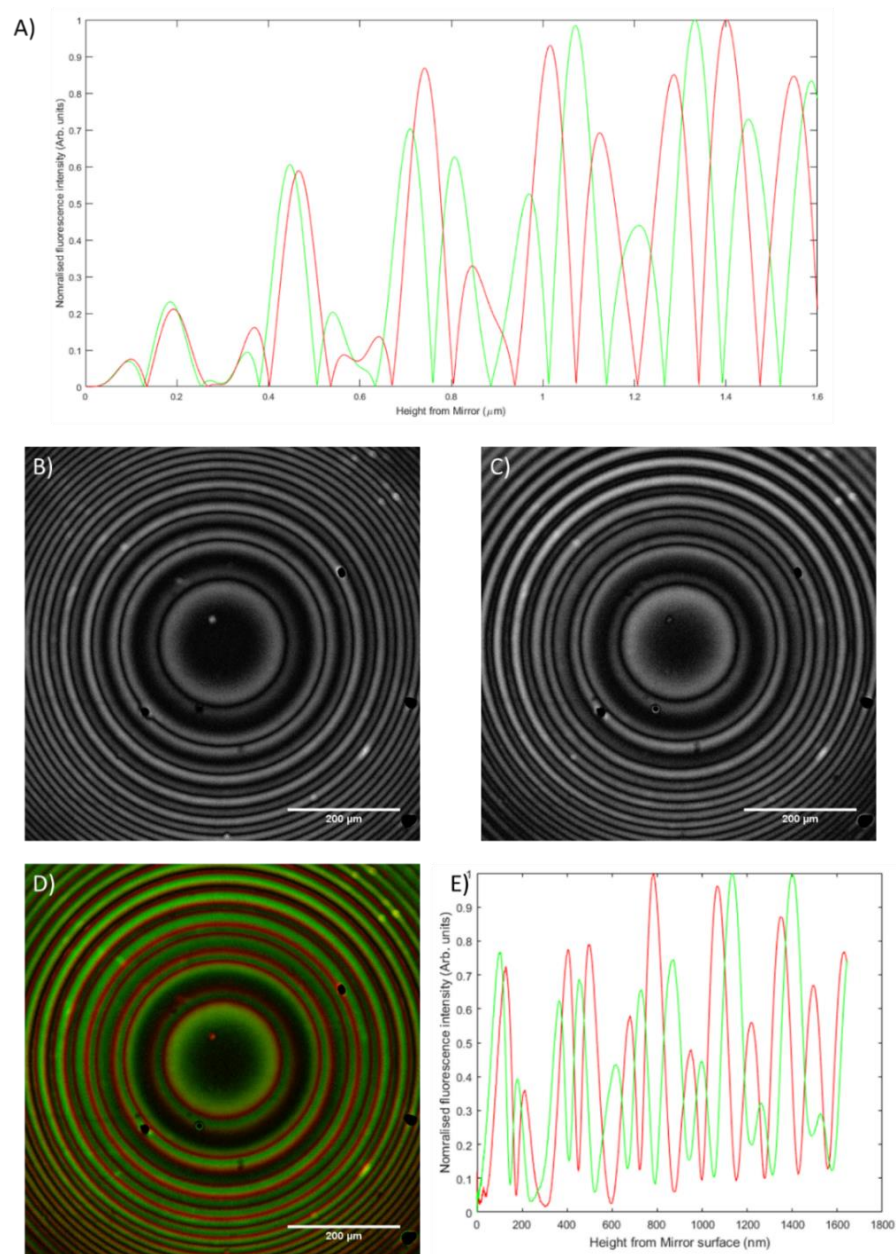


Figure 3.6; A) Theoretical plot of the  $|550-525|$  difference standing wave structure (red) and the  $|525 - 490|$  difference standing wave structure (green) both obtained using equation (3.2). B) TartanSW difference image acquired from the difference of the 525 nm standing wave image of the lens specimen in figure 3.5 from the 550 nm standing wave image in air. C) TartanSW difference image acquired from the difference of the 490 nm standing wave image of the lens specimen in figure 3.5 from the 525 nm standing wave image in air. D) Composite of the two TartanSW difference images with B) in red and C) in green. E) Radially averaged line intensity plot taken of the composite image.

*Table 3.2; A comparison of the experimentally and theoretically determined average FWHM and separation of the antinodal planes observed in the TartanSW difference images obtained in air.*

	Average experimental antinodal FWHM (nm)	Theoretical antinodal FWHM (nm)	Statistical significance	Average experimental antinodal spacing (nm)	Theoretical antinodal spacing (nm)	Statistical significance
550 – 525 difference images	$71.6 \pm 3.2$	75.6	$P > 0.05$	$136.7 \pm 11.2$	131.7	$P > 0.05$
525 – 490 difference images	$64.9 \pm 5.7$	71.8	$P > 0.05$	$129.0 \pm 9.8$	123.2	$P > 0.05$

It was determined by taking the TartanSW difference images in air that the antinodal plane widths were reduced due to the difference of the overlapping antinodal planes at each excitation wavelength, offering a way to increase the axial resolution of the images. It was also found that the experimental values obtained were not significantly different from those obtained theoretically according to equation (3.2). This data is shown in table 3.2.

These imaging and modelling experiments were also repeated for a layer of 4 % BSA and PBS between the lens and mirror in order to determine the resolution increases observed for the live cell imaging experiments shown in table 3.3.

*Table 3.3; A comparison of the experimentally and theoretically determined average FWHM and separation of the antinodal planes observed in the TartanSW difference images obtained in 4 % BSA and PBS.*

	Average experimental antinodal FWHM (nm)	Theoretical antinodal FWHM (nm)	Statistical significance	Average experimental antinodal spacing (nm)	Theoretical antinodal spacing (nm)	Statistical significance
550 – 525 difference images	49.1 ± 2.7	57.6	P < 0.05	102.4 ± 4.9	98.0	P > 0.05
525 – 490 difference images	46.1 ± 5.8	54.1	P > 0.05	97.50 ± 4.3	92.8	P > 0.05

It was also found that the experimental values obtained with a layer of 4 % BSA and PBS, aside from the |550 nm – 525 nm| FWHM, were not significantly different from the theoretical values. This shows that the TartanSW difference method consistently reduced the antinodal plane FWHM in media with different refractive index and could be applied to images of live cell specimens which could allow for axial resolutions on the order of 50 nm to be obtained.

The next experiments that were carried out were the modelling of the theoretical standing wave PSF obtained using the widefield TartanSW emission technique calculated using equation (3.1). The model standing wave structure obtained from this equation allowed the structure obtained experimentally through TartanSW emission imaging of lens to be compared. Specimens excited with the 550 nm LED and imaged using a 10x/0.4 dry objective lens with no camera binning and 100 ms exposure. The results of this can be seen in figure 3.7 where the standing wave intensity modulation can be observed though the plot is different from that obtained theoretically.

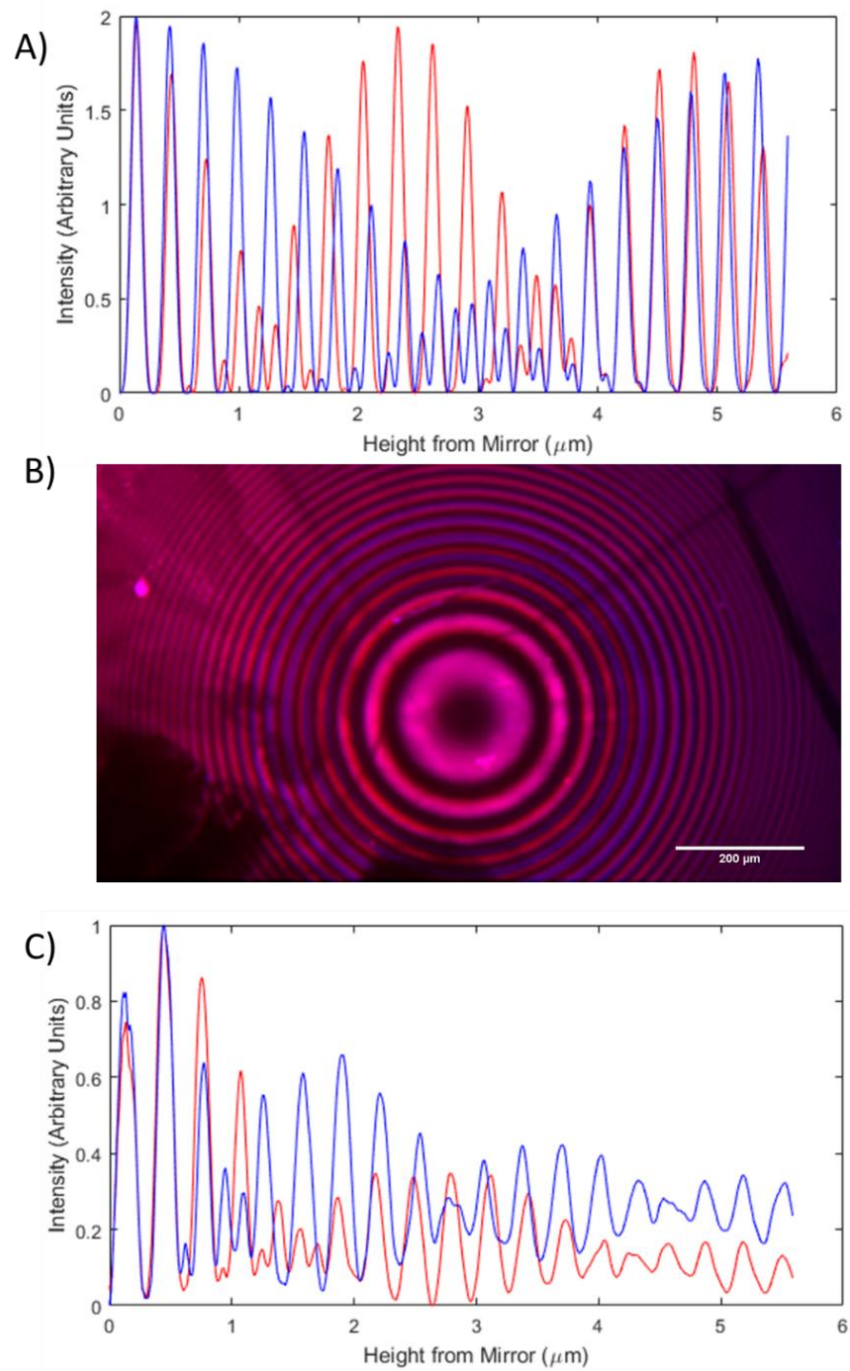


Figure 3.7; A) Widefield TartanSW emission PSF simulated for an 0.4 NA objective lens in air using an excitation wavelength of 549 nm and emission wavelengths of 570 nm (blue line) and 620 nm (red line) using equation (3.1). B) TartanSW emission image of a lens specimen excited using the 550 nm LED with the detection bandwidths centred around 576 nm and 620 nm. C) Line intensity plot for the 570 nm detection channel (blue line) and the 620 nm emission channel (red line) taken through the TartanSW emission image of the lens in B).

It can be seen from figure 3.7B and 3.7C that the widefield setup described in section 3.2.2 supports TartanSW emission imaging of fluorescent lens specimens. The standing wave intensity modulation for each detection channel can be seen clearly in the image and the line intensity plot taken from the centre of the lens specimen. However, when these are compared to the theoretical structure obtained using equation 3.1 it is apparent that the line intensity plots do not agree with each other. This disagreement is only in the intensity modulation observed but the number of antinodal planes that are present in the image is consistent.

This experiment was also repeated using the Leica SP5 confocal microscope where the fluorescently coated lens was excited using the 514 nm laser line with a 10x/0.4 dry objective lens using a scan speed of 100 Hz and an image size of 2048 pixels. The emission bandwidths used for detection were 567 – 572 nm, 592 – 597 nm, and 617 – 622 nm (figure 3.8).

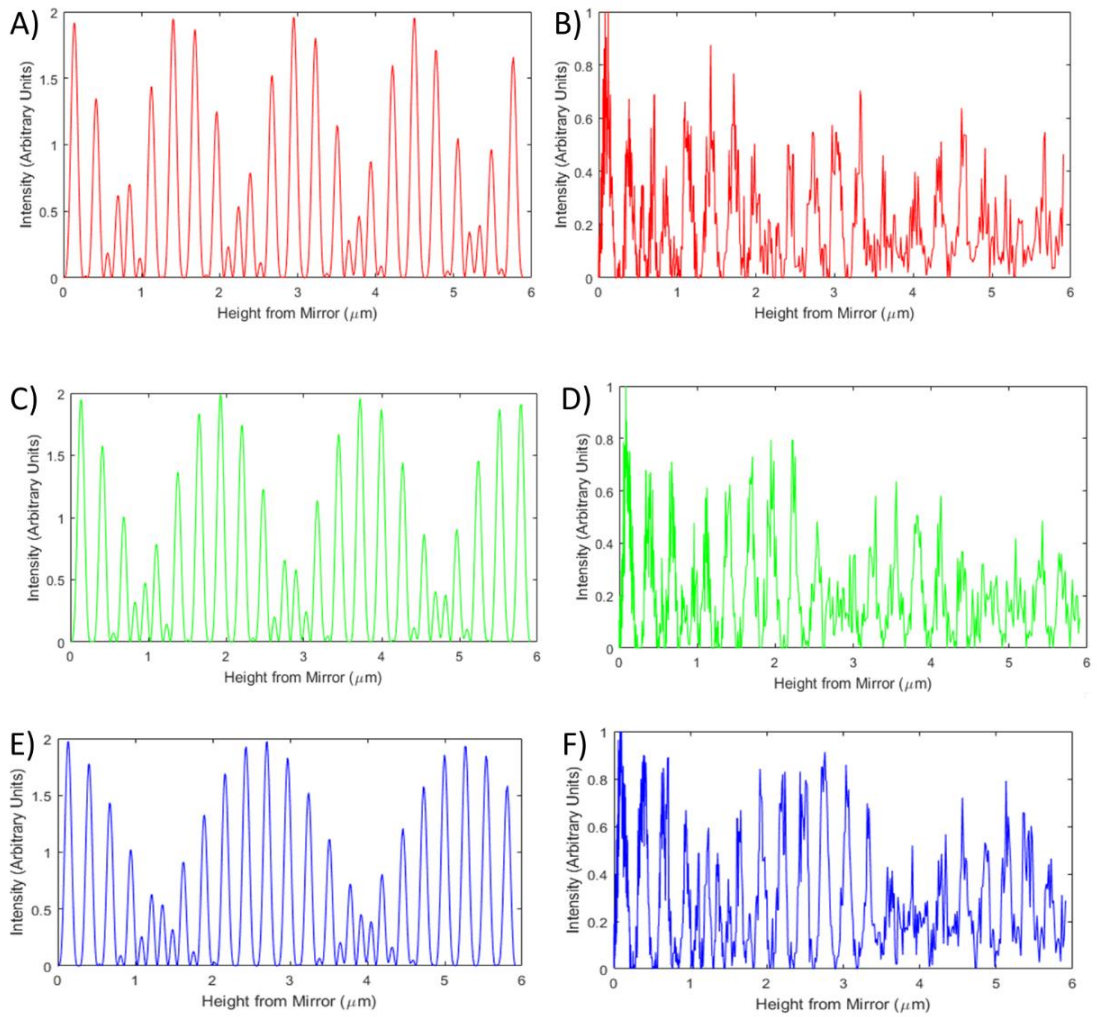
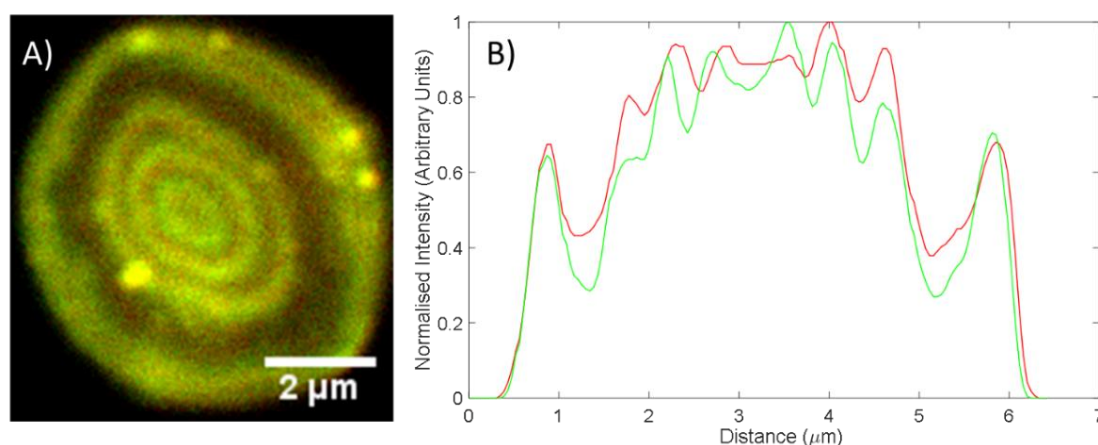


Figure 3.8; Theoretical standing wave structure calculated using equation (3.1) for an excitation wavelength of 514 nm excitation and emission bandwidths A) 617 – 622 nm C) 592 – 597 nm and E) 567 – 572 nm. Experimental line intensity plot through a confocal TartanSW emission image of a lens specimen excited at 514 nm and emission detected at bandwidths B) 617 – 622 nm D) 592 – 597 nm and F) 567 – 572 nm.

It was found when taking a line intensity plot through the lens image obtained using the confocal TartanSW emission setup and comparing them to the theoretical structure that there appears to be good agreement between the two.

### 3.3.2) TartanSW emission imaging of live cell specimens

After using the TartanSW emission technique for the imaging of the lens specimens the next experiments looked to apply this technique to live biological specimens. The first way this was carried out was to repeat the red blood imaging experiments described in Chapter 2 but using the TartanSW emission apparatus shown in figure 3.4. The red blood cells were excited using the 550 nm LED with a specimen plane power of  $5.27 \pm 0.02$  mW. This increase of specimen plane power compared to the experiments carried out in Chapter 2 was required as the use of limited detection emission bandwidths resulted in the reduced detection of fluorescence signal and meant that images obtained when using the previous specimen plane power had a signal to noise ratio that was too poor for observation of the planes from the background.



*Figure 3.9; A) Frame one from a widefield TartanSW movie of a red blood cell imaged acquired at a rate of 30.30 Hz and excited using the 550 nm LED. B) Line intensity plot taken through the red blood cell (Gaussian blur = 2 applied) where the green line is the 570/10 nm emission band and the red line is the 620/14 nm emission band.*

It can be seen that in figure 3.9A that it is indeed possible to carry out widefield TartanSW emission imaging of red blood cells as is apparent in figure 3.9B. It can also be observed that the plane ordering appears to agree with what one would expect from the bi-concave shape of a red blood cell. The shorter emission detection appears slightly below the longer in the middle three sections which is to be expected as it is a

dome rising upwards away from the mirror and the shorter emission wavelength bands would be in locations closer to the mirror than the longer detection bands.

The TartanSW emission effect is not as apparent in the red blood cells compared to the lens imaging due to the steep gradient of the red blood cell membrane compared to the lens. The other factor which reduces the effect is due to only four antinodal planes being detected as a result of the rapid intensity drop off that occurs with high NA lenses. Due to these factors the ability to visualise the spectral separation between emission bands is more limited than what would be the case with a higher number of antinodes (figure 3.7A).

It was found through these experiments that the widefield experimental apparatus does not allow for the acquisition of TartanSW emission imaging of red blood cell images with high enough signal-to-noise to allow for the computational extraction and generation of 3D reconstructions of these data. As such, the decision was made to repeat this experiment using the Leica SP5 confocal microscope in order to make use of its ability to select and image up to three discrete emission bandwidths simultaneously on different photomultiplier tubes with individual gain control on each to balance the channels. The microscope also allowed for the use of frame averaging to be carried out in aid of reducing image noise, though the use of this microscope comes at the sacrifice of temporal resolution.

The cells were prepared using the same method as for widefield imaging described in section 2.2.2, and were excited using the 543 nm laser line and imaged using a 100x/1.3 oil immersion objective lens with the emission detection bandwidths set at 550 – 555 nm, 565 – 570 nm and 580 – 585 nm. Images were set to be 1024 pixels in size with a scan speed of 100 Hz and a frame average of 3. An example of the data obtained from these experiments can be seen in figure 3.10.

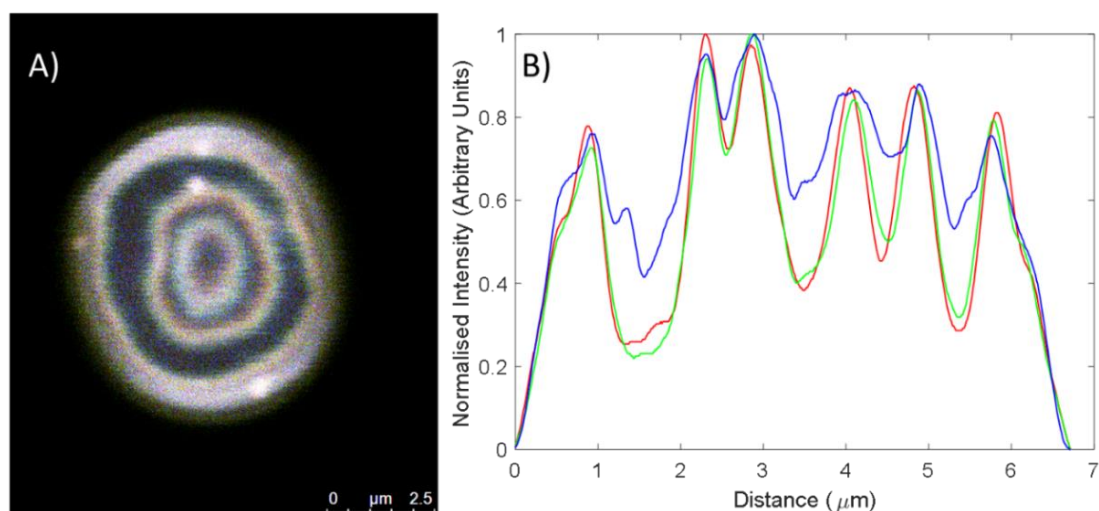


Figure 3.10; A) Confocal TartanSW emission image of a red blood cell excited at 543 nm and using emission detection bands of 550 - 555 nm (blue), 565 - 570 nm (green) and 580 - 585 nm (red) B) Line intensity profile taken through the red blood cell (Gaussian blur = 5 applied).

It can be seen from figure 3.10 that the ability to obtain an extra emission detection band further demonstrates slight plane ordering and frame averaging has reduced the noise present in the planes, though still not enough to allow for computational extraction of the planes. The widefield TartanSW emission setup was limited to only two different detection channels as the addition of extra channels imaged onto the same camera would limit the number of pixels available for each emission channel which would be further compounded when camera binning is used. The intensity plot in figure 3.10B also appears to show the plane ordering that was observed in the widefield images though the effect is still slight and limited by steep membrane gradient and the number of antinodal planes detected with the high NA objective lens.

It was also investigated whether this technique could be applied to other biological specimens. This would not only demonstrate a wider application for the standing wave technique than just red blood cells but also the use of a larger specimen with a more gradual gradient allowed for the use of lower NA objective lenses for imaging means that there is a larger depth of focus allowing for a greater number of antinodal planes to be collected and thus making the TartanSW emission effect more apparent.

Widefield TartanSW emission imaging was carried out on DiI stained MCF-7 breast cancer cells plated out onto mirrors that were submerged in 4% BSA and PBS and excited using the 550 nm LED with a specimen plane power of  $5.51 \pm 0.02$  mW under a 40x/0.8 water dipping objective lens. As the MCF-7 cells adhered to the mirror substrate and did not move as rapidly as the red blood cells, a 100 ms camera exposure time with no binning was used in order to increase the signal collected and reduce the size of the camera pixels.

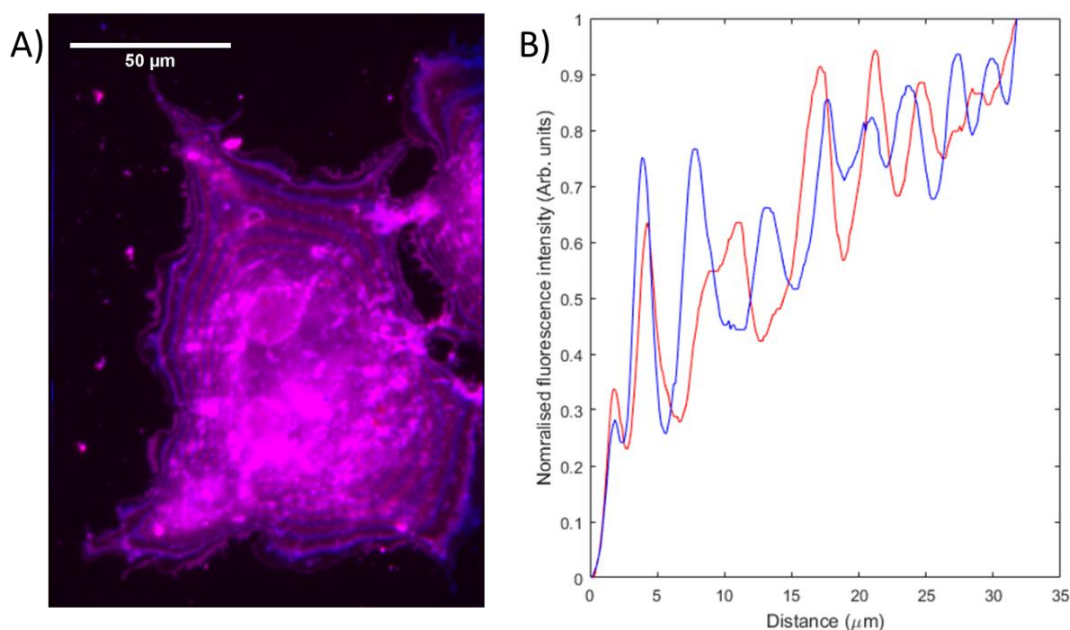
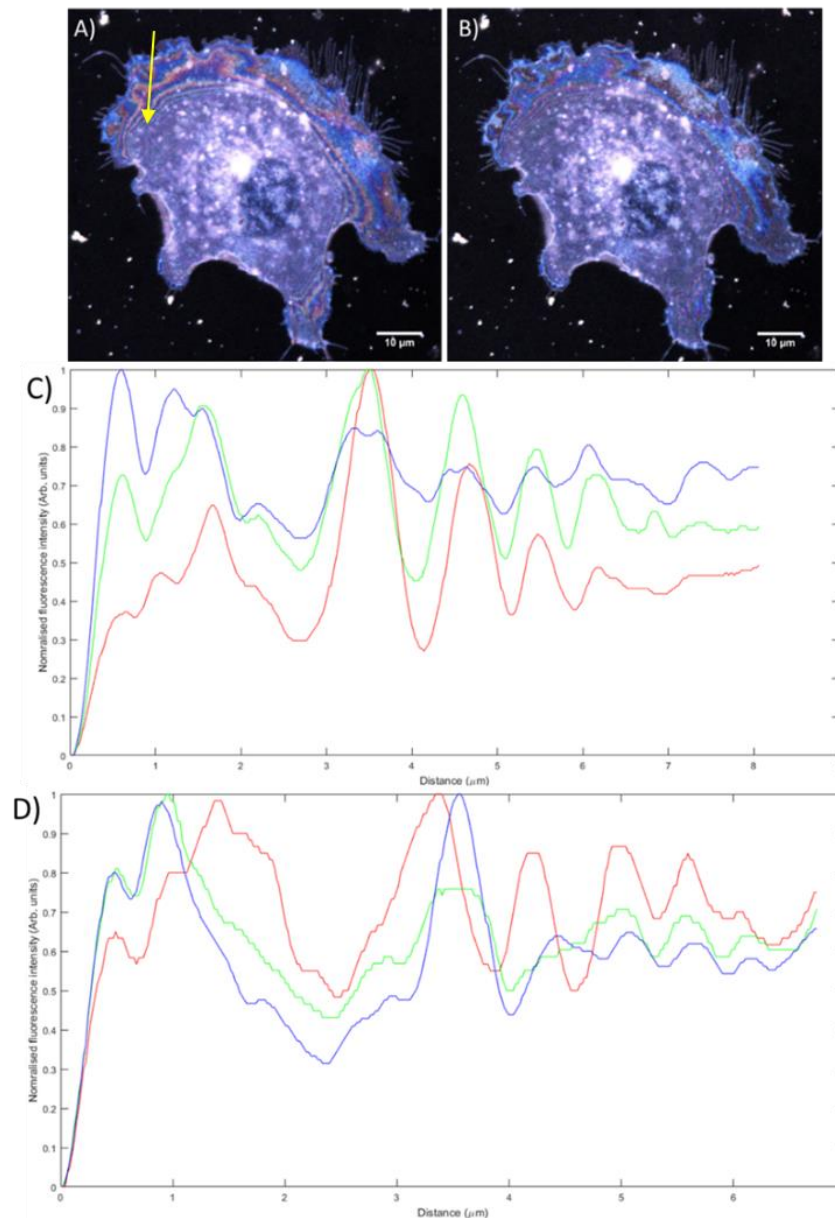


Figure 3.11; A) Widefield TartanSW emission image of MCF-7 breast cancer cells excited using a 550 nm LED with emission detected at bandwidths of 570/10 nm (blue) and 620/14 nm (red). B) Line intensity plot taken through the periphery of the multi-emission image (with a Gaussian blur = 2 applied) with the shorter emission band being plotted in blue and the longer band plotted in red.

It can be seen from figure 3.11 that the combination of using a lower NA objective lens and a larger specimen with a gentler gradient allows for more standing wave planes to be observed increasing the ease of visualisation of the TartanSW emission effect. From the line intensity plot there is a clear difference between the standing wave structures obtained from the two emission bandwidths and the plane ordering is also in agreement with what has been shown previously with the theoretical lens specimen plots.

The TartanSW emission imaging of MCF-7 cells was then repeated using the confocal microscope exciting at either 514 nm or 543 nm. Emission bandwidths were selected at 567 – 572 nm, 592 – 597 nm, and 617 – 622 nm. A 40x/0.8 water dipping objective lens was used with an image size set to be 4096 pixels, a scan speed of 100 Hz and frame averaging of 3. As stated above, the MCF-7 cells were less dynamic than the red blood cells and as such the lack of temporal resolution available to confocal microscopes is less of a concern in this case.

It can be seen from the confocal data that by using different excitation wavelengths, the multi-emission standing wave pattern is shifted. The line intensity plots observed in figure 3.12 resemble those seen in figure 3.11B but the addition of an extra detection bandwidth allows for the multi-emission banding to be more apparent and easier to observe.



*Figure 3.12; Confocal TartanSW emission imaging of MCF-7 cells using emission detection bands 567 – 572 nm (blue), 592 – 597 nm (green) and 617 – 622 nm (red) and excited at A) 514 nm or B) 543 nm. Yellow arrow on A) demonstrates the direction and location that the line intensity plots were taken. C) Line intensity plot through the 514 nm excitation image (Gaussian blur = 5 applied) D) Line intensity plot through the 543 nm excitation image (Gaussian blur = 5 applied). It can be seen from a comparison of A) and B) as well as C) and D) that the TartanSW emission structures obtained using different excitation wavelengths are different from each other. This is to be expected as the TartanSW emission phenomena occurs due to the self-interference of the emission standing wave and the excitation standing wave.*

### 3.3.3) TartanSW excitation imaging of live cell specimens

After the initial experiments confirming that using widefield TartanSW excitation imaging of lens specimens the information gap in the images could be reduced by 32.2 %, the technique was applied to biological specimens, firstly with red blood cells.

The first experiments on the red blood cells were carried out at a video-rate using a camera exposure of 13.33 ms for each excitation wavelength. It was found though that even when using the maximum camera binning of  $n = 4$  the signal to noise of the images was too poor to obtain useful data due to the short exposure times.

The next experiments made use of an exposure time of 40 ms and a camera binning of  $n = 2$ , though when the three excitation images were merged it was found that no spatial separation of the planes could be observed due to the reduced camera resolution caused by the binning.

The final experiments using a widefield microscope to image the red blood cells made use of no camera binning and an exposure time of 100 ms for each excitation wavelength. The 550 nm LED used a specimen plane power of  $5.27 \pm 0.02$  mW, the 525 nm LED  $4.00 \pm 0.02$  mW and the 490 nm LED  $4.90 \pm 0.02$  mW.

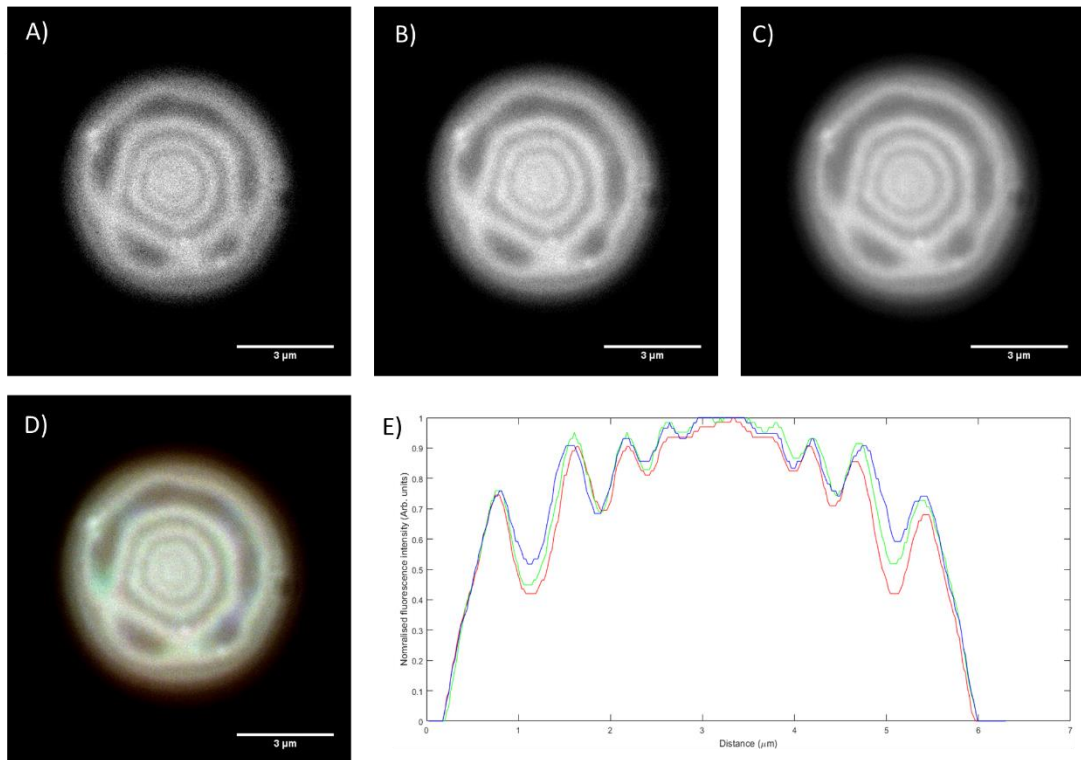


*Figure 3.13; Widefield standing wave images of a red blood cell excited using A) the 490 nm LED B) the 525 nm LED and C) the 550 nm. D) A TartanSW excitation image made up of the images shown in A) through C). E) A line intensity profile taken through the composite TartanSW excitation image showing slight spectral separation between the excitation channels D) where fluorescence emission obtained from the 490 nm LED excitation is plotted in blue, the 525 nm LED is plotted in green and the 550 nm LED is plotted in red.*

It can be seen from figure 3.13 that there is only slight separation between the different excitation channels (though it is still observable) even though that the antinodal planes are being generated at spatially separate points above the mirror.

The TartanSW excitation imaging of the red blood cells was then repeated but this time using confocal microscopy. The cells were imaged under a 100x/1.3 oil immersion objective lens and excited using 488 nm, 514 nm and 543 nm laser lines. The images were set to be 512 pixels in size and were acquired at a rate of 200 Hz.

It is clear to see in figure 3.14 that there is spectral separation between the different excitation wavelengths and due to this a slight information gap reduction in the images.

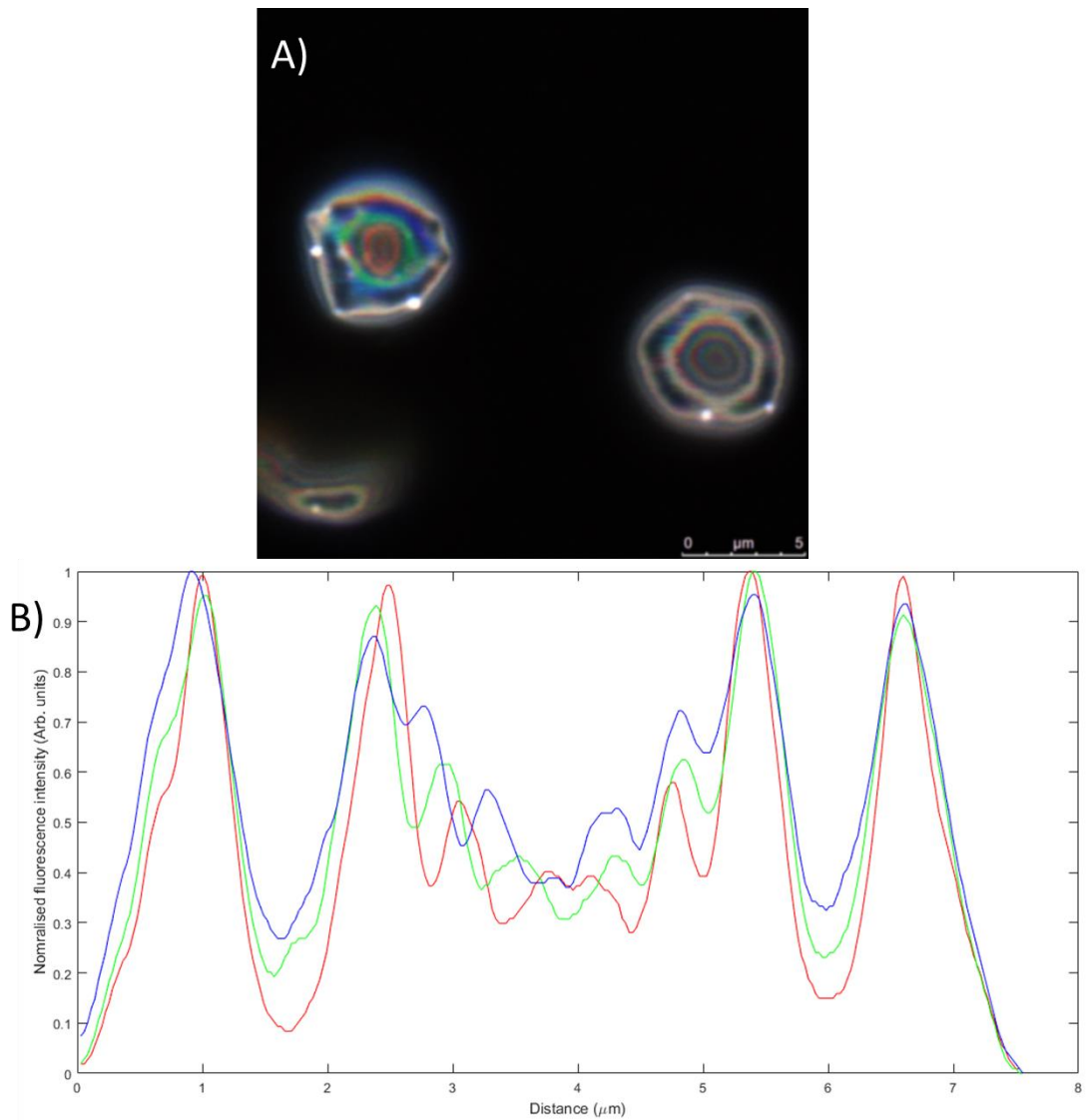


Figure 3.14; A) Confocal TartanSW excitation imaging of red blood cells excited at 489 nm (blue), 513 nm (green) and 543 nm (red) with Gaussian blur = 2 applied. B) Line intensity profile taken through the right red blood cell in A).

The next specimens that the widefield TartanSW excitation technique was applied to were MCF-7 breast cancer cells. These specimens were imaged using the same experimental apparatus as in the multi-emission experiments but utilised the two additional excitation wavelengths and without the emission splitter. The specimen plane powers used for these experiments for the 550 nm, 525 nm and 490 nm LEDs were  $3.04 \pm 0.01$  mW,  $4.92 \pm 0.02$  mW and  $10.1 \pm 0.01$  mW, respectively.

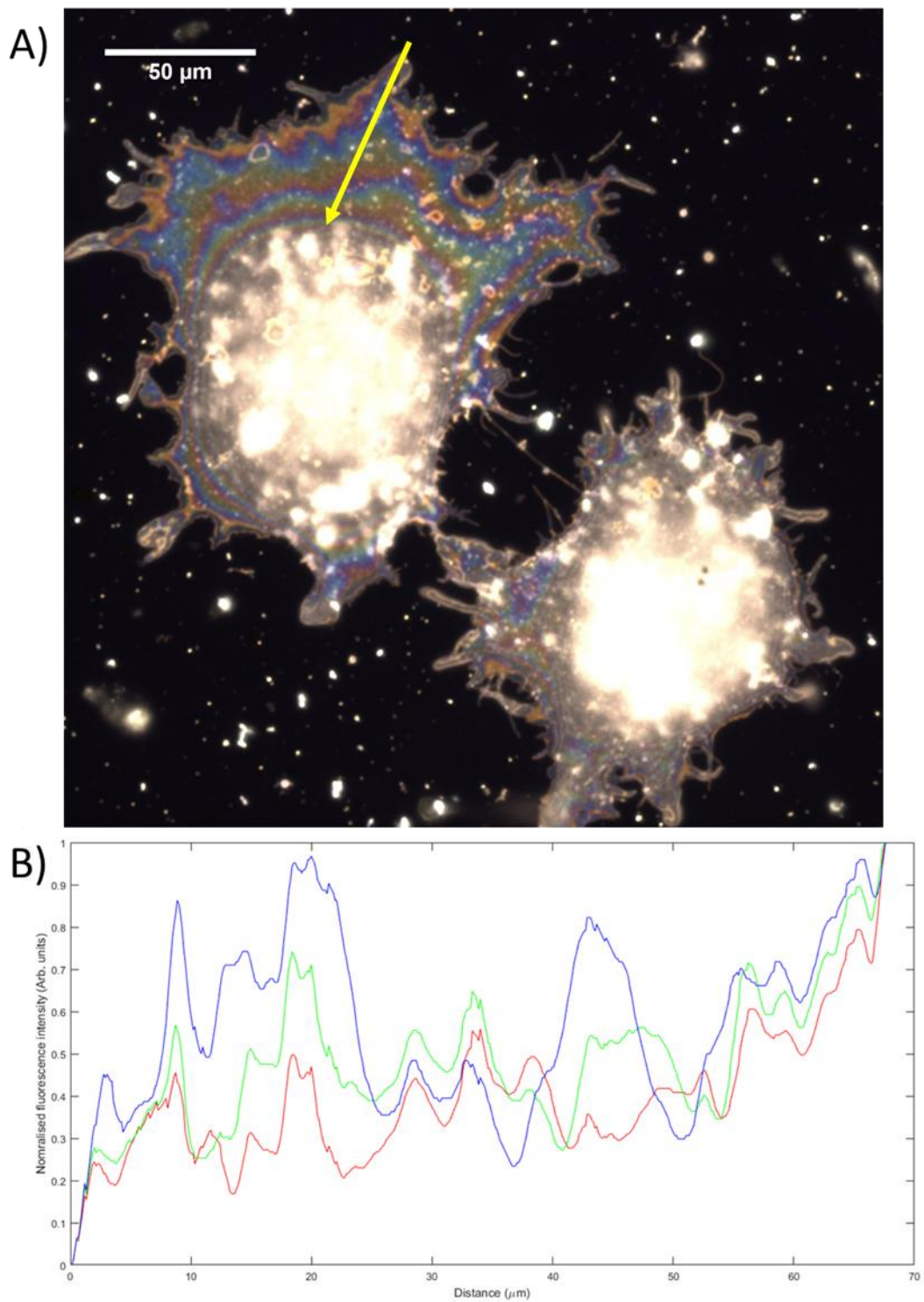


Figure 3.15; A) Widefield TartanSW excitation image of a DiI stained MCF-7 breast cancer cells excited using the 490 nm LED (blue), the 525 nm LED (green) and the 550 nm LED (red). B) Line intensity plot taken through the periphery of one of the MCF-7 cells in the TartanSW excitation image (with a Gaussian blur = 2 applied).

In figure 3.15 the contributions of the different excitation wavelength antinodal planes can be observed much more clearly to run along the periphery of the cell with a large amount of intensity saturation occurring in the centre of the cell. Through the application of the TartanSW excitation technique a more complete image of the membrane structure is obtained than if a single excitation wavelength were used (observable through the line intensity plot in figure 3.15B). The ordering of the different excitation bands also offers the ability to suggest the axial direction of the membrane structure (blue being the shortest excitation wavelength appearing typically before the green and red channels when following along from the leading edge of the cell). The contour map obtained of the MCF-7 specimens do not originate from the basal membrane as in the red blood cell experiments but rather the apical side of the cell. This is due to the basal membrane in contact with the mirror inhabits the initial nodal plane and as such does not contribute fluorescence to the image.

TartanSW difference images were obtained from the different single excitation MCF-7 images to obtain an increased axial resolution in the same way as described in section 3.3.1. The result of the TartanSW difference images and a line intensity plot taken through the periphery of the cell can be seen in figure 3.16. According to the experimental difference standing wave data of the lens images in 4% BSA and PBS, the difference MCF-7 images have a resolution of  $49.1 \pm 2.7$  nm for the  $|550 \text{ nm} - 525 \text{ nm}|$  channel and the  $|525 \text{ nm} - 490 \text{ nm}|$  a resolution of  $46.1 \pm 5.8$  nm.

By taking the TartanSW difference images between the excitation standing wave images not only were the axial resolution of the images enhanced but the contrast of the images was improved as well. This increase in contrast makes the observation of the difference antinodal plane locations to be much clearer than in the raw merged images and also reduces the saturated locations in the centre of the cell. This contrast improvement may also aid in the ability of image segmentation and generating 3D reconstructions of the MCF-7 data.

It was also observed in both the widefield and confocal TartanSW excitation images and the TartanSW difference images of the MCF-7 cells that there existed within the cell, round membrane structures that could be observed even when imaging through the cell nucleus (see figure 3.17).

Time-lapse widefield TartanSW excitation and difference imaging was also carried out on the MCF-7 cells with a 100 ms exposure for each LED, taken every 20.1 seconds for a total duration of 16.3 minutes with no camera binning. In the TartanSW difference standing wave images clear membrane structures were observable which appear to burst near the end of the imaging duration whilst the entire cell appears to flatten which can be inferred from the reduction in the number of anti-nodal planes.

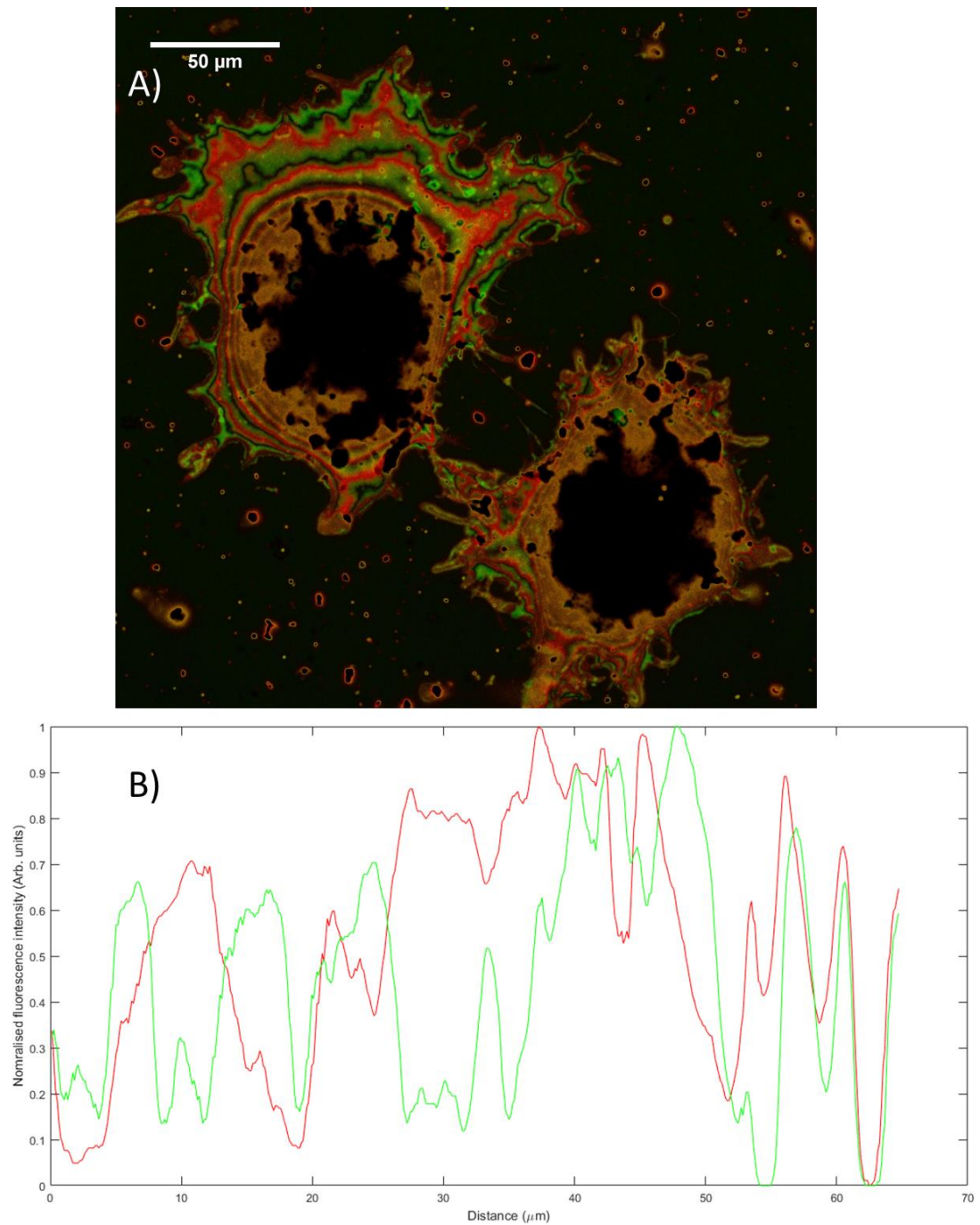
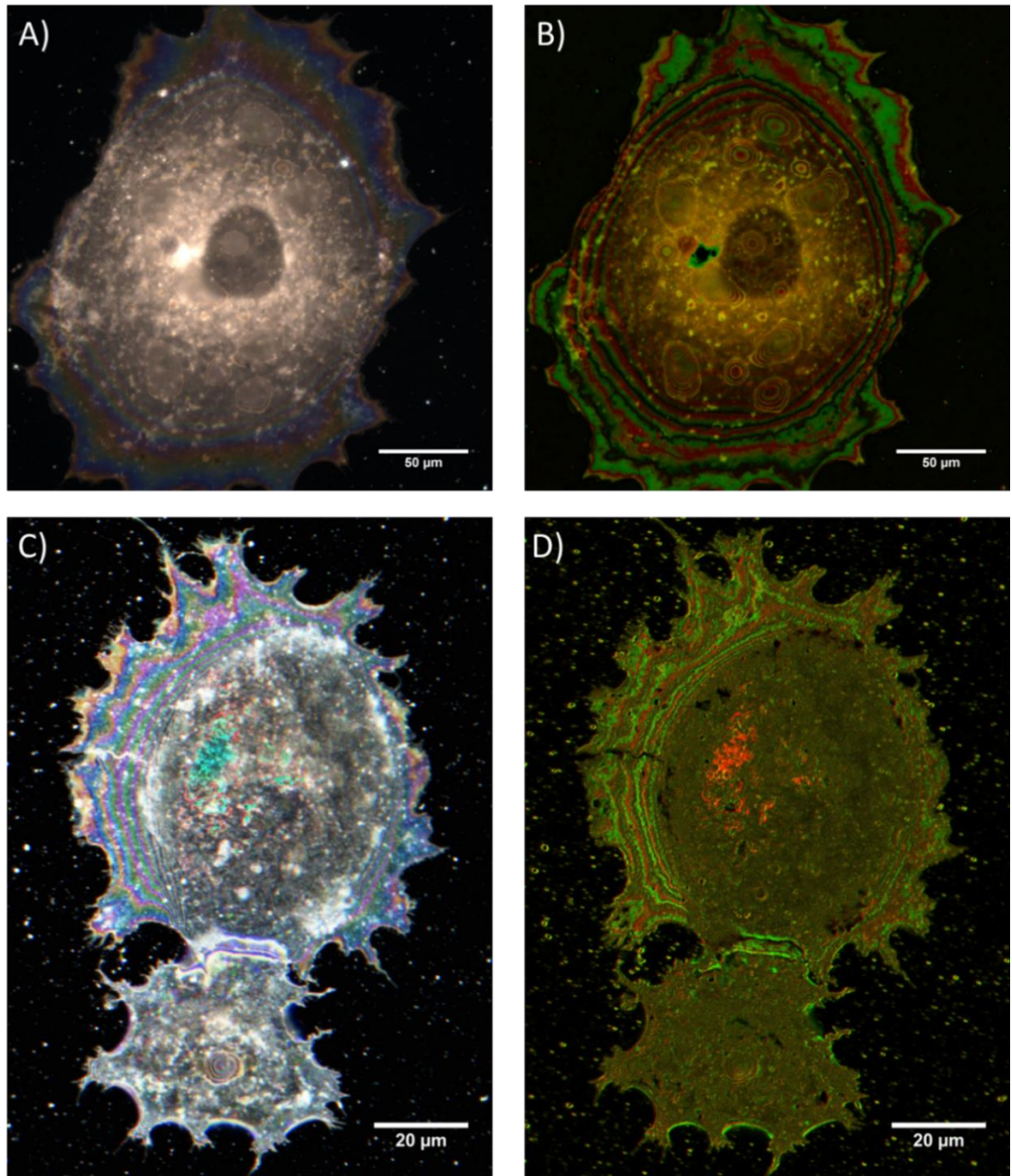
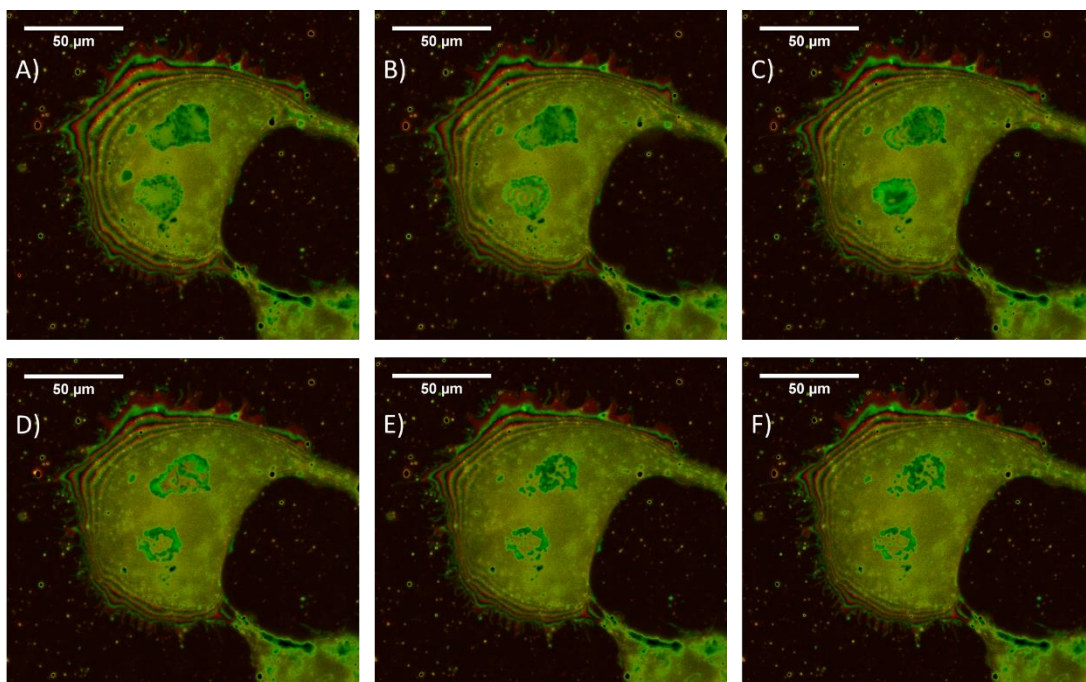


Figure 3.16; A) TartanSW difference image of the MCF-7 cells shown in figure 3.15A where the difference of the 550 nm from the 525 nm is shown in red and the difference of the 525 nm from the 490 nm shown in green. B) Line intensity plot taken through the periphery of A) (with a Gaussian blur = 2 applied) demonstrating a reduction in the antinodal FWHMs compared to figure 3.15B and an increased image contrast.



*Figure 3.17; A) Widefield TartanSW excitation image of a MCF-7 breast cancer cell and B) TartanSW difference image between the excitation wavelengths showing the presence of structures within the cell that can be observed even through the nucleus. C) Confocal TartanSW excitation image of a MCF-7 breast cancer cell and D) TartanSW difference image between the excitation wavelengths also demonstrating an internal structure that can be seen in the bottom most cell.*



*Figure 3.18; Time lapse TartanSW difference multi-excitation images of MCF-7 cells with the  $|550\text{ nm} - 525\text{ nm}|$  channel in red and the  $|525\text{ nm} - 490\text{ nm}|$  in green showing an internal membrane structure that appears to swell and burst throughout the imaging duration. The frames presented as A-F are frames 9, 17, 25, 33, 41 and 48.*

### 3.4) Discussion

Through the previous work on the single colour standing wave imaging several limitations of standing wave microscopy were identified. These were primarily the information gap contribution in the images which reduced the amount of useful information that could be obtained about the specimen and that assumptions had to be made about the specimen shape. In order to investigate ways to overcome these limitations work has been carried out to implement TartanSW excitation and emission imaging in both widefield and confocal microscopy on fluorescent lenses and live biological specimens.

The first experiments made use of fluorescently coated lens specimens to test the experimental setups and compare the experimentally observed results with those calculated theoretically. The LED characterisation was first carried out to ensure that the standing wave antinodal planes obtained using the LEDs that were not characterised in Chapter 2 were not significantly different from the theoretical values which was confirmed.

Widefield TartanSW excitation microscopy was found to theoretically reduce the information gap in lens images from 48.0 % to 17.3 % allowing for an additional 30.7% more topographical information about the specimen to be acquired. From the imaging of the lens specimen it was found that the experimental information gap was reduced from 44.3 % to 12.0 % of the total image which was an 32.3 % information increase and was accurate to within 1.6 % of that found theoretically. This difference between the experimental and theoretical information gap reduction could be attributed to slight errors in the MATLAB script for detecting the FWHM of each plane due to the centre of the image not being detected precisely for the radial average or dye spots in the image shifting the radial average.

As the TartanSW excitation images were comprised of three separate excitation channels it was investigated to what effect taking difference images between them would have upon the resulting standing wave structure. By simulating the TartanSW difference structure in air using equation (3.2) it was found that the |550 nm – 525 nm| excitation channel had a reduced antinodal theoretical FWHM and spacings of 75.6 nm and 131.7 nm. The |525 nm – 490 nm| excitation channel had an antinodal FWHM of 71.8 nm and separation of 123.2 nm. When these were compared to the experimental TartanSW difference images of the lens specimen in air it was found that the experimental structures were not significantly different from the theoretical ones. This means that by simply taking a TartanSW difference image of multiple excitation channels, a post image acquisition axial resolution can be enhanced by approximately a factor of 1.8.

This comparison was repeated but with the lens having a buffer layer of 4 % BSA + PBS between it and the top of the mirror in order to mimic the conditions present during the live cell experiments. Through this it was again found that the TartanSW

difference images resulted in an axial resolution improvement through the reduction in the width of the antinodal planes. The analysis demonstrated that there was an average experimental resolution with the |550 nm – 525 nm| channel of  $49.1 \pm 2.7$  nm and  $46.1 \pm 5.8$  nm for the |525 nm – 490 nm| channel which is an improvement over the single colour standing wave resolution by approximately a factor of 2.1. The TartanSW difference antinodal FWHM for the |550 nm – 525 nm| channel in 4% BSA and PBS was found to be significantly different from the theoretical value, however, this is only different by 8.5 nm and again could be due to slight systematic errors in the radial average MATLAB script.

It was also found that the experimental values obtained in this buffer solution were all within 10 nm of the TartanSW difference FWHMs obtained in air divided by the refractive index of the buffer layer. This was to be expected as by the standing wave equation the structure is modulated by the inverse of the refractive index of the media the light is propagating through.

The next set of experiments looked into the application of the TartanSW excitation method on live cell specimens. This was also the first application of the standing wave technique on whole adherent mammalian cells. The demonstrated ability to use TartanSW microscopy to image other biological specimens than just red blood cells meaning that TartanSW or single colour standing wave microscopy could be used to obtain axial super-resolution information about dynamic morphological cellular processes in mammalian cells.

It was found through the widefield TartanSW excitation imaging of the red blood cell specimens that only slight spectral separation was observable between the different excitation images. The reason for the reduced spectral separation could be due to the steep gradient of the red blood cell membrane surface causing a large amount of overlap between the separate excitation antinodal planes. This overlap leads for them to merge together and cannot be separated by either the lateral or camera resolution capable in the widefield imaging setup. The merging of the different antinodal planes is also exaggerated by the use of a high NA lens. The number of antinodal planes detected is dictated by the emission focal depth of the objective lens, which is between

3 and 4 planes with an NA of 1.4, and greater spectral separation of the antinodal planes does not occur until higher plane numbers, as can be seen in figure 3.5B.

The red blood cell imaging experiments were repeated using confocal microscopy where it was found that spectral separation between the different excitation wavelengths was more visible than was seen in the widefield data, this could possibly be attributed to the  $\sqrt{2}$  increase in resolution over widefield microscopy [48]. However, there is also the possibility that due to the relatively long time (compared to the widefield imaging setup) that is required to acquire an image at a single wavelength and then change the excitation source and rebalance the emission detection levels combined with the highly dynamic nature of the red blood cell membrane that the separation is in reality the result of the specimen deforming or undergoing photo-toxic induced morphological changes [148], [185], [191]. The left-most red blood cell in figure 3.13A certainly appears to indicate that at least this cell was changing shape between excitation wavelengths however separation of the different excitation wavelengths was observable when imaging was repeated on different red blood cell specimens.

It was found when carrying out multi-excitation standing wave imaging that the cell membrane dynamics of the specimen are very important to consider when choosing the type of microscope to use for imaging. The fast wavelength switching and image acquisition available to widefield microscopy is advantageous for the imaging of live, moving specimens, providing the different antinodal planes can be resolved from each other. If the imaging of fixed or static specimens is being carried out, then temporal resolution is not a limiting factor and as such confocal microscopy may be more of a suitable technique as the ability to perform digital zoom and increase pixel numbers for smaller regions could lead to greater understanding about the structure of different sub-regions of the cell such as the leading edge of a cell or the growth cones in neurons.

TartanSW excitation widefield and confocal imaging was also carried out on MCF-7 cells. These cells are much larger than red blood cells and as such a lower magnification and NA water dipping lens was able to be used. These cells are also adherent which meant that every cell was in contact with the mirror and as such it was much easier to carry out standing wave imaging of the specimen compared to red blood

cells where only ones that were attracted to the poly-L-lysine coating could be imaged. This can be a benefit for further experiments because as the cells are adherent they could possibly be imaged live in a pharmacological buffer using a water dipping lens which supports the application of drug washes to the specimens without them being disturbed meaning that morphological changes in response to different stimuli could be observed.

A combination of lower NA lens and larger specimens with more gradual membrane gradients allowed for clear spectral separation between the excitation channels to be observed meaning that a reduction in the information gap was obtained. Within the cell bodies there existed large amount of intensity saturation points which was observed in all widefield and confocal MCF-7 imaging experiments. It is possible that the cause for these saturation points is as a consequence of dye labelled membrane recycling by the cell through a process called endocytosis [210], [211].

Cells undergo a near constant rate of endocytosis in order to transport, proteins and other large essential or foreign molecules into the cell which is mediated by clathrin-coated pits [210], [212]. Once the dye labelled membrane is recycled into the cell they form vesicles which are shuttled to the endosome to be broken down or recycled [213] [212]. Once the dye labelled membrane vesicles are broken down they are either translocated to the plasma membrane by the Golgi apparatus or are repurposed to be used by other parts of the cell [213], [214]. This process could explain the presence of these internal dye spots which are then exaggerated by the contrast and brightness stretching that takes place during the image analysis.

In the widefield and confocal MCF-7 data it was observed that there were internal membrane structures present in the cytosol. Furthermore, it could be seen in the widefield time-lapse data set that these membrane structures began to swell and rupture as the cell flattened and underwent stress over time and also of interest was that these structures were detectable through the cell nucleus which is highly scattering meaning that any internal structures that are close to the basal membrane could be observed.

It appeared that the structures observed within the interior of the cells could possibly be comprised of recycled labelled plasma membrane and resembled internal membrane vacuoles that can be caused by methuosis. Methuosis is a form of non-apoptotic cell

death observed in cancer cells [215], [216] in which the cell generates multiple fluid filled vacuoles within the cytoplasm to such an extent that the cell loses membrane integrity and lyses [217], [218]. It is thought that this process could be a potential method for the eradication of drug-resistant cancer cells [215]. The ability to study this process using standing wave microscopy could result in the technique finding applications within cancer research or imaging the formation and behaviour of other internal organelles.

It was found that by taking the difference between the TartanSW excitation widefield or confocal images that these saturation points were removed, and the contrast of the images was improved in general allowing for easier visualisation of the reduced antinodal planes. This also allowed for widefield TartanSW excitation-difference images with an axial resolution on the order of 50 nm to be achieved with the added benefit that a widefield TartanSW difference microscopy readily supports high temporal resolution imaging.

The axial resolution now available to widefield standing wave microscopy exceeds those possible using other widefield super-resolution technique, such as 3D SIM, [111], [219] or TIRF [79]. TartanSW microscopy also benefits from the fact that a much simpler experimental equipment and analysis is required than compared to techniques such as 3D SIM or iPALM [113], [118]. It must be noted though, that the lateral resolution improvement in SIM and iPALM are not present using TartanSW excitation microscopy and as such for high lateral resolutions imaging requirements, TartanSW may not always be suitable.

As TartanSW excitation-difference microscopy only requires three images for a complete frame, the temporal resolutions possible using this technique also exceed those possible in 3D SIM, in which 15 are required, or iPALM which requires thousands of image triplets [113], [118]. An added benefit is that each individual excitation wavelength image acquired in TartanSW by itself contains axial super-resolution data whereas no individual SIM or iPALM image can be used to extract super-resolution data, the entire ensemble of images must be acquired.

Until recently with the introduction of multifocal SIM [219], the only way to image the volume of a biological specimen using 3D SIM was to image at multiple focal

depths within the specimen in order to generate a z stack [219]–[221] meaning that many images have to be taken which could cause excessive photodamage to the specimen or distort the grating pattern in thick specimens [111], [220]. Using TartanSW excitation microscopy, super-resolved planes are generated with the entire focal depth of the collection objective lens with only three images being required to obtain an almost complete topographical map.

Previously, one of the techniques that had been most commonly used to image the basal region of adherent cell specimens had been using TIRF microscopy. However, TIRF microscopy has only been capable of imaging structures within approximately 100 nm of the cell-coverslip boundary [87]. Using TartanSW excitation/difference microscopy we have not only been able to image internal structures but also obtain a topographical map of the whole cell volume that lies within the focal depth of the objective lens, though as three images are required for an information gap reduction and improved axial resolution in TartanSW excitation – difference, the temporal resolution is less than that which is possible with TIRF microscopy.

Though IRM has also been used to image adherent cells, a discussion on the limitations in the accuracy of the images obtained from this technique compared to standing wave microscopy has been previously discussed in section 2.4. Table 3.4 provides a brief list of the imaging capabilities of several widefield super-resolution techniques that were described in Chapter 1 in order to demonstrate a concise comparison for those capable using TartanSW excitation-difference and single colour standing wave microscopy.

Table 3.4; Comparison of the imaging capabilities of interference based widefield super-resolution microscopy techniques.

<b>Widefield microscopy technique</b>	<b>Lateral resolution (nm)</b>	<b>Axial resolution (nm)</b>	<b>Single image focal depth (nm)</b>	<b>Number of frames required for image</b>	<b>Full image temporal resolution</b>	<b>General limitations</b>
Single colour standing wave	~ 290	< 100	> 750	1	Camera limited	Missing information due to nodal planes.
TartansW excitation (difference)	~ 290	< 100 (55)	> 750	3	Three times camera limit	Prior knowledge about specimen structure is required for image reconstruction
IRM [73], [75]	~ 300	> 15	> 750	1	Camera limited	Can report inaccurate cell topography due to cytoplasm density [177], [178]
TIRF [79]	~ 300 [81]	~ 100	~ 100	1	Camera limited	Can only image objects near the basal membrane.
2D SIM [106]	~ 100	~ 500	~ 500	9	Nine times camera limit + grating shift	Grating contrast degradation in thick specimens [223]
3D SIM [113]	~ 100	~250	~ 250	15	Fifteen times camera limit + grating shift	Grating contrast degradation in thick specimens [223]
iPALM [222]	< 20	< 20	~ 225	< 10,000	60– 300 minutes	High intensity illumination + long image acquisition typically necessitates fixed specimens

The other TartanSW modality utilised in this Chapter was TartanSW emission. This method was used to image fluorescently coated lens specimen and the results were compared to the theoretical structure calculated according to equation (3.1). As can be seen from figure 3.7 the detected widefield fluorescence emission intensity is modulated by the presence of an emission standing wave as shown previously by Amor *et. al.* This can be seen further in figure 3.7B as there is a clear separation between the red and blue emission channels. However, when the line intensity plot was taken through the image and transformed into distance above the mirror there was little correlation found between the experimentally obtained and theoretical intensity modulation.

One theory for where this disagreement between the widefield experimental and theoretical plots comes from is that it could be accounted for if the experimental lens specimen plot was offset from zero. This would suggest that the lens is not in fact in contact with the mirrored surface which could be due to an oxidised layer or other coating being present between the reflective surface and the lens. If this offset is present, then the buffer layer between the lens and mirror would have to be large (on the order of microns) and as such it is currently thought that this may be unlikely to be the case.

This imaging experiment was carried out using both the evaporated aluminium microscope slides and commercial aluminium mirrors and it was found that the experimental modulation was different each time suggesting that the validity of the TartanSW emission technique is highly dependent upon the mirror being used and work is being carried out into identifying the origins of the discrepancy. It was also found that after the image was acquired that registration had to be implemented between the channels due to misalignment being generated within the emission-splitter, which could also have possibly introduced artefacts into the image.

When the TartanSW emission lens imaging experiments were repeated using the confocal microscope the intensity plots lined up almost exactly with the theoretical values. A direct comparison between the two seems to suggest that the difference is small and could be caused in this instance by a slight oxidation layer between the lens and the reflector (on the order of tens of nanometres). My colleague, Ross

Scrimgeour, is currently working on MATLAB code in order to quantify the exact offset between the theoretical and the experimental plots. Due to the nature of the confocal emission channel acquisition it was not necessary to register the images which made post-acquisition processing of the data easier.

Though the widefield TartanSW emission structure did not line up with the theoretical values, the TartanSW emission technique (in both widefield and confocal microscopy) could still be used to infer directionality of a structure by using the colour ordering of the standing wave antinodal emission planes. This could be done as typically the shorter wavelength detection bandwidth is at locations that tend to be slightly before the longer wavelength ones, especially when using high NA objective lenses. By using this principle, the ordering could aid in informing whether a structure was ascending or descending in a given direction.

A computational script utilising phase unwrapping is currently being developed in order to use the confocal data to generate axial height maps of specimens using the emission fringes which will then be implemented with the widefield data if it can be reconciled with the theory. There is also a temporal resolution benefit to the TartanSW emission technique in that for both a widefield and confocal experiments, all of the emission channels are acquired simultaneously whilst in TartanSW excitation microscopy sequential excitation at different wavelengths are required.

The TartanSW emission technique was applied to the red blood and MCF-7 cells using both widefield and confocal microscopy. The widefield red blood cell data did show slight band separation that was observable in the line intensity plot though it still suffered from the membrane gradient issues encountered in the widefield and confocal TartanSW excitation experiments. This is again due to a combination of the high intensity drop off that occurs within the small focal depth of the high NA objective lenses and that the intensity modulation does not begin to become apparent until higher antinodal plane numbers which are not being obtained in these imaging experiments. These limited results were also observed when using confocal microscopy. The red blood cell results obtained in the work from this chapter lead to the conclusion that this specimen, and perhaps other small cells, may only be suitable for single colour

standing wave imaging as the only slight observation of different spectral bands offers little advantage to obtained results.

As with the TartanSW excitation data it was found that the larger MCF-7 cells imaged with lower NA lens allowed more obvious spectral modulation to be observed than with the red blood cell imaging setup. It was also found in the confocal data that changing the excitation wavelength altered the emission patterns detected which is to be expected from equation (3.1).

With the current state of the TartanSW emission technique, being only able to infer directionality of the specimen structure at best, it is thought that TartanSW excitation may be the superior technique for imaging live cell specimens. The TartanSW excitation technique not only allows for the directionality of a structure to be inferred, using plane ordering, but also provides an information gap reduction to obtain more information about the specimen. Also, with the simple addition of an extra step in the image processing stage allows for the enhancement of the axial resolution by approximately a factor of 2. Future investigation, experiments and computational work are required on the TartanSW emission imaging technique in order to convert the intensity modulation into an axial height map of the specimen but once this is complete it could then be combined with the TartanSW excitation modality resulting in a robust high temporal and axial super-resolution technique which is highly compatible with widefield live cell imaging.

### **3.5) Conclusions**

The work in this Chapter has demonstrated the first application of the standing wave technique on the membrane structure of whole adherent mammalian cells and investigated the application of TartanSW excitation and emission imaging to overcome some of the limitations observed with single-wavelength standing wave microscopy.

These experiments have shown that by utilising widefield TartanSW excitation imaging the information gap can be reduced resulting in an additional increase of 32.3 % more information about the specimen being obtained. By taking the difference between the excitation channels it has also been shown that the axial resolution of the standing wave technique can be improved by approximately a factor of two. This TartanSW difference method was also used on TartanSW excitation images of MCF-7 cells to obtain an axial resolution on the order of 50 nm which also increased the contrast of the difference antinodal planes which in future could allow for computational reconstructions to be obtained in the future.

TartanSW emission imaging was applied to both model and biological specimens and whilst it was found to be successfully possible to carry out, there exists some disagreement with the widefield theoretical structure that has to be resolved to allow quantitative analysis to be carried out. However, this disagreement was not found to be present in the confocal imaging and this technique could still be used to infer the directionality of a structure. As a consequence of this, computational methods are being developed in order to extract this information and generate axial height maps of specimens imaged using confocal TartanSW emission microscopy.

These new TartanSW techniques lay the ground work to gain even more information about a wider variety of specimens with an unprecedented widefield axial resolution that supports high temporal resolution imaging.

## **Chapter Four:**

# **Ratiometric Ca<sup>2+</sup> imaging of live cell specimens loaded with Fura-2 AM using a rapid switching 340/380 nm LED illuminator**

**T**he purpose of this Chapter is to discuss the work that was carried out utilising a new 340/380 nm LED illuminator for Fura-2 ratiometric Ca<sup>2+</sup> imaging of live cell specimens and comparing the performance to a commercial 350/380 nm LED system. This work has demonstrated that using the 340/380 nm illuminator allows for the recording of cytosolic Ca<sup>2+</sup> changes below 5 nM, the possibility to reduce the concentration of Fura-2 loaded into cells down to 250 nM without compromising the detection of induced Ca<sup>2+</sup> changes and the ability to image, with high precision, synaptically-driven Ca<sup>2+</sup> events in hippocampal neurons at a video-rate. When this was compared to the results obtained when imaging using the 350/380 nm illuminator it was found that the precision in our experiments was above the precision of the response of Fura-2 and that dye loading concentrations below 500 nM resulted in a statistically significant different Ca<sup>2+</sup> response than that obtained with 1 µM dye loading.

### **4.1) Introduction**

Intracellular calcium (Ca<sup>2+</sup>) plays a varied and integral role in mediating and controlling many biological processes including the regulation of muscle contractions

[224], triggering insulin release from pancreatic cells [225], and the release of neurotransmitters in neurons [226]. Increases in cytosolic  $\text{Ca}^{2+}$  levels can originate from a number of sources including being released from internal stores that are triggered by the activation of G-protein coupled receptors by both endogenous and exogenous stimuli [227], or from external sources via influx across the cell membrane through the opening of voltage-gated  $\text{Ca}^{2+}$  channels [24]. Hence, the measurement of  $\text{Ca}^{2+}$  dynamics has been utilised extensively in biological research as it can reveal how specimens respond to different stimuli and how  $\text{Ca}^{2+}$  signaling is altered in disease states.

#### **4.1.1 Methods for detecting intracellular $\text{Ca}^{2+}$**

The first studies into measuring electrical activity in biological specimens were carried out by Hodgkin and Huxley [228] who probed the axon of a giant squid using a 1 mm diameter glass capillary filled with saline. The basis of this technique has been advanced since then leading to the voltage clamp method [229], [230]. Voltage clamping has been used extensively to study membrane potentials and ion channels allowing the investigation of intracellular and extracellular ion exchanges to be recorded. Though electrophysiological methods are still the gold standard for measuring electrical activity within and between excitable cells due to their high temporal resolution [231], the technique is limited as the spatial resolution is low and the nature of the technique leads to low throughput data production that is highly invasive [231]–[233]. In contrast, the development of  $\text{Ca}^{2+}$  specific fluorescent indicators allows for high throughput data acquisition with good spatial resolution [1], [231], [234], which has allowed intracellular  $\text{Ca}^{2+}$  dynamics to be investigated non-invasively in multiple cells simultaneously using widefield epifluorescence microscopy.

Fluorescent  $\text{Ca}^{2+}$  indicators typically fall into two different categories, namely single excitation wavelength indicators, including Fluo-4 and Fluo-3, or dual-wavelength dyes (emission or excitation) such as Fura-2 or Indo-1 [25], [235]. Single wavelength

indicators have a high quantum yield and allow for a simple excitation and detection setup. The  $\text{Ca}^{2+}$  concentration changes are then identifiable through an intensity change in the fluorescence emission [236]. However, these indicators are unable to provide quantitative  $\text{Ca}^{2+}$  data since the emission intensities may be influenced by dye concentration or photobleaching during imaging [25], [237].

Dual wavelength, or ratiometric,  $\text{Ca}^{2+}$  indicators have either excitation or emission wavelengths that shift in response to concentration changes in cytosolic  $\text{Ca}^{2+}$  [25], [238]. As there is a change in wavelength these dyes require a more complex imaging setup that ensures that the free and bound  $\text{Ca}^{2+}$  wavelengths are recorded separately. The quantitative cytosolic  $\text{Ca}^{2+}$  concentrations are obtained by taking a ratio of the  $\text{Ca}^{2+}$  free and bound wavelengths, with these ratios being unaffected by the optical path lengths, light intensities or the dye concentration within the cytosol [236], [239], [240]. Whilst quantitative data can be acquired, dual wavelength indicators typically have a smaller dynamic range than single wavelength dyes [25].

Fura-2 is a ratiometric fluorescent  $\text{Ca}^{2+}$  indicator that was developed as an improved alternative to the  $\text{Ca}^{2+}$  indicator, Quin2 [241]. Fura-2 holds advantages over another ratiometric dye, Indo-1, as it has a larger dynamic range between  $\text{Ca}^{2+}$  bound and free states [25], and is more resistant to photobleaching [236]. When cytosolic free  $\text{Ca}^{2+}$  binds to Fura-2, the dye undergoes a chemical structure change (see figure 4.1) and the peak excitation wavelength changes from 380 nm to 340 nm whilst the peak emission around 510 nm remains unchanged (figure 4.2) [241]. By sequential excitation of Fura-2 at 340 nm and 380 nm and taking a ratio of the emission signals for each excitation wavelength, these ratios can be calibrated to a measurement of the corresponding cytosolic  $\text{Ca}^{2+}$  concentration by measuring the ratio of the fluorescence emission signal in the presence of known free  $\text{Ca}^{2+}$  concentrations. Fura-2 in its salt form is impermeable to cellular membranes so in order to enter the cytosol of biological specimens acetoxymethyl esters (AM) are added to the molecule [235], [236]. This AM addition allows the dye to cross the plasma membrane and after which is then cleaved from Fura-2 through hydrolysis by cytosolic esterase leaving the dye trapped within the cell [234]–[236].

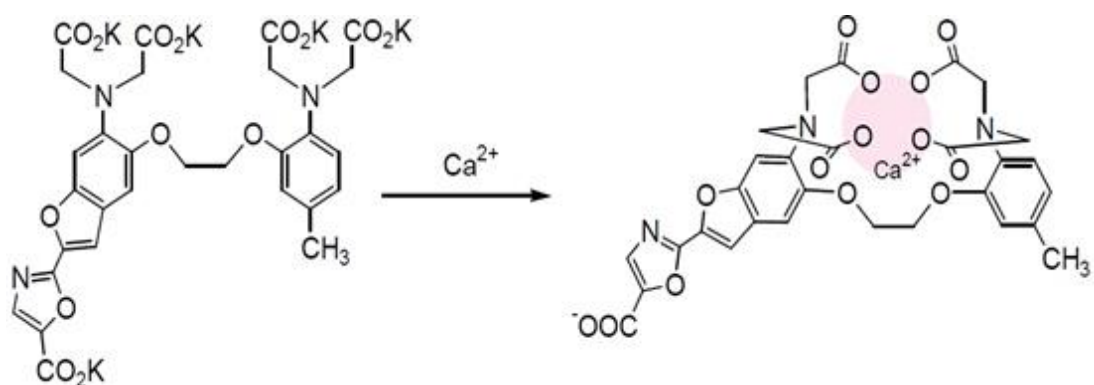


Figure 4.1; Chemical structures of the fluorescent molecule Fura-2 when either unbound or bound to intracellular Ca<sup>2+</sup> adapted from [242].

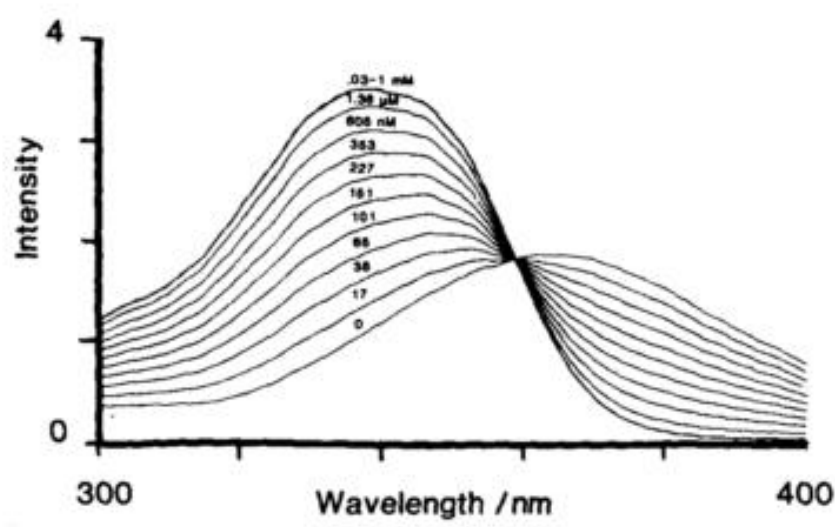


Figure 4.2; Excitation spectrum of Fura-2 in buffer obtained at an emission wavelength of 510 nm in the presence of different concentrations of free Ca<sup>2+</sup> [241].

It can be seen in the excitation spectra shown in figure 4.2 that there exists a wavelength at which there is no intensity change in the presence of different concentrations of Ca<sup>2+</sup>. This point, known as the isosbestic point, occurs around 360 nm for Fura-2 [25], [243] and it has been used in studies in to image intracellular Ca<sup>2+</sup> concentration changes by exciting at 360 nm and 380 nm [244]–[246]. In this configuration increases in Ca<sup>2+</sup> concentration are then identified by a decrease in the emission intensity when excited at 380 nm but there should be no change in the emission intensity obtained at 360 nm excitation.

### 4.1.2 Light sources used for Fura-2 Ca<sup>2+</sup> imaging

Historically, the most commonly used light source for widefield Fura-2 excitation has been an arc lamp and monochromator [25] [236]. Mercury arc lamps were first developed by Peter Cooper Hewitt in 1901 [247] and emit incoherently and non-uniformly across the UV to IR electromagnetic spectrum with several discrete high intensity peaks [36]. Xenon arc lamps, conversely, have an output spectrum which is approximately uniform across the visible spectrum but holds the disadvantage that most of the output occurs in the, less useful, IR region. Light is generated by a high voltage ignition arc between two tungsten electrodes which vaporises the mercury or xenon in the bulb and results in a plasma arc to be held between the two electrodes [248]. After this initial ignition the bulb requires a “warm up” to reach full brightness [36], [249]. The bulbs have relatively short life-times on the order of 200 hours, require a “burn in” period, contain toxic material, are an explosive hazard and have outputs that decrease in intensity the further the bulb is through its lifetime [36], [249], [250].

In addition to these limitations, users of these systems for ratiometric Ca<sup>2+</sup> imaging have had to sacrifice precise and immediate control over light intensity without the use of neutral density filters and are only able to utilise wavelength switching speeds on a millisecond timescale due to monochromator limitations. In addition, arc lamp light sources exhibit inherent amplitude instability on the order of 5% [251], [252], which reduces the accuracy of measurement and as a result small changes in Ca<sup>2+</sup> may go undetected [253]–[255]. This amplitude instability is present due to a number of factors such as arc wander, where the arc moves between the electrodes in a circular motion, arc flare, characterised by a sudden change in brightness, and arc fluttering, an effect caused by convection currents due to the temperature difference between the arc and its surroundings [250], [252], [256]–[258].

Previous investigations have used two-photon microscopy to conduct Fura-2 Ca<sup>2+</sup> imaging [259], [260]. By using this technique, it is possible to reduce photo-bleaching rates in the out of focus planes [261] and image deeper into bulk specimens [262]. However, point-scanning two-photon excitation is slow [263], [264], as is the

wavelength scanning of the laser [265]. This combination of limitations does not readily support the detection and measurement of fast changes in  $\text{Ca}^{2+}$  concentration that are possible with a widefield microscope and a fast acquisition camera. More recently, widefield two photon microscopy has been used to image hippocampal neurons loaded with Fluo-4 [266], but this work does not support quantitative measurement of  $\text{Ca}^{2+}$  concentration.

In recent widefield calcium imaging experiments, LEDs have been utilised to excite Fura-2. This type of illuminator can support high stability switching on microsecond timescales and offer precise output intensity control by simply changing the LED drive current. Until recently, commercial LED systems have only offered LED combinations of 350/380 nm or 360/380 nm for ratiometric Fura-2  $\text{Ca}^{2+}$  imaging, which do not precisely match the excitation wavelengths required or only allow excitation at the isosbestic point [25].

The gallium indium nitride (GaInN) material system can be tailored to produce LEDs that output wavelengths from 360 nm up to 530 nm [267], [268] covering the near UV to blue-green range. The now ease of developing LEDs in this wavelength range made the current LED illuminators for ratiometric Fura-2  $\text{Ca}^{2+}$  imaging readily available. In order to produce LEDs in the range of 340 nm, which is a shorter wavelength that is obtainable with the GaInN system, aluminium gallium indium nitride (AlGaInN) must be used instead. There are several issues with these types of LEDs that typically leads to them having typically a low output efficiency. Al has an extremely high binding affinity for oxygen ( $\text{O}_2$ ) which leads to a largely reduced emission [269], the material system has a low conductivity [270] and the films are very susceptible to cracking [271]. Despite these shortcomings there have been great improvements in recent years by making use of multi-quantum well structures and refining the device substrate leading to 340 nm LEDs with greatly enhanced brightness [272]–[275].

The now commercial availability of the new shorter wavelength, high-brightness LED at 340 nm [272] has made it possible to develop a 340/380 nm switchable LED illuminator and demonstrate its application in microscopy by performing Fura-2 ratiometric  $\text{Ca}^{2+}$  imaging in both an immortalised cell line and in primary cultured neurons exhibiting pharmacologically-induced and synaptically-driven  $\text{Ca}^{2+}$

responses. The ability to excite Fura-2 at both  $\text{Ca}^{2+}$  bound and unbound peaks without the use of an arc lamp and monochromator could result in higher precision measurements made possible due to the use of a high stability light source and that higher temporal resolution could be obtained by removing the limitations seen in monochromator systems.

## **4.2) Materials and methods**

### **4.2.1 Characterisation of 340/380 nm and 350/380 nm LED systems**

In order to compare the performance of both LED systems for ratiometric Fura-2  $\text{Ca}^{2+}$  imaging of live cell specimens and to determine if there was any advantage to using the 340/380 nm illuminator it was first necessary to characterise both light sources.

The peak output spectra for the 340 nm (pE-100-340, CoolLED) and 380 nm LEDs (pE-100-380, CoolLED) were measured using a spectrometer (USB2000+UV-VIS-ES, OceanOptics). The peak wavelength and FWHM were determined using the same method described in Chapter 2, section 2.2.3. The peak wavelength and FWHM for each LED were found to be  $342 \pm 1.50$  (FWHM –  $9.30 \pm 1.50$ ) nm and  $383 \pm 1.50$  (FWHM –  $8.30 \pm 1.50$ ) nm. Plots of these spectra can be seen below (figure 4.3).

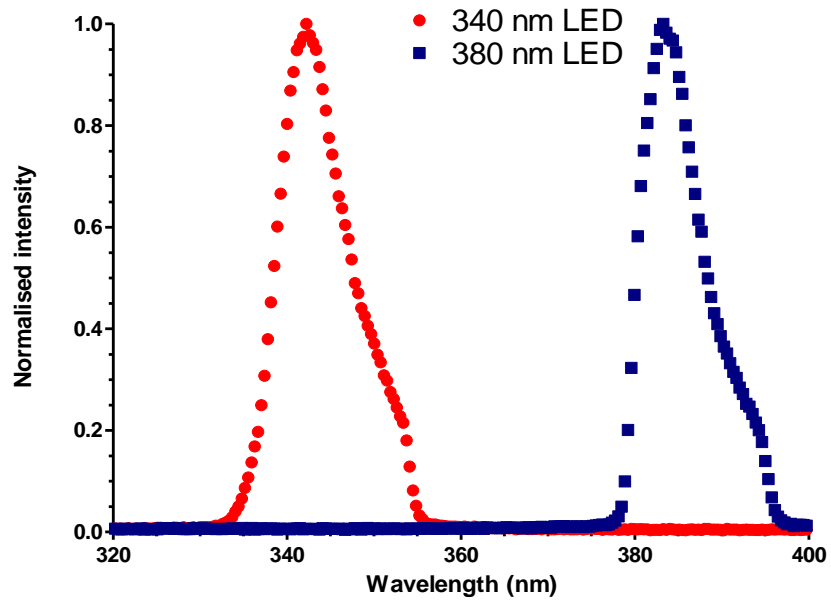


Figure 4.3; Output spectra of 340 nm and 380 nm LEDs obtained at a driving current of  $1.52 \pm 0.16$  A.

The output spectra of the commercial 350/380 nm LED illuminator (OptoLED, Cairn) was measured using the same apparatus as above. It was found that these LEDs had peak wavelengths and FWHM of  $360 \pm 1.50$  nm (FWHM –  $7.60 \pm 1.50$  nm) and  $386 \pm 1.50$  nm (FWHM -  $6.50 \pm 1.50$  nm) (figure 4.4).

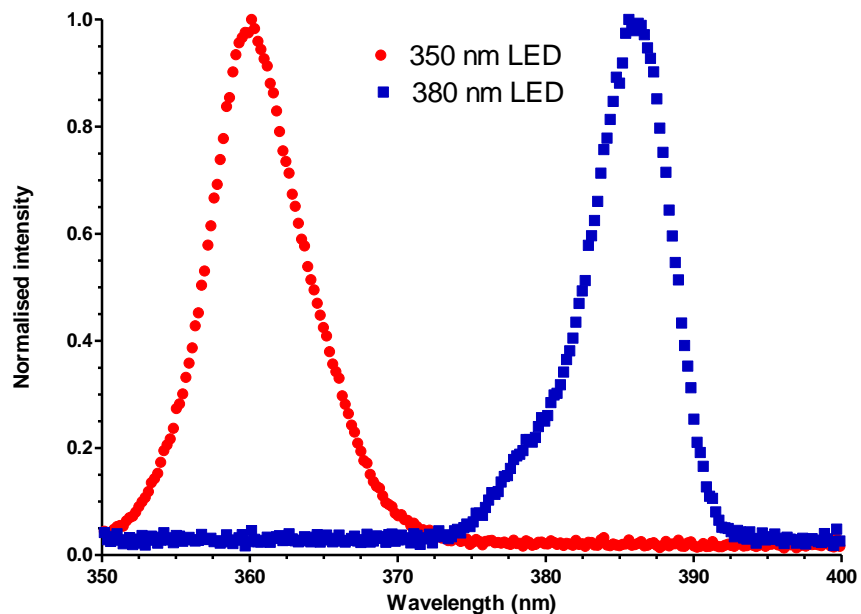


Figure 4.4; Output spectra of 350 nm and 380 nm LED.

Power measurements were recorded using the same equipment and methods described in section 2.2.3. Measurements were taken at the specimen plane under an Olympus 20x/0.5 water dipping objective lens at drive currents from zero to  $1.520 \pm 0.160$  A for the 340 nm and 380 nm LEDs.

The 340 nm LED demonstrated a linear increase in optical power of approximately 6.60 mW/A up to  $0.59 \pm 0.07$  A. Above this current the 340 nm LED exhibited rollover, a phenomenon where with an increase in drive current the optical power begins to plateau or even decrease. The 380 nm LED showed a linear increase in optical power of approximately 14.7 mW/A increase in current up to  $1.52 \pm 0.16$  A. The optical power at different drive currents are shown in figure 4.5.

For the experiments presented, the 340 nm LED was used at an optical power at the microscope specimen plane of  $1.32 \pm 0.01$  mW and the 380 nm LED was kept between  $1.40 \pm 0.02$  and  $3.08 \pm 0.01$  mW.

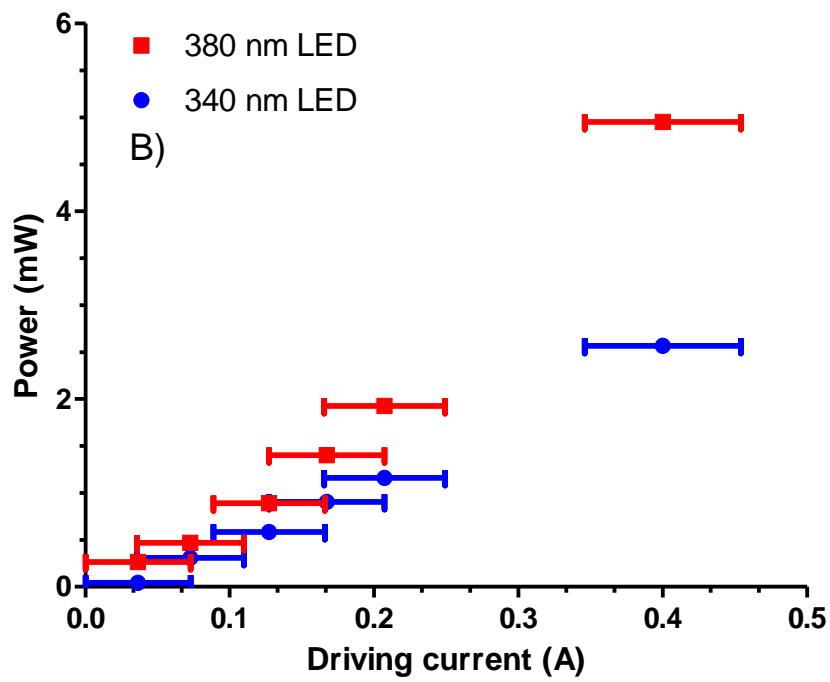
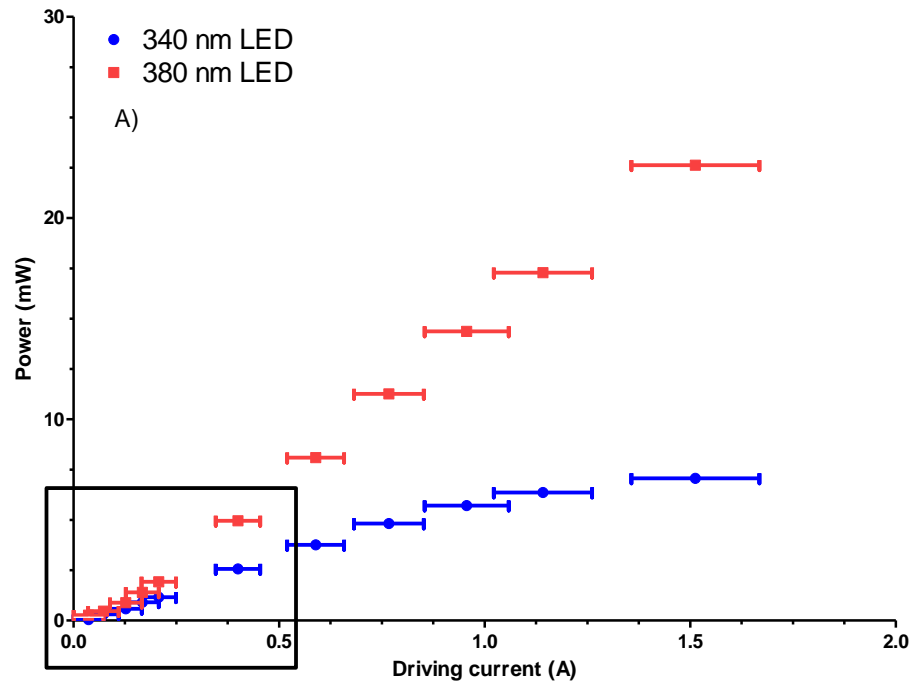


Figure 4.5; A) Optical powers measured at the specimen plane of an Olympus BX50 microscope under a 20x water dipping lens at increasing driving currents. B) Enlarged plot of ROI in A) showing the power ranges used in this Chapter.

The power measurements at the specimen plane for the 350/380 nm LED system were unable to be recorded as our powermeter was not sensitive enough to detect the low optical powers at the specimen plane, furthermore, the sliding intensity control for these LEDs would not allow for accurate replication of any measurements if they had been obtained.

To measure the experimental resolutions with each LED a 20x/0.5 water dipping objective lens was used to image 100 nm diameter fluorescent beads (Fluoresbrite BB Carboxylate Microspheres 0.10  $\mu\text{m}$ , Polysciences Europe GmbH, Germany) sandwiched between a microscope slide and coverslip which was coupled to the objective lens by a layer of water. The FWHM was calculated by taking a line intensity plot through one of the imaged beads. By doing this it was found that due to the camera binning of  $n = 2$  used, the resolution of the imaging system was limited by the size of the pixels which was 649 nm.

#### **4.2.2 tsA-201 cell culture**

tsA-201 cells, a modified HEK-293 cell line, were cultured at 37 °C in a 5% CO<sub>2</sub> humidified incubator in 75 cm<sup>2</sup> tissue culture flasks containing 10 mL of Dulbecco's Modified Eagle's Medium (DMEM) low glucose, pyruvate medium (Gibco, Paisley, UK) including 10% foetal calf serum (Biosera, Sussex, UK), 1% penicillin-streptomycin (Sigma, Dorset, UK) and 1% MEM non-essential amino acids (Gibco, Paisley, UK). After 3 days in culture, the medium was removed, and the cells were washed twice in PBS (Gibco, Paisley, UK). Subsequently, cells were dissociated from the flask using 2 mL of TrypLE (Gibco, Paisley, UK) and incubated at 37 °C until all cells were detached. Cells were then resuspended in 7 mL of the modified DMEM media. 0.5 mL of these resuspended cells was then seeded into wells of a 6 well plate that contained a 13 mm diameter borosilicate coverslips with a thickness type 1.5 and 1 mL of 37 °C modified DMEM per well. The plate was rocked gently to ensure even distribution in the wells. The cells were then left to grow for one day before imaging.

### 4.2.3 Primary hippocampal neuron culture

Mouse hippocampal cultures were prepared as described previously [276], [277]. Briefly, 1 to 2-day-old C57/BL6J pups were sacrificed by cervical dislocation and decapitated. The hippocampi were removed, triturated and the resulting cells were plated at a density of  $5.5 \times 10^5$  cells·mL<sup>-1</sup> onto 13 mm poly-L-lysine (0.01 mg·mL<sup>-1</sup>) coated coverslips. Cultures were incubated in culture medium consisting of Neurobasal-A Medium (Invitrogen, Paisley, UK) supplemented with 2% (v/v) B-27 (Invitrogen, Paisley, UK) and 2 mM L-glutamine and maintained in a humidified atmosphere at 37°C/5% CO<sub>2</sub> for 10–14 days *in vitro* (DIV). All animal care and experimental procedures were in accordance with UK Home Office guidelines and approved by the University of Strathclyde Ethics Committee.

### 4.2.4 Fluo-4 Ca<sup>2+</sup> imaging of pharmacologically-induced Ca<sup>2+</sup> transients in live cell specimens

In preparation of assessing the performance of the 340/380 nm LED for ratiometric Ca<sup>2+</sup> imaging it was first necessary to test our imaging setup and pharmacological stimuli which was done by carrying out Ca<sup>2+</sup> imaging of tsA-201 specimens loaded with the single wavelength Ca<sup>2+</sup> indicator, Fluo-4 AM.

Specimen coverslips were washed three times in the HEPES-buffered saline (HBS) control solution and loaded with Fluo-4 AM (1 μM) (Invitrogen, Paisley, UK) for 45 – 60 minutes at 37 °C, after which they were washed a further three times prior to imaging. Throughout imaging experiments coverslips were under constant perfusion with either control or drug solutions at a rate of 3 – 3.5 mL/minute. The HBS control solution was made up in distilled water and contained (in mM): NaCl, 140; KCl, 5; MgCl<sub>2</sub>, 2; HEPES, 10; D-glucose, 10; CaCl<sub>2</sub>, 2. The pH of the solution was made up to  $7.40 \pm 0.02$  by addition of 10 M NaOH and the osmolality of the solution was

adjusted to  $0.310 \pm 0.002$  mOsm through the addition of sucrose. All drug solutions were made up in the control solution described.

tsA-201 specimens were placed individually in a perfusion bath under a 20x/0.5 water dipping objective lens (Olympus UMPlanFl) which was coupled to an upright widefield epifluorescence microscope (Olympus BX50). The specimens were illuminated by a 470 nm LED (pE-4000, CoolLED) coupled to the microscope with a liquid light guide and a universal collimator (CoolLED) for a duration of 100 ms. The LED had a peak output wavelength of  $479 \pm 1.50$  nm (FWHM -  $27.6 \pm 1.50$  nm) and the optical power at the specimen plane set to  $7.34 \pm 0.02$  mW. Both output spectra and specimen plane power measurements were measured using the same method described in section 2.2.3. Emission was detected  $> 515$  nm using a CMOS camera (ORCA-Flash 4.0LT, Hamamatsu) at a rate of 0.5 Hz using a camera binning  $n = 2$ . A schematic diagram of this setup can be seen in figure 4.6.

During cell imaging, specimens were perfused with the HBS control solution initially to establish a baseline resting  $\text{Ca}^{2+}$  level. Following the initial wash 4.5 mL ATP (5  $\mu\text{M}$ ) (Sigma, Dorset, UK) was perfused into the bath followed by a control solution wash to remove any stimuli and return the cells to the baseline levels. A second drug wash of 4.5 mL trypsin (100 nM) (Sigma, Dorset, UK) was then perfused which was again followed by another wash of control solution.

The pharmacological stimuli used to induce  $\text{Ca}^{2+}$  changes in the tsA-201 cells (a subclone of the HEK-293 cell line) were chosen as they have been previously shown to cause large and gradual increases in intracellular  $\text{Ca}^{2+}$  [278]–[282] allowing it to be imaged using our acquisition rate of 0.5 Hz. The mechanism that causes a  $\text{Ca}^{2+}$  concentration change with the application of ATP is due to the P2X ligand gated ion channels which are found in a wide range of different cell types [278]–[280]. When ATP binds to these extracellular receptors they undergo a conformation change opening a ion permeable channel in the plasma membrane allowing  $\text{Ca}^{2+}$  ions to enter the cell [283]–[285].

Trypsin is an agonist of the G-coupled receptor, protease activated receptor 2 (PAR2) which is present in many cell types [286]–[288]. PAR2 has an extracellular portion which is cleaved by the application of trypsin, the result of this is an intracellular

signalling cascade which releases  $\text{Ca}^{2+}$  from the endoplasmic reticulum into the cytosol to cause many different cellular processes [289]–[291].

All signals were recorded using the WinFluor imaging and electrophysiology analysis software [165], which also synchronised and TTL triggered the 470 nm LED. Using WinFluor, multiple ROI from each coverslip imaged were selected including an area without any cells to establish the background value for each coverslip. The time courses for the resulting background-subtracted fluorescence emission signals for each ROI could then be obtained.

For these experiments five separate cultures of tsA-201 cells were imaged.

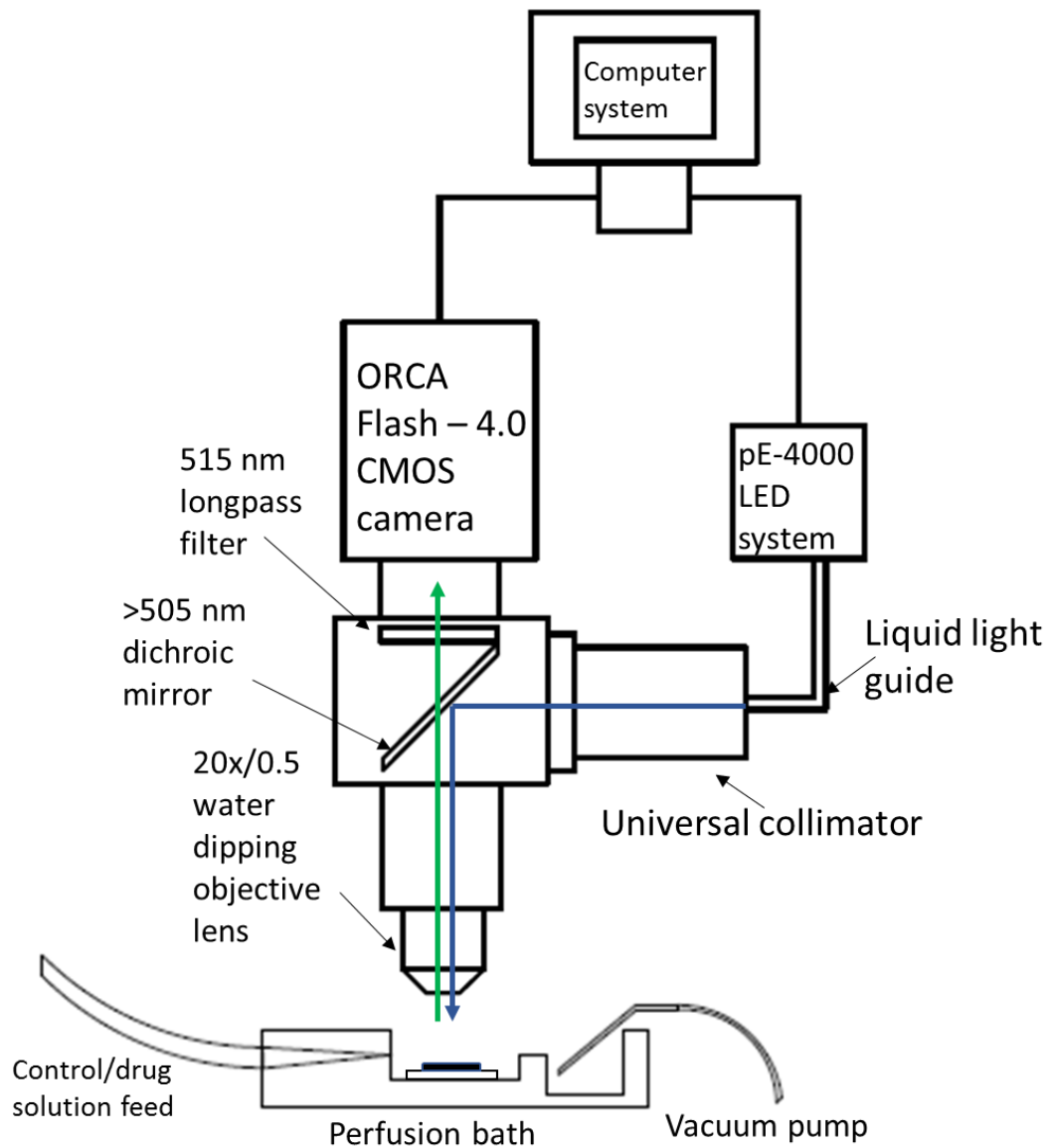
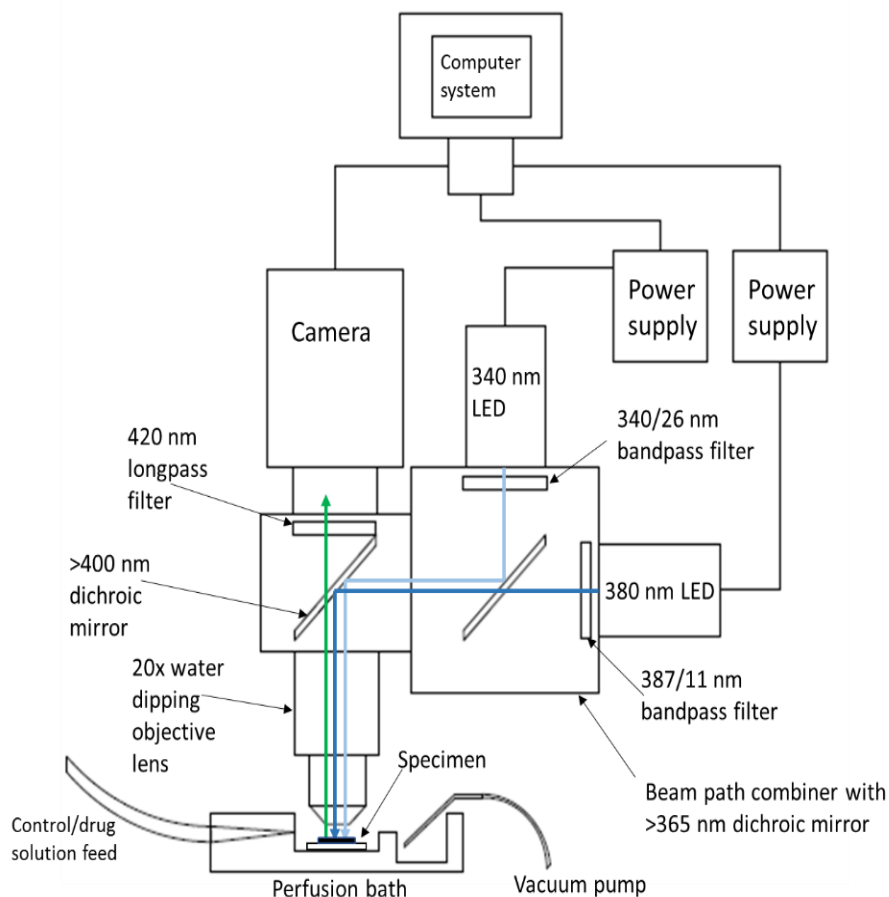


Figure 4.6; Generalised schematic diagram of experimental imaging setup showing the location of the specimen in relation to the objective lens and where the perfused solution flows over the specimen and gets removed from the bath. The light paths of the 470 nm LED are also shown to be collimated and then illuminate the specimen after being reflected by a  $> 505$  nm dichroic mirror. The emitted Fluo-4 fluorescence propagates upwards through the objective lens,  $> 505$  nm dichroic mirror (Olympus) and 515 nm longpass filter (Olympus) to the camera. The camera and pE-4000 are connected to a computer system for triggering and recording fluorescent signals.

#### **4.2.5 Fura-2 ratiometric Ca<sup>2+</sup> imaging of pharmacologically-induced Ca<sup>2+</sup> transients in live cell specimens**

For experiments utilising the 340/380 nm and 350/380 nm LED illuminators for ratiometric Ca<sup>2+</sup> imaging tsA-201 and hippocampal neuron specimens were loaded with Fura-2 AM (1 μM) (Invitrogen, Paisley, UK) in the same manner as used when loading the Fluo-4 AM.

Imaging of the specimens using the 340/380 nm illuminator was carried out using the same microscope and objective lens as in the Fluo-4 experiments but with different filters and light source. The 340/380 nm LED illuminators was coupled to the microscope with a beam path combiner (pE-combiner, CoolLED) which contained a > 365 dichroic mirror (365dmlp, Chroma), and clean up filters for each LED (Semrock BrightLine 340/26 nm bandpass filter for the 340 nm LED and a Semrock BrightLine 387/11 nm bandpass filter for the 380 nm LED). A schematic diagram for this setup can be seen in figure 4.7.



*Figure 4.7; Generalised schematic diagram of experimental imaging setup showing the location of the specimen in relation to the objective lens and where the perfused solution flows over the specimen and gets removed from the bath. The light paths of the 340/380 nm LEDs are also shown to converge through the use of 365 nm dichroic mirror and then illuminate the specimen in the perfusion bath sequentially. The emitted Fura-2 AM fluorescence propagates upwards through the objective lens, >400 nm dichroic mirror (Olympus) and 420 nm longpass filter (Olympus) to the camera. The camera and power supplies for both LEDs are connected to a computer system for triggering and recording fluorescent signals.*

During cell imaging, the tsA-201 cells were exposed to the same pharmacological stimuli as when carrying out the Fluo-4 imaging. The hippocampal neuron specimens were perfused with control solution initially to establish a baseline resting  $\text{Ca}^{2+}$  level followed by 4.5 mL of glutamate (20  $\mu\text{M}$ ) (Sigma, Dorset, UK). The cells were then allowed to return to baseline levels before being washed with potassium chloride (KCl)

(20 mM) (Sigma, Dorset, UK). The cells were then returned to the baseline which concluded imaging.

During this process, the specimens were alternatively illuminated with the 340 nm and 380 nm LEDs each with an exposure time of 100 ms and imaged at a rate of 0.5 Hz with emission being detected above 420 nm by the same CMOS camera used previously in the Fluo-4 imaging experiments.

The  $\text{Ca}^{2+}$  changes in the hippocampal neurons that were mediated through glutamate application results from the activation of inotropic glutamate receptors which are ligand gated ion channels [23], [292], [293]. The two main receptors of this type are  $\alpha$ -amino-3-hydroxy-5-methyl-4-isoxazolepropionic acid (AMPA) and N-methyl-D-aspartate (NMDA), and when glutamate binds to these it opens up a channel through the cell membrane which allows for  $\text{Ca}^{2+}$  ions to enter the cell [23], [292], [294]–[296]. The KCl wash causes a  $\text{Ca}^{2+}$  concentration change in the hippocampal neurons through the depolarisation of the cell membrane and the activation of voltage gated  $\text{Ca}^{2+}$  channels allowing a  $\text{Ca}^{2+}$  influx to the cell as the ions flow along the electrochemical gradient [240], [297], [298].

All signals were recorded using the WinFluor imaging and electrophysiology analysis software [24], which also synchronised and TTL triggered the 340/380 nm illuminator and camera. In this setup, a switching speed between LEDs of 150  $\mu\text{s}$  was available. The ROIs and background subtraction were obtained in the same method described in the Fluo-4 imaging section.

The experimental procedure described in this section was repeated using all the same optics but placed under a different widefield microscope (BX51W, Olympus) with a 350/380 nm LED illuminator coupled to it.

For the experiments carried out using this procedure, six different cultures of tsA-201 cells and four different hippocampal neuron cultures were used with each different illuminator.

#### **4.2.6 Imaging trypsin mediated Ca<sup>2+</sup> transients in tsA-201 cells using low concentrations of Fura-2 AM**

To determine the minimal practical concentration of Fura-2 AM that could be used with this new light source, tsA-201 cells prepared as above but loaded with either 750 nM, 500 nM or 250 nM concentrations of the dye. Ratiometric Ca<sup>2+</sup> imaging was then carried out on the tsA-201 cells using the same procedure previously described except the only drug the specimens were washed with was the trypsin (100 nM) solution.

This experimental procedure was repeated loading the cells with either 500 nM or 250 nM Fura-2 AM using the 350/380 nm LED microscope setup.

#### **4.2.7 Fura-2 video-rate ratiometric Ca<sup>2+</sup> imaging of synaptically-driven Ca<sup>2+</sup> transients in hippocampal neurons using the 340/380 nm illuminator**

Ratiometric Fura-2 imaging of synaptically-driven Ca<sup>2+</sup> events in hippocampal neurons at a video-rate was carried out. This was made possible as the 340/380 nm LED illuminators were capable of 150  $\mu$ s switching speeds. The hippocampal neurons were loaded with 1  $\mu$ M of Fura-2 AM in the manner described previously. In order to stimulate action potential firing in the neurons perfused the cells with HBS solution without any magnesium ions (Mg<sup>2+</sup>) which removes the voltage-dependent blockade of NMDA receptors [299], [300]. To facilitate imaging at a video-rate, the exposure times of illumination were decreased to 20.5 ms for each LED and the rate of imaging was increased to 24.39 Hz.

## 4.2.8 Data analysis and statistics

The background-corrected emission fluorescence time courses from the 470 nm excitation for the Fluo-4 experiments or the 340/380nm excitation or the 350/380 nm excitation for the Fura-2 experiments obtained from WinFluor were read into a custom MATLAB script to determine the average baseline  $\text{Ca}^{2+}$  level detected during the initial HBS solution wash. Each ROI was then normalised to the associated calculated average baseline. The average peak fold increases of the emission signal or ratios above the baseline for drug washes were then calculated using the normalised emission ratios.

To convert the background corrected emission ratios from the 340/380 nm excitation into a measurement of the free cytosolic  $\text{Ca}^{2+}$  concentration the following equation was used [241],

$$[\text{Ca}^{2+}] = K_D \cdot \frac{F_{\max}}{F_{\min}} \cdot \frac{(R - R_{\min})}{(R_{\max} - R)} \quad (4.1)$$

where  $K_D$  is the dissociation constant for Fura-2 which is 224 nM [241],  $R$  is the experimental emission ratios and  $F_{\min}$ ,  $R_{\max}$ ,  $F_{\max}$  and  $R_{\min}$  are the 380 nm fluorescence emission signals and emission ratio from 340/380 nm excitation at saturating and zero free  $\text{Ca}^{2+}$  levels, respectively. In order to determine the experimental values required for equation (4.1) the background-corrected emission ratios were obtained from 39  $\mu\text{M}$  and 0  $\mu\text{M}$  free  $\text{Ca}^{2+}$  solutions using a Fura-2  $\text{Ca}^{2+}$  imaging calibration kit (Invitrogen, Paisley, UK). The values for  $F_{\max}$ ,  $R_{\max}$ ,  $F_{\min}$  and  $R_{\min}$  at the experimental optical powers used can be seen below (table 4.1).

*Table 4.1; Experimentally determined variables required for equation (4.1) at the experimental optical powers at the specimen plane used for each LED.*

340 nm Power (mW)	380 nm Power (mW)	F <sub>min</sub>	F <sub>max</sub>	R <sub>max</sub>	R <sub>min</sub>
1.32	1.40	2157	262	13.56	0.37
1.32	2.29	2246	273	11.76	0.33
1.32	2.54	2265	280	11.27	0.31
1.32	2.76	2502	322	11.14	0.29
1.32	3.08	2895	409	9.56	0.25

The MATLAB scripts used to analyse the results can be found in Appendix 1. All biological replicates are reported as an ‘n’ number which are equal to the total number of ROIs investigated throughout each experiment taken from at least 4 different cultures. All data are expressed as mean  $\pm$  standard error of the mean. Data were compared by using either an unpaired student t-test or a one-way ANOVA with Tukey’s comparison, when appropriate, with P values  $< 0.05$  considered significant.

### **4.3) Results**

#### **4.3.1 Fluo-4 Ca<sup>2+</sup> imaging of pharmacologically-induced Ca<sup>2+</sup> transients in live cell specimens**

Using tsA-201 cells (n = 240) loaded with Fluo-4 AM it was possible to successfully use our imaging apparatus to carry out Ca<sup>2+</sup> imaging (see figure 4.8). With the application of ATP (5  $\mu$ M) a normalised emission fluorescence fold increase above the baseline was recorded of  $3.70 \pm 0.10$  (n = 240) and for the trypsin (100 nM) a fold increase of  $4.80 \pm 0.10$  (n = 240).

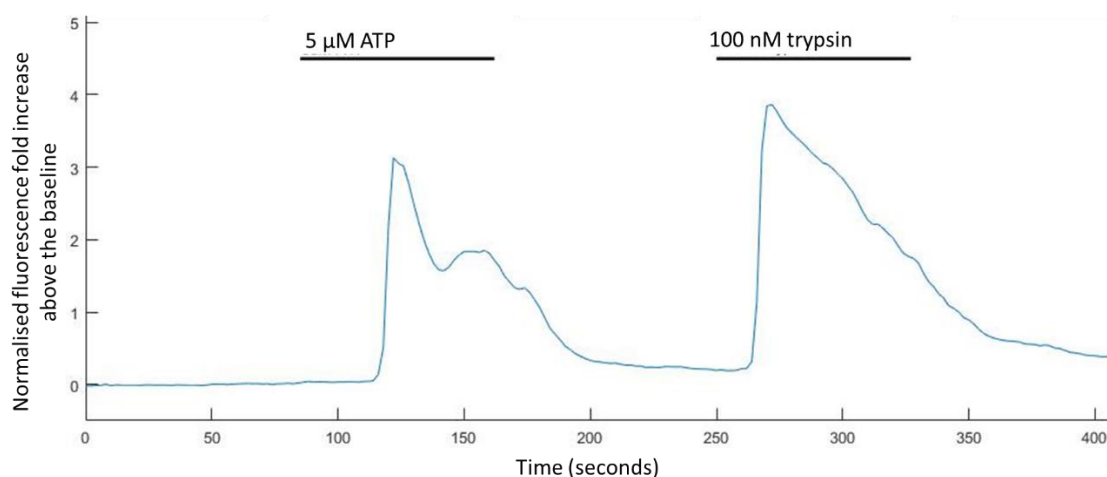


*Figure 4.8; Representative trace of Fluo-4 emission fold increases above the baseline in tsA-201 cells with emission increases being induced by application of ATP (5  $\mu$ M) and trypsin (100 nM) and imaged a 470 nm LED.*

### **4.3.2 Fura-2 ratiometric Ca<sup>2+</sup> imaging of pharmacologically-induced Ca<sup>2+</sup> transients in live cell specimens**

Once it was confirmed that it possible to carry out Ca<sup>2+</sup> imaging using our perfusion and imaging setup the next step was to move on to imaging tsA-201 cells and hippocampal neurons loaded with 1  $\mu$ M Fura-2 AM and illuminated using a commercial 350/380 nm LED illuminator. The normalised emission ratio fold increases above the resting baseline recorded in the tsA-201 cells were  $0.81 \pm 0.02$  (n = 411) evoked by ATP (5  $\mu$ M) and  $1.49 \pm 0.05$  (n = 411) by trypsin (100 nM). The hippocampal neurons showed an increase of  $2.50 \pm 0.06$  (n = 289) with the application of glutamate (20  $\mu$ M) and  $1.05 \pm 0.03$  (n = 289) by KCl (20 mM). Representative traces for these specimens are presented in figure 4.9.

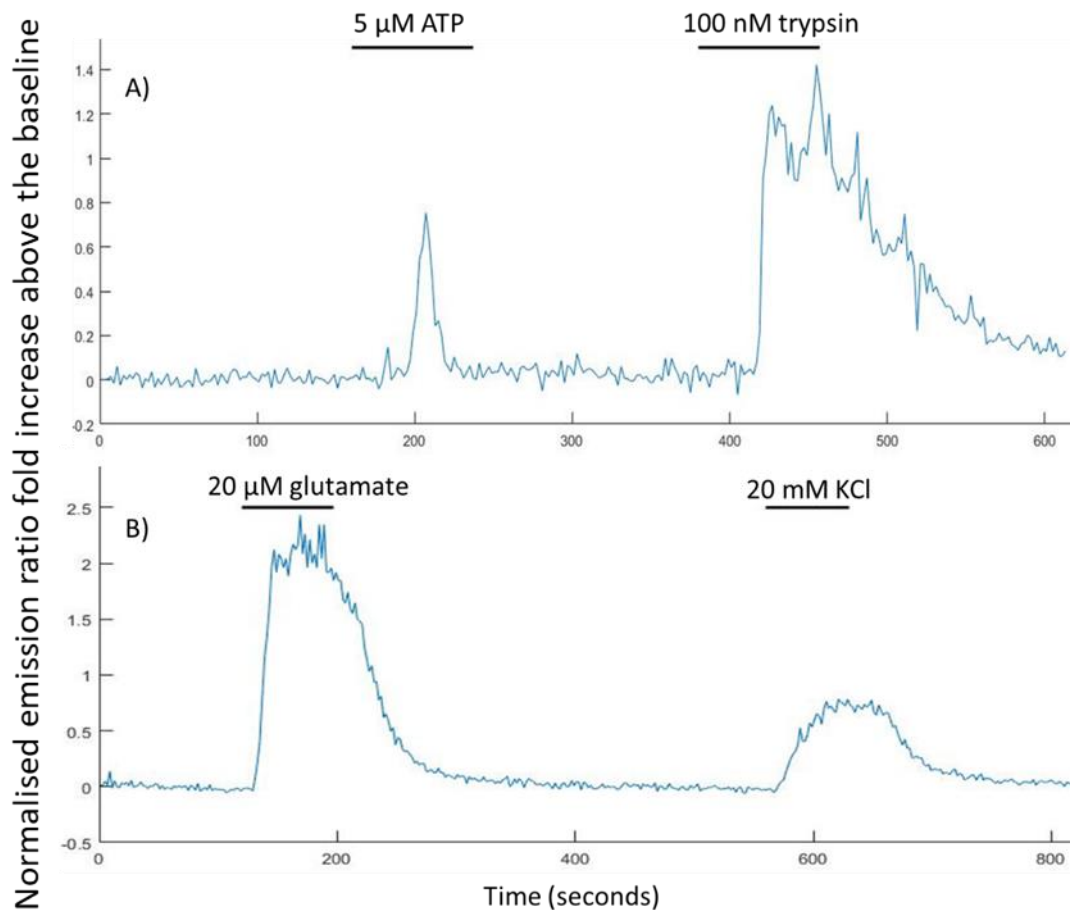
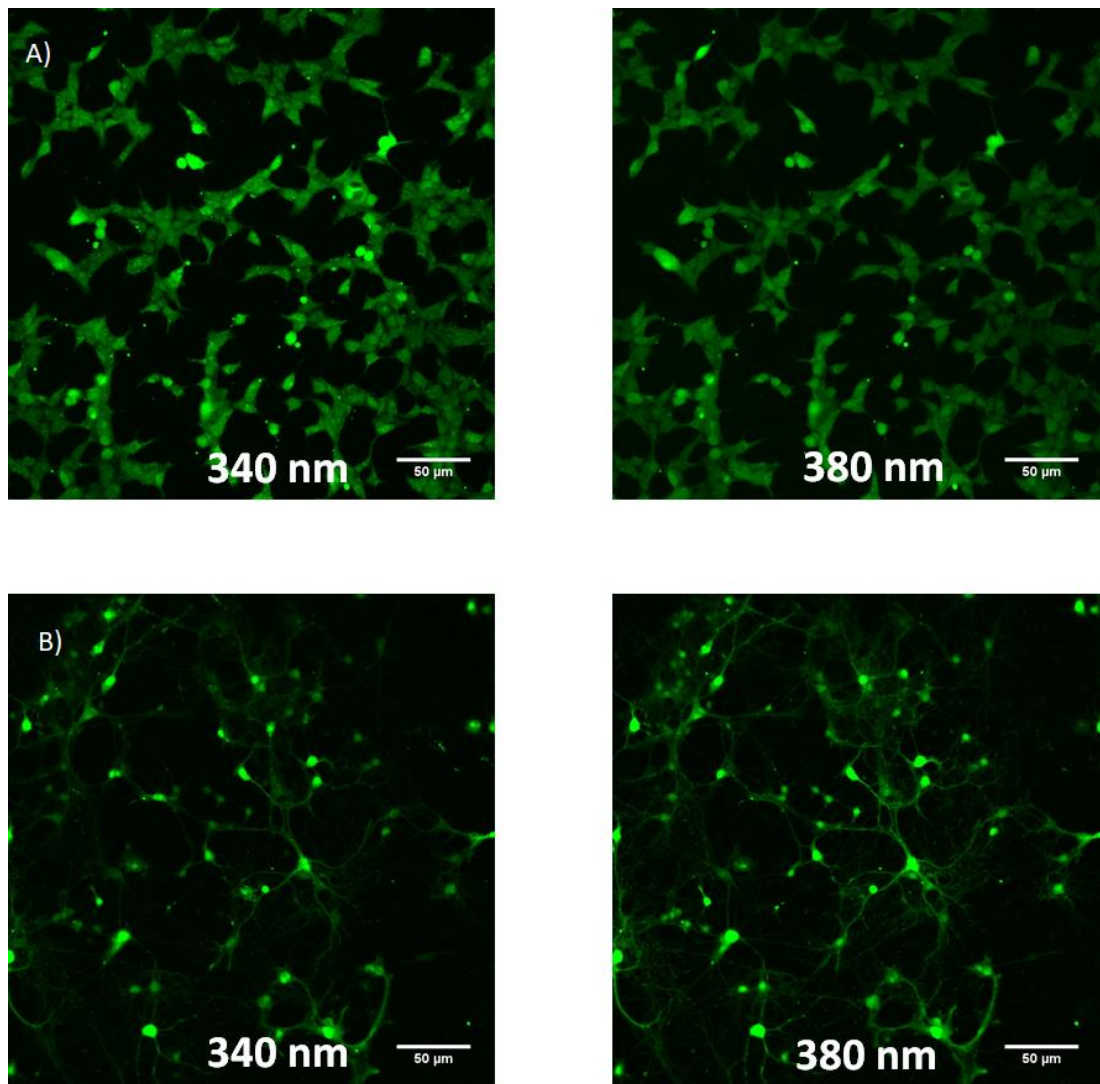


Figure 4.9; A) Representative trace of normalised emission ratio changes in tsA-201 cells with  $\text{Ca}^{2+}$  changes being caused by application of ATP (5  $\mu\text{M}$ ) and trypsin (100 nM) and imaged using the 350/380 nm LED illuminator. B) Representative trace of normalised emission ratio changes in hippocampal neurons with changes being caused by washes of glutamate (20  $\mu\text{M}$ ) and KCl (20 mM) and imaged using the 350/380 nm LED illuminator.

It was then demonstrated that it was possible to image pharmacologically-induced  $\text{Ca}^{2+}$  concentration changes in tsA-201 cells ( $n = 572$ ) and cultured hippocampal neurons ( $n = 388$ ) using the 340/380 nm LED illuminator (representative images of the tsA-201 cells and hippocampal neurons are showing in figure 4.10).



*Figure 4.10; A) Representative images of tsA-201 cells excited at both 340 nm and 380 nm. B) Representative images of hippocampal neurons excited at both 340 nm and 380 nm.*

The normalised emission ratio fold increases above the resting baseline in the tsA-201 cells were  $1.67 \pm 0.04$  ( $n = 572$ ) evoked by ATP ( $5 \mu\text{M}$ ) and  $3.08 \pm 0.04$  ( $n = 572$ ) by trypsin ( $100 \text{ nM}$ ). The hippocampal neurons demonstrated an increase of  $4.23 \pm 0.01$  ( $n = 388$ ) with the application of glutamate ( $20 \mu\text{M}$ ) and  $2.51 \pm 0.06$  ( $n = 388$ ) by KCl ( $20 \text{ mM}$ ). Representative traces can be seen in figure 4.11.

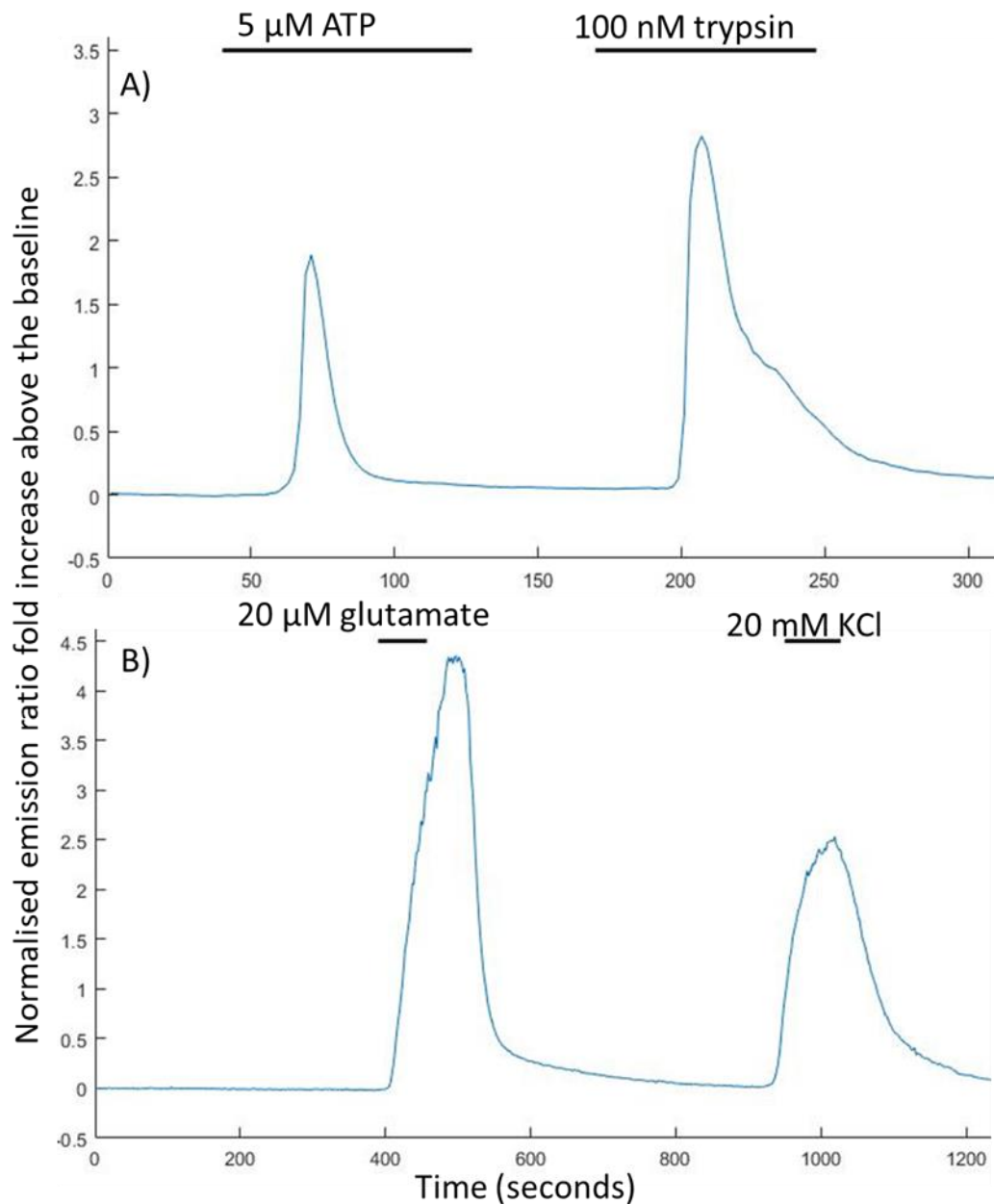
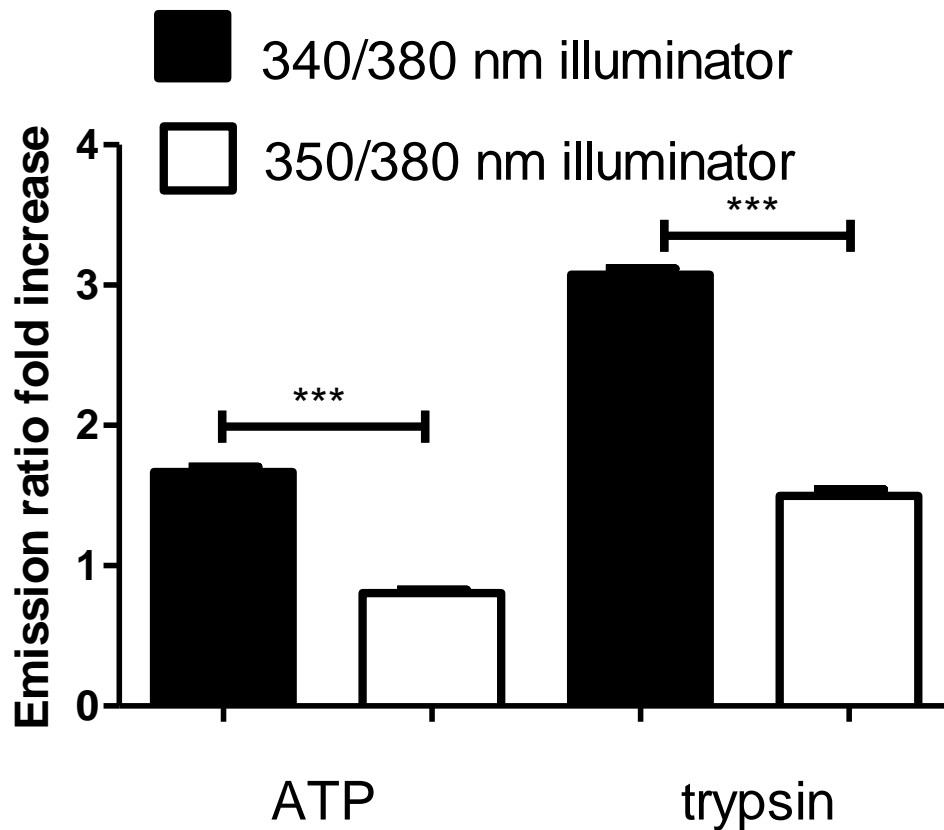


Figure 4.11; A) Representative trace of normalised emission ratio changes in tsA-201 cells with  $\text{Ca}^{2+}$  changes being caused by application of ATP (5  $\mu\text{M}$ ) and trypsin (100 nM) and imaged using the 340/380 nm LED illuminator. B) Representative trace of normalised emission ratio changes in hippocampal neurons with changes being caused by washes of glutamate (20  $\mu\text{M}$ ) and KCl (20 mM) and imaged using the 340/380 nm LED illuminator.

When comparing the responses obtained using both light sources it was found that those recorded using the 340/380 nm LED illuminator were significantly larger than those detected with the 350/380 nm illuminator ( $P < 0.001$ ). The comparison for each specimen can be seen in figures 4.12 and 4.13.



*Figure 4.12; Comparison of the pharmacologically-induced fluorescent fold increases above the baseline in tsA-201 cells obtained when illuminating with either the 340/380 nm illuminator or the 350/380 nm illuminator.*

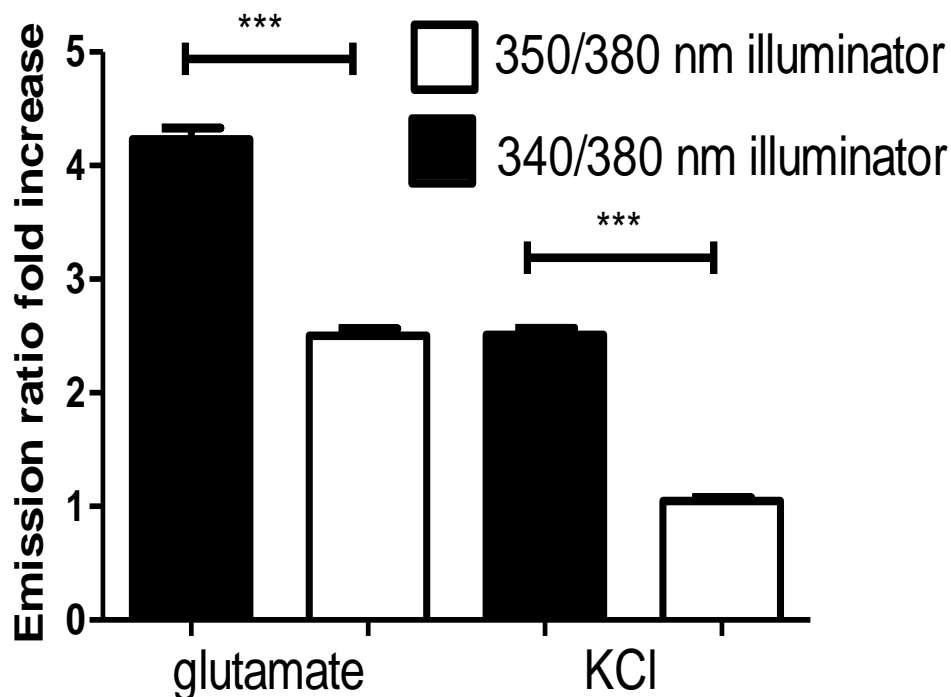


Figure 4.13; Comparison of the pharmacologically-induced fluorescent fold increases above the baseline in hippocampal neurons obtained when illuminating with either the 340/380 nm illuminator or the 350/380 nm illuminator.

Using equation (4.1) each ROI recorded using the 340/380 nm illuminator was converted to a measurement of cytosolic  $\text{Ca}^{2+}$  to allow quantitative data to be extracted. From the measurement of the cytosolic  $\text{Ca}^{2+}$  concentrations, it was found that the ATP (5  $\mu\text{M}$ ) induced cytosolic  $\text{Ca}^{2+}$  increases of  $280.40 \pm 7.80$  nM ( $n = 572$ ,  $P < 0.0001$  compared to baseline of  $81.20 \pm 5.60$  nM, figure 4.14A,) and the trypsin (100 nM) caused a  $581.90 \pm 10.20$  nM ( $n = 572$ ,  $P < 0.0001$  compared to baseline of  $81.60 \pm 5.60$  nM, figure 4.14A) in the tsA-201 cells. In hippocampal neurons, glutamate (20  $\mu\text{M}$ ) induced  $\text{Ca}^{2+}$  increases of  $645.40 \pm 18.20$  nM ( $n = 388$ ,  $P < 0.0001$  compared to baseline of  $92.29 \pm 10.12$  nM, figure 4.14B) with KCl (20 mM) eliciting increases in  $\text{Ca}^{2+}$  of  $357.60 \pm 9.18$  nM ( $n = 388$ ,  $P < 0.0001$  compared to baseline of  $92.29 \pm 10.12$  nM, figure 4.14B).

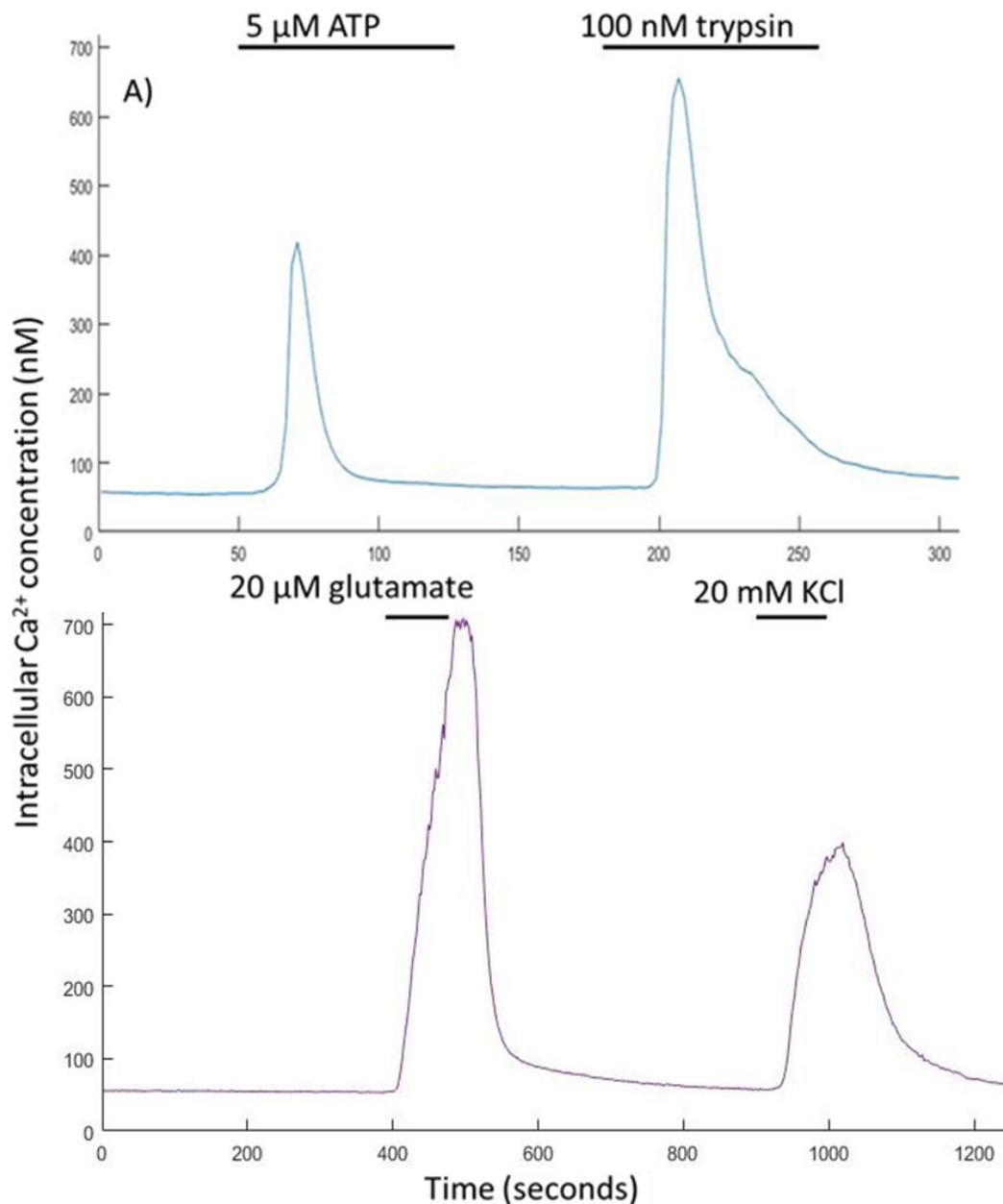


Figure 4.14; A) Representative trace of cytosolic  $\text{Ca}^{2+}$  concentrations in tsA-201 cells with  $\text{Ca}^{2+}$  increases being caused by application of ATP (5  $\mu\text{M}$ ) and trypsin (100 nM) and imaged using the 340/380 nm LED illuminator. B) Representative trace of cytosolic  $\text{Ca}^{2+}$  concentrations in hippocampal neurons with calcium increases being caused by washes of glutamate (20  $\mu\text{M}$ ) and KCl (20 mM) and imaged using the 340/380 nm LED illuminator.

### **4.3.3 Full duration at the half maximum intensity of the Ca<sup>2+</sup> responses obtained in hippocampal neurons when illuminating with either LED system**

After comparing the fluorescence-fold increases of the pharmacologically-induced Ca<sup>2+</sup> responses using each LED illuminator system, it was investigated whether the full duration at the half maximum (FDHM) intensity of the responses in hippocampal neurons were affected by choice of light source.

When using the 340/380 nm LED illuminator it was found that the FDHM of the Ca<sup>2+</sup> responses in the hippocampal neurons (n = 388) were  $165.8 \pm 5.3$  seconds and  $225.2 \pm 5.3$  seconds for the glutamate and KCl applications, respectively. The FDHM responses with 350/380 nm illumination (n = 289) were  $154.3 \pm 5.4$  seconds and  $237.0 \pm 3.4$  seconds for glutamate and KCl, respectively.

It was found when comparing the FDHM of the responses with each light source that there was no significant change when using either light source ( $P > 0.05$ ) (see figure 4.15).

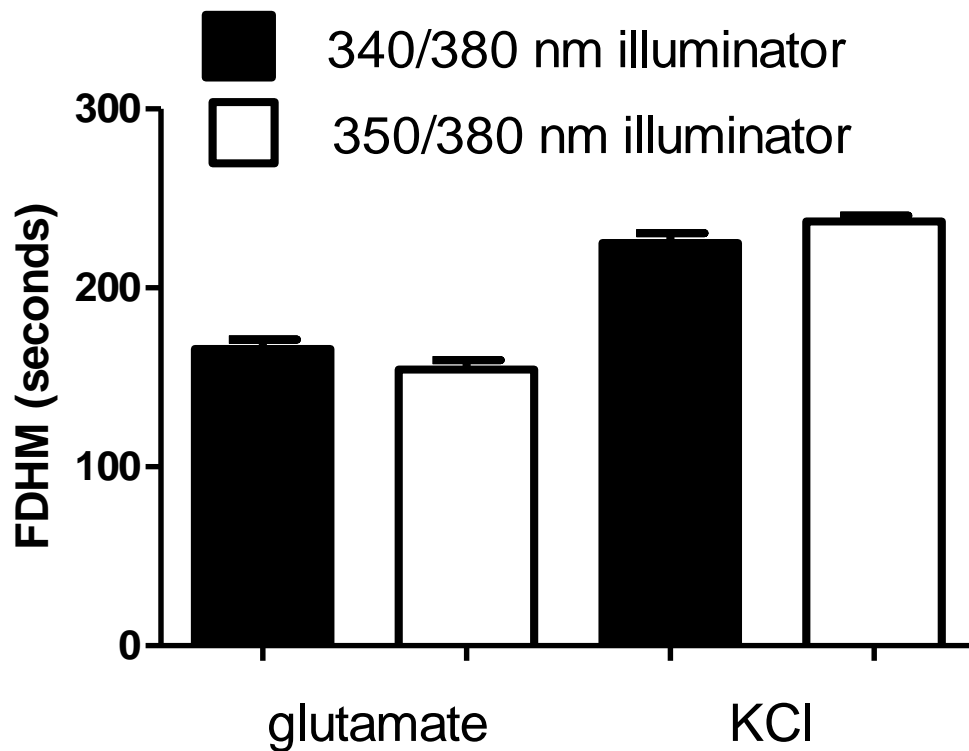


Figure 4.15; FDHM of the  $Ca^{2+}$  responses evoked in hippocampal neurons imaged using either the 350/380 nm and the 340/380 nm LED illuminators.

#### 4.3.4 Fura-2 $Ca^{2+}$ baseline fluctuation measurements

To determine the minimum cytosolic  $Ca^{2+}$  concentration change that could be accurately detected from the baseline levels using the 340/380 nm or the 350/80 nm illuminators, the baseline fluctuations observed in the experiments reported above were analysed. To do this the maximum and minimum emission ratios in the baseline measurements for each ROI were determined and calculated what this corresponded to as a percentage of the associated average baseline.

It was found that when using the 340/380 nm illuminator, an average peak-to-peak fluctuation of  $5.9 \pm 0.2$  % (n = 572) for the tsA-201 cells was measured and  $4.2 \pm 0.2$  % (n = 388) for the hippocampal neurons. A representative plot of the baseline normalised emission ratio in a single neuron can be seen in figure 4.16.

The fluctuations in the 340/380 nm signals equate to a cytosolic  $\text{Ca}^{2+}$  concentration fluctuation of  $4.85 \pm 0.19$  nM in the tsA-201 cells and  $3.88 \pm 0.15$  nM in the hippocampal neurons, calculated using equation (4.1).

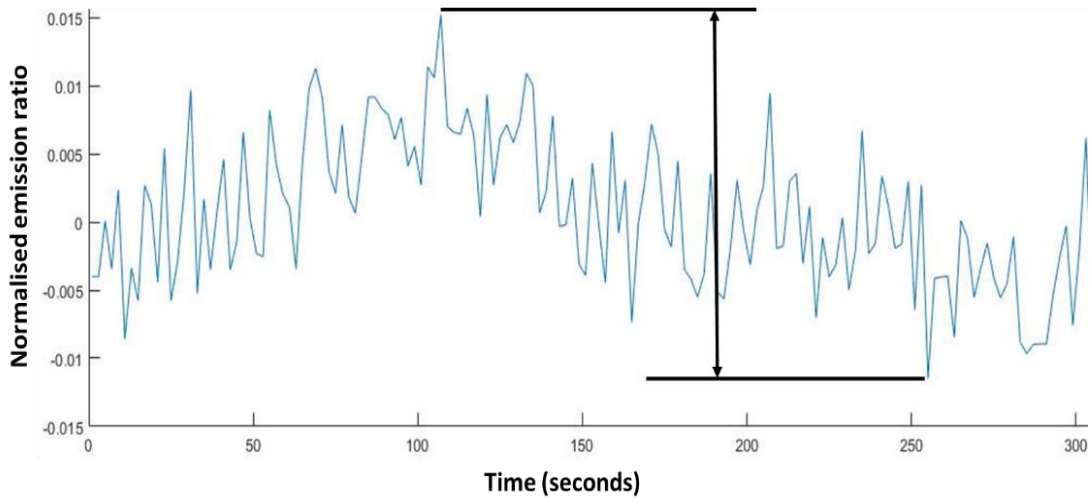


*Figure 4.16; Representative plot of the noise observed in the normalised baselines of the hippocampal neuron whilst carrying out 0.5 Hz ratiometric Fura-2  $\text{Ca}^{2+}$  imaging of the specimens using the 340/380 nm illuminator.*

When the specimens were illuminated using the 350/380 nm LEDs the tsA-201 cells had an average peak-to-peak fluctuation of  $17.9 \pm 0.6$  % ( $n = 411$ ,  $P < 0.0001$  compared to the 340/380 nm tsA-201 fluctuation) and  $12.8 \pm 0.5$  % ( $n = 289$ ,  $P < 0.0001$  compared to the 340/380 nm hippocampal neuron fluctuation). A representative plot of the baseline of a hippocampal neuron can be seen in figure 4.17 and a statistical comparison between the average fluctuations observed each light source can be seen in figure 4.18.

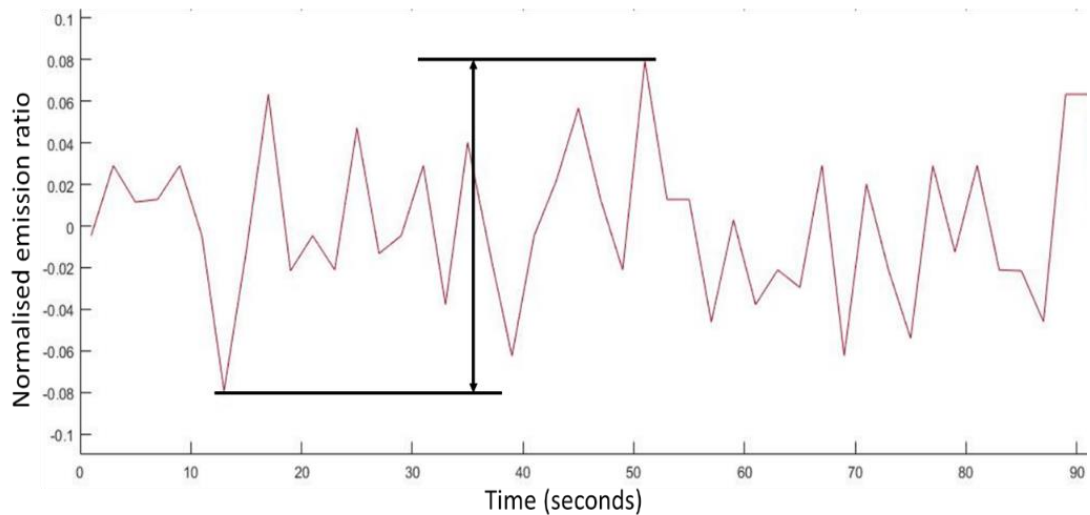


*Figure 4.17; Representative plot of the noise observed in the normalised baselines of the hippocampal neuron whilst carrying out 0.5 Hz ratiometric Fura-2  $Ca^{2+}$  imaging of the specimens using the 350/380 nm illuminator.*

To determine whether cellular auto-fluorescence fluctuations due to UV excitation of mitochondrial NADH were significantly contributing to our fluctuation measurements [301] 0.5 Hz acquisition rate  $Ca^{2+}$  imaging using the 340/380 nm LEDs was carried out on hippocampal neurons and HEK-293 cells not loaded with Fura-2 AM. As the cells were not loaded with Fura-2 AM any fluorescence detected must be due to cellular auto-fluorescence. The results of which can be seen in table 4.2.

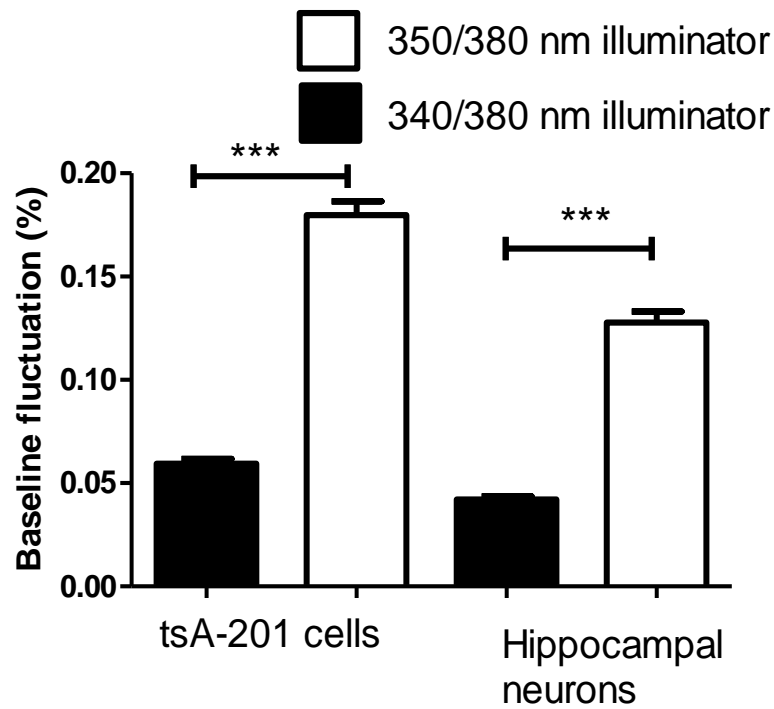
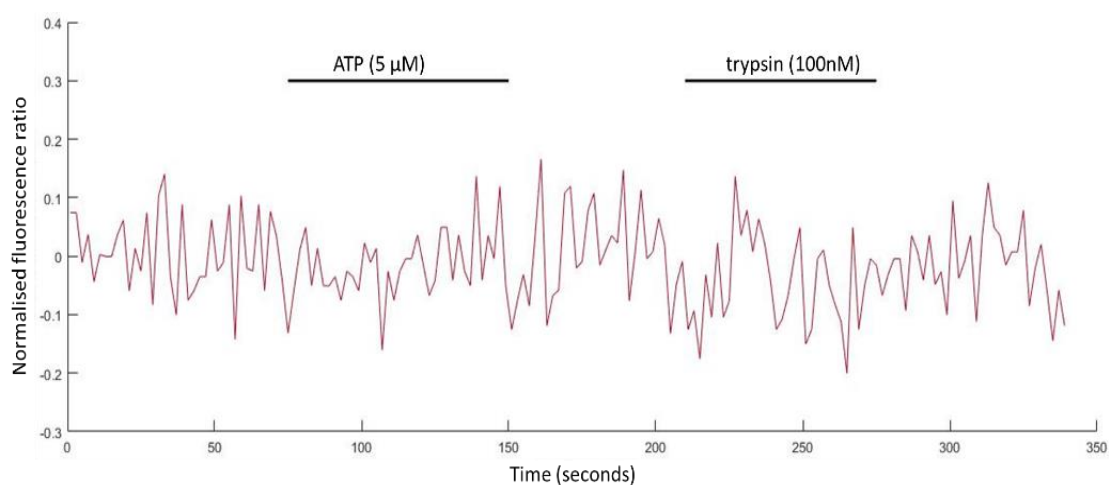


Figure 4.18; A comparison of the average baseline noise obtained in each specimen when illuminated with either the 340/380 nm system or the 350/380 nm system.

Table 4.2; Baseline emission counts for each excitation wavelength obtained in specimens that were either unlabelled or loaded with Fura-2 AM.

	Specimens not loaded with Fura-2 AM		Specimens loaded with Fura-2 AM	
	HEK-293 cells (n = 10)	Hippocampal neurons (n = 9)	tsA-201 cells (n = 27)	Hippocampal neurons (n = 54)
Baseline emission counts from 340 nm excitation	58.9 ± 7.8	81.5 ± 14.3	765.4 ± 39.5	7451 ± 512.2
Baseline emission counts from 380 nm excitation	37.2 ± 3.7	111.5 ± 18.2	894.8 ± 47.7	8237 ± 560.7

An unpaired student t-test applied to the baseline emission counts for each excitation wavelength in cell specimens with and without Fura-2 AM demonstrated that the auto-fluorescence signal was not significant with respect to the fluorescence emission signal in the loaded cells ( $P < 0.0001$ ) which in agreement with previous observations [302]. Also, in agreement with the work of Gryniewicz et. al. [241], it was observed that there was no change in auto-fluorescence signal in response to stimuli, shown in figures 4.19 and 4.20, suggesting that the contribution to the overall fluorescence data from changes in mitochondrial NADH or other intracellular dynamics is negligible and can be discounted from our analysis.



*Figure 4.19; Representative plot of normalised emission ratio obtained when imaging HEK-293 cells not loaded with Fura-2 AM.*

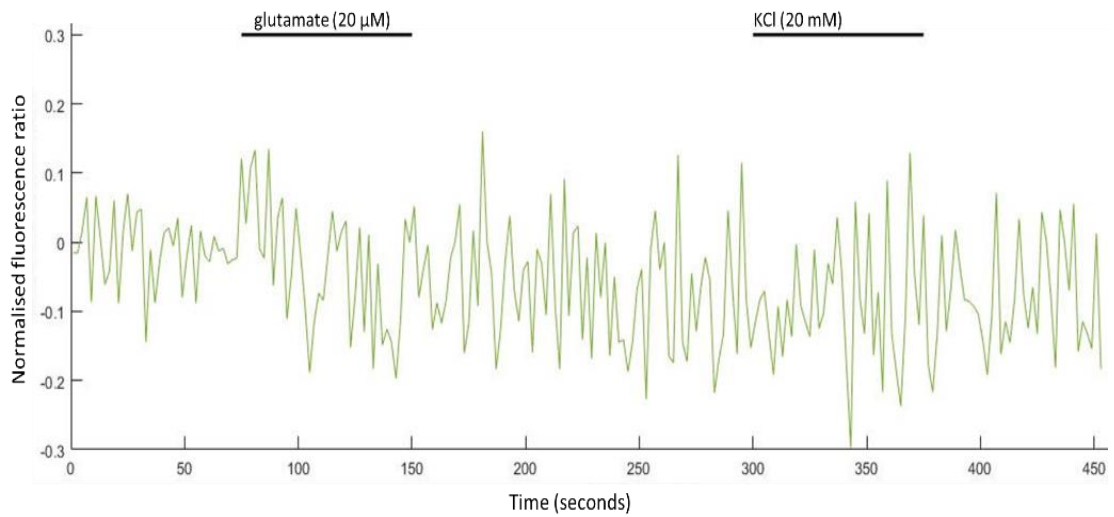


*Figure 4.20; Representative plot of normalised emission ratio obtained when imaging hippocampal neurons not loaded with Fura-2 AM.*

It was also confirmed again that using the 340/380 nm illuminator sub-5 nM precision was obtained using known  $\text{Ca}^{2+}$  concentrations. To do this, a 17 nM free  $\text{Ca}^{2+}$  solution from a Fura-2  $\text{Ca}^{2+}$  imaging calibration kit was diluted (Invitrogen, Paisley, UK) with distilled water to create a series of solutions with free  $\text{Ca}^{2+}$  concentrations that decreased in steps of 2 nM. Through imaging 5  $\mu\text{L}$  of each solution for 60 seconds at a rate of 0.5 Hz and obtaining the average background corrected fluorescence emission ratio it was determined that at concentrations above 5 nM changes in  $\text{Ca}^{2+}$  on the order of 2 nM were identifiable (see figure 4.21).

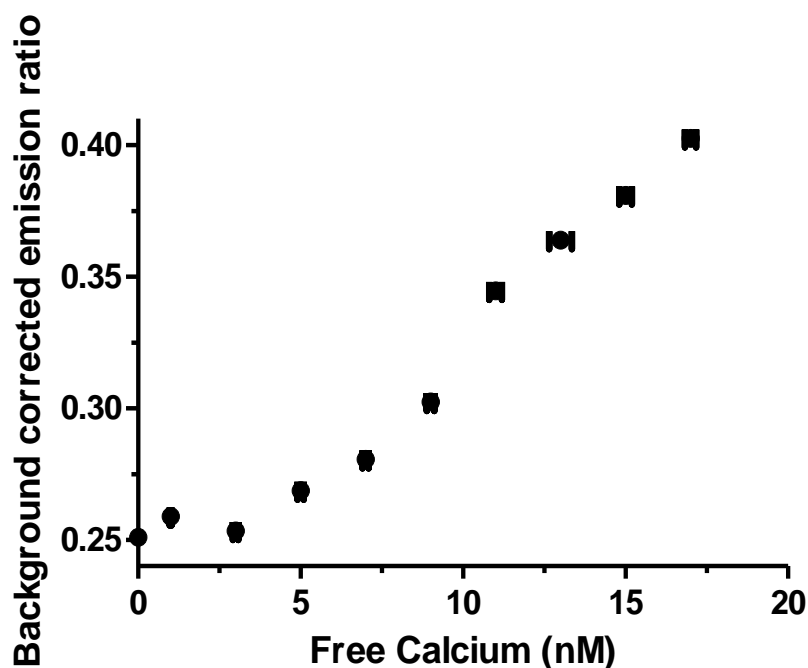
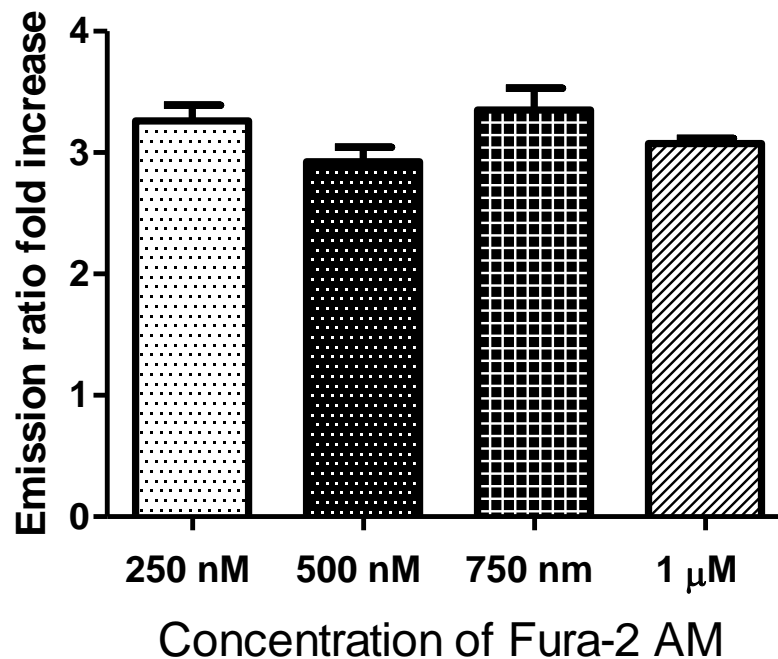


Figure 4.21; Background corrected 340/380 nm emission ratios obtained from imaging solution with different concentrations of free  $\text{Ca}^{2+}$ . The errors observed in the background corrected emission ratios is the SEM over the 60 second imaging period and the errors in the free calcium is the systematic error in the pipettes used.

#### 4.3.5 Imaging trypsin mediated $\text{Ca}^{2+}$ transients in tsA-201 cells using low concentrations of Fura-2 AM

The possibility of using lower concentrations of dye than those typically recommended in Fura-2 AM loading protocols was investigated [240], [303]. To do this the trypsin (100 nM) mediated  $\text{Ca}^{2+}$  transients were imaged in tsA-201 cells loaded with either 750 nM (n = 111), 500 nM (n = 119) or 250 nM (n = 130) Fura-2 AM and compared the average peak normalised fluorescence ratio increase to the value obtained in the initial experiments when using 1  $\mu\text{M}$  of Fura-2 AM (n = 572, figure 4.22). The fluorescent fold increases above the baseline for the 750 nM, 500 nM and 250 nM were  $3.35 \pm 0.18$  (n = 111,  $P > 0.05$  compared to 1  $\mu\text{M}$  Fura-2 AM)  $2.93 \pm 0.12$  (n =

119,  $P > 0.05$  compared to 1  $\mu\text{M}$  Fura-2 AM) and  $3.26 \pm 0.13$  ( $n = 130$ ,  $P > 0.05$  compared to 1  $\mu\text{M}$  Fura-2 AM) respectively.



*Figure 4.22; Comparison of 340/380 nm emission ratios obtained from cytosolic  $\text{Ca}^{2+}$  increase when tsA-201 cells loaded with different concentrations of Fura-2 AM were perfused with trypsin (100 nM).*

This experiment was repeated using the 350/380 nm LED illumination system loading the tsA-201 cells with either 500 nM ( $n = 120$ ) or 250 nM ( $n = 100$ ) of Fura-2 AM. For the tsA-201 cells loaded with 500 nM of Fura-2 AM an average fluorescence fold increase above the baseline of  $1.52 \pm 0.04$  ( $n = 120$ ,  $P > 0.05$  compared to 1  $\mu\text{M}$  Fura-2 AM) was recorded and for the cells loaded with 250 nM Fura-2 AM a response of  $1.28 \pm 0.06$  ( $n = 100$ ,  $P < 0.05$  compared to 1  $\mu\text{M}$  Fura-2 AM) (see figure 4.23).

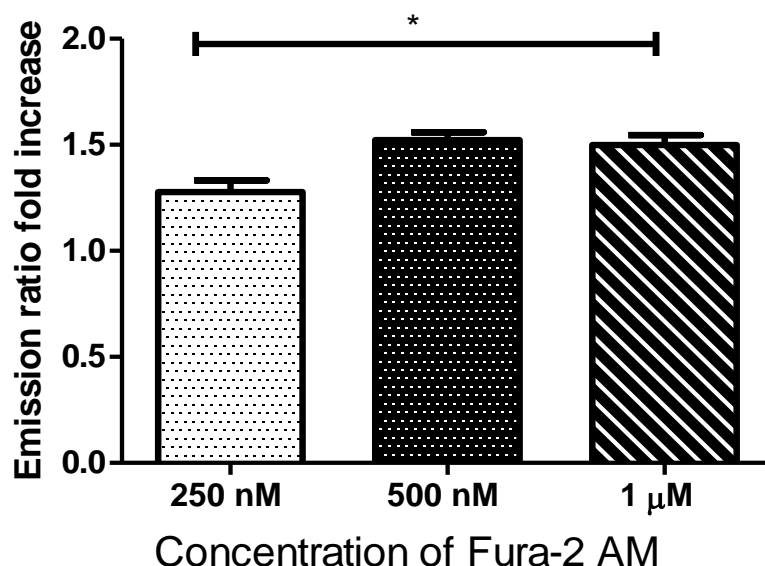


Figure 4.23; Comparison of 350/380 nm emission ratios obtained from cytosolic  $\text{Ca}^{2+}$  increase when tsA-201 cells loaded with different concentrations of Fura-2 AM were perfused with trypsin (100 nM).

#### 4.3.6 Fura-2 video-rate ratiometric $\text{Ca}^{2+}$ imaging of synaptically-driven $\text{Ca}^{2+}$ transients in hippocampal neurons using the 340/380 nm illuminator

It has been shown previously using widefield two photon microscopy at imaging speeds between 10 and 100 Hz that synaptically-driven  $\text{Ca}^{2+}$  events could be detected in hippocampal neurons loaded with Fluo-4 AM [266]. Here the 340/380nm LEDs were utilised to image at 0.5 Hz and 24.39 Hz acquisition rates synaptically driven  $\text{Ca}^{2+}$  events in hippocampal neurons, induced by the application of  $\text{Mg}^{2+}$ -free HBS. At 0.5 Hz, a clear increase in intracellular  $\text{Ca}^{2+}$  levels were observed when  $\text{Mg}^{2+}$ -free HBS was applied but individual events were difficult to decipher (figure 4.24A). However, at an image acquisition rate of 24.39 Hz, the fastest rate possible with the camera used in this study, individual increases in intracellular  $\text{Ca}^{2+}$  levels were observed that are similar to action potential firing seen when using patch clamping [266], with some

synchronicity in firing between different neurons also being observed (figure 4.24B). Indeed, a peak-to-peak measurement of the baseline fluctuations at 24.39 Hz found an average fluctuation of  $7.10 \pm 0.04 \%$  ( $n = 21$ ) which equates to a fluctuation in the average resting  $\text{Ca}^{2+}$  ( $104.50 \pm 4.10 \text{ nM}$ ) of  $7.42 \pm 0.04 \text{ nM}$  ( $n = 21$ ). The imaging at 0.5 Hz had an average baseline fluctuation of  $5.22 \pm 0.06 \%$  ( $n = 39$ ) which is a fluctuation in the basal  $\text{Ca}^{2+}$  ( $87.90 \pm 5.30 \text{ nM}$ ) of  $4.59 \pm 0.05 \text{ nM}$ .

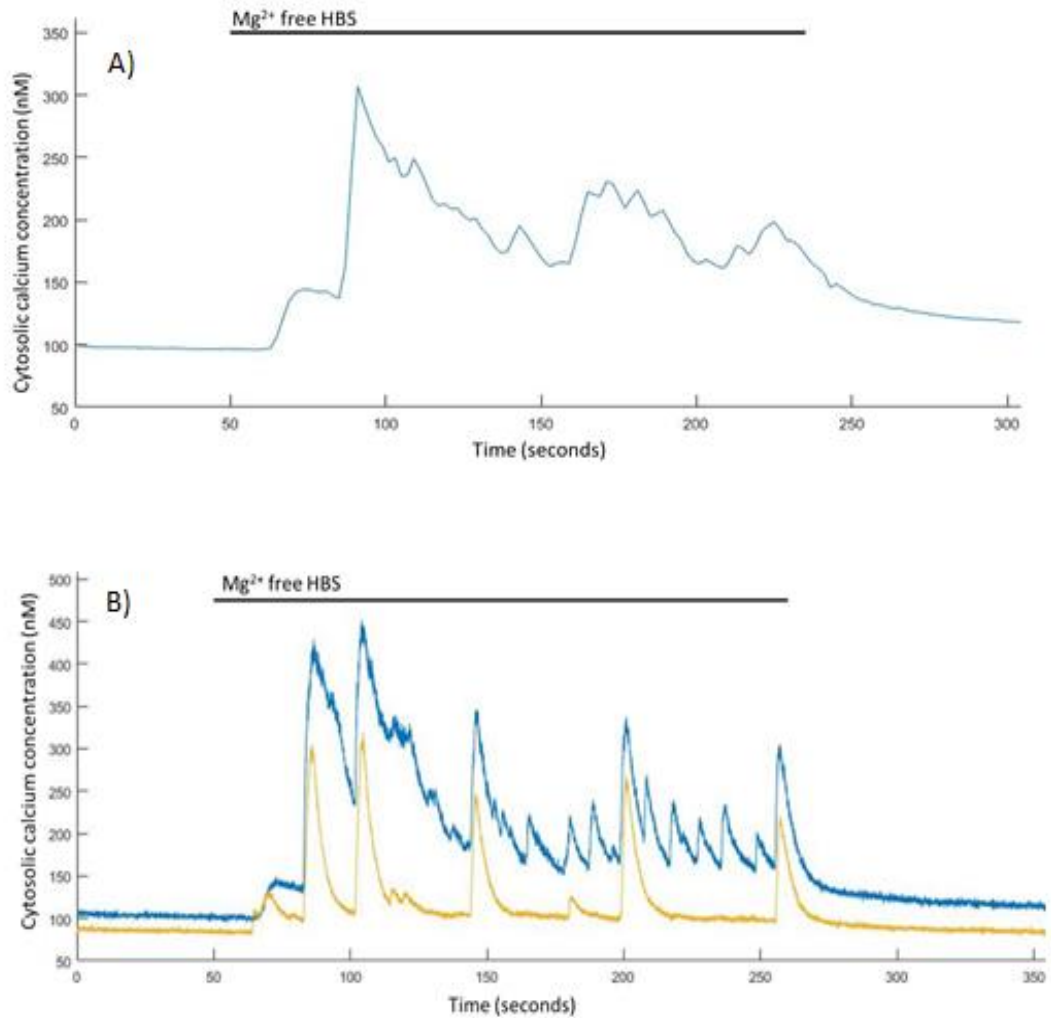


Figure 4.24; Spontaneous  $\text{Ca}^{2+}$  events are induced in  $\text{Mg}^{2+}$ -free HBS. A) representative trace from a single hippocampal neuron of  $\text{Mg}^{2+}$ -free induced  $\text{Ca}^{2+}$  events imaged at 0.5 Hz and B) representative trace from two hippocampal neurons of  $\text{Mg}^{2+}$ -free induced  $\text{Ca}^{2+}$  events imaged at 24.39 Hz.

## 4.4) Discussion

In this work the first experiments began with testing our perfusion system and confirming that  $\text{Ca}^{2+}$  responses were observed in our specimens with the application of different pharmacological stimuli. To do this the decision was made to make use a simpler optical setup and hence the single wavelength  $\text{Ca}^{2+}$  indicator Fluo-4 was used and it was found that it was possible to record induced  $\text{Ca}^{2+}$  responses in the tsA-201 cells. This work aided in becoming familiar with the experimental process and provided insight into what was required when writing the MATLAB script for our  $\text{Ca}^{2+}$  analysis which was adapted to be used for the Fura-2 AM  $\text{Ca}^{2+}$  experiments.

The work then progressed to image induced  $\text{Ca}^{2+}$  responses in tsA-201 cells and hippocampal neurons loaded with Fura-2 AM illuminated with a commercial 350/380 nm LED illuminator that was being used by other researchers in the university to carry out pharmacological studies. One of the observations that was made from the characterisation of the LED system was that whilst being advertised as a 350/380 nm system the measured peak wavelengths were actually  $360 \pm 1.50$  nm and  $386 \pm 1.50$  nm. This means that this system would not detect any increase in cytosolic  $\text{Ca}^{2+}$ , rather it will be exciting at the isosbestic point and only decreases in the non-bound  $\text{Ca}^{2+}$  state of Fura-2 can be detected through the 386 nm excitation. Even with this observation though it was possible to image the pharmacologically induced  $\text{Ca}^{2+}$  in both specimens as expected.

Using the new 340/380 nm LED illuminator, it was confirmed that it was also possible to be used to image induced  $\text{Ca}^{2+}$  responses in the specimens. When the responses from each light source were compared it was found that the responses recorded using the 340/380 nm LEDs were significantly higher than those with the 350/380 nm system ( $P < 0.0001$ ). This result is attributed to the 340/380 nm LEDs more accurately matching the Fura-2 excitation wavelengths of bound and free  $\text{Ca}^{2+}$  states. This accurate matching leads to more efficient excitation of the dye and a higher signal-to-noise. It also results in an emission change occurring with  $\text{Ca}^{2+}$  increases during 340 nm excitation rather than remaining static at the isosbestic point. The ability to

accurately recreate the optical powers at the specimen plane using the 340/380 nm illuminator allowed us to calibrate our emission ratios into quantitative cytosolic  $\text{Ca}^{2+}$  concentrations. The fluorescence fold increases and cytosolic  $\text{Ca}^{2+}$  changes measured in the live cell specimens using the 340/380 nm LED are also in agreement with previous studies and personal observations in hippocampal neurons, tsA-201 cells and HEK-293 cells illuminated using an arc lamp system [282], [288], [304]–[306].

Another parameter of interest to investigate was the FDHM of the  $\text{Ca}^{2+}$  responses observed when using either light sources. It was found when the FDHM of the  $\text{Ca}^{2+}$  responses in the hippocampal neurons were analysed that there was no statistically significant change in the times observed with either light source. This means that users of the 350/380 nm illuminator will still record accurately the duration of responses though the amplitude will be significantly smaller than those when using the 340/380 nm LEDs which could be an issue when high noise levels are present.

Through analysis of the baseline  $\text{Ca}^{2+}$  peak-to-peak noise in the tsA-201 cells and the hippocampal neurons illuminated with each light source it was found that the 340/380 nm LEDs demonstrated a significantly lower baseline noise than what was recorded using the 350/380 nm illuminator ( $P < 0.0001$ , figure 4.18). As it was not possible to calibrate the 350/380 nm emission ratios to cytosolic  $\text{Ca}^{2+}$  a definitive measurement on the precision of these measurements is not obtainable, though with the assumption that the baseline  $\text{Ca}^{2+}$  levels remained approximately equal between light sources then there were fluctuations of  $14.70 \pm 0.60$  nM in the tsA-201 cells and  $11.80 \pm 0.60$  nM in the hippocampal neurons. The theoretical precision of Fura-2 to changes in cytosolic  $\text{Ca}^{2+}$  is between 5 – 10 nM [307] and as the responses obtained using the 340/380 nm illuminator are below the theoretical precision of Fura-2 leads our recordings only to be limited by the response of the dye.

In addition to the dye limited  $\text{Ca}^{2+}$  responses, it has been shown that using the 340/380 nm illumination system it is possible to load our cells with lower concentrations of Fura-2 AM than recommended in loading protocols. Statistical analysis of the emission ratios obtained using the concentrations of Fura-2 AM down to 250 nM showed no statistically significant difference between them. When repeating this experiment using the 350/380 nm illuminator concentrations of Fura-2

AM down to 500 nM were only possible. Below this value the evoked  $\text{Ca}^{2+}$  responses were statistically different from those when the cells were loaded with 1  $\mu\text{M}$  of Fura-2 AM ( $P < 0.05$ ). The utility of lower dye concentrations is not only an economical advantage by allowing more uses from a vial but also may increase the viability of cells by reducing the concentrations of formaldehyde and acetic acid created through the hydrolysis of AM-ester [308].

A recent study has demonstrated that Fura-2 (as well as several other frequently used fluorescent  $\text{Ca}^{2+}$  indicators) loaded in five separate cell types at different concentration (1 - 8  $\mu\text{M}$ ) reduced cellular viability and suppressed both Na,K-ATPase and spontaneous  $\text{Ca}^{2+}$  activity [309]. In this recent paper it was found that these effects only occurred at a statistically significant level at higher concentrations of the dye and not at the typical loading concentration of 1  $\mu\text{M}$  [309], [310]. As such, the ability to use lower concentrations of dye (down to 250 nM) could alleviate most if not all the negative effects caused by the presence of the indicator.

Finally, this work has demonstrated the functionality of the new 340/380 nm illuminator system by utilising the intrinsic LED advantages of rapid wavelength switching and amplitude stability to image synaptically-driven  $\text{Ca}^{2+}$  events in hippocampal neurons at a video-rate of 24.39 Hz. When the  $\text{Ca}^{2+}$  traces recorded imaging at video-rate were compared to those recorded when imaging at 0.5 Hz (figure 4.24A). It can be seen from this comparison that due to the slow image capture rate of 0.5 Hz, many of the rapid synaptically driven  $\text{Ca}^{2+}$  events cannot be imaged. The appearance of these events in the presence of  $\text{Mg}^{2+}$  free HBS is due to the relief of the voltage-dependent blockade of NMDA receptors by  $\text{Mg}^{2+}$  [299], [300]. This is a well-established phenomenon that is used extensively both in academia and in the pharmaceutical industry to induce synaptically driven  $\text{Ca}^{2+}$  events and epileptiform-like activity [311], [312], but the clear discrimination between individual events has not previously been possible due to the limitations of arc lamp systems. It is also apparent that some synchronicity between larger  $\text{Ca}^{2+}$  events exists as has been reported previously for neuronal networks under  $\text{Mg}^{2+}$  free conditions [312], [313]. The increase in baseline fluctuation observed in these measurements compared to the slower imaging rates can be attributed to a decrease in the signal-to-noise ratio due to the lower exposure times used which reduces the number of photons collected for each

image though this increased fluctuation is not significantly different from that obtained at 0.5 Hz imaging rates ( $P > 0.05$ ). The ability to observe these spontaneous changes in  $\text{Ca}^{2+}$  using widefield microscopy allows for improved temporal resolution of imaging synaptically-driven neuronal  $\text{Ca}^{2+}$  events whilst maintaining the high spatial resolution afforded by  $\text{Ca}^{2+}$  imaging leading to a higher throughput of more informative measurements than currently offered with existing  $\text{Ca}^{2+}$  imaging methods [231].

## **4.5) Conclusions**

This work has demonstrated the application of a truly 340/380 nm LED illuminator for ratiometric  $\text{Ca}^{2+}$  imaging of live cells loaded with Fura-2 AM. The application of this new illuminator has also been compared to a commercial 350/380 nm LED illuminator currently being used in research. By matching the wavelengths of the illuminator to the optimum excitation wavelengths of the free and  $\text{Ca}^{2+}$  bound states of Fura-2 more efficient excitation of the dye is achieved which leads to higher signal-to-noise and dye limited accuracy in detecting changes in cytosolic  $\text{Ca}^{2+}$ . This work has also demonstrated the ability to image  $\text{Ca}^{2+}$  transients with cells loaded with lower concentrations of Fura-2 AM than is recommended in loading protocols and even lower than that which is possible using the 350/380 nm illuminator. By combining the intrinsic benefits of the high stability measurements with the rapid wavelength switching available to the 340/380 nm LEDs allowed the imaging synaptically-driven  $\text{Ca}^{2+}$  events in hippocampal neuron. The benefits demonstrated by this illuminator represent a significant improvement over existing LED-based illuminators and frees Fura-2 ratiometric imaging from the problems of arc lamps.

# Chapter Five:

## Conclusions

### 5.1) Summary

**T**he contents of this thesis have presented the body of work carried out over the duration of my PhD in developing and advancing the standing wave microscopy technique and applying it to image multiple biological specimens. It also shows the development and testing of a new 340/380 nm LED illuminator for ratiometric  $\text{Ca}^{2+}$  imaging and comparing the performance to a current commercial light source.

The work contained in Chapter 2 is the application and reconstruction of video-rate widefield axial super resolution standing wave imaging of the red blood cell membrane using a LED illuminator. It was shown that by imaging a fluorescent lens specimen upon a mirror and using the radius of curvature of the lens the average experimental antinodal FWHM and distance between planes could be determined for the 550 nm and 525 nm LEDs used for illumination. This was done in air and with a layer of 4% BSA and PBS between the lens and the mirror to demonstrate the refractive index dependence of the standing wave structure and to obtain the axial resolution for the following red blood cell experiments. It was determined as well that the experimental values obtained were not statistically different from the theoretical values which was useful to determine as this was the first experiments in which a laser source was not used for illumination. The Chapter then applied this technique to DiI labelled red blood cell specimens imaged continuously with an exposure time of 33 ms for a duration of 33 seconds providing 1000 frame movies. This allowed dynamic red blood cell membrane fluctuations to be observed in real time which was not something that could be carried out when using confocal microscopy as was done in the prior work by Amor

et. al. Using a script developed by my colleague, Ross Scrimgeour, it was possible to take the video rate standing wave movies and generate 2D and 3D reconstructions of the red blood cell membrane which could allow quantitative analysis to be carried out and also eases visualisation of the specimen. It was found when the standing wave imaging red blood cell emission intensities were compared to the same experiment carried out in widefield that there were no greater rates of photobleaching between the two and when imaging was carried out over longer time periods that both techniques caused the red blood cell to decay at the same rate. This shows that there are no observable increase in the detrimental effects caused to the specimens by carrying out standing wave imaging and with the simple addition of the mirror any widefield microscope can be made capable of axial super-resolution.

In Chapter 3 two multi-wavelength standing wave imaging modalities (TartanSW excitation and emission) were investigated and applied to live cell specimens. This work also demonstrated the first application of standing wave microscopy to investigate the membrane of whole adherent mammalian cells.

The motivation of using multi-excitation standing wave imaging was to reduce the nodal contributions of the standing wave structure in the image by using three different excitation wavelengths to generate antinodal planes at different heights above the mirror. It was found that information gap was reduced from 44.3 % to only 12.0 % of the image by imaging fluorescent lens specimens which was found to be accurate when compared to the theoretical models. The technique was then applied to red blood cells and MCF-7 cells where it was found that the technique was less effective on red blood cells as the cell membrane gradient was too steep to obtain much spectral separation between the planes. This, however, was not the case when imaging the MCF-7 cells where not only was the spectral separation between the channels observed but it was possible to also detect internal membrane vacuoles.

Using the TartanSW excitation images it was also found that by taking the difference between the separate excitation channels using the ImageJ image calculator that the resolution of the resulting images was improved by a factor of approximately 2. This was achieved as the difference between the channels reduced the widths of the antinodal planes allowing resolutions on the order of 50 nm to be obtained when

imaging fluorescent lens specimens. This was first compared to theoretical models by using the lens specimen images and then was applied to the MCF-7 images so as to improve the resolution. This simple ImageJ post acquisition process allows the widefield standing wave technique to obtain axial and temporal resolutions in live cell specimens that surpasses those currently possible with other widefield super-resolution techniques. It was also found that the difference technique greatly improved the contrast of the MCF-7 cell images which would allow for 3D reconstruction of the specimens to be carried out in the future.

Chapter 3 has also demonstrated the application of multi-emission standing wave microscopy on fluorescent lenses, red blood cells and MCF-7 cells using both widefield and confocal microscopy. The intensity moiré pattern obtained due to the interference between the excitation and emission standing wave could be used to provide an exact axial height for the individual planes rather than relying on prior knowledge of the specimen structure to infer where an antinodal plane is in relation to another. It was found when comparing the theoretical multi-emission standing wave structure to that obtained using widefield multi-emission standing wave microscopy that there was a discrepancy between the two that was not present when comparing the confocal data. Further work is required to investigate the presence of this discrepancy though multi-emission can still be used qualitatively to infer the directionality of a specimen structure.

The final experimental Chapter describes the work carried out in developing a new 340/380 nm LED illuminator for ratiometric Fura-2  $\text{Ca}^{2+}$  imaging and comparing its performance to a commercial 360/380 nm LED system. It was discovered through the imaging of pharmacologically induced  $\text{Ca}^{2+}$  events in hippocampal neurons and tsA-201 cells that though both light sources were capable of detecting the events with no change in the FWHM, the 340/380 nm light source gave significantly higher responses than the commercial source with the additional benefit that it was possible to convert the responses from the new light source into actual cytosolic  $\text{Ca}^{2+}$  concentrations. It was also investigated whether loading the cells with dye concentrations less than the recommended levels affected the obtained  $\text{Ca}^{2+}$  response and it was found that it was indeed possible to reduce the dye concentration down to 25 % of the recommended without observing any change in response with the 340/380 nm illuminator however

with the commercial light source the dye could only be reduced to 50 % of recommended.

The fluctuations present in the resting  $\text{Ca}^{2+}$  levels of the cells were also investigated and found that when using the 340/380 nm illuminator precisions in  $\text{Ca}^{2+}$  below 5 nM were obtained which was not possible using the commercial source. As Fura-2 has a detection precision to  $\text{Ca}^{2+}$  changes that is between 5 and 10 nM these results show that by simply using the new light source experiments can be carried out which are only limited by the dye response. The final experiments made use of the fast wavelength switching properties of the 340/380 nm illuminator in order to image the  $\text{Ca}^{2+}$  changes caused by spontaneous firing in hippocampal neurons at a video rate allowing for individual responses to be resolved. This allows for highly accurate and fast  $\text{Ca}^{2+}$  imaging to be carried out in future which would not have been possible using previous light sources.

## **5.2) Future Work**

The standing wave microscopy techniques demonstrated here could have applications for a wide variety of cell types imaging many different processes due to the axial and temporal resolutions available. One of the most attractive benefits of standing wave microscopy is the simplicity in the technique which allows regular microscope users to carry out axial super resolution imaging by simply replacing their usual imaging substrate with a readily affordable mirror.

The TartanSW modalities allows for more data about the specimen structure to be obtained but requires either a specialist light source or an emission splitter to be added. It is worth of note though that with the rising availability of modular LED systems and emission splitters this is no longer as much of a barrier to entry as it may first seem.

The TartanSW excitation modality in particular could be of interest to many due to the more complete map of the specimen being obtained and the difference method between channels allowing for imaging with an axial resolution on the order of 50 nm.

Resolutions of this order typically require costly equipment or the expertise to home build systems which is not always available to those carrying out biomedical imaging.

Current work within the group between myself and others is the application of these techniques to SH-SY5Y cells which are neuronal in structure meaning that it could find application in imaging the growth of neuronal cells. To date, fixed cells are being used with rhodamine phalloidin to stain the actin filaments to carry out TartanSW imaging of the internal cytoskeleton structure. There are live cell dyes available to stain the actin filaments, so this work could be carried forward to obtain standing wave images of neuronal growth cones as the cells propagate and form neuronal networks.

The standing wave technique could also be used for membrane potential imaging in excitable cells. Membrane potential probes typically have emission intensities that change in response to either the depolarisation or hyperpolarisation of the cell membrane. It is possible that as standing wave imaging with high temporal resolution is available that the membrane potential within different anti-nodal planes could be obtained in response to stimuli and plotted to investigate the local membrane potential at axially separate points of the cell.

Other areas in which standing wave microscopy could be applied are cell mitosis, migration or blebbing. These are all dynamic cellular processes which are of interest in many different fields of research and standing wave microscopy could aid in understanding the structure of the cell in real time. The computational reconstruction side of standing wave microscopy complementing these studies as the 3D visualisation of the cellular dynamics eases visualisation and understanding. With the wealth of possibilities in applications and studies it is apparent that standing wave microscopy could have a major role to play in biomedical investigations.

Finally, through the work that was carried out for this thesis on the 340/380 nm LED illuminator has led the industrial sponsor to commercialise the technology and packaging in into a product named the pE-340<sup>FURA</sup>. The ability to now rapidly excite the peak excitation wavelengths of Fura-2 with detection precisions not possible before will hopefully be a boon to those in the field and should free Fura-2 Ca<sup>2+</sup> imaging from the light source compromises that were had to be made in the past.

# References

- [1] S. W. Hell, “Far-field optical nanoscopy.,” *Science (80-. )*, vol. 316, no. 5828, pp. 1153–1158, 2007.
- [2] S. E. Kirk, J. N. Skepper, and A. M. Donald, “Application of environmental scanning electron microscopy to determine biological surface structure,” *Journal of Microscopy*, vol. 233, no. 2. Blackwell Publishing Ltd, pp. 205–224, Feb-2009.
- [3] A. C. Zonneville, R. F. C. Van Tol, N. Liv, A. C. Narvaez, A. P. J. Effting, P. Kruit, and J. P. Hoogenboom, “Integration of a high-NA light microscope in a scanning electron microscope,” *J. Microsc.*, vol. 252, no. 1, pp. 58–70, 2013.
- [4] N. Liv, A. C. Zonneville, A. C. Narvaez, A. P. J. Effting, P. W. Voorneveld, M. S. Lucas, J. C. Hardwick, R. A. Wepf, P. Kruit, and J. P. Hoogenboom, “Simultaneous Correlative Scanning Electron and High-NA Fluorescence Microscopy,” *PLoS One*, vol. 8, no. 2, p. 55707, 2013.
- [5] L. Gross, F. Mohn, N. Moll, G. Meyer, R. Ebel, W. M. Abdel-Mageed, and M. Jaspars, “Organic structure determination using atomic-resolution scanning probe microscopy.,” *Nat. Chem.*, vol. 2, no. 10, pp. 821–825, Oct. 2010.
- [6] R. Erni, M. D. Rossell, C. Kisielowski, and U. Dahmen, “Atomic-resolution imaging with a sub-50-pm electron probe,” *Phys. Rev. Lett.*, vol. 102, no. 9, p. 096101, Mar. 2009.
- [7] J. Selinummi, P. Ruusuvuori, I. Podolsky, A. Ozinsky, E. Gold, O. Yli-Harja, A. Aderem, and I. Shmulevich, “Bright field microscopy as an alternative to whole cell fluorescence in automated analysis of macrophage images,” *PLoS One*, vol. 4, no. 10, 2009.
- [8] E. H. Keller and R. D. Goldman, “Light Microscopy,” in *Basic Methods in Microscopy Protocols and Concepts from Cells: A Laboratory Manual*, Cold Spring Harbor protocols, 2006, pp. 1–16.
- [9] D. J. Stephens and V. J. Allan, “Light microscopy techniques for live cell

- imaging,” *Science*, vol. 300, no. 5616. pp. 82–86, 2003.
- [10] R. Cole, “Live-cell imaging: The cell’s perspective,” *Cell Adhesion and Migration*, vol. 8, no. 5. pp. 452–459, 2014.
- [11] D. B. Murphy, “Phase contrast microscopy and dark-field microscopy,” in *Fundamentals of Light Microscopy and Electronic Imaging*, Shock, 2002, pp. 97–116.
- [12] E. H. Keller and S. Watkins, “Contrast enhancement in light microscopy.,” *Curr. Protoc. Cytom.*, vol. Chapter 2, p. Unit2.1, 1997.
- [13] G. A. Jamjoomt, “Dark-Field Microscopy for Detection of Malaria in Unstained Blood Films,” *J. Clin. Microbiol.*, vol. 17, no. 5, pp. 717–721, 1983.
- [14] M. Shribak, “Chapter 2 – Differential Interference Contrast Microscopy (DIC),” in *Biomedical Optical Phase Microscopy and Nanoscopy*, 2013, pp. 19–42.
- [15] D. B. Murphy, “Differential interference contrast (DIC) microscopy and modulation contrast microscopy,” in *Fundamentals of Light Microscopy and Electronic Imaging*, 2002, pp. 153–168.
- [16] C. Burch, “Phase Contrast Microscopy,” *J. Sci. Instrum.*, vol. 71, pp. 3–18, 1941.
- [17] S. A. Johnson, “Chapter 1 – Phase Contrast Microscopy,” in *Biomedical Optical Phase Microscopy and Nanoscopy*, 2013, pp. 3–18.
- [18] G. G. Stokes, “On the change of refrangibility of light,” *Philos. Trans. R. Soc. London*, vol. 142, pp. 463–562, 1852.
- [19] B. Valeur and M. N. Berberan-Santos, “A brief history of fluorescence and phosphorescence before the emergence of quantum theory,” *Journal of Chemical Education*, vol. 88, no. 6. pp. 731–738, Jun-2011.
- [20] M. Hesse, A. Raulf, G.-A. Pilz, C. Haberlandt, A. M. Klein, R. Jabs, H. Zaehres, C. J. Fügemann, K. Zimmermann, J. Trebicka, A. Welz, A. Pfeifer,

- W. Röhl, M. I. Kotlikoff, C. Steinhäuser, M. Götz, H. R. Schöler, and B. K. Fleischmann, “Direct visualization of cell division using high-resolution imaging of M-phase of the cell cycle,” *Nat. Commun.*, vol. 3, p. 1076, 2012.
- [21] E. Loiseau, J. A. M. Schneider, F. C. Keber, C. Pelzl, G. Massiera, G. Salbreux, and A. R. Bausch, “Shape remodeling and blebbing of active cytoskeletal vesicles,” *Sci. Adv.*, vol. 2, no. 4, 2016.
- [22] D. S. Peterka, H. Takahashi, and R. Yuste, “Imaging Voltage in Neurons,” *Neuron*, vol. 69, no. 1. pp. 9–21, 2011.
- [23] C. Grienberger and A. Konnerth, “Imaging Calcium in Neurons,” *Neuron*, vol. 73, no. 5, pp. 862–885, 2012.
- [24] M. J. Berridge, P. Lipp, and M. D. Bootman, “The Versatility and Universality of Calcium Signalling,” *Nat. Rev. Mol. Cell Biol.*, vol. 1, pp. 11–21, 2000.
- [25] M. D. Bootman, K. Rietdorf, T. Collins, S. Walker, and M. Sanderson, “Ca<sup>2+</sup>-sensitive fluorescent dyes and intracellular Ca<sup>2+</sup> imaging,” *Cold Spring Harb. Protoc.*, vol. doi:10.110, 2013.
- [26] V. Bernard, *Molecular Fluorescence: Principles and Applications*, vol. 41, no. 16. Wiley-VCH Verlag GmbH, 2001.
- [27] J. R. Lakowicz, “Fluorophores,” in *Principles of Fluorescence Spectroscopy*, Boston, MA: Springer US, 2006, pp. 63–95.
- [28] J. W. Lichtman and Conchello J., “Fluorescence microscopy,” *Nat. Methods*, vol. 2, no. 12, pp. 910–919, 2005.
- [29] T. Bernas, J. P. Robinson, E. K. Asem, and B. Rajwa, “Loss of image quality in photobleaching during microscopic imaging of fluorescent probes bound to chromatin,” *J. Biomed. Opt.*, vol. 10, no. 6, p. 064015, 2015.
- [30] L. Song, E. J. Hennink, I. T. Young, and H. J. Tanke, “Photobleaching kinetics of fluorescein in quantitative fluorescence microscopy,” *Biophys. J.*, vol. 68, no. 6, pp. 2588–2600, 1995.
- [31] T. Ha and P. Tinnefeld, “Photophysics of Fluorescent Probes for Single-

- Molecule Biophysics and Super-Resolution Imaging,” *Annu. Rev. Phys. Chem.*, vol. 63, no. 1, pp. 595–617, 2012.
- [32] L. Guo and F. Gai, “Simple method to enhance the photostability of the fluorescence reporter R6G for prolonged single-molecule studies,” *J. Phys. Chem. A*, vol. 117, no. 29, pp. 6164–6170, 2013.
- [33] M. Swoboda, J. Henig, H. M. Cheng, D. Brugger, D. Haltrich, N. Plumeré, and M. Schlierf, “Enzymatic oxygen scavenging for photostability without pH drop in single-molecule experiments,” *ACS Nano*, vol. 6, no. 7, pp. 6364–6369, 2012.
- [34] C. E. Aitken, R. A. Marshall, and J. D. Puglisi, “An oxygen scavenging system for improvement of dye stability in single-molecule fluorescence experiments,” *Biophys. J.*, vol. 94, no. 5, pp. 1826–1835, 2008.
- [35] S. Howorka and Z. Siwy, *Handbook of Single-Molecule Biophysics*. Springer Science + Business Media LLC, 2009.
- [36] D. J. Webb and C. M. Brown, “Epi-fluorescence microscopy,” *Methods Mol. Biol.*, vol. 931, pp. 29–59, 2013.
- [37] C. Boudreau, T.-L. E. Wee, Y.-R. S. Duh, M. P. Couto, K. H. Ardakani, and C. M. Brown, “Excitation Light Dose Engineering to Reduce Photo-bleaching and Photo-toxicity,” *Sci. Rep.*, vol. 6, p. 30892, 2016.
- [38] T. Nishigaki, C. D. Wood, K. Shiba, S. A. Baba, and A. Darszon, “Stroboscopic illumination using light-emitting diodes reduces phototoxicity in fluorescence cell imaging,” *Biotechniques*, vol. 41, no. 2, pp. 191–197, 2006.
- [39] T. T. T. Tan, C. Khaw, and M. M. L. Ng, “Challenges and recent advances in live cell bioimaging,” *Microsc. Sci. Technol. Appl. Educ.*, pp. 1495–1505, 2010.
- [40] M. Steinbauer, A. G. Harris, C. Abels, and K. Messmer, “Characterization and prevention of phototoxic effects in intravital fluorescence microscopy in the hamster dorsal skinfold model,” *Langenbeck’s Arch. Surg.*, vol. 385, no. 4,

pp. 290–298, 2000.

- [41] J. Icha, M. Weber, J. C. Waters, and C. Norden, “Phototoxicity in live fluorescence microscopy, and how to avoid it,” *BioEssays*, vol. 39, no. 8, pp. 1–15, 2017.
- [42] R. A. Hoebe, C. H. Van Oven, T. W. J. Gadella Jr., P. B. Dhonukshe, C. J. F. Van Noorden, and E. M. M. Manders, “Controlled light-exposure microscopy reduces photobleaching and phototoxicity in fluorescence live-cell imaging,” *Nat. Biotechnol.*, vol. 25, no. 2, pp. 249–253, 2007.
- [43] B. R. Masters, “The Development of Fluorescence Microscopy,” *Encycl. Life Sci.*, pp. 1–9, 2010.
- [44] B. Redding, A. Cerjan, X. Huang, M. L. Lee, A. D. Stone, M. A. Choma, and H. Cao, “Low spatial coherence electrically pumped semiconductor laser for speckle-free full-field imaging,” *Proc. Natl. Acad. Sci.*, vol. 112, no. 5, pp. 1304–1309, 2015.
- [45] A. Nolte, J. B. Pawley, and L. Höring, “Non-laser light sources for three-dimensional microscopy,” in *Handbook of Biological Confocal Microscopy: Third Edition*, 3rd ed., J. B. Pawley, Ed. New York: Springer Science + Business Media LLC, 2006, pp. 126–144.
- [46] T. Allen, “Microscopy: A very short introduction,” in *Microscopy: A very short introduction*, First Edit., Oxford: Oxford University Press, 2001, p. 53.
- [47] J. G. White, W. B. Amos, and M. Fordham, “An Evaluation of Confocal Versus Conventional Imaging of Biological Structures by Fluorescence Light Microscopy,” *Cell*, vol. 105, no. 1, pp. 41–48, 1987.
- [48] W. B. Amos, G. McConnell, and T. Wilson, “Confocal Microscopy,” *Handb. Compr. Biophys.*, pp. 3–23, 2012.
- [49] N. S. Claxton, T. J. Fellers, and M. W. Davidson, “Laser Scanning Confocal Microscopy,” *Encycl. Med. Devices Instrum.*, vol. 1979, no. 21, pp. 1–37, 2006.

- [50] J. A. Conchello and J. W. Lichtman, “Optical sectioning microscopy.,” *Nat. Methods*, vol. 2, no. 12, pp. 920–931, Dec. 2005.
- [51] L. Schermelleh, R. Heintzmann, and H. Leonhardt, “A guide to super-resolution fluorescence microscopy,” *J. Cell Biol.*, vol. 190, no. 2, pp. 165–175, 2010.
- [52] A. Ernst, “A contribution to the Theory of the Microscope, and the nature of Microscopic Vision,” *Proceedings of the Bristol Naturalists’s Society*, vol. 1. pp. 200–261, 1874.
- [53] P. Wang, N. Mohammad, and R. Menon, “Chromatic-aberration-corrected diffractive lenses for ultra-broadband focusing,” *Sci. Rep.*, vol. 6, no. November 2015, p. 21545, Feb. 2016.
- [54] M. Born and E. Wolf, “Chromatic aberration. Dispersion by a prism,” in *Principles of Optics: Electromagnetic theory of propagation, interference and diffraction of light*, 6th ed., Peragamon Press, 1970, pp. 174–180.
- [55] C. J. Sheppard, M. Gu, K. Brain, and H. Zhou, “Influence of spherical aberration on axial imaging of confocal reflection microscopy.,” *Appl. Opt.*, vol. 33, no. 4, pp. 616–624, 1994.
- [56] E. Wolf and M. Born, “Geometrical theory of aberrations,” in *Principles of Optics: Electromagnetic theory of propagation, interference and diffraction of light*, 6th ed., Peragamon Press, 1970, pp. 203–230.
- [57] E. Keller, “Objective Lenses for Confocal Microscopy,” *Handb. Biol. Confocal Microsc.*, pp. 145–161, 2006.
- [58] A. Egner and S. W. Hell, “Aberrations in confocal and multi-photon fluorescence microscopy induced by refractive index mismatch,” in *Handbook of Biological Confocal Microscopy: Third Edition*, 3rd ed., J. B. Pawley, Ed. New York: Springer Science + Business Media, 2006, pp. 404–413.
- [59] C. Cremer and B. R. Masters, “Resolution enhancement techniques in microscopy,” *Eur. Phys. J. H*, vol. 38, no. 3, pp. 281–344, Apr. 2013.

- [60] S. Inoué, “Foundations of Confocal Scanned Imaging in Light Microscopy,” in *Handbook Of Biological Confocal Microscopy*, Boston, MA: Springer US, 2006, pp. 1–19.
- [61] D. B. Murphy, “Diffraction and Interference in Image Formation,” in *Fundamentals of Light Microscopy and Electronic Imaging*, 2002, pp. 61–84.
- [62] D. B. Murphy, “Diffraction and Spatial Resolution,” in *Fundamentals of Light Microscopy and Electronic Imaging*, 2002, pp. 85–95.
- [63] G. H. Patterson, “Fluorescence microscopy below the diffraction limit,” *Semin. Cell Dev. Biol.*, vol. 20, no. 8, pp. 886–893, 2009.
- [64] T. Wilson, “Resolution and optical sectioning in the confocal microscope,” *Journal of Microscopy*, vol. 244, no. 2. Blackwell Publishing Ltd, pp. 113–121, Nov-2011.
- [65] J. Heine, C. A. Wurm, J. Keller-Findeisen, A. Schönle, B. Harke, M. Reuss, F. R. Winter, and G. Donnert, “Three dimensional live-cell STED microscopy at increased depth using a water immersion objective,” *Rev. Sci. Instrum.*, vol. 89, no. 5, p. 53701, 2018.
- [66] U. V. Nägerl, K. I. Willig, B. Hein, S. W. Hell, and T. Bonhoeffer, “Live-cell imaging of dendritic spines by STED microscopy,” *Proc. Natl. Acad. Sci. U. S. A.*, vol. 105, no. 48, pp. 18982–7, 2008.
- [67] S. W. Hell and J. Wichmann, “Breaking the diffraction resolution limit by stimulated-emission - Stimulated-emission-depletion fluorescence microscopy,” *Opt. Lett.*, vol. 19, no. 11, pp. 780–782, 1994.
- [68] S. A. Jones, S.-H. Shim, J. He, and X. Zhuang, “Fast, three-dimensional super-resolution imaging of live cells,” *Nat. Methods*, vol. 8, no. 6, pp. 499–505, Jun. 2011.
- [69] M. J. Rust, M. Bates, and X. W. Zhuang, “Sub-diffraction-limit imaging by stochastic optical reconstruction microscopy (STORM),” *Nat. Methods*, vol. 3, no. 10, pp. 793–796, 2006.

- [70] S. H. Shim, C. Xia, G. Zhong, H. P. Babcock, J. C. Vaughan, B. Huang, X. Wang, C. Xu, G.-Q. Bi, and X. Zhuang, “Super-resolution fluorescence imaging of organelles in live cells with photoswitchable membrane probes,” *Proc. Natl. Acad. Sci.*, vol. 109, no. 35, pp. 13978–13983, 2012.
- [71] G. B. Airy, “VI. On the phænomena of Newton’s rings when formed between two transparent substances of different refractive powers,” *Philos. Mag. Ser. 3*, vol. 2, no. 7, pp. 20–30, Jan. 1833.
- [72] A. Vašíček, “Theory of Light Reflection from a Thin Absorbing Film Deposited on a Metal,” *Opt. Spectrosc.*, vol. 11, p. 128, 1961.
- [73] A. S. G. Curtis, “The mechanism of adhesion of cells to glass. A study by interference reflection microscopy,” *J. Cell Biol.*, vol. 20, no. 2, pp. 199–215, Feb. 1964.
- [74] H. Verschueren, “Interference reflection microscopy in cell biology: methodology and applications,” *J. Cell Sci.*, vol. 75, pp. 279–301, 1985.
- [75] V. A. Barr and S. C. Bunnell, “Interference Reflectance Microscopy,” *Curr Protoc Cell Biol*, pp. 1–21, 2010.
- [76] M. Abercrombie and G. A. Dunn, “Adhesions of fibroblasts to substratum during contact inhibition observed by interference reflection microscopy,” *Exp. Cell Res.*, vol. 92, no. 1, pp. 57–62, Apr. 1975.
- [77] S. L. Godwin, M. Fletcher, and R. P. Burchard, “Interference Reflection Microscopic Study of Sites of Association between Gliding Bacteria and Glass Substrata,” vol. 171, no. 9.
- [78] J. Bereiter-Hahn, C. H. Fox, and B. B. Thorell, “Quantitative reflection contrast microscopy of living cells,” *J. Cell Biol.*, vol. 82, no. 3, pp. 767–779, 1979.
- [79] D. Axelrod, “Cell-substrate contacts illuminated by total internal reflection fluorescence,” *J. Cell Biol.*, vol. 89, no. 1, pp. 141–145, 1981.
- [80] R. M. Weis, K. Balakrishnan, B. A. Smith, and H. M. McConnell,

- “Stimulation of fluorescence in a small contact region between rat basophil leukemia cells and planar lipid membrane targets by coherent evanescent radiation,” *J. Biol. Chem.*, vol. 257, no. 11, pp. 6440–6445, 1982.
- [81] A. L. Mattheyses, S. M. Simon, and J. Z. Rappoport, “Imaging with total internal reflection fluorescence microscopy for the cell biologist,” *J. Cell Sci.*, vol. 123, no. Pt 21, pp. 3621–8, 2010.
- [82] R. D. Vale, T. Funatsu, D. W. Pierce, and L. Romberg, “Direct observation of single kinesin molecules moving along microtubules,” *Nature*, vol. 380, no. 6573. Nature Publishing Group, pp. 451–453, 04-Apr-1996.
- [83] M. Tokunaga, K. Kitamura, K. Saito, A. H. Iwane, and T. Yanagida, “Single molecule imaging of fluorophores and enzymatic reactions achieved by objective-type total internal reflection fluorescence microscopy,” *Biochem. Biophys. Res. Commun.*, vol. 235, no. 1, pp. 47–53, Jun. 1997.
- [84] G. M. Omann and D. Axelrod, “Membrane-proximal calcium transients in stimulated neutrophils detected by total internal reflection fluorescence,” *Biophys. J.*, vol. 71, no. 5, pp. 2885–91, Nov. 1996.
- [85] D. Axelrod, T. P. Burghardt, and N. L. Thompson, “Total internal reflection fluorescence,” *Annu. Rev. Biophys. Bioeng.*, vol. 13, no. 17, pp. 247–268, 1984.
- [86] E. Chung, D. Kim, Y. Cui, Y. H. Kim, and P. T. C. So, “Two-dimensional standing wave total internal reflection fluorescence microscopy: superresolution imaging of single molecular and biological specimens,” *Biophys. J.*, vol. 93, no. September, pp. 1747–1757, 2007.
- [87] D. Axelrod, “Total internal reflection fluorescence microscopy in cell biology,” *Traffic*, vol. 2, no. 11, pp. 764–774, Nov. 2001.
- [88] T. P. Burghardt, “Measuring incidence angle for through-the-objective total internal reflection fluorescence microscopy,” *J. Biomed. Opt.*, vol. 17, no. 12, p. 126007, Dec. 2012.
- [89] S. W. Hell and E. H. K. Stelzer, “Properties of a 4Pi confocal fluorescence

- microscope,” *J. Opt. Soc. Am. A*, vol. 9, no. 12, p. 2159, 1992.
- [90] C. Cremer and T. Cremer, “Considerations on a laser-scanning-microscope with high resolution and depth of field,” *Microsc. Acta*, vol. 81, no. 1, pp. 31–44, 1978.
- [91] S. W. Hell and E. H. K. Stelzer, “Fundamental improvement of resolution with a 4Pi-confocal fluorescence microscope using two-photon excitation,” *Opt. Commun.*, vol. 93, no. 5–6, pp. 277–282, 1992.
- [92] J. Bewersdorf, A. Egner, and S. W. Hell, “4Pi microscopy,” in *Handbook Of Biological Confocal Microscopy*, vol. 3rd Editio, 2006, pp. 561–571.
- [93] M. Nagorni and S. W. Hell, “Coherent use of opposing lenses for axial resolution increase in fluorescence microscopy. I. Comparative study of concepts,” *America (NY)*, vol. 18, no. 1, 2001.
- [94] J. Bewersdorf, A. Egner, and S. W. Hell, “4Pi-Confocal Microscopy Is coming of Age,” *Imaging Microsc.*, pp. 24–25, 2004.
- [95] J. Bewersdorf, R. Schmidt, and S. W. Hell, “Comparison of I5M and 4Pi-microscopy,” *J. Microsc.*, vol. 222, no. 2, pp. 105–117, 2006.
- [96] S. W. Hell, S. Lindek, C. Cremer, and E. H. K. Stelzer, “Measurement of the 4Pi-confocal point spread function prove 75 nm axial resolution,” *Appl. Phys. Lett.*, vol. 64, pp. 1335–1337.
- [97] E. H. K. Stelzer, “Beyond the diffraction limit?,” *Nature*, vol. 417, no. 6891, pp. 806–7, Jun. 2002.
- [98] S. W. Hell, M. Schrader, and H. T. van der Voort, “Far-field fluorescence microscopy with three-dimensional resolution in the 100-nm range.,” *J. Microsc.*, vol. 187, no. Pt 1, pp. 1–7, Jul. 1997.
- [99] M. Schrader, K. Bahlmann, G. Giese, and S. W. Hell, “4Pi-confocal imaging in fixed biological specimens.,” *Biophys. J.*, vol. 75, no. October, pp. 1659–1668, 1998.
- [100] K. Bahlmann, S. Jakobs, and S. W. Hell, “4Pi-confocal microscopy of live

- cells,” *Ultramicroscopy*, vol. 87, no. 3, pp. 155–164, 2001.
- [101] M. G. Gustafsson, “Extended resolution fluorescence microscopy,” *Curr. Opin. Struct. Biol.*, vol. 9, no. 5, pp. 627–634, 1999.
- [102] M. G. L. Gustafsson, D. A. Agard, and J. W. Sedat, “I5M: 3D widefield light microscopy with better than 100 nm axial resolution,” *J. Microsc.*, vol. 195, no. 1, pp. 10–16, Jul. 1999.
- [103] M. G. L. Gustafsson, D. A. Agard, and J. W. Sedat, “Sevenfold improvement of axial resolution in 3D wide-field microscopy using two objective lenses,” *Proc. SPIE*, vol. 2412, no. 1, pp. 147–156, 1995.
- [104] M. G. L. Gustafsson, D. A. Agard, and J. W. Sedat, “3D widefield microscopy with two objective lenses: experimental verification of improved axial resolution,” in *Electronic Imaging: Science & Technology*, 1996, vol. 2655, pp. 62–66.
- [105] L. Shao, B. Isaac, S. Uzawa, D. A. Agard, J. W. Sedat, and M. G. L. Gustafsson, “I5S: wide-field light microscopy with 100-nm-scale resolution in three dimensions,” *Biophys. J.*, vol. 94, no. 12, pp. 4971–83, 2008.
- [106] M. G. L. Gustafsson, “Surpassing the lateral resolution limit by a factor of two using structured illumination microscopy,” *J. Microsc.*, vol. 198, no. 2, pp. 82–87, 2000.
- [107] L. M. Hirvonen, K. Wicker, O. Mandula, R. Heintzmann, A. Ondrej, M. Ae, and R. Heintzmann, “Structured illumination microscopy of a living cell,” *Eur. Biophys. J.*, vol. 38, no. 6, pp. 807–812, 2009.
- [108] H. L. Fu, J. L. Mueller, M. J. Whitley, D. M. Cardona, R. M. Willett, D. G. Kirsch, J. Q. Brown, and N. Ramanujam, “Structured illumination microscopy and a quantitative image analysis for the detection of positive margins in a pre-clinical genetically engineered mouse model of sarcoma,” *PLoS One*, vol. 11, no. 1, 2016.
- [109] L. Turnbull, M. P. Strauss, A. T. F. Liew, L. G. Monahan, C. B. Whitchurch, and E. J. Harry, “Super-resolution Imaging of the Cytokinetic Z Ring in Live

- Bacteria Using Fast 3D-Structured Illumination Microscopy (f3D-SIM),” *J. Vis. Exp.*, no. 91, p. 51469, Sep. 2014.
- [110] L. Schermelleh, P. M. Carlton, S. Haase, L. Shao, L. Winoto, P. Kner, B. Burke, M. C. Cardoso, D. A. Agard, M. G. L. Gustafsson, H. Leonhardt, and J. W. Sedat, “Subdiffraction Multicolor Imaging of the Nuclear Periphery with 3D Structured Illumination Microscopy,” *Science* (80-. ), vol. 320, no. 5881, pp. 1332–1336, Jun. 2008.
- [111] Y. Hirano, A. Matsuda, and Y. Hiraoka, “Recent advancements in structured-illumination microscopy toward live-cell imaging,” *Microscopy*, vol. 64, no. 4, pp. 237–249, 2015.
- [112] A. Stemmer, M. Beck, and R. Fiolka, “Widefield fluorescence microscopy with extended resolution,” *Histochem. Cell Biol.*, vol. 130, no. 5, pp. 807–817, 2008.
- [113] M. G. L. Gustafsson, L. Shao, P. M. Carlton, C. J. R. Wang, I. N. Golubovskaya, W. Z. Cande, D. A. Agard, and J. W. Sedat, “Three-dimensional resolution doubling in wide-field fluorescence microscopy by structured illumination.,” *Biophys. J.*, vol. 94, no. 12, pp. 4957–4970, 2008.
- [114] M. Saxena, G. Eluru, and S. S. Gorthi, “Structured illumination microscopy,” *Adv. Opt. Photonics*, vol. 7, no. 2, p. 241, 2015.
- [115] P. W. Winter, A. G. York, D. D. Nogare, M. Ingaramo, R. Christensen, A. Chitnis, G. H. Patterson, and H. Shroff, “Two-photon instant structured illumination microscopy improves the depth penetration of super-resolution imaging in thick scattering samples,” *Optica*, vol. 1, no. 3, p. 181, 2014.
- [116] P. J. Keller, A. D. Schmidt, A. Santella, K. Khairy, Z. Bao, J. Wittbrodt, and E. H. K. Stelzer, “Fast, high-contrast imaging of animal development with scanned light sheet–based structured-illumination microscopy,” *Nat. Methods*, vol. 7, no. 8, pp. 637–642, Aug. 2010.
- [117] M. G. L. Gustafsson, “Nonlinear structured-illumination microscopy: wide-field fluorescence imaging with theoretically unlimited resolution.,” *Proc.*

*Natl. Acad. Sci. U. S. A.*, vol. 102, no. 37, pp. 13081–13086, 2005.

- [118] G. Shtengel, J. A. Galbraith, C. G. Galbraith, J. Lippincott-Schwartz, J. M. Gillette, S. Manley, R. Sougrat, C. M. Waterman, P. Kanchanawong, M. W. Davidson, R. D. Fetter, and H. F. Hess, “Interferometric fluorescent super-resolution microscopy resolves 3D cellular ultrastructure.,” *Proc. Natl. Acad. Sci.*, vol. 106, no. 9, pp. 3125–3130, Mar. 2009.
- [119] M. Bates, B. Huang, G. T. Dempsey, and X. Zhuang, “S-Multicolor super-resolution imaging with photo-switchable fluorescent probes.,” *Science (80-. )*, vol. 317, no. September, pp. 1749–53, 2007.
- [120] M. J. Rust, M. Bates, and X. Zhuang, “Stochastic optical reconstruction microscopy (STORM) provides sub-diffraction-limit image resolution,” *Nat Meth*, vol. 3, no. 10, pp. 793–796, 2006.
- [121] E. Betzig, G. H. Patterson, R. Sougrat, O. W. Lindwasser, S. Olenych, J. S. Bonifacino, M. W. Davidson, J. Lippincott-Schwartz, and H. F. Hess, “Imaging Intracellular Fluorescent Proteins at Nanometer Resolution,” *Science (80-. )*, vol. 313, no. 5793, pp. 1642–1645, 2006.
- [122] B. Huang, “Super-resolution optical microscopy: multiple choices,” *Current Opinion in Chemical Biology*, vol. 14, no. 1. pp. 10–14, 2010.
- [123] B. O. Leung and K. C. Chou, “Review of super-resolution fluorescence microscopy for biology.,” *Appl. Spectrosc.*, vol. 65, no. 9, pp. 967–80, Sep. 2011.
- [124] S. T. Hess, T. P. K. Girirajan, and M. D. Mason, “Ultra-High Resolution Imaging by Fluorescence Photoactivation Localization Microscopy,” *Biophys. J.*, vol. 91, no. 11, pp. 4258–4272, 2006.
- [125] A. Egner, C. Geisler, C. von Middendorff, H. Bock, D. Wenzel, R. Medda, M. Andresen, A. C. Stiel, S. Jakobs, C. Eggeling, A. Schönle, and S. W. Hell, “Fluorescence nanoscopy in whole cells by asynchronous localization of photoswitching emitters.,” *Biophys. J.*, vol. 93, no. 9, pp. 3285–3290, 2007.
- [126] M. A. Schwartz, “Super-resolution microscopy: A new dimension in focal

- adhesions,” *Curr. Biol.*, vol. 21, no. 3, pp. R115–R116, 2011.
- [127] B. Hajj, M. El Beheiry, I. Izeddin, X. Darzacq, and M. Dahan, “Accessing the third dimension in localization-based super-resolution microscopy,” *Phys. Chem. Chem. Phys.*, vol. 16, no. 31, pp. 16340–8, 2014.
- [128] Y. Zhang, H. Chang, L. Gu, Y. Zhao, T. Xu, and W. Ji, “Super-resolution microscopy of live cells using single molecule localization,” *Chinese Sci. Bull.*, vol. 58, no. 36, pp. 4519–4527, 2013.
- [129] F. Lanni, “Standing-Wave Fluorescence Microscopy,” in *Applications of Fluorescence in the Biomedical Science*, D. L. Taylor, A. Waggoner, F. Lanni, B. Robert, and M. Robert, Eds. New York: Alan R. Liss, 1986.
- [130] B. Bailey, D. L. Farkas, D. L. Taylor, and F. Lanni, “Enhancement of axial resolution in fluorescence microscopy by standing-wave excitation,” *Nature*, vol. 366, no. 6450, pp. 44–8, 1993.
- [131] F. Lanni, B. Bailey, D. L. Farkas, and D. L. Taylor, “Excitation field synthesis as a means for obtaining enhanced axial resolution in fluorescence microscopes,” *Bioimaging*, vol. 1, no. 4, pp. 187–196, Sep. 1993.
- [132] K. Elsayad, A. Urich, P. S. Tan, M. Nemethova, J. V. Small, K. Unterrainer, and K. G. Heinze, “Spectrally coded optical nanosectioning (SpecON) with biocompatible metal-dielectric-coated substrates,” *Proc. Natl. Acad. Sci. U. S. A.*, vol. 110, no. 50, pp. 20069–74, 2013.
- [133] R. Amor, S. Mahajan, W. B. Amos, and G. McConnell, “Standing-wave-excited multiplanar fluorescence in a laser scanning microscope reveals 3D information on red blood cells,” *Sci. Rep.*, vol. 4, p. 7359, 2014.
- [134] X. Yang, H. Xie, E. Alonas, Y. Liu, X. Chen, P. J. Santangelo, Q. Ren, P. Xi, and D. Jin, “Mirror-enhanced super-resolution microscopy,” *Light Sci. Appl.*, vol. 5, no. 6, p. e16134, 2016.
- [135] M. Born and E. Wolf, “7.4. Standing Waves,” in *Principles of Optics: Electromagnetic theory of propagation, interference and diffraction of light*, 6th ed., Peragamon Press, 1970, pp. 277–280.

- [136] F. A. Jenkins and H. E. White, “The superposition of waves,” in *Fundamentals of Optics*, 4th ed., F. A. Jenkins and H. E. White, Eds. New York: McGraw-Hill Primis Custom Publishing, 2001, pp. 242–244.
- [137] R. W. Ditchburn, “Wave theory - Combination of wave motions,” in *Light*, 1st ed., R. W. Ditchburn, Ed. Glasgow: Blackie & Son Limited, 1957, pp. 60–63.
- [138] O. Weiner, “Stehende lichtwellen und die schwingungsrichtung polarisirten lichtes,” *Ann. Phys.*, vol. 276, pp. 203–242, 1890.
- [139] P. Drude and W. Nernst, “Ueber die Fluoreszenzwirkungen stehender Lichtwellen,” *Ann. Phys.*, vol. 281, no. 3, pp. 460–474, Jan. 1892.
- [140] R. Freimann, S. Pentz, and H. Hörler, “Development of a standing-wave fluorescence microscope with high nodal plane flatness.,” *J. Microsc.*, vol. 187, no. Pt 3, pp. 193–200, 1997.
- [141] V. C. Abraham, V. Krishnamurthi, D. L. Taylor, and F. Lanni, “The actin-based nanomachine at the leading edge of migrating cells.,” *Biophys. J.*, vol. 77, no. 3, pp. 1721–1732, 1999.
- [142] B. Bailey, V. Krishnamurthi, D. L. Farkas, D. L. Taylor, and F. Lanni, “Three-Dimensional Imaging of Biological Specimens with Standing Wave Fluorescence Microscopy,” *SPIE Vol. 2184 Three-Dimensional Microsc.*, vol. 2184, pp. 208–213, 1994.
- [143] V. Krishnamurthi, B. Bailey, and F. Lanni, “Image processing in 3D standing wave fluorescence microscopy,” *SPIE 2655, Three-Dimensional Microsc. Image Acquis. Process. III*, vol. 2655, no. 1, pp. 18–25, Apr. 1996.
- [144] B. Schneider, J. Bradl, I. Kirsten, M. Hausmann, and C. Cremer, “High precision localization of fluorescent targets in the nanometer range by spatially modulated excitation fluorescence microscopy,” *Fluoresc. Microsc. Fluoresc. Probes*, vol. 2, no. February 2015, pp. 63–68, 1998.
- [145] M. Born and E. Wolf, “Elements of the theory of diffraction,” in *Principles of Optics: Electromagnetic theory of propagation, interference and diffraction of light*, Peragamon Press, 1970, pp. 439–441.

- [146] C. H. Wang and A. S. Popel, “Effect of red blood cell shape on oxygen transport in capillaries.,” *Math. Biosci.*, vol. 116, no. 1, pp. 89–110, Jul. 1993.
- [147] T. Browicz, “Further observation of motion phenomena on red blood cells in pathological states,” *Zbl Med. Wiss.*, vol. 28, pp. 625–627, 1890.
- [148] H. Turlier, D. A. Fedosov, B. Audoly, T. Auth, N. S. Gov, C. Sykes, J.-F. Joanny, G. Gompper, and T. Betz, “Equilibrium physics breakdown reveals the active nature of red blood cell flickering,” *Nat. Phys.*, vol. 12, no. 5, pp. 513–519, 2016.
- [149] Y. Z. Yoon, H. Hong, A. Brown, C. K. Dong, J. K. Dae, V. L. Lew, and P. Cicuta, “Flickering analysis of erythrocyte mechanical properties: Dependence on oxygenation level, cell shape, and hydration level,” *Biophys. J.*, vol. 97, no. 6, pp. 1606–1615, 2009.
- [150] F. Brochard and J. F. Lennon, “Frequency spectrum of the flicker phenomenon in erythrocytes,” *J. Phys.*, vol. 36, no. 11, pp. 1035–1047, 1975.
- [151] M. Diez-Silva, M. Dao, J. Han, C.-T. Lim, and S. Suresh, “Shape and Biomechanical Characteristics of Human Red Blood Cells in Health and Disease.,” *MRS Bull.*, vol. 35, no. 5, pp. 382–388, 2010.
- [152] L. Pauling, H. A. Itano, S. J. Singer, and I. C. Wells, “Sickle Cell Anemia, a Molecular Disease,” *Science (80- )*, vol. 110, no. 2865, pp. 543–548, 1949.
- [153] S. Eber and S. E. Lux, “Hereditary Spherocytosis - Defects in Proteins That Connect the Membrane Skeleton to the Lipid Bilayer,” *Seminars in Hematology*, vol. 41, no. 2, pp. 118–141, Apr-2004.
- [154] M. Diez-Silva, M. Dao, J. Han, C.-T. Lim, and S. Suresh, “Shape and Biomechanical Characteristics of Human Red Blood Cells in Health and Disease.,” *MRS Bull.*, vol. 35, no. 5, pp. 382–388, 2010.
- [155] R. W. Cole and J. N. Turner, “Light-emitting diodes are better illumination sources for biological microscopy than conventional sources.,” *Microsc. Microanal.*, vol. 14, no. 3, pp. 243–250, Jun. 2008.

- [156] J. T. Wessels, U. Pliquet, and F. S. Wouters, “Light-emitting diodes in modern microscopy-from David to Goliath?,” *Cytom. Part A*, vol. 81 A, no. 3, pp. 188–197, 2012.
- [157] T. Sato and V. N. Murthy, “Light-emitting diodes for biological microscopy,” *Cold Spring Harb. Protoc.*, vol. 7, no. 12, pp. 1211–1222, 2012.
- [158] D. Axelrod, “Carbocyanine dye orientation in red cell membrane studied by microscopic fluorescence polarization.,” *Biophys. J.*, vol. 26, no. June, pp. 557–573, 1979.
- [159] S. Himbert, R. J. Alsop, M. Rose, L. Hertz, A. Dhaliwal, J. M. Moran-Mirabal, C. P. Verschoor, D. M. E. Bowdish, L. Kaestner, C. Wagner, and M. C. Rheinstädter, “The Molecular Structure of Human Red Blood Cell Membranes from Highly Oriented, Solid Supported Multi-Lamellar Membranes,” *Sci. Rep.*, vol. 7, p. 39661, 2017.
- [160] M. G. Honig and R. I. Hume, “DiI and DiO: versatile fluorescent dyes for neuronal labeling and pathway tracing,” *Tins*, vol. 12, pp. 333–341, 1989.
- [161] Y. Li, Y. Song, L. Zhao, G. Gaidosh, A. M. Laties, and R. Wen, “Direct labeling and visualization of blood vessels with lipophilic carbocyanine dye DiI,” *Nat. Protoc.*, vol. 3, no. 11, pp. 1703–1708, 2008.
- [162] M. G. Honig and R. I. Hume, “Fluorescent carbocyanine dyes allow living neurons of identified origin to be studied in long-term cultures,” *J. Cell Biol.*, vol. 103, no. 1, pp. 171–187, 1986.
- [163] “m-Fluoroliposome-DiI – Clodrosome: Liposomal Clodronate.” [Online]. Available: <https://www.clodrosome.com/products/m-fluoroliposome-dii/>. [Accessed: 17-Apr-2018].
- [164] E. Yavin and Z. Yavin, “Attachment and culture of dissociated cells from rat embryo cerebral hemispheres on polylysine-coated surface.,” *J. Cell Biol.*, vol. 62, no. 2, pp. 540–6, 1974.
- [165] J. Dempster, D. L. Wokosin, K. D. McCloskey, J. M. Girkin, and A. M. Gurney, “WinFluor-An integrated system for the simultaneous recording of

- cell fluorescence images and electrophysiological signals on a single computer system,” *Br. J. Pharmacol.*, vol. 137, pp. 146–146, 2002.
- [166] J. J. Cargille, “Cargille - Immersion Oil and the Microscope,” *Cargille-Sacher Lab. Inc.*, pp. 1–6, 2014.
- [167] M. J. Schnepf, M. Mayer, C. Kuttner, M. Tebbe, D. Wolf, M. Dulle, T. Altantzis, P. Formanek, S. Förster, S. Bals, T. A. F. König, and A. Fery, “Supporting information - Nanorattles with tailored electric field enhancement,” *Nanoscale*, vol. 9, no. 27, pp. 9376–9385, 2017.
- [168] D. Fischer, “Radial Average,” 2014. [Online]. Available: <https://uk.mathworks.com/matlabcentral/fileexchange/46468-radialavg->.
- [169] R. A. Macrae, J. A. McClure, and P. Latimer, “Spectral transmission and scattering properties of red blood cells,” *J. Opt. Soc. Am.*, vol. 51, no. 12, pp. 1366–1372, Dec. 1961.
- [170] A. Renn, J. Seelig, and V. Sandoghdar, “Oxygen-dependent photochemistry of fluorescent dyes studied at the single molecule level,” *Mol. Phys.*, vol. 104, no. 3, pp. 409–414, 2006.
- [171] D. S. English, A. Furube, and P. F. Barbara, “Single-molecule spectroscopy in oxygen-depleted polymer films,” *Chem. Phys. Lett.*, vol. 324, no. 1–3, pp. 15–19, 2000.
- [172] Y. Lill and B. Hecht, “Single dye molecules in an oxygen-depleted environment as photostable organic triggered single-photon sources,” *Appl. Phys. Lett.*, vol. 84, no. 10, p. 1665, 2004.
- [173] F. Göttfert, T. Pleiner, J. Heine, V. Westphal, D. Görlich, S. J. Sahl, and S. W. Hell, “Strong signal increase in STED fluorescence microscopy by imaging regions of subdiffraction extent,” *Proc. Natl. Acad. Sci.*, vol. 114, no. 9, pp. 2125–2130, Feb. 2017.
- [174] M. Fernández-Suárez and A. Y. Ting, “Fluorescent probes for super-resolution imaging in living cells,” *Nat. Rev. Mol. Cell Biol.*, vol. 9, no. 12, pp. 929–943, 2008.

- [175] Z. W. Zhang and B. Neu, “Role of macromolecular depletion in red blood cell adhesion,” *Biophys. J.*, vol. 97, no. 4, pp. 1031–1037, 2009.
- [176] B. Neu and H. J. Meiselman, “Depletion interactions in polymer solutions promote red blood cell adhesion to albumin-coated surfaces,” *Biochim. Biophys. Acta - Gen. Subj.*, vol. 1760, no. 12, pp. 1772–1779, 2006.
- [177] I. Todd, J. S. Mellor, and D. Gingell, “Mapping cell-glass contacts of *Dictyostelium amoebae* by total internal reflection aqueous fluorescence overcomes a basic ambiguity of interference reflection microscopy,” *J. Cell Sci.*, vol. 89 ( Pt 1), no. 1, pp. 107–14, Jan. 1988.
- [178] Y. Iwanaga, D. Braun, and P. Fromherz, “No correlation of focal contacts and close adhesion by comparing GFP-vinculin and fluorescence interference of DiI,” *Eur. Biophys. J.*, vol. 30, no. 1, pp. 17–26, 2001.
- [179] S. Cho, S. Kim, Y. Kim, and Y. Park, “Optical imaging techniques for the study of malaria,” *Trends Biotechnol.*, vol. 30, no. 2, pp. 71–79, 2012.
- [180] B. Huang, M. Bates, and X. Zhuang, “Super resolution fluorescence microscopy,” *Annu. Rev. Biochem.*, vol. 78, pp. 993–1016, 2010.
- [181] C. Monzel and K. Sengupta, “Measuring shape fluctuations in biological membranes,” *J. Phys. D. Appl. Phys.*, vol. 49, no. 24, p. 243002, 2016.
- [182] S. Chen, C. Li, and Y. Zhu, “Low-coherence wavelength shifting interferometry for high-speed quantitative phase imaging,” *Opt. Lett.*, vol. 41, no. 15, p. 3431, 2016.
- [183] N. T. Shaked, L. L. Satterwhite, N. Bursac, and A. Wax, “Whole-cell-analysis of live cardiomyocytes using wide-field interferometric phase microscopy,” *Biomed. Opt. Express*, vol. 1, no. 2, p. 706, 2010.
- [184] Y. Park, C. A. Best, T. Auth, N. S. Gov, S. A. Safran, G. Popescu, S. Suresh, and M. S. Feld, “Metabolic remodeling of the human red blood cell membrane,” *Proc. Natl. Acad. Sci.*, vol. 107, no. 4, pp. 1289–1294, 2010.
- [185] Y. Park, C. A. Best, K. Badizadegan, R. R. Dasari, M. S. Feld, T. Kuriabova,

- M. L. Henle, A. J. Levine, and G. Popescu, "Measurement of red blood cell mechanics during morphological changes.," *Proc. Natl. Acad. Sci. U. S. A.*, vol. 107, no. 15, pp. 6731–6, 2010.
- [186] P. A. Santi, "Light Sheet Fluorescence Microscopy," *J. Histochem. Cytochem.*, vol. 59, no. 2, pp. 129–138, 2011.
- [187] J. Huisken, J. Swoger, F. Del Bene, J. Wittbrodt, and E. H. K. Stelzer, "Optical sectioning deep inside live embryos by selective plane illumination microscopy," *Science (80-. )*, vol. 305, no. 5686, pp. 1007–1009, Aug. 2004.
- [188] T. A. Planchon, L. Gao, D. E. Milkie, M. W. Davidson, J. A. Galbraith, C. G. Galbraith, and E. Betzig, "Rapid three-dimensional isotropic imaging of living cells using Bessel beam plane illumination," *Nat. Methods*, vol. 8, no. 5, pp. 417–423, 2011.
- [189] P. N. Hedde and E. Gratton, "Selective plane illumination microscopy with a light sheet of uniform thickness formed by an electrically tunable lens," *Microscopy Research and Technique*, 2016.
- [190] T. Vettenburg, H. I. C. Dalgarno, J. Nylk, C. Coll-Lladó, D. E. K. Ferrier, T. Čižmár, F. J. Gunn-Moore, and K. Dholakia, "Light-sheet microscopy using an Airy beam," *Nat. Methods*, vol. 11, no. 5, pp. 541–544, 2014.
- [191] F. H. C. Wong, J. S. Ng-Kamstra, N. L. H. Chen, and C. Fradin, "Localized photodamage of the human erythrocyte membrane causes an invagination as a precursor of photohaemolysis," *J. Microsc.*, vol. 226, no. 1, pp. 6–17, Mar. 2007.
- [192] M. P. Sheetz and D. E. Koppel, "Membrane damage caused by irradiation of fluorescent concanavalin A.," *Proc. Natl. Acad. Sci. U. S. A.*, vol. 76, no. 7, pp. 3314–7, 1979.
- [193] J. P. Pooler, "A New Hypothesis for the Target in Photohemolysis: Dimers of the Band 3 Protein," *Photochem. Photobiol.*, vol. 43, no. 3, pp. 263–266, 1986.
- [194] I. Saytashev, R. Glenn, G. A. Murashova, S. Osseiran, D. Spence, C. L. Evans,

- and M. Dantus, “Multiphoton excited hemoglobin fluorescence and third harmonic generation for non-invasive microscopy of stored blood.,” *Biomed. Opt. Express*, vol. 7, no. 9, pp. 3449–3460, 2016.
- [195] K. H. Drexhage, “Monomolecular layers and light,” *Sci. Am.*, vol. 222, pp. 108–119, 1970.
- [196] P. Selenyi, “Wide-Angle Interferences and the Nature of the Elementary Light Sources,” *Phys. Rev.*, vol. 56, pp. 477–479, 1939.
- [197] A. Lambacher and P. Fromherz, “Luminescence of dye molecules on oxidized silicon and fluorescence interference contrast microscopy of biomembranes,” *J. Opt. Soc. Am. B Opt. Phys.*, vol. 19, no. 6, pp. 1435–1453, 2002.
- [198] A. Lambacher and P. Fromherz, “Fluorescence interference-contrast microscopy on oxidized silicon using a monomolecular dye layer,” *Appl. Phys. A Mater. Sci. Process.*, vol. 216, pp. 207–216, 1996.
- [199] F. L. H. Wolfs, M. McDonald, J. Ha, B. H. McGuyer, and T. Zelevinsky, “Visible optical beats at the hertz level,” *Am. J. Phys.*, vol. 82, no. 10, pp. 1003–1004, 2014.
- [200] K. H. Drexhage, “Interaction of light with monomolecular dye layers,” in *Progress in Optics XII*, Amsterdam, North Holland, 1974, pp. 165–231.
- [201] D. Braun and P. Fromherz, “Fluorescence interferometry of nerve cells on microstructured silicon,” *Eur. J. Cell Biol.*, vol. 78, no. SUPPL. 49, p. 42, 1999.
- [202] J. T. Groves, R. Parthasarathy, and M. B. Forstner, “Fluorescence Imaging of Membrane Dynamics,” *Annu. Rev. Biomed. Eng.*, vol. 10, no. 1, pp. 311–338, 2008.
- [203] V. Kiessling and L. K. Tamm, “Measuring distances in supported bilayers by fluorescence interference-contrast microscopy: Polymer supports and SNARE proteins,” *Biophys. J.*, vol. 84, no. 1, pp. 408–418, 2003.
- [204] G. L. Rogers, “A Geometrical Approach to Moiré Pattern Calculations,” *Opt.*

*Acta Int. J. Opt.*, vol. 24, no. 1, pp. 1–13, 1977.

- [205] A. V Lee, S. Oesterreich, and N. E. Davidson, “MCF-7 Cells - Changing the Course of Breast Cancer Research and Care for 45 Years,” *J. Natl. Cancer Inst.*, vol. 107, no. 7, p. 73, 2015.
- [206] Ş. Comsa, A. M. Cimpean, and M. Raica, “The Story of MCF-7 Breast Cancer Cell Line: 40 years of Experience in Research,” *Anticancer Res.*, vol. 35, pp. 3147–3154, 2015.
- [207] T. Karpanen, M. Egeblad, M. J. Karkkainen, H. Kubo, S. Yla, and M. Ja, “Advances in Brief Vascular Endothelial Growth Factor C Promotes Tumor Lymphangiogenesis and Intralymphatic Tumor Growth,” *Cancer Res.*, vol. 61, pp. 1786–1790, 2001.
- [208] L. Lian, W. Li, Z. Y. Li, Y. X. Mao, Y.-T. Zhang, Y.-M. Zhao, K. Chen, W. M. Duan, and M. Tao, “Inhibition of MCF-7 breast cancer cell-induced platelet aggregation using a combination of antiplatelet drugs,” *Oncol. Lett.*, vol. 5, no. 2, pp. 675–680, 2013.
- [209] R. A. Wood, M. J. Barbour, G. W. Gould, M. R. Cunningham, and R. J. Plevin, “Conflicting evidence for the role of JNK as a target in breast cancer cell proliferation: Comparisons between pharmacological inhibition and selective shRNA knockdown approaches,” *Pharmacol. Res. Perspect.*, vol. 6, no. 1, pp. 1–10, 2017.
- [210] D. Brown, “Membrane recycling and epithelial cell function,” *Am. J. Physiol.*, vol. 256, no. 1 Pt 2, pp. F1–F12, 1989.
- [211] M. Hao and F. R. Maxfield, “Characterization of rapid membrane internalization and recycling,” *J. Biol. Chem.*, vol. 275, no. 20, pp. 15279–15286, 2000.
- [212] B. Alberts, A. Johnson, J. Lewis, D. Morgan, M. Raff, K. Roberts, and P. Water, “Intracellular Membrane Traffic,” in *Molecular Biology of the Cell*, 6th ed., New York: Garland Science, 2015, pp. 695–752.
- [213] J. F. Presley, C. Smith, K. Hirschberg, C. Miller, N. B. Cole, K. J. M. Zaal,

- and J. Lippincott-schwartz, "Golgi Membrane Dynamics," *Mol. Biol. Cell*, vol. 9, no. July 1998, pp. 1617–1626, 2011.
- [214] V. Puri, R. Watanabe, R. D. Singh, M. Dominguez, J. C. Brown, C. L. Wheatley, D. L. Marks, and R. E. Pagano, "Clathrin-dependent and -independent internalization of plasma membrane sphingolipids initiates two Golgi targeting pathways," *J. Cell Biol.*, vol. 154, no. 3, pp. 535–547, 2001.
- [215] W. A. Maltese and J. H. Overmeyer, "Methuosis: Nonapoptotic cell death associated with vacuolization of macropinosome and endosome compartments," *American Journal of Pathology*, vol. 184, no. 6. pp. 1630–1642, 2014.
- [216] H. Bhanot, A. M. Young, J. H. Overmeyer, and W. A. Maltese, "Induction of Nonapoptotic Cell Death by Activated Ras Requires Inverse Regulation of Rac1 and Arf6," *Mol. Cancer Res.*, vol. 8, no. 10, pp. 1358–1374, 2010.
- [217] C. J. Trabbic, H. M. Dietsch, E. M. Alexander, P. I. Nagy, M. W. Robinson, J. H. Overmeyer, W. A. Maltese, and P. W. Erhardt, "Differential induction of cytoplasmic vacuolization and methuosis by novel 2-indolyl-substituted pyridinylpropenones," *ACS Med. Chem. Lett.*, vol. 5, no. 1, pp. 73–77, 2014.
- [218] N. E. Mbah, J. H. Overmeyer, and W. A. Maltese, "Disruption of endolysosomal trafficking pathways in glioma cells by methuosis-inducing indole-based chalcones," *Cell Biol. Toxicol.*, vol. 33, no. 3, pp. 263–282, 2017.
- [219] S. Abrahamsson, H. Blom, A. Agostinho, D. C. Jans, A. Jost, M. Müller, L. Nilsson, K. Bernhem, T. J. Lambert, R. Heintzmann, and H. Brismar, "Multifocus structured illumination microscopy for fast volumetric super-resolution imaging," *Biomed. Opt. Express*, vol. 8, no. 9, p. 4135, 2017.
- [220] R. Heintzmann and T. Huser, "Super-Resolution Structured Illumination Microscopy," *Chemical Reviews*, vol. 117, no. 23. pp. 13890–13908, 2017.
- [221] L. Shao, P. Kner, E. H. Rego, and M. G. L. Gustafsson, "Super-resolution 3D microscopy of live whole cells using structured illumination.," *Nat. Methods*,

- vol. 8, no. 12, pp. 1044–1046, 2011.
- [222] G. Shtengel, J. Galbraith, C. Galbraith, P. Kanchanawong, C. Waterman, and H. Hess, “Multi-Color Interferometric Photo-Activation Localization Microscopy with Extended Axial Range,” *Microsc. Microanal.*, vol. 17, no. S2, pp. 6–7, 2011.
- [223] S. W. Hell, S. J. Sahl, M. Bates, X. Zhuang, R. Heintzmann, M. J. Booth, J. Bewersdorf, G. Shtengel, H. Hess, P. Tinnefeld, A. Honigmann, S. Jakobs, I. Testa, L. Cognet, B. Lounis, H. Ewers, S. J. Davis, C. Eggeling, D. Klenerman, K. I. Willig, G. Vicidomini, M. Castello, A. Diaspro, and T. Cordes, “The 2015 super-resolution microscopy roadmap,” *J. Phys. D. Appl. Phys.*, vol. 48, no. 44, p. 443001, 2015.
- [224] A. G. Szent-Györgyi, “Calcium regulation of muscle contraction,” *Biophys. J.*, vol. 15, no. 7, pp. 707–23, 1975.
- [225] O. Dyachok and E. Gylfe, “Store-operated influx of Ca(2+) in pancreatic beta-cells exhibits graded dependence on the filling of the endoplasmic reticulum,” *J. Cell Sci.*, vol. 114, no. Pt 11, pp. 2179–2186, 2001.
- [226] B. G. Frenguelli and R. Malinow, “Fluctuations in Intracellular Calcium Responses to Action Potentials in Single En Passage Presynaptic Boutons of Layer V Neurons in Neocortical Slices,” *Learn. Mem.*, vol. 3, pp. 150–159, 1996.
- [227] M. D. Bootman, “Calcium Signaling,” *Cold Spring Harb Perspect Biol*, vol. ;4:a011171, 2012.
- [228] A. L. Hodgkin and A. F. Huxley, “Action potentials recorded from inside a nerve fibre,” *Nature*, vol. 144, pp. 710–711, 1939.
- [229] G. Marmont, “Studies on the axon membrane. I. A new method,” *J. Cell. Comp. Physiol.*, vol. 34, no. 3, pp. 351–382, Dec. 1949.
- [230] K. S. Cole, “Dynamic electrical characteristics of the squid axon membrane,” *Arch. sci. physiol*, vol. 3, no. 253–258, p. 20, 1949.

- [231] M. Scanziani and M. Häusser, “Electrophysiology in the age of light.,” *Nature*, vol. 461, no. 7266, pp. 930–939, 2009.
- [232] B. A. Wilt, L. D. Burns, E. T. Wei Ho, K. K. Ghosh, E. A. Mukamel, and M. J. Schnitzer, “Advances in Light Microscopy for Neuroscience,” *Annu. Rev. Neurosci.*, vol. 32, no. 1, pp. 435–506, 2009.
- [233] M. E. Spira and A. Hai, “Multi-electrode array technologies for neuroscience and cardiology,” *Nat. Nanotechnol.*, vol. 8, no. 2, pp. 83–94, 2013.
- [234] R. Y. Tsien, “Monitoring Cell Calcium,” in *Calcium as a Cellular Regulator*, 1st ed., E. Carafoli and C. B. Klee, Eds. New York: Oxford University Press, 1999, pp. 28–54.
- [235] A. Takahashi, P. Camacho, J. D. Lechleiter, and B. Herman, “Measurement of intracellular calcium.,” *Physiol. Rev.*, vol. 79, no. 4, pp. 1089–1125, 1999.
- [236] R. M. Paredes, J. C. Etzler, L. T. Watts, W. Zheng, and J. D. Lechleiter, “Chemical calcium indicators,” *Methods*, vol. 46, no. 3, pp. 143–151, 2008.
- [237] M. Maravall, Z. F. Mainen, B. L. Sabatini, and K. Svoboda, “Estimating intracellular calcium concentrations and buffering without wavelength ratioing.,” *Biophys. J.*, vol. 78, no. 5, pp. 2655–2667, 2000.
- [238] R. Rudolf, M. Mongillo, R. Rizzuto, and T. Pozzan, “Looking forward to seeing calcium.,” *Nat. Rev. Mol. Cell Biol.*, vol. 4, no. 7, pp. 579–586, 2003.
- [239] P. A. P. Gomes, R. A. Bassani, and J. W. M. Bassani, “Measuring  $[Ca^{2+}]$  with fluorescent indicators: Theoretical approach to the ratio method,” *Cell Calcium*, vol. 24, no. 1, pp. 17–26, 1998.
- [240] O. L. Barreto-Chang and R. E. Dolmetsch, “Calcium Imaging of Cortical Neurons using Fura-2 AM,” *J. Vis. Exp.*, vol. 23, no. 23, pp. 3–5, 2009.
- [241] G. Grynkiewicz, M. Poenie, and R. Y. Tsien, “A new generation of  $Ca^{2+}$  indicators with greatly improved fluorescence properties,” *Journal of Biological Chemistry*, vol. 260, no. 6, pp. 3440–3450, 1985.
- [242] “Fura 2 | Dojindo.” [Online]. Available: <http://www.dojindo.com/store/p/543->

Fura-2.html. [Accessed: 05-Apr-2018].

- [243] E. Neher, “The use of fura-2 for estimating ca buffers and ca fluxes,” *Neuropharmacology*, vol. 34, no. 11, pp. 1423–1442, 1995.
- [244] M. Bidet, G. De Renzis, S. Martial, I. Rubera, M. Tauc, and P. Poujeol, “Extracellular ATP increases [CA<sup>2+</sup>]<sub>i</sub> in distal tubule cells. I. Evidence for a P2Y<sub>2</sub> purinoceptor,” *Am. J. Physiol. - Ren. Physiol.*, vol. 279, no. 1, 2000.
- [245] T. L. Pallone, C. Cao, and Z. Zhang, “Inhibition of K<sup>+</sup> conductance in descending vasa recta pericytes by ANG II,” *Am. J. Physiol. Renal Physiol.*, vol. 287, no. 6, pp. F1213-22, 2004.
- [246] A. Malgaroli, D. Milani, J. Meldolesi, and T. Pozzan, “Fura-2 measurement of cytosolic free Ca<sup>2+</sup> in monolayers and suspensions of various types of animal cells,” *J. Cell Biol.*, vol. 105, no. November, pp. 2145–2155, 1987.
- [247] P. C. Hewitt, “Method of manufacturing electric lamps,” US682692 A, 1901.
- [248] M. W. Davidson, “ZEISS Microscopy Online Campus | Light-Emitting Diodes.” .
- [249] T. Regan Baird, D. Kaufman, and C. M. Brown, “Mercury free microscopy: An opportunity for core facility directors,” *J. Biomol. Tech.*, vol. 25, no. 2, pp. 48–53, 2014.
- [250] U. Kubitscheck, “Fluorescence Microscopy: From Principles to Biological Applications,” in *Fluorescence Microscopy: From Principles to Biological Applications*, 2013, pp. 107–142.
- [251] H. R. Petty, “Fluorescence microscopy: Established and emerging methods, experimental strategies, and applications in immunology,” *Microscopy Research and Technique*, vol. 70, no. 8. pp. 687–709, 2007.
- [252] R. H. Breeze and B. Ke, “Some Comments on Xenon Arc Lamp Stability,” *Rev. Sci. Instrum.*, vol. 43, no. 5, pp. 821–823, 1972.
- [253] D. A. Wagenaar, “An Optically Stabilized Fast-Switching Light Emitting Diode as a Light Source for Functional Neuroimaging,” *PLoS One*, vol. 7, no.

1, 2012.

- [254] A. McDonald, J. Harris, D. MacMillan, J. Dempster, and G. McConnell, "Light-induced  $\text{Ca}^{2+}$  transients observed in widefield epi-fluorescence microscopy of excitable cells," *Biomed. Opt. Express*, vol. 3, no. 6, p. 1266, 2012.
- [255] R. Lavi, A. Shainberg, H. Friedmann, V. Shneyvays, O. Rickover, M. Eichler, D. Kaplan, and R. Lubart, "Low Energy Visible Light Induces Reactive Oxygen Species Generation and Stimulates an Increase of Intracellular Calcium Concentration in Cardiac Cells," *J. Biol. Chem.*, vol. 278, no. 42, pp. 40917–40922, 2003.
- [256] T. J. Ebner and G. Chen, "Use of voltage-sensitive dyes and optical recordings in the central nervous system," *Progress in Neurobiology*, vol. 46, no. 5, pp. 463–506, 1995.
- [257] T. D. Dreeben, "Modelling of fluid-mechanical arc instability in pure-mercury HID lamps," *J. Phys. D. Appl. Phys.*, vol. 41, no. 14, p. 144023, 2008.
- [258] A. C. H. Lee, D. S. Elson, M. A. Neil, S. Kumar, B. W. Ling, F. Bello, and G. B. Hanna, "Solid-state semiconductors are better alternatives to arc-lamps for efficient and uniform illumination in minimal access surgery," *Surg. Endosc. Other Interv. Tech.*, vol. 23, no. 3, pp. 518–526, 2009.
- [259] S. Ricken, J. Leipziger, R. Greger, and R. Nitschke, "Simultaneous measurements of cytosolic and mitochondrial  $\text{Ca}^{2+}$  transients in HT29 cells.," *J. Biol. Chem.*, vol. 273, no. 52, pp. 34961–34969, 1998.
- [260] G. E. Stutzmann, F. M. LaFerla, and I. Parker, " $\text{Ca}^{2+}$  signaling in mouse cortical neurons studied by two-photon imaging and photoreleased inositol triphosphate.," *J. Neurosci.*, vol. 23, no. 3, pp. 758–765, 2003.
- [261] G. H. Patterson and D. W. Piston, "Photobleaching in Two-Photon Excitation Microscopy," *Biophys. J.*, vol. 78, no. 4, pp. 2159–2162, 2000.
- [262] A. Birkner, C. H. Tischbirek, and A. Konnerth, "Improved deep two-photon calcium imaging in vivo," *Cell Calcium*, vol. 64, pp. 29–35, 2016.

- [263] W. Denk, J. H. Strickler, and W. W. Webb, “Two-Photon Laser Scanning Fluorescence Microscopy,” *Science* (80-. ), vol. 248, pp. 73–76, 1990.
- [264] B. O. Watson, V. Nikolenko, and R. Yuste, “Two-photon imaging with diffractive optical elements,” *Front Neural Circuits*, vol. 3, pp. 1–11, 2009.
- [265] D. C. Flynn, A. R. Bhagwat, M. H. Brenner, M. F. Núñez, B. E. Mork, D. Cai, J. A. Swanson, and J. P. Ogilvie, “Pulse-shaping based two-photon FRET stoichiometry,” *Opt. Express*, vol. 23, no. 3, pp. 3353–3372, 2015.
- [266] R. Amor, A. McDonald, J. Trägårdh, G. Robb, L. Wilson, N. Z. A. Rahman, J. Dempster, W. B. Amos, T. J. Bushell, and G. McConnell, “Widefield two-photon excitation without scanning: Live cell microscopy with high time resolution and low photo-bleaching,” *PLoS One*, vol. 11, no. 1, 2016.
- [267] H. Jeong, R. Salas-Montiel, G. Lerondel, and M. S. Jeong, “Indium gallium nitride-based ultraviolet, blue, and green light-emitting diodes functionalized with shallow periodic hole patterns,” *Sci. Rep.*, vol. 7, p. 45726, Apr. 2017.
- [268] E. F. Schubert, *Light-Emitting Diodes*, 2nd ed. New York: Cambridge University Press, 2006.
- [269] C. Wetzel, H. Amano, I. Akasaki, J. W. Ager, I. Grzegory, and B. K. Meyer, “DX-like behavior of oxygen in GaN,” in *Physica B: Condensed Matter*, 2001, vol. 302–303, pp. 23–38.
- [270] I. D. Goepfert, E. F. Schubert, A. Osinsky, P. E. Norris, and N. N. Faleev, “Experimental and theoretical study of acceptor activation and transport properties in p- type superlattices,” *J. Appl. Phys. Appl. Phys. Lett.*, vol. 88, no. 101, pp. 2030–92108, 2000.
- [271] S. J. Hearne, J. Han, S. R. Lee, J. A. Floro, D. M. Follstaedt, B. Chason, and B. T. T Tsong, “Brittle-ductile relaxation kinetics of strained AlGaIn/GaN heterostructures,” *J. Appl. Phys. Lett.*, vol. 761, no. 10, pp. 1534–67, 2000.
- [272] S. Fujikawa, T. Takano, Y. Kondo, and H. Hirayama, “Realization of 340-nm-band high-output-power (>7mW) InAlGaIn quantum well ultraviolet light-emitting diode with p-type InAlGaIn,” *Jpn. J. Appl. Phys.*, vol. 47, pp. 2941–

2944, 2008.

- [273] S. R. Jeon, M. Gherasimova, Z. Ren, J. Su, G. Cui, J. Han, H. Peng, Y. K. Song, A. V Nurmikko, L. Zhou, W. Goetz, and M. Krames, “High performance AlGaInN ultraviolet light-emitting diode at the 340 nm wavelength,” *Japanese J. Appl. Physics, Part 2 Lett.*, vol. 43, no. 11 A, 2004.
- [274] V. Adivarahan, A. Chitnis, J. P. Zhang, M. Shatalov, J. W. Yang, G. Simin, M. A. Khan, R. Gaska, and M. S. Shur, “Ultraviolet light-emitting diodes at 340 nm using quaternary AlInGaN multiple quantum wells,” *Applied Physics Letters*, vol. 79, no. 25. pp. 4240–4242, 2001.
- [275] A. Yasan, R. McClintock, K. Mayes, S. R. Darvish, H. Zhang, P. Kung, M. Razeghi, S. K. Lee, and J. Y. Han, “Comparison of ultraviolet light-emitting diodes with peak emission at 340 nm grown on GaN substrate and sapphire,” *Appl. Phys. Lett.*, vol. 81, no. 12, pp. 2151–2153, 2002.
- [276] J. Gan, S. M. Greenwood, S. R. Cobb, and T. J. Bushell, “Indirect modulation of neuronal excitability and synaptic transmission in the hippocampus by activation of proteinase-activated receptor-2,” *Br. J. Pharmacol.*, vol. 163, no. 5, pp. 984–994, 2011.
- [277] N. Z. Abdul Rahman, S. M. Greenwood, R. R. Brett, K. Tossell, M. A. Ungless, R. Plevin, and T. J. Bushell, “Mitogen-Activated Protein Kinase Phosphatase-2 Deletion Impairs Synaptic Plasticity and Hippocampal-Dependent Memory,” *J. Neurosci.*, vol. 36, no. 8, pp. 2348–54, Feb. 2016.
- [278] A. Di Garbo, S. Alloisio, and M. Nobile, “P2X7 receptor-mediated calcium dynamics in HEK293 cells: experimental characterization and modelling approach,” *Phys. Biol.*, vol. 9, 2012.
- [279] M. L. He, H. Zemkova, T. A. Koshimizu, M. Tomić, and S. S. Stojilkovic, “Intracellular calcium measurements as a method in studies on activity of purinergic P2X receptor channels,” *Am. J. Physiol. Cell Physiol.*, vol. 285, no. 2, pp. C467-79, 2003.
- [280] C. Coddou, Z. Yan, and S. S. Stojilkovic, “Role of domain calcium in

- purinergic P2X2 receptor channel desensitization.” *Am. J. Physiol. Cell Physiol.*, vol. 308, no. 9, pp. C729-36, 2015.
- [281] R. Ramachandran, K. Mihara, M. Mathur, M. D. Rochdi, M. Bouvier, K. Defea, and M. D. Hollenberg, “Agonist-biased signaling via proteinase activated receptor-2: differential activation of calcium and mitogen-activated protein kinase pathways.” *Mol. Pharmacol.*, vol. 76, no. 4, pp. 791–801, 2009.
- [282] S. R. Jung, J. B. Seo, Y. Deng, C. L. Asbury, B. Hille, and D.-S. Koh, “Contributions of protein kinases and  $\beta$ -arrestin to termination of protease-activated receptor 2 signaling,” *J. Gen. Physiol.*, vol. 147, no. 3, pp. 255–271, 2016.
- [283] R. A. North, “P2X receptors,” *Philos. Trans. R. Soc. B Biol. Sci.*, vol. 371, no. 1700, p. 20150427, 2016.
- [284] M. Hattori and E. Gouaux, “Molecular mechanism of ATP binding and ion channel activation in P2X receptors,” *Nature*, vol. 485, no. 7397, pp. 207–212, 2012.
- [285] L. E. Browne, “Structure of P2X receptors,” *Wiley Interdiscip. Rev. Membr. Transp. Signal.*, vol. 1, no. 1, pp. 56–69, 2012.
- [286] S. J. Compton, J. A. Cairns, K. J. Palmer, B. Al-Ani, M. D. Hollenberg, and A. F. Walls, “A polymorphic protease-activated receptor 2 (PAR2) displaying reduced sensitivity to trypsin and differential responses to PAR agonists,” *J. Biol. Chem.*, vol. 275, no. 50, pp. 39207–39212, 2000.
- [287] S. R. Jung, J. B. Seo, Y. Deng, C. L. Asbury, B. Hille, and D.-S. Koh, “Contributions of protein kinases and B-arrestin to termination of protease-activated receptor 2 signaling,” *J. Gen. Physiol.*, vol. 147, no. 3, pp. 255–271, 2016.
- [288] D. P. Poole, S. Amadesi, N. A. Veldhuis, F. C. Abogadie, T. M. Lieu, W. Darby, W. Liedtke, M. J. Lew, P. McIntyre, and N. W. Bunnett, “Protease-activated receptor 2 (PAR2) protein and transient receptor potential vanilloid 4

- (TRPV4) protein coupling is required for sustained inflammatory signaling,” *J. Biol. Chem.*, vol. 288, no. 8, pp. 5790–5802, 2013.
- [289] A. Jairaman, M. Yamashita, R. P. Schleimer, and M. Prakriya, “Store-Operated Ca<sup>2+</sup> Release-Activated Ca<sup>2+</sup> Channels Regulate PAR2-Activated Ca<sup>2+</sup> Signaling and Cytokine Production in Airway Epithelial Cells,” *J. Immunol.*, vol. 195, no. 5, pp. 2122–2133, 2015.
- [290] M. S. Grace, T. Lieu, B. Darby, F. C. Abogadie, N. Veldhuis, N. W. Bunnett, and P. McIntyre, “The tyrosine kinase inhibitor bafetinib inhibits PAR2-induced activation of TRPV4 channels in vitro and pain in vivo,” *Br. J. Pharmacol.*, vol. 171, no. 16, pp. 3881–3894, 2014.
- [291] M. D. Hollenberg, K. Mihara, D. Polley, J. Y. Suen, A. Han, D. P. Fairlie, and R. Ramachandran, “Biased signalling and proteinase-activated receptors (PARs): targeting inflammatory disease,” *Br. J. Pharmacol.*, vol. 171, no. 5, pp. 1180–1194, 2014.
- [292] C. Hammond, “The Ionotropic Glutamate Receptors,” in *Cellular and Molecular Neurophysiology*, 4th ed., Academic Press, 2015, pp. 221–244.
- [293] R. Dingledine, K. Borgers, D. Bowie, and S. F. Traynelis, “The glutamate receptor ion channels,” *Pharmacol. Rev.*, vol. 51, pp. 7–61, 1999.
- [294] M. J. Berridge, “Neuronal calcium signaling,” *Neuron*, vol. 21, no. 1, pp. 13–26, 1998.
- [295] E. Gouaux, “Structure and function of AMPA receptors,” *J. Physiol.*, vol. 554, no. 2, pp. 249–253, 2004.
- [296] S. Zhu, R. A. Stein, C. Yoshioka, C. H. Lee, A. Goehring, H. S. McHaourab, and E. Gouaux, “Mechanism of NMDA Receptor Inhibition and Activation,” *Cell*, vol. 165, no. 3, pp. 704–714, 2016.
- [297] B. A. Simms and G. W. Zamponi, “Neuronal voltage-gated calcium channels: Structure, function, and dysfunction,” *Neuron*, vol. 82, no. 1. Cell Press, pp. 24–45, 02-Apr-2014.

- [298] C. Hammond and F. Michel, “The voltage-gated channels of Ca<sup>2+</sup> action potentials: Generalization,” in *Cellular and Molecular Neurophysiology: Fourth Edition*, 2015, pp. 93–120.
- [299] S. Sombati and R. J. DeLorenzo, “Recurrent spontaneous seizure activity in hippocampal neuronal networks in culture,” *J. Neurophysiol.*, vol. 73, no. 4, pp. 1706–1711, 1995.
- [300] P. S. Mangan and J. Kapur, “Factors underlying bursting behavior in a network of cultured hippocampal neurons exposed to zero magnesium,” *J. Neurophysiol.*, vol. 91, no. 2, pp. 946–57, 2004.
- [301] H. Andersson, T. Baechi, M. Hoechl, C. Richter, S. Fujikawa, T. Takano, Y. Kondo, and H. Hirayama, “Autofluorescence of living cells,” *Phys. Status Solidi Curr. Top. Solid State Phys.*, vol. 5, no. 6, pp. 1–7, 2008.
- [302] S. M. Brooke, J. A. Trafton, and R. M. Sapolsky, “Autofluorescence as a confound in the determination of calcium levels in hippocampal slices using fura-2AM dye,” *Brain Res.*, vol. 706, no. 2, pp. 283–288, 1996.
- [303] M. D. Bootman, K. Rietdorf, T. Collins, S. Walker, and M. Sanderson, “Loading fluorescent Ca<sup>2+</sup> indicators into living cells,” *Cold Spring Harb. Protoc.*, vol. doi:10.110, 2013.
- [304] F. J. Aulestia, P. C. Redondo, A. Rodríguez-García, J. A. Rosado, G. M. Salido, M. T. Alonso, and J. García-Sancho, “Two distinct calcium pools in the endoplasmic reticulum of HEK-293T cells,” *Biochem. J.*, vol. 435, no. 1, pp. 227–35, 2011.
- [305] J. Wu, D. L. Prole, Y. Shen, Z. Lin, A. Gnanasekaran, Y. Liu, L. Chen, H. Zhou, S. R. W. Chen, Y. M. Usachev, C. W. Taylor, and R. E. Campbell, “Red fluorescent genetically encoded Ca<sup>2+</sup> indicators for use in mitochondria and endoplasmic reticulum,” *Biochem. J.*, vol. 464, no. 1, pp. 13–22, 2014.
- [306] C. Verderio, S. Coco, G. Fumagalli, and M. Matteoli, “Calcium-dependent glutamate release during neuronal development and synaptogenesis: different involvement of omega-agatoxin IVA- and omega-conotoxin GVIA-sensitive

- channels,” *Proc. Natl. Acad. Sci. U. S. A.*, vol. 92, no. 14, pp. 6449–6453, 1995.
- [307] F. C. Toescu and A. Verkhrats, “Dyes and hardware required,” in *Measuring Calcium and Calmodulin Inside and Outside Cells*, 1st ed., O. H. Petersen, Ed. Berlin Heidelberg: Springer-Verlag Berlin Heidelberg, 2013, p. 301.
- [308] C. Plieth and U. P. Hansen, “Methodological aspects of pressure loading of Fura-2 into Characean cells,” *J. Exp. Bot.*, vol. 47, no. 10, pp. 1601–1612, 1996.
- [309] N. A. Smith, B. T. Kress, Y. Lu, D. Chandler-militello, A. Benraiss, and M. Nedergaard, “Fluorescent Ca<sup>2+</sup> indicators directly inhibit the Na<sup>+</sup>, K-ATPase and disrupt cellular functions,” *Sci. Signal*, vol. 2039, no. January, 2018.
- [310] M. D. Bootman, S. Allman, K. Rietdorf, and G. Bultynck, “Deleterious effects of calcium indicators within cells; an inconvenient truth,” *Cell Calcium*, vol. 73, pp. 82–87, Jul. 2018.
- [311] L. Xiang, Y. Ren, H. Cai, W. Zhao, and Y. Song, “MicroRNA-132 aggravates epileptiform discharges via suppression of BDNF/TrkB signaling in cultured hippocampal neurons,” *Brain Res.*, vol. 1622, pp. 484–495, Oct. 2015.
- [312] R. J. DeLorenzo, D. A. Sun, and L. S. Deshpande, “Cellular mechanisms underlying acquired epilepsy: The calcium hypothesis of the induction and maintainance of epilepsy,” *Pharmacology and Therapeutics*, vol. 105, no. 3. pp. 229–266, 2005.
- [313] H. P. C. Robinson, “Periodic synchronized bursting and intracellular calcium transients elicited by low magnesium in cultured cortical neurons,” *J. Neurophysiol.*, vol. 70, no. 4, pp. 1606–1616, 1993.

# Appendix 1 – Calcium analysis

## MATLAB script

### Conversion of 340/380 fluorescence signal ratios to Ca<sup>2+</sup> concentrations

```
clc;
clearvars;
close all;

%%-----Following script for fura-2 AM work -----
%Section imports 340 and 380 plots and divides them from
each other and
%isolates only the ROIs and creates a time vector

filename = uigetfile
data340 = xlsread(filename);
filename = uigetfile
data380 = xlsread(filename);

% create time vector
Time = data340(:,1);

% selects only ROI intensity counts from spreadsheets.
Change final number to double the number of ROIs
ROI340 = data340(:,2:2:36);
ROI380 = data380(:,2:2:36);
ROIs = ROI340./ROI380;

%Set the baseline range
Baseline = ROIs(1:78,:);
```

```

%Determinee the average baseline for each ROI
Averagebaseline = mean(Baseline);

%Normalise the fluorescent signal against the average base
line
for i = 1:81
    Normalisedsignal(:,i) = (ROIs(i,:) -
Averagebaseline)./Averagebaseline;
End

% %Plot the ROIs against Time
figure(1);plot(Time,Normalisedsignal)

% Allows the wash times to be placed at a custom time and
height on the plots
line('XData', [85 162], 'YData', [3.5 3.5], 'LineStyle',
'-', 'LineWidth', 2, 'Color',[0 0 0])
line('XData', [227 304], 'YData', [3.5 3.5], 'LineStyle',
'-', 'LineWidth', 2, 'Color',[0 0 0])

% set this value to the number of ROIs for later
No.ROIs = 1:18;

%Sets the time ranges that the different drugs were applied
DrugOneRange = 1:214;
DrugTwoRange = 215:429;

%Finds the ratios at the ranges dictated by the drug wash
times
Drugonenormalised = Normalisedsignal(DrugOneRange,:);
Drugwonormalised = Normalisedsignal(DrugTwoRange,:);
DrugOneROI = ROIs(DrugOneRange,:);

```

```

DrugTwoROI = ROIs(DrugTwoRange,:);
Drugonetime = Time(DrugOneRange,:);
Drugtwotime = Time(DrugTwoRange,:);

% find the minimum value of each ROI at the timepoint just
before the second drug wash incase the cells have not
returned to baseline.
Drug2min = Normalisedsignal(123);

%Determine the max value in the drug 1 range for each ROI
drug1 = max(DrugOneROI);

%Find the average peak response for first drug wash
Averagedrug1 = mean(drug1)

%Determine the peak signal for the second drug for each
ROI
drug2 = max(Drugtwonormalised);

%Incase cells had not returned to baseline then subtract
the baseline level prior to drug wash from the drug
response
drug2actual = drug2-Drug2min;

% %Determine average peak signal increase for drug two
Averagedrug2 = mean(drug2actual)

%-----Following script to change to free
calcium ---

% Experimental 340/380 ratios in high calcium
MAXRAT54 = 13.55567686;
MAXRAT58 = 11.75544318;

```

MAXRAT6 = 11.26621568;  
MAXRAT64 = 11.13556475;  
MAXRAT7 = 9.545291077;

% Experimental 340/380 ratios in low calcium  
MINRAT54 = 0.373218912;  
MINRAT58 = 0.327243869;  
MINRAT6 = 0.317324211;  
MINRAT64 = 0.285767276;  
MINRAT7 = 0.250995247;

% Experimental 380 counts in low calcium  
MAXSIG54 = 2157;  
MAXSIG58 = 2265;  
MAXSIG6 = 2246;  
MAXSIG64 = 2502;  
MAXSIG7 = 2895;

% Experimental 380 counts in high calcium  
  
MINSIG54 = 262;  
MINSIG58 = 280;  
MINSIG6 = 273;  
MINSIG64 = 322;  
MINSIG7 = 409;

% Kd for Fura-2  
kd = 225;

```

% Pre calculations in order to convert the average baseline
and ratios into intracellular Ca2+
HighCalcium = MAXRAT58 - ROIs;
LowCalcium = ROIs-MINRAT58;
HighCalBase = MAXRAT58 - Averagebaseline;
LowCalBase = Averagebaseline - MINRAT58;

% Fura-2 conversion equation converting ROIs and
baseline measurements to Ca2+
for p = No.ROIs

    Calciumlevel(:,p) =
(LowCalcium(:,p) ./ (HighCalcium(:,p))) * (MAXSIG58/MINSIG58)
*kd;
    Calciumbaseline(:,p) =
(LowCalBase(:,p) ./ (HighCalBase(:,p))) * (MAXSIG58/MINSIG58)
*kd;

end

% Determine the peak and average calcium increases in
the drug ranges
Calciumleveldrug1 =Calciumlevel(DrugOneRange,:);
MaxCalciumleveldrug1 = max(Calciumleveldrug1);
Calciumincreasedrug1 = MaxCalciumleveldrug1 -
Calciumbaseline;
MeanCalciumleveldrug1 = mean(Calciumincreasedrug1);
Calciumleveldrug2 =Calciumlevel(DrugTwoRange,:);
MaxCalciumleveldrug2 = max(Calciumleveldrug2);
Calciumincreasedrug2 = MaxCalciumleveldrug2 -
Calciumbaseline;
MeanCalciumleveldrug2 = mean(Calciumincreasedrug2);

```

```
% Plot the Ca2+ traces against time and add lines to
demonstrate when washes were carried out
figure(2);plot(Time,Calciumlevel)
line('XData', [50 127], 'YData', [700 700], 'LineStyle',
'-', 'LineWidth', 2, 'Color',[0 0 0])
line('XData', [180 257], 'YData', [700 700], 'LineStyle',
'-', 'LineWidth', 2, 'Color',[0 0 0])

%-----
-----
```

## Baseline fluctuation code

```
clc;
clearvars;
close all;

%%-----Following script for fura-2 AM work -----
%Section imports 340 and 380 plots and divides them from
each other and
%isolates only the ROIs and creates a time vector to
establish baseline fluctuations.
filename = uigetfile
data340 = xlsread(filename);
filename = uigetfile
data380 = xlsread(filename);
time = data340(:,1);
ROI340 = data340(:,2:2:18);
ROI380 = data380(:,2:2:18);
ROIs = ROI340./ROI380

%Isolate the baseline times and ratio values for each ROI
and the 380 counts
Basetime = time(1:45,:);
Baseline = ROIs(1:45,:);
Base380 = ROI380(1:45,:);

%isolates only the ROIs and creates a time vector to
establish baseline fluctuations.
for i = 1:9
meanbase(:,i) = mean(Baseline(:,i));
end
```

```

%Normaliase the baseline for each ROI
for j = 1:9
normalisedbase(:,j) = (Baseline(:,j) -
meanbase(:,j))/meanbase(:,j) ;
end

%Determine the max and min value for in the baseline for
each ROI and the max/min for the 380 counts
Maxfluct = max(Baseline);
Minfluct = min(Baseline);
Maxflut380 = max(Base380);
Minfluct = min(Base380);

%Determine what the percentage fluctuation is for each ROI
for g = 1:15
Baselinefluct(:,g) = (Maxfluct(:,g) -
Minfluct(:,g))/meanbase(:,g);
end

%Plot the normalised baseline for each ROI
plot (Basetime,normalisedbase)

% Variables outputted can now be used to calculate the
actual Ca2+ fluctuation in the baseline measurements

```